



# **Computational Homogenisation based Multiscale Failure Modelling Application to Cortical Bone Tissue**

**Wenjin Xing**

College of Science and Engineering  
Flinders University

This dissertation is submitted for the degree of  
*Doctor of Philosophy*

May 2020



I would like to dedicate this thesis to my loving parents . . .



## Declaration

I certify that this thesis:

1. does not incorporate without acknowledgment any material previously submitted for a degree or diploma in any university; and
2. to the best of my knowledge and belief, does not contain any material previously published or written by another person except where due reference is made in the text.

Wenjin Xing  
May 2020



## Acknowledgements

This PhD project of multiscale failure modelling was carried out at Flinders University in the last four and a half years, with this thesis typeset using Latex and submitted in November, 2019.

First of all, I would like to express my gratitude to my first supervisor Dr Stuart Wildy for his support, freedom and encouragement in the course of my PhD. Besides, I am very grateful to my second supervisor Dr Tony Miller. He was always around when I felt frustrated due to academic difficulties. His meticulous review helped improve the quality of this thesis. I definitely will miss those interesting meetings and discussions we had before.

Thanks also go to several external scholars including Erik Svenning, Milan Jirasek, Joseph Goldmann and Giang Nguyen for their kindly answering some of my technical questions. I would like to thank Dr John Codrington at Adelaide University for introducing to me the bone research topic.

I would like to thank IT guys for offering computer services. Thanks are also directed to those Flinders administrative staff who helped me resolve admission matters.

Living abroad would be more difficult to manage without the companion of my friends from different countries I met in the city of Adelaide. We shared together a lot of happiness and stories in the life outside of research. There are too many names to list, so I decide not to mention any of them.

Last but not least, I would like to deliver my deepest appreciation to my parents for their constant support and trust in me. Without them, this thesis is impossible to complete.

*Wenjin Xing*

Flinders University, Australia



## Summary

Computational approaches to the fracture of engineering components or structures are of ongoing research interest. The development of an accurate, robust and efficient computational fracture framework is not an easy task. To properly account for the effect of material microstructure on the overall response and to understand structure-property connections, multiscale modelling is deemed necessary. However, conventional multiscale approaches have limitations when simulating highly nonlinear phenomena, such as strain localisation. In the presence of strain localisation, at the macroscale the governing equations of equilibrium lose ellipticity, leading to the mesh sensitivity of finite element solutions; furthermore, the homogenised response with standard averaging methods depends on the size of a Representative Volume Element (RVE).

This thesis aims to develop computational multiscale failure approaches for linking fracture or failure events across scales in a manner that alleviates the difficulties mentioned previously. To this end, two different continuous-discontinuous multiscale approaches based on computational homogenisation are proposed. Both are capable of capturing the hardening and softening portions of the material response prior to and after the strength limit. This is accomplished by coupling intact RVE models with Gauss points within the predefined critical regions of macroscopic structures at the beginning of analysis. After the material becomes unstable due to softening, a new crack segment is inserted for which cohesive RVE models are assigned to crack integration points. Such cohesive RVE models are associated with extended computational homogenisation schemes in order to resolve RVE size dependence in the presence of strain localisation.

Inspired by the classical crack band model of Bazant and Oh, the first multiscale failure approach is developed on the basis of an extended computational homogenisation scheme called macro-discontinuity enhanced FE<sup>2</sup>. The weakly periodic BCs that are aligned with the localisation direction are employed to minimise the boundary effects. One major advantage of this model is its simplicity since it does not require the knowledge of evolution details of strain localisation at the microscale. However, it

does not strictly enforce the kinematical consistency between the macroscopic crack and microscopic strain localisation band. To this end, the second multiscale failure approach is developed on the basis of the Failure-Oriented Multiscale Variational Formulation (FOMVF) proposed in the literature. The FOMVF is built upon the requirement of kinematic admissibility and the principle of multiscale virtual power. For both multiscale failure approaches, the crack at the macroscale is represented with the XFEM method to address mesh sensitivity issues. A series of numerical studies are illustrated to show both multiscale failure approaches are capable of handling strain localisation or fracture problems.

Multiscale failure modelling is then applied to explore the failure mechanisms of cortical bone tissue. The effects of fracture properties of the cement line on the effective fracture strength and toughness are investigated by means of microscopic modelling. The extrinsic toughening mechanisms observed in the RVE models are discussed. A three-point bending test for the cortical bone specimen is simulated with the first multiscale failure modelling approach.

# Table of contents

<b>List of figures</b>	<b>xiii</b>
<b>List of tables</b>	<b>xxi</b>
<b>1 Introduction</b>	<b>1</b>
1.1 Background . . . . .	1
1.2 Scope and outline . . . . .	3
1.3 Notation . . . . .	5
1.4 Numerical tools . . . . .	6
<b>2 Literature Review</b>	<b>7</b>
2.1 Computational fracture modelling . . . . .	7
2.2 Multiscale modelling . . . . .	19
2.3 Research gaps . . . . .	24
<b>3 Computational approaches for modelling cracks</b>	<b>25</b>
3.1 Finite element method . . . . .	25
3.2 Continuous crack approaches . . . . .	31
3.3 Discontinuous crack approaches . . . . .	43
3.4 Path following strategy . . . . .	60
3.5 Summary . . . . .	63
<b>4 Multiscale Failure Modelling based on Macro-discontinuity Enhanced FE<sup>2</sup></b>	<b>65</b>
4.1 Preliminaries . . . . .	66
4.2 Boundary conditions on RVE . . . . .	70
4.3 Failure zone averaging . . . . .	79
4.4 Macro-discontinuity enhanced FE <sup>2</sup> . . . . .	87
4.5 Computational implementation . . . . .	92

---

4.6	Numerical studies . . . . .	102
4.7	Concluding remarks . . . . .	112
<b>5</b>	<b>Multiscale Failure Modelling based on Failure-Oriented Multiscale Variational Formulation</b>	<b>113</b>
5.1	Introduction . . . . .	113
5.2	Classical Multiscale variational Model (ClaMM) formulation . . . . .	116
5.3	Cohesive Multiscale variational Model (CohMM) formulation . . . . .	121
5.4	Computational implementation . . . . .	128
5.5	Numerical verification . . . . .	129
5.6	Summary . . . . .	141
<b>6</b>	<b>Application of Multiscale Modelling to Cortical Bone Fracture</b>	<b>143</b>
6.1	Bone hierarchy and fracture toughness . . . . .	144
6.2	Multiscale failure study of cortical bone . . . . .	154
6.3	Summary . . . . .	166
<b>7</b>	<b>Conclusions and Perspective</b>	<b>167</b>
7.1	Main Contributions . . . . .	167
7.2	Plans for future work . . . . .	169

# List of figures

1.1	Cement-based composite materials show different observation scales. Reproduced with permission from (Constantinides and Ulm, 2004), © 2004, Elsevier. . . . .	1
1.2	Steel framed building in ChuanXinDian Chemical Park in Shifang County, suffered heavy damage during the 2008 Sichuan earthquake in China. Source: <a href="https://commons.wikimedia.org/wiki/File:Shifa_Chuanxindian_earthquake_park_05.jpg">https://commons.wikimedia.org/wiki/File:Shifa_Chuanxindian_earthquake_park_05.jpg</a> , via Wikimedia Commons. .	2
2.1	Schematic of cohesive zone model. . . . .	9
2.2	Two crack representation forms: (a) implicit (smeared) approach, and (b) explicit (discrete) approach. . . . .	10
2.3	Schematic of weak and strong discontinuities: with (a) continuous displacement and discontinuous strain at the crack, and (b) discontinuous displacement and infinite strain at the crack. . . . .	11
2.4	Level set functions for discrete crack representation. . . . .	18
2.5	Different multiscale modelling approaches: (a) sequential, (b) concurrent and (c) semi-concurrent. . . . .	20
2.6	The semi-concurrent multiscale method proposed by Nguyen et al. (2012c) for modelling mode-I cohesive failure. Reprinted with permission from (Karamnejad and Sluys, 2014), © 2014, Elsevier. . . . .	23
3.1	A two-dimensional solid body under external loading. . . . .	26
3.2	Exponential softening law $q - r$ for the isotropic damage model. . . .	36
3.3	Damage criterion based on the equivalent strain type, degradation only in tension. . . . .	36
3.4	Projection method for the estimation of crack band width: (a) crack band along element diagonals, and (b) effective band size computed by projecting along the direction perpendicular to the crack band. .	38

3.5	L-shaped panel test (thickness 100 mm): (a) damage profile at the final load level and (b) force-displacement curves for two different mesh sizes (coarse and fine). The modified von Mises equivalent strain has been adopted. . . . .	42
3.6	A two-dimensional fracture problem. The cohesive crack behaviour is characterised by the cohesive zone model in the wake of the fictitious crack. . . . .	43
3.7	Schematic of two types of traction-separation laws. . . . .	45
3.8	1D linear cohesive elements are embedded between continuum elements to model the crack. Global coordinates and local coordinates are denoted by $(\mathbf{x}, \mathbf{y})$ and $(\mathbf{t}, \mathbf{n})$ , respectively. The nodes for the typical cohesive element are ordered 1, 2, 3, 4. . . . .	46
3.9	Definition of the local axes $(\mathbf{t}, \mathbf{n})$ , midplane $AB$ and rotation angle $\theta$ in a cohesive element. . . . .	47
3.10	Deformed configuration of a compact-tension specimen under mode-I fracture with the crack modelled with cohesive elements. $U_2$ represents the vertical displacement. . . . .	50
3.11	A crack with kinks to approximate a smooth curved crack with a local polar coordinate system at the crack tip. $\mathbf{x}^*$ is the closest point to $\mathbf{x}$ on the crack. . . . .	55
3.12	A typical FE mesh with a crack. The circled nodes are enriched with the Heaviside function, and the squared nodes are enriched with near-tip asymptotic fields. . . . .	56
3.13	Energy dissipation based arc-length control of equilibrium path with a snap back. The energy dissipation increment $\Delta E$ is prescribed for time step from $t_n$ to $t_{n+1}$ . . . . .	61
4.1	Schematic of the first-order CH. . . . .	66
4.2	Schematic representation of a periodic RVE with mapped boundaries; Corner vertices are labelled 1,2,3,4. . . . .	71
4.3	Schematic representation of hybrid BCs for tensile failure mode, in which periodic constraints are applied on the top and bottom edges and linear displacement constraints on the left and right edges. . . .	73
4.4	Illustration of weakly periodic BCs with periodicity along the horizontal direction. Piecewise constant boundary traction discretisation has been adopted. . . . .	73
4.5	BC comparison test: mesh for the used unit cell. . . . .	77

4.6	BC comparison test: effective stress-RVE size curves. LBC: linear BC, MKBC: minimal kinematic BC, PBC: periodic BC and WPBC: weakly periodic BC. . . . .	78
4.7	BC comparison test: deformed configurations (magnified by 5000) obtained with different boundary conditions for the RVE made of $2 \times 2$ unit cells. . . . .	78
4.8	Square RVE with a vertical localisation band across the boundary. . . . .	79
4.9	Three meshed RVE configurations of different sizes with holes. They are identified with $RVE_1$ , $RVE_2$ and $RVE_3$ . . . . .	81
4.10	Homogenised stress-strain responses of three voided samples under uniaxial tensile loading, using the standard first-order computational homogenisation scheme. . . . .	82
4.11	Homogenised cohesive responses of three voided samples under tensile loading, where the failure zone averaging scheme is employed. Note that the curves are already shifted to the left by an amount of the damage displacement at the onset of strain localisation. . . . .	82
4.12	Damage patterns at the end of analyses of two voided samples under tensile loading: (a) $RVE_1$ and (b) $RVE_2$ . . . . .	83
4.13	Extracted cohesive laws with shifting for three different values of parameter $c$ using a regular RVE of size $10 \times 10 \text{ mm}^2$ with a central circular hole. . . . .	83
4.14	Strain localisation bands for different values of parameter $c$ . . . . .	84
4.15	Idealisation of material composition of plain concrete at the mesoscale. . . . .	85
4.16	Softening concrete RVEs in tension: standard averaging (a) vs. failure zone averaging (b). . . . .	85
4.17	Damage patterns of concrete RVEs ( $\rho = 40\%$ ) of five sizes: $10 \times 10$ , $15 \times 15$ , $20 \times 20$ , $30 \times 30$ from left to right (unit of length is mm). . . . .	86
4.18	Cohesive responses (unshifted) of three realisations of concrete RVEs ( $\rho = 40\%$ ): size $10 \times 10$ (left) and size $15 \times 15$ (right). . . . .	87
4.19	Damage patterns of three different realisations of concrete RVEs of size $15 \text{ mm}$ ( $\rho = 40\%$ ). . . . .	87
4.20	Macroscale domain with a macroscale crack $\Gamma_d$ corresponding to a strain localisation band $\Omega_d$ . Also given is the an rotated RVE that coincides with the crack normal direction $\mathbf{n}_M$ . The RVE with microstructural details is used to simulate material responses, including strain localisation. . . . .	88

4.21 Equivalent macroscopic crack: mechanical quantities of interest at (a) microscale and (b) macroscale. . . . .	90
4.22 Extended computational homogenisation for the multiscale constitutive model of cohesive cracks. . . . .	92
4.23 Macroscopic fracture problem modelled with XFEM: integration scheme, description of material constitutive models and propagation direction based on the maximum principal stress criterion on the nonlocal stress at the crack tip. . . . .	95
4.24 Multiscale failure modelling: at the beginning, four bulk RVEs are coupled to the four bulk GPs in a quadrilateral element. When strain localisation emerges in one of the bulk RVEs, a macroscale crack segment is inserted (in this case, it goes through the element centre). The two cohesive GPs are coupled to cohesive RVEs with their initial state copied from the localised RVE. The bulk GPs of the fractured element behave elastically with the elastic stiffness matrix $D_{un}$ from unloading the localised RVE. . . . .	96
4.25 Recursive sub-stepping for a typical failed step $[t_n, t_{n+1}]$ in solving the RVE equilibrium problem. Reproduced with permission from (Sommer et al., 2009), © 2009, Elsevier. . . . .	99
4.26 Adhesive layer failure (Example 4.6.1): DNS model - (a) geometry and boundary conditions; Multiscale failure model - (b) macroscale geometry meshed with 2 quadrilateral elements and 1 interface element, and (c) RVE geometry. All units are in mm. . . . .	102
4.27 Adhesive layer failure (Example 4.6.1: (a) mesh for the DNS model and (b) mesh for the RVE representing the adhesive layer. . . . .	103
4.28 Comparison between results from the DNS and multiscale failure simulation in the Example 4.6.1. . . . .	103
4.29 Uniaxial tension test on a plate with holes: DNS model - (a) geometry and boundary conditions; Multiscale failure model - (b) macroscale geometry meshed with 3 quadrilateral elements and boundary conditions and (c) RVE geometry. All units are in mm. . . . .	104
4.30 Uniaxial tension test (Example 4.6.2.1): load-displacement curves obtained by DNS and multiscale failure model. with various microstructures. . . . .	105

4.31 Uniaxial tension test (Example 4.6.2.1): damage profile obtained by DNS (left) and (right) $y$ -direction displacement contour at the macroscale and damage profiles of cohesive RVEs, obtained by multiscale failure model. with various microstructures. . . . .	105
4.32 Handling snap-back test: two different values for maximum dissipated energy increment $\Delta E_{max}$ are chosen for comparison. Marked points except the origin on the curves denote the time steps at which the energy dissipation based arc-length control is used. . . . .	106
4.33 Multiscale inclined crack problem: geometry of the macroscopic structure and boundary and loading conditions; RVE with an inclined microscopic crack modelled with cohesive elements. The angle $\beta$ characterises the crack direction and loading direction. . . . .	107
4.34 Multiscale inclined crack problem: simulation results of force versus displacement at the right edge for different loading directions determined by $\beta$ . . . . .	108
4.35 Multiscale inclined crack problem: deformed configurations of the macroscopic structure (magnified by a factor of 500) and the $1 \times 1$ RVE (magnified by a factor of 50) for different crack angles with the horizontal direction, $30^\circ$ , $45^\circ$ , $60^\circ$ and $90^\circ$ , at total loss of the strength. . . . .	109
4.36 Three-point bending test in Example 4.6.3. DNS model: geometry, boundary and loading conditions. The central region is resolved with explicit mesostructural details with aggregate volume fraction as 30%. . . . .	109
4.37 Three-point bending test in Example 4.6.3: macroscale mesh and $8\text{ mm} \times 8\text{ mm}$ RVE mesh. . . . .	110
4.38 Three-point bending test in Example 4.6.3: comparison of load versus midspan deflection curves for the DNS approach and the multiscale failure approach. . . . .	110
4.39 Three-point bending test in Example 4.6.3: localisation patterns of the DNS model at four different deflection magnitudes. . . . .	111
4.40 Three-point bending test in Example 4.6.3: propagating macroscale crack at four different deflection magnitudes. . . . .	111
5.1 Schematic illustration of the multiscale failure model built upon the failure-oriented multiscale variational formulation. Two material states that are stable and unstable are distinguished, signified by the bifurcation time $t_N$ . . . . .	114

5.2	A mixed-mode strain localisation band signified by the normal $\mathbf{n}$ . The direction pointed by $\gamma$ coincides with the initial opening velocity direction. . . . .	116
5.3	Prescription of boundary conditions on the bulk RVE and cohesive RVE models. . . . .	123
5.4	Definition of strain localisation region $\Omega_m^L$ for a complex microstructure. It includes softening material $\Omega_m^{Ls}$ and traverses a weak elastic inclusion $\Omega_m^e$ and a void inclusion $\Omega_m^v$ . . . . .	127
5.5	Three RVE configurations with different sizes and different numbers of homogeneous damageable localisation bands. Each localisation band of thickness $l_m$ forms an angle $\alpha$ with the horizontal line. . . .	131
5.6	Homogenised stress-strain curves for three different RVE sizes: the ClaMM is adopted during the whole simulation. . . . .	132
5.7	Homogenised cohesive response ( $T_x$ vs. $\llbracket u \rrbracket_{Mx}$ ) resulted from the CohMM scheme adopted after the strain localisation is detected on the RVE: a linear softening law is taken. . . . .	133
5.8	The deformed RVEs with a vertical softening band: the red colour identifies the location of the damaging zone modelled with the smeared crack approach. Amplification factor is set to 200. . . . .	133
5.9	Homogenised cohesive response ( $T_{My}$ vs. $\llbracket u \rrbracket_{My}$ ) resulted from the CohMM scheme adopted after the strain localisation is detected on the RVE: a linear softening law is taken. . . . .	134
5.10	Homogenised cohesive response using the CohMM after the strain localisation: (a) $T_{Mx}$ vs. $\llbracket u \rrbracket_{Mx}$ and (b) $-T_{My}$ vs. $-\llbracket u \rrbracket_{My}$ . A linear softening damage law is adopted. (Note that a negative sign is added before the $y$ -components to ease the display. ) . . . . .	135
5.11	Homogenised cohesive response using the CohMM after the strain localisation: (a) $T_{Mx}$ vs. $\llbracket u \rrbracket_{Mx}$ and (b) $-T_{My}$ vs. $-\llbracket u \rrbracket_{My}$ . An exponential softening damage law is adopted. (Note that a negative sign is added before the $y$ -components to ease the display. ) . . . . .	136
5.12	Three RVE configurations of different sizes and their material composition: each RVE domain is meshed into quadrilateral elements with lengths $1/11w$ and $1/11h$ ; material model of $M_1$ is linear elastic, material model of $M_2$ is isotropic elastic damage and material $M_3$ represents void or hard inclusion. . . . .	136

5.13 Homogenised cohesive responses ( $T_x$ vs. $\llbracket u \rrbracket_{Mx}$ ) of RVEs with inhomogeneous localisation bands in Case a, resulted from the CohMM scheme. The red shaded circle (labelled $T$ ) marks the transition from energy dissipation states to elastic states hereafter. . . . .	138
5.14 Homogenised cohesive responses ( $T_x$ vs. $\llbracket u \rrbracket_{Mx}$ ) of RVEs with inhomogeneous localisation bands in Case b, resulted from the CohMM scheme. The solution from RVE with a homogeneous band is selected as reference. . . . .	138
5.15 An unloading and reloading process is inserted to the equilibrium path. Homogenised cohesive response using the CohMM after the strain localisation: (a) $T_{Mx}$ vs. $\llbracket u \rrbracket_{Mx}$ and (b) $-T_{My}$ vs. $-\llbracket u \rrbracket_{My}$ . . . . .	139
5.16 Geometry of the uniaxial tensile test in 5.5.4 with full resolution (unit of length: mm). . . . .	140
5.17 Load-displacement diagrams of the uniaxial tensile test in 5.5.4 with the DNS and multiscale failure simulation. . . . .	141
6.1 Hierarchical structural organisation of bone. Reprinted from (Rho et al., 1998) with permission granted from Elsevier. . . . .	144
6.2 Schematic microstructure of cortical bone (cross-sectional view). The osteons with Haversian canals are distributed within the interstitial matrix, separated by cement lines (not shown). The outer are the circumferential lamellae. . . . .	146
6.3 Schematic illustration of extrinsic toughening mechanisms possible in cortical bone. a. Crack bridging by collagen fibres, b. crack deflection by osteons, c. constrained microcracking, and d. uncracked-ligament bridging. . . . .	147
6.4 Schematic illustration of: a. a long human femur; b. cortex positions in anatomical terms (letters A, P, M and L stand for anterior, posterior, medial and lateral respectively); c. fracture specimens fabricated for testing radial, longitudinal, transverse fracture toughness. Arrows point towards the anticipated crack propagation direction. . . . .	150
6.5 Satisfactory prediction (right) of crack path around osteons without penetration using a new crack orientation criterion, in good agreement with experimental evidence (left) by Budyn et al. (Budyn and Hoc, 2010). Reprinted from (Marco et al., 2018) with permission from Elsevier. . . . .	154
6.6 A typical mesoscopic sample for cortical bone tissue. . . . .	156

6.7	Effective traction-separation laws for different sample sizes of cortical bone, obtained by averaging over five realisations. . . . .	158
6.8	Computed effective fracture properties (Mode I) for cortical bone tissue. The error bars represent the standard deviations. . . . .	159
6.9	Final crack paths for bone samples of different sizes. Red circles highlight local bridging zones located on crack paths. . . . .	160
6.10	Parametric study of fracture strength $\sigma_{cl}$ of cement line: effective traction-separation laws. . . . .	160
6.11	Parametric study of fracture strength $\sigma_{cl}$ of cement line: computed effective fracture properties (Mode I), $\sigma_{eff}$ and $G_{eff}$ . . . . .	161
6.12	Parametric study of critical fracture energy $G_{cl}$ of cement line: effective traction-separation laws. . . . .	162
6.13	Parametric study of critical fracture energy $G_{cl}$ of cement line: computed effective fracture properties (Mode I), $\sigma_{eff}$ and $G_{eff}$ . . . . .	162
6.14	Three-point bending test of cortical bone: geometry, boundary and loading conditions. . . . .	163
6.15	Three-point bending test of cortical bone: load versus deflection curves for two different cement line strengths (reduced and reference) using a multiscale failure approach. . . . .	164
6.16	Three-point bending multiscale simulation of cortical bone: macroscale deformation (x10), and typical bulk and cohesive RVE deformed configurations (magnified for visualisation purposes) at the final load step. . . . .	165

# List of tables

4.1	Material constants for the voided microstructure. . . . .	82
4.2	Material constants of the heterogeneous three-phase concrete material.	85
5.1	Material parameters of two phases of the heterogeneous material used in Section 5.5.1. . . . .	131
5.2	Material parameters of three phases of the heterogeneous material used in Section 5.5.2. . . . .	137
6.1	Material constants of the mesoscopic constituents in cortical bone. .	157



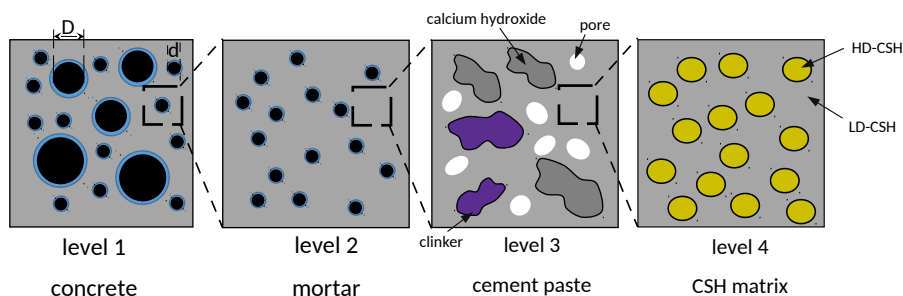
# Chapter 1

## Introduction

### 1.1 Background

Research on advanced material design and assessment has been on the rise and become the most important part of innovation in technologies in last few decades. Natural or man-made composite materials are broadly applied across the spectrum of industrial sectors, such as aerospace, defence, energy, manufacturing, construction and transport.

The majority of materials are heterogeneous, consisting of diverse constituents, and displaying a complex topology of microstructures. Figure ?? shows a simplified



When  $d/D \ll 1$ , consider aggregates with ITZ embedded in a mortar matrix.

When  $d/D \sim 1-5$ , consider gradation of aggregates/sand inclusions embedded in a cement paste matrix.

Calcium silicate hydrate (CSH) matrix comprises high-density CSH (HD-CSH) and low-density CSH (LD-CSH).

**Figure 1.1** Cement-based composite materials show different observation scales. Reproduced with permission from (Constantinides and Ulm, 2004), © 2004, Elsevier.

model of the four-level microstructure of concrete. At each observation scale, the structure may display different deformation and failure mechanisms. Furthermore, it is recognised that the constituents and their evolution and interactions largely contribute to the mechanical performance of materials at coarser scales.

Failure, especially fracture, reduces the load-bearing capacity, and would make components or structures unfit for service in an engineering application. Figure 1.2 illustrates such an example of collapse caused by a severe earthquake in 2008 in China. Therefore, damage tolerance design and fracture prediction are essential to enhance and maintain the mechanical reliability of composite structures. However, it is difficult to fabricate and test full-size specimens because of enormous experimental labour and cost. An alternative to experimental exploration is a computational approach.



**Figure 1.2** Steel framed building in ChuanXinDian Chemical Park in Shifang County, suffered heavy damage during the 2008 Sichuan earthquake in China. Source: [https://commons.wikimedia.org/wiki/File:Shifa\\_Chuanxindian\\_earthquake\\_park\\_05.jpg](https://commons.wikimedia.org/wiki/File:Shifa_Chuanxindian_earthquake_park_05.jpg), via Wikimedia Commons.

With the aid of computational tools, the effects of the external environment (e.g., loading and chemicals) can be studied in great detail. To date, continuous efforts are still being made to improve the predictive ability of computational models, particularly for fracture. Phenomenological constitutive material models are typically employed to describe highly nonlinear material behaviours at the structural scale. However, the mathematical derivation of these material models is often obscure to derive and a large set of material parameters are needed to calibrate. Furthermore, most of these analytical material laws are not of high accuracy since they lack enough information such as interactions from the fine scales.

To this end, brute-force simulation approaches can be potential options where the

details of microstructures are explicitly resolved at the coarse scale, but they are not feasible in practice since the computational burden is prohibitive. Therefore, during the last two decades, a number of numerical and computational models, referred to as multiscale models, have been proposed to get around this problem. These are models based on the data of microstructures. One major category of multiscale models is based on “homogenisation” ( similar to “coarse graining” in physics) (Matoš et al., 2017). The fundamental idea behind homogenisation methods is to replace the heterogeneous material by an equivalent homogenous one. Among homogenisation methods, one noticeable branch is computational homogenisation. By means of computational homogenisation, a phenomenological constitutive model is no longer needed for those material points coupled with micro samples, known as Representative Volume Elements (RVEs) or Statistical Volume Elements (SVEs). The conventional computational homogenisation methods have been successfully applied to characterise the linear or nonlinear behaviour of heterogeneous materials. Nonetheless, they show deficiencies when dealing with strain localisation problems, which are common to the class of quasi-brittle materials. Upon strain localisation, the existence of RVE is questioned. One major reason is the violation of the principle of scale separation. Furthermore, the boundary value problem of statics at the macroscale becomes ill-posed, when strain localisation occurs. This is caused by the loss of ellipticity of stress governing equations. Existing regularisation techniques or discontinuous crack approaches have to be employed. To date, several examples of extended computational homogenisation schemes have appeared in the literature which are able to deal with strain localisation. However, they have shortcomings (e.g., complexity and practicability) and have not been widely applied to real-world situations. Therefore, the development of computational homogenisation for capturing material instability is still worth more attention.

In view of few practical applications of multiscale approaches, the developed multiscale failure modelling tool is applied to explore fracture mechanisms of cortical bone.

## 1.2 Scope and outline

### 1.2.1 Scope

With the fact in mind that a comprehensive understanding of heterogeneous materials in terms of mechanical behaviours is not a simple task, this PhD work aims

to explore some existing and well-developed computational failure and fracture approaches in the literature and to propose novel multiscale (two-scale) approaches for structural and material failure problems. This project involves the disciplines of continuum solid mechanics, numerical methods and computer science. Much effort has been directed towards the final goal in mind, that computer-based simulations to mimic real-world engineering structural fracture or investigate material degradation mechanisms should be more reliable and effective. However, this is not a simple task to accomplish, though a multitude of theories, approaches, and techniques are there for references.

In this project, the following research questions need to be answered:

1. What is the state-of-art research in computational fracture mechanics?
2. The failure events such as microcracking and debonding in the microstructure of hierarchical and heterogeneous materials adversely affect macrostructural behaviour. How to capture the interplay between the failure events at the microscale and the opening crack at the macroscale by means of multiscale approaches that are built upon computational homogenisation?
3. How can the developed multiscale failure modelling techniques be applied to the failure study of cortical ( compact ) bone, which possesses a multitude of length scales in its structural composition?

### 1.2.2 Thesis outline

The thesis consists of seven chapters. The remainder of the thesis is organised as follows:

Chapter 2 gives a comprehensive review of some existing computational methods to fracture and multiscale modelling techniques. The research gaps are identified.

In Chapter 3, the theoretical basics and algorithmic aspects of several computational fracture methods that will be used in the following chapters are explained.

Chapter 4 presents a new multiscale failure model that is based on an extended CH scheme called the macro-discontinuity enhanced FE<sup>2</sup>. Theoretical derivation and implementation details are elaborated. Numerical examples with direct numerical simulation results as reference solutions are illustrated to demonstrate the effectiveness of the multiscale failure model in dealing with strain localisation.

In Chapter 5, a new multiscale failure model that is based on the Failure-Oriented

Multiscale Variational Formulation proposed in the literature is presented, with emphasis on the numerical implementation aspects.

Chapter 6 deals with the application of the multiscale failure modelling to study cortical bone failure. The effects of fracture properties of cement lines on overall strength and fracture toughness are explored. A three-point bending specimen made of cortical bone is simulated with the multiscale approach presented in Chapter 4. The thesis ends up with Chapter 7 where the main contributions are outlined and future research directions are pointed out.

## 1.3 Notation

Three style of notation are adopted in this manuscript, namely indicial notation, tensor notation and matrix notation. Equations in continuum mechanics are expressed in indicial or tensor notation. Finite element formulations are expressed in matrix notation. Three notation forms are illustrated by the inner product of two vectors

$$a_i b_i = \mathbf{a} \cdot \mathbf{b} = \mathbf{a}^T \mathbf{b} . \quad (1.1)$$

In indicial notation, the components of tensors are explicitly specified e.g., a vector in indicial notation is hence represented by  $x_i$ , where the index  $i$  ranges from one to the number of spatial dimensions. Indices follow the convention of the Einstein summation, that is, when an index variable appears twice in a single term and is not otherwise defined, it implies summation of that term over all the values of the index. In tensor notation, tensors of order one or greater are written in boldface. Lower case bold-face letters are used for first-order tensors, whereas upper case bold-face letters indicate high-order tensors. The major exceptions to this rule are the stress tensor and the strain tensor which are second-order tensors, but are denoted by lower case symbols as  $\boldsymbol{\sigma}$  and  $\boldsymbol{\varepsilon}$ . Major tensor operators include tensor products denoted by  $\otimes$  and inner product denoted by  $(\cdot)$ . The symbol  $\otimes^s$  means the symmetric part of a tensor product.

In matrix notation, the same symbols as for tensors are used to denote the matrices but the connective symbols for indicating the operation are omitted. Symmetric high order tensors are expressed in matrix or vector forms using Voigt notation. For example, a two-dimensional stress tensor  $\boldsymbol{\sigma}$  is written as a vector  $(\sigma_{11}, \sigma_{22}, \sigma_{12})$  in Voigt notation, a two-dimensional strain tensor  $\boldsymbol{\varepsilon}$  is written as a vector  $(\varepsilon_{11}, \varepsilon_{22}, \varepsilon_{12})$  in Voigt notation and the corresponding fourth-order elastic stiffness tensor  $\mathbf{D}$  is

represented by a  $3 \times 3$  matrix  $\mathbf{D}$ . The right superscript  $T$  is used to represent the transpose of a vector or matrix.

Subscripts  $M$  and  $m$  are used to indicate if a quantity belongs to the macroscale or microscale, respectively. Symbols will be defined at their first appearance.

## 1.4 Numerical tools

All the computational implementation was performed in the open source platform called OOFEM ([Patzák, 2012](#)), which is written in C++ and follows object oriented programming paradigm. All the finite element meshes were generated with the Gmsh ([Geuzaine and Remacle, 2009](#)). Matlab ([MATLAB, 2014](#)) was used to write several scripts, such as generating the geometry of random microstructures and conducting data analysis. 2D Plots were done in Gnuplot ([Janert, 2010](#)) and Paraview was used for scientific visualisation purposes ([Ayachit, 2015](#)).

# Chapter 2

## Literature Review

In this chapter, some widely used methods in the fields of computational fracture modelling and multiscale modelling are reviewed. The focus is restricted to finite element based methods.

### 2.1 Computational fracture modelling

In the literature, a plethora of computational failure or fracture modelling methods have been developed and further developments based on continuum mechanics or discrete mechanics are taking place. Only continuum mechanics based methods in the context of the Finite Element Method (FEM) will be examined in this review, without any claim of completeness. The broad class of meshless methods and discrete models is outside the scope of this review.

Failure simulations of quasi-brittle materials are of considerable research interest for the following reasons:

- In engineering, most natural or man-made materials are heterogeneous at fine scales and exhibit complicated progressive failure processes across length and time scales.
- The need to ensure structural integrity calls for robust and efficient numerical tools to model the damage evolution and crack propagation in structures.
- The introduction of strong discontinuities (e.g. cracks) in FEM approximations is not a simple task. For example, the predicted response of a material with discontinuities can be very sensitive to the mesh size and other geometrical features of mesh such as direction.

- Accurate representations of the crack opening and crack path are important for accurately predicting global structural responses.
- Material failure may be of a complex mixed-mode form. In addition, surrounding environmental factors, such as temperature and the presence of fluids and chemical species, affecting material deterioration may need to be accounted for.

## 2.1.1 Crack behaviour models

The mechanical behaviour of a physical crack can be described as traction-free or cohesive. The major difference between these two models lies in whether or not there are transmitted stresses between the two near-tip crack surfaces, provided by different mechanisms such as uncracked ligaments and plasticity.

### 2.1.1.1 LEFM

Linear elastic fracture mechanics (LEFM) provides the fundamental principles and methodologies concerned with assessing the integrity of elastic structures or components with traction-free cracks under loading. The earliest work in LEFM can date back to ([Griffith and Eng, 1921](#)) for the study of failure of brittle materials, where the significant contribution was Griffith's criterion. The Griffith's criterion states that a crack will propagate when the reduction in potential energy that occurs due to crack growth is not less than the increase in surface energy needed for the creation of new free surfaces. It is also assumed that energy dissipation takes place only at the crack tip.

### 2.1.1.2 CZM

The applicability of the LEFM is restricted for cases where no initial cracks are predefined (e.g., fracture study for geometry with notches) and the fracture process zone is not small compared with the structural dimensions (e.g., concrete specimen failure). Therefore, it lacks the ability to predict the failure onset of an intact structure and even to capture the size effect prevalent in quasi-brittle materials ([Bazant and Planas, 1997](#), [Bažant, 2000](#)). This is the primary reason why the cohesive zone models (CZM) (see Figure 2.1) have attracted so much research attention and contributed to a number of successful engineering applications ([Elices et al., 2002](#),

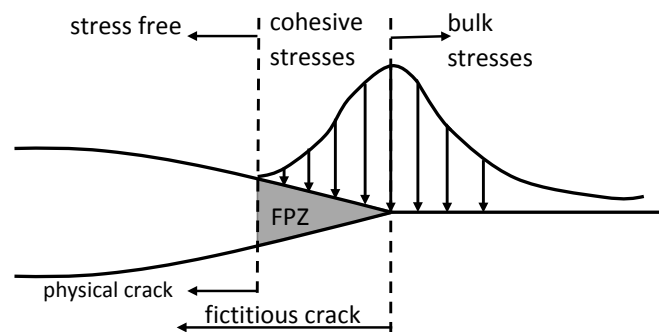


**Figure 2.1** Schematic of cohesive zone model.

[Yang and Cox, 2005](#)).

In the cohesive zone model, it is assumed that the effects of the nonlinear fracture process zone (FPZ) are collapsed onto a displacement discontinuity surface, instead of at the crack tip. The fundamental assumption for the cohesive zone model is that material split or fracture is a progressive process at the microscale in the sense that there are still cohesive forces that the material is able to transfer up to the final zero stress state. As a consequence, the cohesive constitutive model represents the failure characteristics of the material.

The pioneering theoretical work of cohesive zone models can be traced back to [Barenblatt \(1962\)](#) and [Dugdale \(1960\)](#). They introduced the cohesive zone concept from different perspectives during their studies of fracture of brittle and ductile materials, respectively. The CZM development, in the form of nonlinear spring foundations, was adopted by [Ungsuwarungsri and Knauss \(1987\)](#) to study crazing in polymers considering the cohesive zone as a softening material, and by [Song and Waas \(1993\)](#) to study delamination fracture in laminated composites. An important aspect in the use of cohesive zone models is the characterisation of traction-separation laws. The most widely employed forms among others include the potential based exponential model proposed by [Xu and Needleman \(1994\)](#), the trapezoidal model by [Tvergaard and Hutchinson \(1996\)](#) and the bilinear model by [Geubelle and Baylor \(1998\)](#). Compared to the originally proposed exponential cohesive laws in the literature, the bilinear models are favoured in some sense due to the advantage of providing an adjustable initial slope to reduce artificial compliance. Calibration examples of the fracture parameters involved in traction-separation laws can be found in ([Song et al., 2006](#), [Alfano et al., 2009](#)).

### 2.1.2 Crack representations

The FEM is a well-established but constantly evolving numerical method which is widely used to solve boundary value problems (BVPs). When simulating structural or material failure with the FEM, a key question arises of how to represent cracks in the discretisation. In the literature, implicit and explicit crack descriptions exist, see Figure 2.2. The implicit crack representation simply smears the crack discontinuity over some discretised region, being a row of single elements or a layer of several elements in width. The kinematics are sketched in Figure 2.3(a). Alternatively, the explicit crack representation geometrically models the actual displacement jump, as in Figure 2.3(b). On the basis of these two representations at the discrete level, two families of computational approaches to fracture are distinguished, the continuous or smeared crack approaches and the discontinuous or discrete crack approaches.

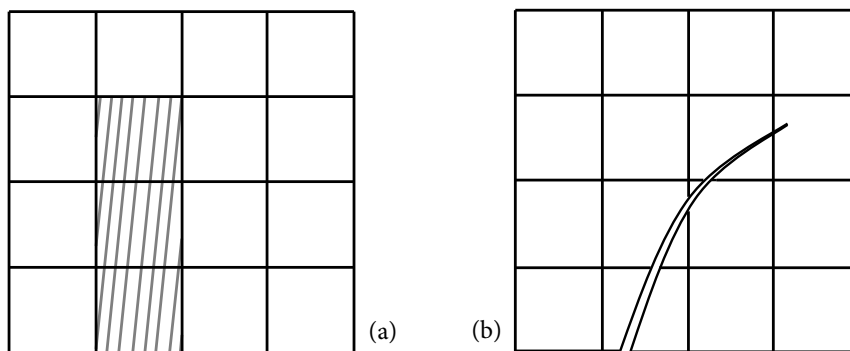


**Figure 2.2** Two crack representation forms: (a) implicit (smeared) approach, and (b) explicit (discrete) approach.

The smeared crack approaches introduce a strain localisation band with concentrated strains. Outside this band the material normally undergoes elastic unloading. Strain localisation may occur due to the mechanism of material softening. Material softening is realised in smeared crack approaches by defining the material constitutive laws with strain softening (e.g., continuum damage models and plasticity models with softening). The smeared crack approaches have two distinct versions, the *local* smeared crack approach (the crack band approach as proposed in (Bažant and Oh, 1983) ) and the family of *fully regularised* smeared crack approaches. They share common features of the bounded strains at the crack and assuming standard stress-strain constitutive equations.

In the local smeared crack approach, only a single element transverses the width of the strain localisation band as shown in Figure 2.2(a). The displacement jump presents two (finite) weak discontinuities (that is, discontinuities in strains) across

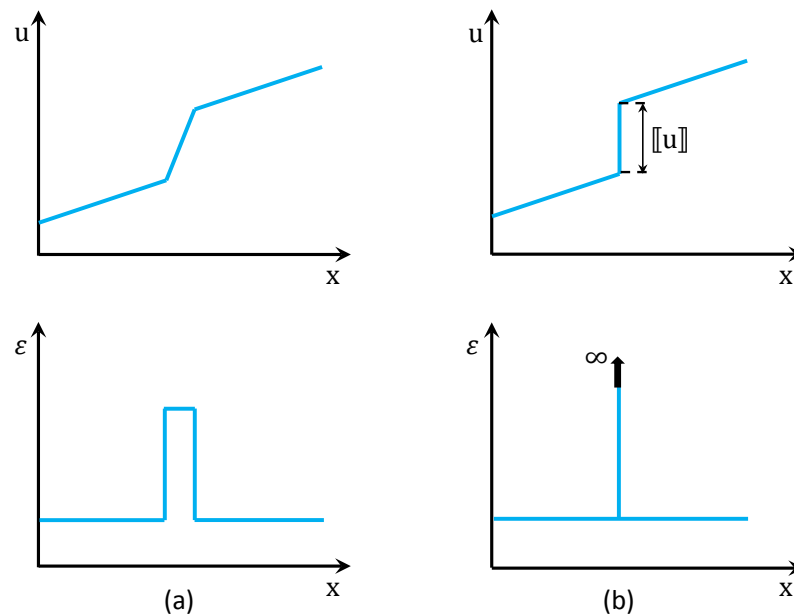


**Figure 2.3** Schematic of weak and strong discontinuities: with (a) continuous displacement and discontinuous strain at the crack, and (b) discontinuous displacement and infinite strain at the crack.

the intersections between the strain localisation element and the adjacent ones. The fully regularised smeared crack approaches are formulated within continuum damage mechanics and mostly employ more elements across the strain localisation band, which leads to a smoother variation of the displacement and strain fields over the band width. The significant difference between two versions is that the fully regularised smeared crack approaches recover the ellipticity of the underlying partial differential equations, whereas the other does not.

In the discrete crack approaches, the crack can be placed along inter-element edges or embedded in a single element as shown in Figure 2.2(b). Due to the appearance of the strong displacement discontinuity, the strains at the crack become infinite and need to be interpreted in a distributional sense, see Figure 2.3(b). Therefore, the standard stress-strain constitutive laws are no longer meaningful at the crack. For this reason, upon crack initiation based on some criterion, the displacement jump across the crack needs to be related to the stress vectors (tractions) on the crack surfaces. In a displacement-driven FE analysis, a traction-separation law is usually introduced instead of a stress-strain law for describing the cohesive crack behaviour. The link between the smeared crack approaches (either local or fully regularised) and the discrete crack approaches is an active research issue (Planas et al., 1993, Bazant and Planas, 1997, Borst et al., 2004, Cazes et al., 2009). However, generally

speaking, a smeared crack can be regarded as a sort of regularisation of a discrete crack over a certain width, while on the other hand, a discrete crack can be interpreted as the limit case of a smeared crack with a vanishing width. Moreover, these two crack representations are considered equivalent to each other from a viewpoint of energetic equivalence.

## 2.1.3 Continuous (smeared) crack approaches

### 2.1.3.1 Local smeared crack approach

The “local” in the phrase “local smeared crack approach” means that this approach is built on conventional continuum mechanics assumptions, which are distinguished from the generalised continuum mechanics theories. The local smeared crack approach does not take into account any discontinuities in the topology of FE meshes; instead the cracked material is assumed a continuum, whose constitutive law is equipped with a strain softening branch after the peak stress to account for the effects of cracks at the microscale.

This approach was first taken by [Rashid \(1968\)](#) to deal with cracking in prestressed concrete vessels. Due to the simplicity of the smeared crack concept, for many years it almost monopolised the modelling of crack propagation. However, later on it was realised that if a smeared crack is only one element across, the total dissipated energy is severely dependent on the size of the element ([Bazant and Planas, 1997](#)). The dissipated energy tends to null upon mesh refinement, which is obviously not physical. To remove this fault, [Bažant and Oh \(1983\)](#) proposed the seminal *crack band model* in the context of continuum mechanics. This crack band model is quite similar to the cohesive crack model developed by [Hillerborg et al. \(1976\)](#) in the context of fracture mechanics. In these models, it was suggested that the notion of strain softening numerically mimicked should not be considered as a characteristic of the material, but it is actually closely connected to the fracture energy of the material and the size of the finite element within the strain localisation band to recover an objective representation of the energy dissipation. This regularisation on the post-peak stress-strain branch, related to fracture energy and the element size, is satisfactory to remove mesh size sensitivity of the solution.

Besides the mesh size sensitivity drawback, the directional mesh-bias dependency is another problem, which however is more difficult to solve. If the spatial discretisation is deliberately arranged in such a manner that the elements edges on the crack path are aligned to the crack propagation direction (so-called “well-aligned” finite element

meshes), the solutions obtained become more satisfactory (Cervera et al., 2010a). However, this fact has not generally been recognised, as stated in (Cervera and Chiumenti, 2006b).

To alleviate this directional mesh-bias dependency, several solutions have been proposed in the literature. Specific FE formulations have been developed for this purpose. Belytschko et al. (1988) introduced an assumed strain field that incorporated a localisation band rather than just a discontinuity. This localisation field can be triggered in a state of homogeneous strain, whereas the additional modes in (Ortiz et al., 1987) are triggered only in the presence of bilinear displacement fields. This methodology was further elaborated by Simo and Rifai (1990) and resulted in the class of Enhanced Assumed Strain (EAS) finite elements.

Along a different track, tracking algorithms widely used in the context of discrete crack approaches have been considered as an auxiliary device in local smear crack approaches for alleviating the mesh-bias dependency, see (Cervera and Chiumenti, 2006b,a).

### 2.1.3.2 Fully regularised smeared crack approaches

The local smear crack approach can furnish a good tool for capturing the material deterioration and loss of load carrying capacity of structures. However, this approach is locality based and the loss of ellipticity of the underlying mathematical stress governing equations for rate independent constitutive laws still remains (Pijaudier-Cabot and Bažant, 1987). In the last few decades, the mechanics community preferred to attribute the mesh dependence of strain softening problems to this ill-posedness of the underlying BVP from the viewpoint of mathematical formulations (De Borst et al., 1993). Therefore, one has rigorous justifications for the fact that the discrete FE solutions are not convergent to the exact solutions with respect to mesh refinement. Also, people may associate the directional mesh-bias to the loss of ellipticity (Cervera and Chiumenti, 2006b).

To assure the well-posedness of the boundary value problem, considerable efforts have been made to apply generalised continuum mechanics theories to resolve the difficulties with material softening. Pertinent work includes the micropolar theory (Aifantis, 1984, Steinmann and Willam, 1991), non-local integral-type models (Pijaudier-Cabot and Bažant, 1987, Jirasek, 1998), gradient enhanced damage models (Peerlings et al., 1996, Geers et al., 1998) and phase field models (Francfort and Marigo, 1998, Verhoosel and de Borst, 2013) for modelling strain localisation. These generalized continuum mechanics theories introduce a material characteristic length.

We categorise this large class of approaches as fully regularised smeared crack approaches, different from the crack band approach which is partially regularised with fracture energy.

A common feature of regularised smeared crack approaches is the introduction of a characteristic length parameter as “localisation limiter” into the constitutive models to preclude the occurrence of sharp strains and to limit the strain localisation to a band of finite width. In physics, this length is closely related to the size and average spacing of microcracks, and the size of inhomogeneities in materials (Bažant and Jirásek, 2002). The micropolar theory introduces independent rotational degrees of freedom additional to the translational degrees of freedom (Steinmann and Willam, 1991). In the nonlocal integral-type damage approaches (Pijaudier-Cabot and Bažant, 1987, Bažant and Jirásek, 2002), the local stress at a material point of interest is dependent on the deformation of its neighbourhood. A common practice is to perform a weighted averaging of certain internal variables (e.g. equivalent strain) within such a volume, determined by the introduced length parameter. Similar to the nonlocal theory, the gradient dependent or enhanced continuum theory with the advantage of being strictly local in a mathematical sense has been widely used first for the plasticity theory (De Borst and Mühlhaus, 1992) and then for isotropic damage models by Peerlings et al. (1996). In (Peerlings et al., 1996), a gradient formulation can be conceived as the differential counterpart to the integral formulation.

## 2.1.4 Discontinuous (discrete) crack approaches

Discontinuous or discrete crack approaches are geometrically realistic considering the fact that cracks are nothing else but real discontinuities within the material itself.

### 2.1.4.1 Cohesive elements

As a discretisation technique, cohesive elements are the simplest method to incorporate the cohesive zone model in the context of FE analysis. The crack behaviour (displacement discontinuity) is simulated with cohesive elements equipped with a traction-separation law. In such simulations, cohesive elements are naturally placed between neighbouring continuum elements along the potential propagation path. Situations with crack paths known in advance include delamination of laminated composites (Schellekens and De Borst, 1993a, Alfano and Crisfield, 2001) and fibre-matrix debonding (Xu and Needleman, 1993). Camacho and Ortiz (1996)

presented a stress-based extrinsic cohesive law where a new surface is adaptively created by duplicating nodes which were previously bonded.

**Remark 1** *Under the name of nonlinear spring models, cohesive calculations were introduced in (Ungsuwarungsri and Knauss, 1987, Song and Waas, 1993, 1995).*

#### 2.1.4.2 EFEM and XFEM

Simo et al. (1993) presented kinematics of strong discontinuities and introduced the notion of strong discontinuity analysis (SDA). As mentioned there, the continuum softening modulus is reinterpreted in the distributional sense to make mathematical and physical sense of the continuum equations. Based on Simo's work, discontinuity Embedded Finite Element Methods (EFEM) have been developed in the references (Armero and Garikipati, 1996, Oliver, 1996, Oliver et al., 1999, Borja, 2000, Jirásek, 2000, Wells and Sluys, 2001a, Oliver et al., 2014). The main goal of the EFEM is to provide a non intrusive way to embed a strong discontinuity in a single element. (Oliver et al., 2002) showed the links between SDA and nonlinear decohesive fracture mechanics. The regularised kinematic state of discontinuity can be regarded as a means to model the formation of a strong discontinuity as the collapsed state of a weak discontinuity.

The eXtended Finite Element Method (XFEM) has seen a significant amount of development and various applications, since its inception (Belytschko and Black, 1999, Moës et al., 1999). The XFEM is able to resolve non-smooth features such as discontinuities, singularities, high gradients, compared to standard FEM. This is achieved by incorporating enrichment functions into the approximation space by exploiting the concept of partition of unity of shape functions. Sukumar et al. (2000) employed the XFEM in three-dimensional fracture mechanics. Sukumar and Prévost (2003) discussed the aspects of computer implementation. Daux et al. (2000) dealt with arbitrary branched and intersecting cracks with the XFEM. Wells and Sluys (2001b) combined the XFEM with cohesive zone models to simulate the propagation of cohesive cracks. Zi and Belytschko (2003) developed a new formulation for elements containing the crack tip of cohesive cracks. Asferg et al. (2007) formulated a partly cracked tip element for three-node constant strain elements for cohesive crack growth, permitting variations in the discontinuous displacement field on both sides of the discontinuity. Remmers et al. (2003) proposed to represent cohesive cracks with a set of overlapping cohesive segments inserted into finite elements by exploiting the XFEM. Unger et al. (2007) applied the XFEM to simulate concrete

fracture and compared different criteria for predicting the propagation direction of cohesive cracks. [Hansbo and Hansbo \(2004\)](#) proposed an alternative formulation of the XFEM, called the phantom node method, where the original element is replaced by two elements initially coincident. The phantom node method is employed to study splitting in laminates by [Van der Meer and Sluys \(2009\)](#). [Liu and Borja \(2008\)](#) presented an incremental quasi-static contact algorithm for path-dependent frictional crack propagation in the framework of the XFEM, where the contact constraint was embedded within a localised element by a penalty method. The XFEM was also adopted to study crack growth in saturated porous media ([Khoei et al., 2014](#)) and the topology optimisation of structures ([Belytschko et al., 2003](#)). A comprehensive review can be found in ([Belytschko et al., 2009](#), [Fries and Belytschko, 2010](#)).

A comprehensive comparison ([Oliver et al., 2006](#)) has been performed between the EFEM and XFEM, which showed that both the numerical accuracy and the efficiency of the EFEM is largely improved by the adoption of elemental enrichment instead of nodal enrichment in the XFEM. Wu et al. ([Wu et al., 2015](#)) enhanced the EFEM by combining the advantages of the XFEM and EFEM. In their work, a non-uniform discontinuity mode was considered as in the XFEM. As well, the condition of traction continuity was applied in the statically optimal form as in most EFEMs. A novel robust method called variational multiscale cohesive model (VMCM), inspired by ([Garikipati and Hughes, 1998](#)), has been proposed ([Rudraraju et al., 2010, 2012a](#)). It shares a significant degree of similarity to the EFEM, but is formulated following the classical variational multiscale paradigm ([Hughes et al., 1998](#)). This method starts with the additive decomposition of the displacement field into coarse and fine scale parts and incorporates a discontinuous function for resolving displacement discontinuity within a continuum element.

There are some other notable contributions to discrete crack modelling, e.g. augmented FEM ([Ling et al., 2009](#)), floating node method ([Chen et al., 2014](#)), extended cohesive damage model ([Li and Chen, 2017](#)) and continuum decohesive finite element method ([Prabhakar and Waas, 2013](#), [Lin et al., 2019](#)) inspired by the VMCM, just to name a few. They have been developed for handling discrete crack geometries and already have presented promising applications mainly to composite structures.

### 2.1.5 Tracking algorithms

One of the most important ingredients in modelling crack propagation is the determination of when and how a crack will propagate. The first involves a postulated

fracture or damage initiation criterion, whereas the second deals with the identification of the crack propagation direction and potential crack paths. In order to realistically mimic an actual crack path, tracking algorithms are a crucial aspect, complementary to the kinematic representation of a crack.

A tracking algorithm serves as a device to identify the direction of crack propagation, recognise the consolidated crack and assign the new crack path during the simulation. It is typically used in intraelement discrete crack approaches (XFEM or EFEM) with a strong discontinuity captured inside elements. As stated in (Saloustros et al., 2018), the a tracking algorithm can help choose the expected solution by minimising the number of potential ones, provide a more realistic crack representation especially for curved cracks and limit the energy dissipation outside the crack to reflect the localising character after material softening. In the discrete crack approaches, the enforcement of crack path continuity is beneficial for avoiding spurious stress locking induced by incompatible deformation modes between adjacent elements (refer to (Jirásek and Zimmermann, 2001) for more details).

#### 2.1.5.1 Local tracking algorithms

The underlying idea behind local tracking algorithms, a branch of tracking algorithms, is to identify the elemental crack location on an element-by-element basis. In local tracking algorithms, the coordinates of crack tips are stored for each crack only when a converged solution is found. The crack propagation direction is computed locally from the stresses or strains within the element or averaged over a small circular domain (in 2D). The local tracking algorithm was discussed in (Alfaiate et al., 2002, Dias-da Costa et al., 2009) for the EFEM, in (Moës et al., 1999) for the XFEM, and in (Cervera et al., 2010b) for the local smeared crack approach.

#### 2.1.5.2 Global tracking algorithms

Oliver et al. (2004), Oliver and Huespe (2004) proposed a global tracking algorithm which is based on solving an additional linear anisotropic heat conduction-like BVP at each time step accompanying the standard mechanical BVP for failure. The unknown field variable  $\theta$  of the newly introduced BVP is a scalar whose isolevel curves (in 2D) represent those candidate crack paths from which the envelope labelled by a constant value of the  $i - th$  crack root element is the expected crack position. In a discrete solution setting, the crack path identification is performed by looping through all the domain elements and compare their values for  $\theta$  with values

associated to all the cracks in case of multiple non-intersecting cracks. In order to provide a non-uniform field, two arbitrary values for  $\theta$  should be prescribed, at least, in two nodes. This global tracking algorithm was combined with discrete crack modelling techniques, the EFEM in (Oliver et al., 2004), the XFEM in (Dumstorff and Meschke, 2007), and the local smeared crack approach in (Cervera and Chiumenti, 2006b,a).

Although the global tracking algorithms have drawbacks, compared to local tracking algorithms, such as computationally demanding, code invasive, inability to deal with intersecting cracks, it is worth mentioning that their extension to the three-dimensional case is straightforward and simple (Oliver et al., 2004, Jäger et al., 2008) compared to the level set methods to be discussed below.

### 2.1.5.3 Level set methods

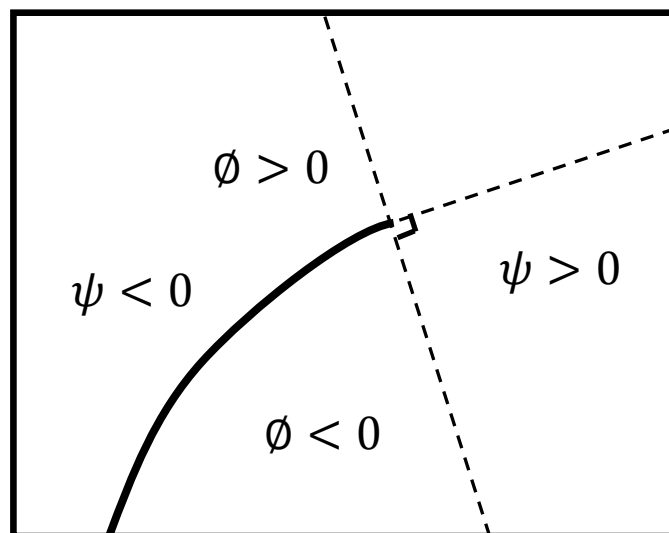


**Figure 2.4** Level set functions for discrete crack representation.

Level set methods are the most commonly used techniques for tracking and updating moving interfaces or propagating cracks. The level set method was originally introduced for tracking the evolution of closed boundaries. Later on, Belytschko et al. (2001) and Stolarska et al. (2001) modified the original version for use in the context of XFEM for the crack representation. To track an open crack in terms of connectivity, two (or three) level set functions are essential, one for the crack surface, one (or two) for each crack tip. The crack surface and crack tips are identified by corresponding zero level values (Dufloot, 2007), refer to Figure 2.4. Note that the zero level set must

not be updated behind the tip to consider that a material point remains cracked once cracked. In a discrete solution setting, the level set values can be readily interpolated with nodal values using the standard FE approximation basis for the displacement interpolation. For instance, to represent a crack with curvature within an element, higher-order interpolation for level sets has been considered (Stazi et al., 2003).

### 2.1.6 Transition from continuous to discontinuous cracks

Both kinds of continuous and discontinuous crack approaches show limitations. A continuous approach is more appropriate for capturing crack initiation while a discontinuous one provides a more realistic way for describing crack propagation. To take advantage of them, in recent years, attempts have been made to combine them to capture the entire fracture process. A transition criterion is required from a diffuse damage state to a discrete sharp crack. Most of such transition schemes are based on the consideration of energetic equivalence (Cazes et al., 2009). Simone et al. (2003) described material degradation with a implicit gradient damage model and introduced traction-free discrete cracks at fully damaged positions. Thus, in the final stage of failure, the spurious damage growth known in the continuous model can be effectively avoided. Cuvilliez et al. (2012), Wu et al. (2014) coupled implicit gradient damage models and cohesive zone models in which way the switch from diffuse damage to cohesive cracks can be made at any damage level. Bobiński and Tejchman (2016) developed a transition algorithm between a non-local continuum damage model and XFEM, where the transition was carried out when softening parameter for cohesive cracks exceeded a predefined value. Wang and Waisman (2016) proposed a coupled continuous and discontinuous approach where an integral-type nonlocal continuum damage model was coupled with an extrinsic discrete interface model implemented within the XFEM. The transition was established via an equivalent thermodynamic framework. The dissipated energy was obtained numerically and weakly matched at the transition.

## 2.2 Multiscale modelling

Multiscale modelling of failure has been a major subject of research in the mechanics community during the last two decades. Applications arise in many engineering fields such as the design and analysis of mechanical components and large structures. In the sequel, we will summarise the work in this area, especially with emphasis

on two-scale failure modelling. The term “multiscale” here refers to multiple length scales. The focus will be on two scale situations. Three categories of multiscale methods can be classified according to the computational structure, as shown in Figure 2.5.

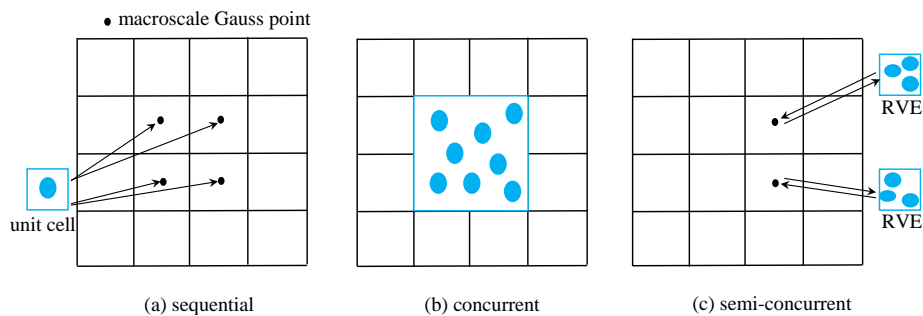


**Figure 2.5** Different multiscale modelling approaches: (a) sequential, (b) concurrent and (c) semi-concurrent.

## 2.2.1 Introduction

Most materials are heterogeneous and multiscale. Multiscale methods furnish great promise to exploit the physically existing multiscale character of the material. Comprehensive review in this direction can be found in (Kanouté et al., 2009) for composites, (Otero et al., 2018) for computational homogenisation, (Geers et al., 2010, Matouš et al., 2017) for nonlinear problems, and (Nguyen et al., 2011b) particularly for failure.

## 2.2.2 Sequential multiscale methods

In these methods ( Figure 2.5a ), information is passed in one direction from the fine scale to the coarse scale. The information exchange is accomplished in a preprocessing step before the coarse scale analysis starts. In most situations, apparent elastic constants are extracted by virtual numerical testing on a unit cell by numerical homogenisation procedures (a unit cell is such that its periodical repetition constitutes the microstructure, resulting in a ordered representation). In some cases, these material constants can also be obtained in a closed-form by analytical homogenisation techniques but with limited applications to simple microstructure topologies (Hill, 1963, Nemat-Nasser and Hori, 2013). For a complex heterogeneous structure, the numerical homogenisation methods are recommended and frequently

used in practice to compute effective elastic constants of the homogenised media. Though the sequential multiscale methods are successful in deriving effective or homogenised behaviour for heterogeneous media, the main weakness is that they are unable to handle complex material behaviour, such as material softening and strain localisation, which involves an evolution or dynamic character.

### 2.2.3 Concurrent multiscale methods

Concurrent multiscale methods are strong coupling techniques that couple the fine and coarse scale discretisations into a single system of algebraic equations to be solved, as illustrated in Figure 2.5b. This strong coupling calls for techniques to couple the meshes of coarse scale and fine scale and moreover efficient algorithms for adaptive addition of fine scale features. The transition to fine scale is performed as a consequence of adaptive local refinement. When confronting softening and strain localisation phenomena, these methods, owing to strong coupling across scales, do not suffer from the RVE size dependence and macro-element sensitivity of solutions as in the computational homogenisation. Furthermore, failure processes can be accurately described, from crack nucleation, through crack coalescence up to the formation of a stress-free crack. Another advantage is that, compared to the direct numerical solutions, the concurrent multiscale methods employ fewer computational resources due to the local refinement in discretisation.

In the literature, the variational multiscale method introduced by [Hughes et al. \(1998\)](#) has become the theoretical paradigm for a large class of new schemes for multiscale failure. Relevant works include ([Loehnert and Belytschko, 2007](#), [Hund and Ramm, 2007](#), [Hettich et al., 2008](#), [Mergheim, 2009](#), [Rudraraju et al., 2010, 2012a](#)). Common features among these are the two-scale decomposition of the displacement field into a coarse-scale and a fine-scale component (fluctuation), and the specification of locality assumptions on fine-scale solutions. Concurrent multiscale methods for material failure based on domain decomposition methods were given in ([Guidault et al., 2007](#), [Lloberas-Valls et al., 2012](#)). The domain decomposition methods split the global domain into two parts, one discretised by a coarse mesh wherein the response is smooth and the other wherein the fluctuations are severe so that microstructural details are needed to be explicitly resolved. The fine-scale domain can embody strain localisation or high gradients so that these methods are ideal for modelling material failure.

Note that the concurrent multiscale methods, due to strong coupling, are best suited

to problems where the coarse and fine scales are not far separated. If this is not the case, computational homogenisation methods to be discussed in the following are favoured when strong scale jumps are required.

## 2.2.4 Semi-concurrent multiscale methods

Semi-concurrent multiscale methods as in Figure 2.5c exchange data between two separate scales. One widely used method among semi-concurrent multiscale methods is the  $FE^2$  method (also known as computational homogenisation), with the superscript “2” indicating that two scales are involved (Feyel and Chaboche, 2000). In  $FE^2$  method, the element method is used at both scales.

In computational homogenisation (CH) based methods (or  $FE^2$ ), the effective macroscopic constitutive behaviour is defined on the fly during the simulation. The validity of CH methods relies on the underlying assumption of strong scale separation and the existence of an RVE (Hill, 1963). The scale separation signifies that the characteristic length at the coarse scale should be far larger than that at the fine scale so that the fluctuations of field variables are not pronounced at the coarse scale. As a result, the material behaviour at a point at the coarse scale is representative of the fine scale behaviour in a statistical sense. The first-order CH is a widely used one of which the earliest development can date back to the time around the year 2000 (Smit et al., 1999, Feyel and Chaboche, 2000, Terada et al., 2000, Kouznetsova et al., 2001, Miehe et al., 2002). As mentioned by Matouš et al. (2017), the scale separation principle may be violated either when the macroscopic fluctuations are fairly small due to strain localisation or high gradients, or when a microscopic characteristic length is relatively large because of large microstructural constituents or the presence of long-range correlations. For that reason, the standard first-order homogenisation scheme fails for these situations.

Modified and extended CH schemes on the basis of the standard first-order homogenisation scheme have been developed to overcome the deficiencies of the standard first-order CH. A typical example is the second-order CH which couples the first-order continuum microstructure to the higher-order gradient continuum at the coarse scale. This allows for moderate localisation of the coarse-scale field and it captures the effect of the size of the microstructure into the homogenisation scheme. Seminal works include (Geers et al., 2001, Kouznetsova et al., 2004, Kaczmarczyk et al., 2008, 2010a). The implementation of the second-order CH scheme is usually more involved than the first-order CH scheme owing to the incorporation of strain

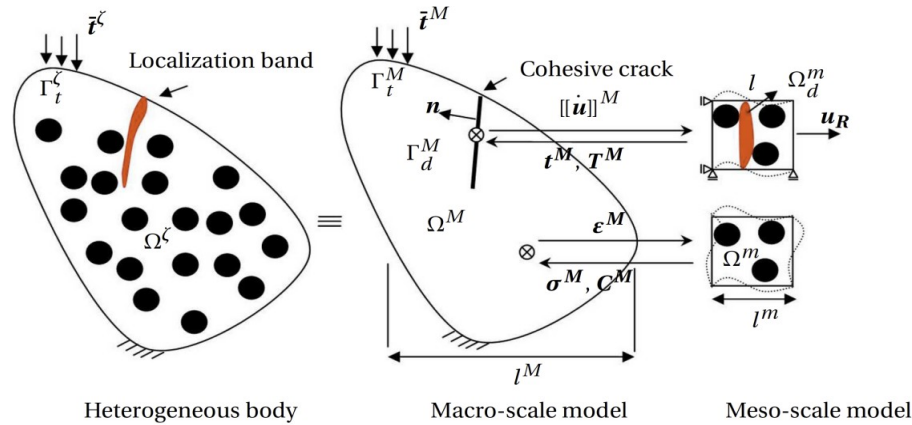


**Figure 2.6** The semi-concurrent multiscale method proposed by [Nguyen et al. \(2012c\)](#) for modelling mode-I cohesive failure. Reprinted with permission from ([Karamnejad and Sluys, 2014](#)), © 2014, Elsevier.

gradient and associated higher-order stress.

Although the second-order can resolve problems of moderate strain localisation and high gradients within the RVE, when the macroscopic fluctuations are close to the order of the fine scale during the loading, as is the case of strain localisation phenomena, the assumption of scale separation does not hold any longer as pointed by [Gitman et al. \(2007\)](#).

Representative works include ([Matouš et al., 2008](#), [Belytschko et al., 2008](#), [Hirschberger et al., 2009](#), [Verhoosel et al., 2010](#), [Souza and Allen, 2011](#), [Nguyen et al., 2011a, 2012c](#), [Coenen et al., 2012a](#), [Unger, 2013](#), [Karamnejad and Sluys, 2014](#), [Bosco et al., 2015](#), [Oliver et al., 2015](#), [Toro et al., 2014, 2016a](#), [Petracca et al., 2016](#), [Svenning et al., 2017b](#), [Turteltaub et al., 2018](#)) to name a few. Most of these works attempt to extract from the microscale problem an objective effective macro crack response in the form of traction-separation laws, as shown in Figure 2.6. More specifically, the localisation of an RVE is interpreted as the formation of a strong discontinuity on the macroscale model. A coupled-volume multiscale method that abandoned the separation of scales principle was introduced in ([Gitman et al., 2008](#)) where the area associated with a macroscale integration point, rather than the macroscale integration point itself, was closely linked to the size of RVE.

Although CH based multiscale modelling has enormous advantages compared to full-scale resolution methods, its real-world applications remain very restricted, regarding algorithmic complexity and computational costs, in particular for highly nonlinear phenomena. Such challenges can be alleviated by considering model order reduction and parallel computing techniques.

Model order reduction techniques aim to reduce the dimension of the state-space system and hence to decrease computational expense, while retaining the dominant characteristics of the original system. In multiscale modelling, the reduced basis is computed on the basis of a number of so-called snapshots, which are determined from a series of pre-computations on the RVE model subjected to different loading conditions. Relevant examples of in the context of multiscale modelling can be found in (Yvonnet et al., 2009, Kerfriden et al., 2013, Oliver et al., 2017, Zhang and Oskay, 2017). Parallel computations for CH based multiscale modelling are naturally feasible because the local RVE computations are independent of each other. Nguyen et al. (2012d) presented a parallel implementation of the discontinuous CH method for simulating cohesive cracks.

## 2.3 Research gaps

This chapter has reviewed the widely used computational fracture approaches and multiscale modelling approaches in the literature. The following gaps can be identified in the course of literature study:

- Although many extended CH based multiscale models for fracture or strain localisation problems have been proposed, most of them are complex in their formulation or implementation. There seems to be a need for developing a simple but working CH based multiscale failure model.
- Some of the existing multiscale failure models have made confusing hypotheses during formulating. Therefore, it is necessary to have a multiscale failure framework derived from rigorous variational principles.
- Although multiscale failure modelling has been applied to concrete and composite materials, less effort has been made to study toughening mechanisms and failure events across length scales in cortical bone.

# Chapter 3

## Computational approaches for modelling cracks

This chapter details several popular numerical approaches for modelling damage or cracks in the literature. In the computational mechanics community, these approaches have been under extensive research and development for solving various failure or fracture problems and improving their numerical performance. These numerical approaches will be employed in the multiscale failure modelling approaches discussed in the following chapters. In Section 3.1, the FEM is briefly reviewed to provide fundamental notions for other nonlinear FEM-based approaches. Section 3.2 focuses on two continuous crack approaches: the local smeared crack approach (3.2.2) and the gradient enhanced damage model (3.2.3). As discrete crack approaches which are advantageous in representing the kinematics of cracks, cohesive elements (3.3.1) and XFEM (3.3.2) are described in Section 3.3. The energy dissipation based arc-length control is described in Section 3.4. Some concluding remarks are given in the last section (3.5).

### 3.1 Finite element method

The finite element method (FEM) is a powerful and prevalent numerical technique for solving physical problems governed by partial differential equations (PDEs). The central idea behind the FEM is spatial discretisation and local approximation such that approximated solutions are obtained by solving a system of assembled algebraic equations. The FEM has a wide range of applications in areas such as fluid mechanics, solid mechanics, structural engineering, materials science,

aerodynamics, and heat transfers. Excellent textbooks devoted to the application of the nonlinear FEM in the subject of solid mechanics have been written by Bonet and Wood (Bonet and Wood, 1997), de Borst et al. (de Borst et al., 2012), and Belytschko et al. (Belytschko et al., 2013), just to name a few, whereas a rigorous description of the mathematical theory on the FEM can be found in (Brenner and Scott, 2007) and (Oden and Reddy, 2012). In what follows, a short introduction to this method for material nonlinear solids is provided in the case where small displacements, infinitesimal strains and quasi-static loadings apply.

### Strong and weak forms of the BVP

Assume a solid body occupies the domain  $\Omega$  bounded by  $\Gamma$  in space with each material particle identified by the coordinates  $\mathbf{x}$ , as shown in Figure 3.1. The boundary  $\Gamma$  is partitioned into nonintersecting Neumann and Dirichlet boundaries,  $\Gamma_t$  and  $\Gamma_u$ , which are subjected to prescribed tractions  $\bar{\mathbf{t}}$  and prescribed displacements  $\bar{\mathbf{u}}$ , respectively. The extent of deformation and especially stress distribution of this solid body are of much importance in the field of engineering. In the following, the analysis is confined to small deformations.

The BVP problem corresponding to the mechanical deformation process is to find

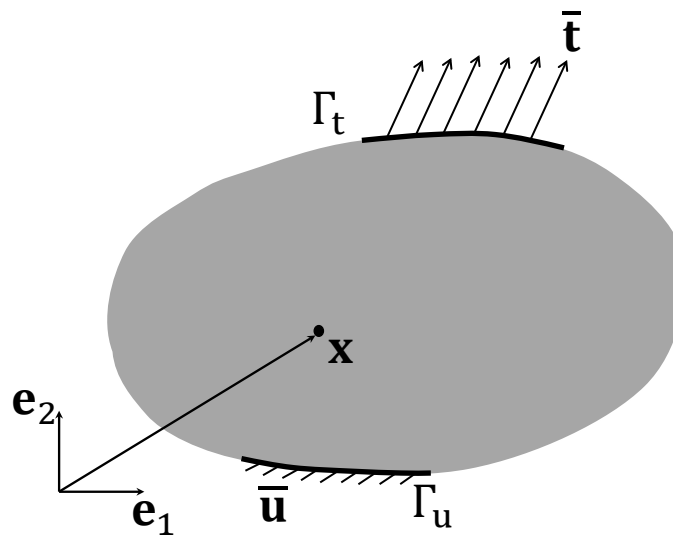


**Figure 3.1** A two-dimensional solid body under external loading.

the unknown displacement field  $\mathbf{u}$  such that the following field conditions are satisfied

pointwise

$$\nabla \cdot \boldsymbol{\sigma} + \mathbf{b} = \mathbf{0} \quad \text{in } \Omega \quad (3.1a)$$

$$\boldsymbol{\varepsilon} = \nabla^s \mathbf{u} \quad \text{in } \Omega \quad (3.1b)$$

$$\mathbf{u} = \bar{\mathbf{u}} \quad \text{on } \Gamma_u \quad (3.1c)$$

$$\boldsymbol{\sigma} \cdot \mathbf{n} = \bar{\mathbf{t}} \quad \text{on } \Gamma_t \quad (3.1d)$$

$$\boldsymbol{\sigma} = \Sigma(\boldsymbol{\varepsilon}, \boldsymbol{\alpha}) \quad \text{in } \Omega \quad (3.1e)$$

where  $\boldsymbol{\sigma}$  and  $\boldsymbol{\varepsilon}$  are the second order (symmetric) Cauchy stress and infinitesimal strain tensors, respectively;  $\mathbf{b}$  are the body forces;  $\nabla$  means the gradient operator and  $\nabla^s$  is its symmetric counterpart. Eq. (3.1a) represents the force equilibrium equation derived from the balance of linear momentum. Eq. (3.1b) is the compatibility condition of motion. The constitutive relation Eq. (3.1e) completes the set of governing equations with  $\boldsymbol{\alpha}$  denoting a set of material internal variables. The remaining two equations Eq. (3.1c) and Eq. (3.1d) are the displacement and traction boundary conditions, respectively.

By the use of the principle of virtual work, a weak form corresponding to the strong form Eq. (3.1a) is obtained and the problem then turns into finding the displacement field  $\mathbf{u} \in \mathcal{U}$  such that

$$\int_{\Omega} \boldsymbol{\sigma} : \boldsymbol{\varepsilon}(\delta \mathbf{v}) \, d\Omega = \int_{\Omega} \mathbf{b} \cdot \delta \mathbf{v} \, d\Omega + \int_{\Gamma_t} \bar{\mathbf{t}} \cdot \delta \mathbf{v} \, d\Gamma \quad \forall \delta \mathbf{v} \in \mathcal{V} \quad (3.2)$$

In the above formula, the newly introduced symbols  $\mathcal{U}$  and  $\mathcal{V}$  are the respective function spaces of admissible displacements and admissible variations of displacements (so-called virtual displacements) with the following definitions

$$\mathcal{U} := \left\{ \mathbf{u} \mid \mathbf{u} \in [H^1(\Omega)]^{dim}; \mathbf{u}|_{\Gamma_u} = \bar{\mathbf{u}} \right\} \quad (3.3a)$$

$$\mathcal{V} := \left\{ \mathbf{v} \mid \mathbf{v} \in [H^1(\Omega)]^{dim}; \mathbf{v}|_{\Gamma_u} = \mathbf{0} \right\} \quad (3.3b)$$

where  $H^1(\Omega)$  is the space of square integrable functions whose first derivatives are also square integrable. The function space  $\mathcal{V}$  requires that the virtual displacements ought to fulfil the homogeneous Dirichlet boundary conditions.

### 3.1.1 Spatial discretisation by finite elements

In what follows, matrix-vector notation has been adopted and hence, symmetric second order or symmetric fourth order tensors are correspondingly represented in their Voigt forms (i.e. vector or matrix).

A pure displacement-based formulation is considered to discretise the weak form Eq. (3.2). To this end, the entire body is firstly partitioned into  $n_e$  non-overlapping elements  $\Omega_e$ , relatively regular in shape. Each element has  $nn$  nodes. The displacements and the virtual displacements within an element can be interpolated with the shape functions  $N_I(x)$  at their associated nodes of the element

$$\mathbf{u}_e(\mathbf{x}) = \mathbf{N}(\mathbf{x})\mathbf{a}_e \quad (3.4a)$$

$$\delta\mathbf{v}_e(\mathbf{x}) = \mathbf{N}(\mathbf{x})\delta\mathbf{a}_e \quad (3.4b)$$

where  $\mathbf{N}$  is the matrix that consists of shape functions;  $\mathbf{a}_e$  and  $\delta\mathbf{a}_e$  are the vectors (the length is  $nn \times ndim$ ) of nodal displacement degrees of freedom and their virtual counterparts, respectively. Note that the subscript  $e$  refers to an element related quantity that may be a vector, matrix, or tensor.

Each shape function possesses a locally compact support and should be at least first order smooth so that they can be differentiated once to obtain the connection between the strain and the displacement within the element

$$\boldsymbol{\varepsilon}_e(\mathbf{u}) = \mathbf{B}_e(\mathbf{x})\mathbf{a}_e \quad (3.5a)$$

$$\boldsymbol{\varepsilon}_e(\delta\mathbf{v}) = \mathbf{B}_e(\mathbf{x})\delta\mathbf{a}_e \quad (3.5b)$$

where Voigt notation for representing the strain tensor has been used and  $\mathbf{B}_e$  denotes the elemental strain-displacement matrix  $\mathbf{B}_e = [\mathbf{B}_1, \mathbf{B}_2, \dots, \mathbf{B}_{nn}]$  which gathers  $nn$  submatrices, each associated with a node  $I$

$$\mathbf{B}_I = \begin{bmatrix} N_{I,x} & 0 \\ 0 & N_{I,y} \\ N_{I,y} & N_{I,x} \end{bmatrix}$$

Note that a comma followed by a variable  $x$  in a subscript represents the partial derivative with respect to  $x$ , as in the rest of this thesis. The strains within a single element are obvious to obtain using  $\mathbf{B}_e$  upon knowing the nodal displacements which relies on solving a global system of algebraic equations. To set up such a global system, the nodal displacements of each single element are assembled into a global

nodal displacement vector via a location matrix  $\mathbf{L}_e$  only having a few ones besides the remaining zeros

$$\mathbf{a}_e = \mathbf{L}_e \mathbf{a} \quad (3.6a)$$

$$\delta \mathbf{a}_e = \mathbf{L}_e \delta \mathbf{a} \quad (3.6b)$$

With the aid of Eq. (3.4), (3.5) and (3.6), and due to the arbitrariness of the global vector of virtual displacements  $\delta \mathbf{a}$ , the continuous weak form (3.2) finally is discretised as

$$\sum_{e=1}^{n_e} \mathbf{L}_e^T \int_{\Omega_e} \mathbf{B}_e^T \boldsymbol{\sigma}_e d\Omega = \sum_{e=1}^{n_e} \mathbf{L}_e^T \int_{\Omega_e} \mathbf{N}_e^T \mathbf{b}_e d\Omega + \sum_{e=1}^{n_e} \mathbf{L}_e^T \int_{\Gamma_e} \mathbf{N}_e^T \bar{\mathbf{t}}_e d\Gamma \quad (3.7)$$

where all integrals extend over all the elements in the mesh. Of Eq. (3.7), the left-hand side and right-hand side are the so-called internal force vector  $\mathbf{f}_{int}$  and external force vector  $\mathbf{f}_{ext}$ , respectively. They are given by

$$\mathbf{f}_{int} = \sum_{e=1}^{n_e} \mathbf{L}_e^T \int_{\Omega_e} \mathbf{B}_e^T \boldsymbol{\sigma}_e d\Omega \quad (3.8a)$$

$$\mathbf{f}_{ext} = \sum_{e=1}^{n_e} \mathbf{L}_e^T \left( \int_{\Omega_e} \mathbf{N}_e^T \mathbf{b}_e d\Omega + \int_{\Gamma_e} \mathbf{N}_e^T \bar{\mathbf{t}}_e d\Gamma \right) \quad (3.8b)$$

Hence, Eq. (3.7) is equivalent to

$$\mathbf{f}_{int} = \mathbf{f}_{ext} \quad \text{OR} \quad \mathbf{f}_{ext} - \mathbf{f}_{int} = \mathbf{0} \quad (3.9)$$

If there are not any nonlinearities involved in Eq. (3.9), it can be solved in a single step. On the other hand, when geometric or material nonlinearities are included (the latter is of concern in this thesis), the solution of Eq. (3.9) necessitates *iterative solvers*. Newton's method (also called Newton-Raphson method) is a powerful iteration based technique which is frequently adopted for addressing nonlinear FEM formulations.

### 3.1.2 Newton's method

For nonlinear mechanical problems with FEM, it is sensible to define a time concept (pseudo-time) and apply the ultimate external load in a number of incremental load steps. For a given load step, the aim is to solve for the displacement vector at the end of the load step. This requires a number of iterations until the final equilibrium is reached. To launch the iteration process, initial values for the displacement and

other state variables are chosen as those from the last equilibrated load step. The procedure for the displacement update at iteration  $i + 1$  is summarised as

$$\mathbf{r}_i = \mathbf{f}_{ext} - \mathbf{f}_{int,i} \quad (3.10a)$$

$$\Delta \mathbf{a}_i = \mathbf{K}_i^{-1} \mathbf{r}_i \quad (3.10b)$$

$$\mathbf{a}_{i+1} = \mathbf{a}_i + \Delta \mathbf{a}_i \quad (3.10c)$$

where  $\mathbf{K}$  is the tangent stiffness matrix,  $\mathbf{r}$  is the force residual vector that controls the accuracy of the solution and  $\Delta \mathbf{a}$  is the displacement increment vector. After obtaining the updated displacement, we are able to update the temporary states of the strain, stress and internal variables for each element. Then, the global internal force vector is computed again by Eq. (3.8a) and a check of whether the residual satisfies the specified convergence criteria is called. The above process is repeated until convergence is attained.

The derivation of the tangent stiffness involves an indispensable process called *linearisation* which consists in the differentiation of the negative residual with respect to the displacement vector

$$\mathbf{K} = -\frac{\partial \mathbf{r}}{\partial \mathbf{a}} = \frac{\partial \mathbf{f}_{int}}{\partial \mathbf{a}} = \sum_{e=1}^{n_e} \mathbf{L}_e^T \left( \int_{\Omega_e} \mathbf{B}_e^T \mathbf{D} \mathbf{B}_e \right) \mathbf{L}_e \quad (3.11)$$

where  $\mathbf{D}$  is the so-called material tangent operator, a fourth order tensor, which has the form  $\mathbf{D} = \frac{\partial \dot{\boldsymbol{\sigma}}}{\partial \dot{\boldsymbol{\varepsilon}}}$ . The material tangent operator assigns a stress increment to a strain increment and as its name indicates, is the slope of the tangent line to the stress-strain curve at a strain state (1D case). It is sometimes analytically derived from differentiation of the phenomenological constitutive equation Eq. (3.1e); however, for sophisticated material behaviour, other techniques for numerically approximating it may be preferable.

**Remark 2** *In the derivation of the tangent stiffness Eq. (3.11), only the internal force vector is linearised and the linear dependency between the strain and displacement is used since we only consider material nonlinearities through this thesis.*

**Remark 3** *The material tangent stiffness, known as Jacobian matrix in mathematics, plays a crucial role in Newton's methods, since it considerably affects the rate of convergence to the state of equilibrium. Errors in the tangent stiffness can cause slow convergence or sometimes divergence. In a multiscale setting, the material tangent can be obtained from a homogenisation process, which will be deeply studied in later.*

**Remark 4** *Quadratic convergence in the Newton's method means that the  $l_2$  norm of the difference between the actual solution and the iterate decreases quadratically in each iteration.*

### 3.1.3 Numerical integration

It is evident that the finite element implementation demands the evaluation of integrals. In most situations, the Gauss integration rule is employed to compute integrals numerically. The numerical integral formula via the Gauss rule for Eq. (3.8a) reads (Belytschko et al., 2013)

$$\mathbf{f}_{int} = \sum_{e=1}^{n_e} \mathbf{L}_e^T \sum_{p=1}^{n_p} w_p \det(\mathbf{J}_p) \mathbf{B}_p^T \boldsymbol{\sigma}_p \quad (3.12)$$

with  $n_p$  being the number of integration points in the element  $e$ ,  $\mathbf{J}_p$  the Jacobian matrix at integration point  $p$  and  $w_p$  the corresponding weight at integration point  $p$ . In the above, the subscript  $e$  for element quantities related to the element  $e$  is already omitted for simplicity. Likewise, the numerical integration formula for the external force vector has a similar structure. The evaluation of global internal force and external force present in Eq. (3.10a) is performed by a nested loop; within the loop over elements, the other loop over all the integration points resides.

## 3.2 Continuous crack approaches

### 3.2.1 Isotropic damage models

There is no doubt that large-scale failure phenomena are closely associated with microscopic degradation events at local material points, which may manifest as microcracks or microvoids. Failure is typically a progressive process which consists of initiation, growth and coalescence of these distributed microcracks or microvoids inside materials. This internal evolution is difficult to monitor with experimental techniques and describe in a rigorous mathematical manner. Despite these difficulties, *continuum damage mechanics* has been widely accepted as a simple but effective model to deal with such complicated mechanical behaviour (Lemaitre, 2012, Kachanov, 2013).

A valid damage mechanics model is normally derived from the fundamental thermodynamics laws providing a framework to develop a variety of continuum damage

models. Among these, the *isotropic damage models* are the simplest ones. For this family of isotropic damages models, it is postulated that the average mechanical response of microcracks or microvoids is independent of their orientation but sensitive to density, which indicates the isotropy property is maintained. Therefore, a single scalar variable is sufficient to describe the whole deterioration course of a material. Here, we follow the family of isotropic damage models proposed in (Oliver et al., 1990) and describe the basic ingredients. The constitutive expression for the isotropic damage models reads

$$\boldsymbol{\sigma} = (1 - \omega) \mathbf{D}_e : \boldsymbol{\varepsilon} = (1 - \omega) \bar{\boldsymbol{\sigma}} \quad (3.13)$$

with  $\omega$  the scalar damage variable and  $\mathbf{D}_e$  the fourth-order isotropic linear elastic tensor having the following form

$$\mathbf{D}_e = \lambda \mathbf{1} \otimes \mathbf{1} + 2\mu \mathbf{I} \quad (3.14)$$

where  $\lambda$  and  $\mu$  are the Lamé constants;  $\mathbf{1}$  and  $\mathbf{I}$  are the second and fourth order unit tensors, respectively. Eq. (3.13) introduces the effective elastic stress  $\bar{\boldsymbol{\sigma}}$  (Lemaitre, 2012, Kachanov, 2013).

The damage variable  $\omega$  in Eq. (3.13) only exists within the range  $[0, 1]$  and depicts the extent of material degradation with values 0 and 1 indicating the virgin and totally failed material states respectively. The damage variable should be evaluated at every instant of the deformation according to a specific evolution law, of which a general form is (Oliver et al., 1990)

$$\omega = 1 - \frac{q(r)}{r} \quad (3.15)$$

where  $r$  is a strain-like internal variable and  $q$  a work-conjugate stress-like internal variable to  $r$ , termed the softening variable. The evolution law for the internal variable  $r$  reads

$$\dot{r} = \lambda, \quad r \in [r_0, \infty) \quad (3.16)$$

with  $r_0$  being the initial threshold at time  $t = 0$ .  $\lambda$  is a damage consistency parameter to be used to define damage loading/unloading conditions later.

The evolution law (softening rule) in rate form for  $q$  is expressed in terms of the softening parameter  $\mathcal{H}$  as

$$\dot{q} = \frac{\partial q}{\partial r} \dot{r} = \mathcal{H}(r) \dot{r}, \quad q \in [0, r_0] \quad (3.17)$$

where  $\mathcal{H}$  is negative or zero in the softening case and at the initial time  $q_0 = r_0$ . Different definitions of  $\mathcal{H}$  lead to different softening forms. The linear and exponential softening laws have the following respective expressions

$$\text{linear softening:} \quad q = r_0 + \mathcal{H}_0(r - r_0) \quad (3.18a)$$

$$\text{exponential softening:} \quad q = r_0 \exp(\mathcal{A}(\frac{r - r_0}{r_0})) \quad (3.18b)$$

In order to compare different stress states (tensors), it is desirable to define a scalar measure of stress, denoted by  $\tau_\sigma$ . This measure is also termed *equivalent stress*. Two candidate measures may be defined as (Oliver et al., 1990)

$$\tau_\sigma = \|\boldsymbol{\sigma}\|_{D_e^{-1}} = \sqrt{\boldsymbol{\sigma} : D_e^{-1} : \boldsymbol{\sigma}} \quad (3.19)$$

and (Mazars and Pijaudier-Cabot, 1989)

$$\tau_\sigma = \|\boldsymbol{\sigma}\|_{D_e^{-1}} = \sqrt{\boldsymbol{\sigma}^+ : D_e^{-1} : \boldsymbol{\sigma}^+} \quad (3.20)$$

where in the above,  $\|\bullet\|_{D_e^{-1}}$  denotes the scalar norm of  $(\bullet)$  in the metric defined by  $D_e^{-1}$  and  $\bar{\boldsymbol{\sigma}}^+$  denotes the positive part of the effective stress tensor with the expression

$$\bar{\boldsymbol{\sigma}}^+ = \sum_{i=1}^3 \langle \bar{\sigma}_i \rangle \mathbf{p}_i \otimes \mathbf{p}_i \quad (3.21)$$

where  $\bar{\sigma}_i$  and  $\mathbf{p}_i$  are the  $i$ -th principal stress and the  $i$ -th principal direction and  $\langle \bullet \rangle$  represents the Macaulay brackets, for scalar  $x$  defined as  $\langle x \rangle = \max(x, 0)$ .

**Remark 5** *The expression Eq. (3.19) (damage energy release rate-based equivalent stress) assigns the same weighting to the tensile and compressive strengths, which is unrealistic for failure behaviour of quasi-brittle materials like concrete, which exhibits a much larger compressive strength than the tensile strength. However, the expression Eq. (3.20) (Rankine-type equivalent stress) only takes material degradation in tension into account, therefore it is more appropriate for those situations where tension is dominant and no high compression stresses appear.*

With a definition for the equivalent stress, the damage criterion may be envisaged as

$$f(\boldsymbol{\sigma}, q) := \tau_\sigma - q \leq 0 \quad (3.22)$$

The quantity  $q$ , already introduced in Eq. (3.17), represents here the current damage threshold. Eq. (3.22) identifies a damage bounding surface which is an ellipsoid with the centre at the origin in the principal stress space. If the current stress state lies inside the bounding surface, then at the moment there is no further damage. Only when the scalar measure  $\tau_\sigma$  exceeds the current damage threshold value, can damage evolve.

Another key ingredient for formulating damage mechanics models is the specification of damage loading-unloading conditions, just as for plasticity models, based on classical Kuhn-Tucker conditions

$$\lambda \geq 0; f \leq 0; \lambda f = 0 \quad (3.23)$$

A consistency condition is also needed to close the set of constitutive equations and determine the value of  $\lambda$

$$\lambda \dot{f} = 0. \quad (3.24)$$

### Time integration of the constitutive equations

The previous formulation for the isotropic damage model can be integrated in closed form in terms of strains by introducing the corresponding norms in the strain space (i.e. equivalent strains) for Eqs. (3.19) and (3.20)

$$\tau_\varepsilon = \|\bar{\sigma}\|_{D_e^{-1}} = \sqrt{\bar{\sigma} : D_e^{-1} : \bar{\sigma}} = \sqrt{\varepsilon : D_e : \varepsilon} \quad (3.25)$$

$$\tau_\varepsilon^+ = \|\bar{\sigma}^+\|_{D_e^{-1}} = \sqrt{\bar{\sigma}^+ : D_e^{-1} : \bar{\sigma}^+} = \sqrt{\varepsilon^+ : D_e : \varepsilon^+} \quad (3.26)$$

By comparing the two distinct norm definitions  $\tau_\sigma$  and  $\tau_\varepsilon$ , it is interesting to observe the equality below

$$\tau_\sigma = (1 - \omega)\tau_\varepsilon \quad (3.27)$$

Then, another form of the damage criterion Eq. (3.22) is able to obtain

$$g(\varepsilon, r) := \tau_\varepsilon - r \leq 0 \quad (3.28)$$

where Eqs. (3.22), (3.27) and (3.15) have been considered. By the use of Eqs. (3.16) and (3.28) in combination with conditions (3.23), the strain-like internal variable  $r$  is integrated as

$$r = \max_{s \in [0, t]} (\tau_\varepsilon^s, r_0) \quad (3.29)$$

Eqs. (3.28) and (3.29) are the classical forms expressed for the family of continuum damage models formulated in the strain space (Oliver et al., 1990, Simo and Ju, 1987).

**Remark 6** Besides the strain-based and stress-based continuum damage models in the literature, another formulation type is the energy release rate based for coupled damage plasticity constitutive modelling. Interested readers are referred to (Ju, 1989, Wu et al., 2006) for more details.

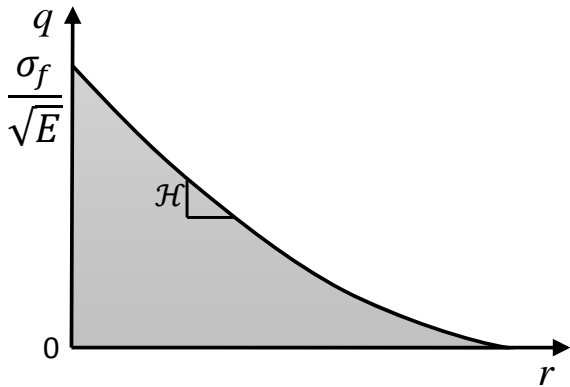
### Material tangent operator

The generic format for the material tangent operator is derived on the basis of Eqs. (3.13), (3.15) and (3.17) as follows

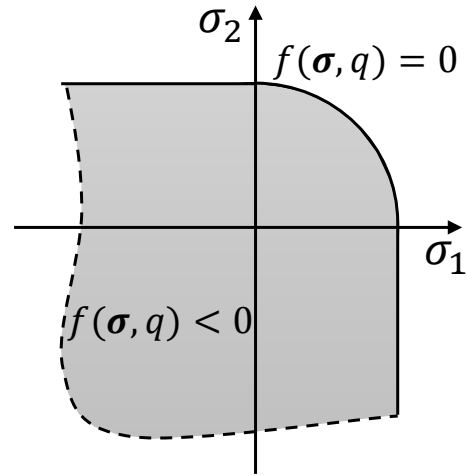
$$\begin{aligned}
 \mathbf{D}_{tan} &= \frac{\partial \dot{\boldsymbol{\sigma}}}{\partial \dot{\boldsymbol{\varepsilon}}} \\
 &= \begin{cases} (1 - \omega) \mathbf{D}_e = \frac{q}{r} \mathbf{D}_e & \text{if } \lambda = 0 \\ (1 - \omega) \mathbf{D}_e - \frac{\partial \omega}{\partial r} \frac{\partial r}{\partial \dot{\boldsymbol{\varepsilon}}} = \begin{cases} \frac{q}{r} \mathbf{D}_e - \frac{q-Hr}{r^3} \bar{\boldsymbol{\sigma}} \otimes \bar{\boldsymbol{\sigma}} & \text{if } \lambda > 0 \text{ \& Eq.(3.25) used} \\ \frac{q}{r} \mathbf{D}_e - \frac{q-Hr}{r^3} \bar{\boldsymbol{\sigma}}^+ \otimes \bar{\boldsymbol{\sigma}} & \text{if } \lambda > 0 \text{ \& Eq.(3.26) used} \end{cases} \end{cases}
 \end{aligned} \tag{3.30}$$

Figure 3.2 displays the exponential softening law given by Eq. (3.18b). Figure 3.3 illustrates the elastic domain and damage surface based on the Rankine-type equivalent strain with degradation only in tension considered.

The box 3.2.1 sums up the principal ingredients of a particular isotropic damage constitutive model.



**Figure 3.2** Exponential softening law  $q-r$  for the isotropic damage model.



**Figure 3.3** Damage criterion based on the equivalent strain type, degradation only in tension.

**Box 3.2.1: Adopted isotropic damage model.**

$$\text{Damage variable} \quad \omega = 1 - \frac{q(r)}{r} \quad (3.31)$$

$$\text{Constitutive equation} \quad \boldsymbol{\sigma} = (1 - \omega(r)) \mathbf{D}_e : \boldsymbol{\varepsilon} \quad (3.32)$$

$$\text{Damage criterion} \quad g(\boldsymbol{\varepsilon}, r) = \tau_\varepsilon - r, \quad \tau_\varepsilon = \sqrt{\bar{\boldsymbol{\sigma}}^+ : \mathbf{D}_e^{-1} : \bar{\boldsymbol{\sigma}}^+} \quad (3.33)$$

$$\text{Evolution law} \quad \dot{r} = \lambda, \quad r \in [r_0, \infty), \quad r|_{t=0} = r_0 = \frac{\sigma_f}{\sqrt{E}} \quad (3.34)$$

$$\text{Softening law} \quad \dot{q} = \mathcal{H}(r) \dot{r}, \quad q \in [0, r_0], \quad q|_{t=0} = q_0 = r_0 \quad (3.35)$$

$$\mathcal{H}(r) = -\frac{r_0^2}{g_f} \exp\left[-\frac{r_0}{g_f}(r - r_0)\right] \quad (3.36)$$

$$\text{Loading-unloading conditions} \quad \lambda \geq 0; \quad f \leq 0; \quad \lambda f = 0 \quad (3.37)$$

material properties:

$E$  : Young's modulus  $\mathbf{D}_e$  : elastic constitutive tensor

$\sigma_f$  : maximum tensile strength  $g_f$  : specific fracture energy

### 3.2.2 Local smeared crack approach (crack band approach)

In fracture mechanics, fracture energy (per unit surface area) is a characteristic physical property of materials, which should be independent of the numerical method used for the simulation of material failure. However, when using standard local constitutive laws with strain softening in FE codes, deformation and energy dissipation are concentrated in a row of elements; thus, the results and the dissipated energy strongly rely on the mesh size. The local smeared crack approach (or crack band approach) has been proposed and developed to overcome the size dependence issue (Bažant and Oh, 1983, Rots et al., 1985, Oliver, 1989, Cervera and Chiumenti, 2006a, Jirásek and Bauer, 2012). The fundamental idea is to adjust the softening branch of stress-strain curves according to the characteristic element size. The notable advantage is that the formulation remains local and the algorithmic structure of the finite element code requires only minor adjustments.

Let us consider a 1D bar under uniaxial tension and an axial coordinate  $x$  is attached to the bar. The bar is discretised with elements. Damage is assumed to be continuously distributed only within one element of length  $l_w$ . By distributing the fracture energy  $G_f$  over  $l_w$ , we have

$$G_f = \int_{x=0}^{l_w} \int_{\varepsilon=0}^{\infty} \sigma d\varepsilon dx , \quad (3.38)$$

with  $\sigma$  and  $\varepsilon$  as the normal stress and normal strain. Assume that linear elements were used whose strain is constant. Therefore, the following equality will hold

$$G_f = g_f l_w , \quad (3.39)$$

where the quantity  $g_f$  defines the energy dissipated per unit volume until total failure

$$g_f = \int_{\varepsilon=0}^{\infty} \sigma d\varepsilon . \quad (3.40)$$

As can be seen, Eq. (3.39) sets up a direct connection between the fracture toughness  $G_f$  and dissipated energy density  $g_f$ . The former quantity is physically objective and equal to the area under the traction-separation law employed in the cohesive crack model. However,  $g_f$  is not an objective parameter and needs to be adjusted at each integration point according to the numerically estimated value of  $l_w$ . The modification to the value of  $g_f$  is made by adjusting the softening branch of stress-strain curves.

The length scale  $l_w$  introduced in the crack band approach is related to the element size and thus has a numerical nature. When incorporating  $l_w$ , the computed load-displacement diagrams are no longer sensitive to the used mesh size. However, the numerical results are still affected by the mesh bias. Indeed, cracks tend to propagate along the lines of the discretisation, thus deviating from the physical crack path.

A variety of formulas have been developed to estimate the numerical length scale  $l_w$ , which may depend on the interpolation order, the spatial integration scheme and the angle between the crack and the mesh lines (Oliver, 1989, Jirásek and Bauer, 2012). It should be remarked that when quadratic or higher-order finite elements are employed for discretisation, the crack band width is not equivalent to the characteristic element size.

### 3.2.2.1 Estimation of band width

There are several means to define the effective crack band width in a multi-dimensional setting at each integration point of elements in the context of FEM. Take quadrilateral elements for example. One rough but straightforward estimate is the square root  $\sqrt{A}$  of the element area  $A$ . This method works well for elements with aspect ratios equal or close to 1. However, in general it may show large deviations in the dissipated energy for highly irregular shapes (e.g., elongated quadrilateral elements).

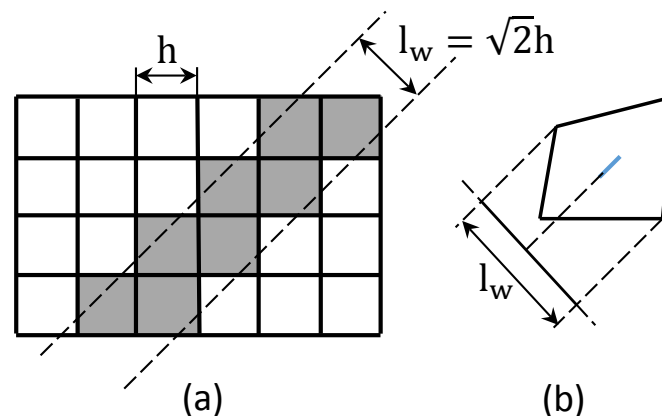


**Figure 3.4** Projection method for the estimation of crack band width: (a) crack band along element diagonals, and (b) effective band size computed by projecting along the direction perpendicular to the crack band.

The accurate value of the effective band width  $l_w$  is affected not only by the mesh size but also by the inclination of the crack band with respect to the mesh lines. This

motivates the projection method in which  $l_w$  is computed by projecting the element onto the direction perpendicular to the assumed crack band direction (Cervenka, 1995, Bazant and Planas, 1997), as illustrated in Figure 3.4. The effective band width  $l_w$  can be either determined individually at each integration point or determined once at the element centre and then applied at all integration points. The standard projection method may lead to excessive dissipation in crack bands that are not inclined with respect to the mesh lines. It was proposed in (Cervenka, 1995) to multiply the band width from the projection method by a corrective orientation factor. This factor is typically set equal to 1 for crack bands perpendicular to the mesh lines, equal to 1.5 for crack bands inclined by  $45^\circ$ , and linearly interpolated for general angles.

Oliver (1989) proposed a discretisation consistent method for estimating  $l_w$  that takes the orientation of the crack band into account. This method is based on an auxiliary continuous and derivable scalar function  $\phi$  such that it takes 0 on nodes at one side of the crack band and 1 on nodes at the other side. The effective width of the crack band can be estimated as the reciprocal value of the directional derivative of function  $\phi$ .

**Remark 7** 1. *The crack band approach can be considered as the cohesive zone model in a continuum setting.*

2. *To prevent a snap-back at the material-point level, parameter  $\varepsilon_f$  must not be smaller than  $\varepsilon_0$ , where  $\varepsilon_0$  and  $\varepsilon_f$  correspond to the strain at maximum strength and that at zero strength. This implies that the element size cannot be too large.*

3. *The crack band approach still suffers from directional mesh bias for the general case of meshes that are not well aligned.*

### 3.2.3 Gradient enhanced damage model

Let us define a new form of damage loading and unloading function based on the concept of equivalent strain measure  $\varepsilon_{eq}$ , which is an alternative to the stress-like variable based damage criterion in Eq. (3.22)

$$f = \varepsilon_{eq} - \kappa, \quad (3.41)$$

with  $\kappa$  as the internal history variable that records the largest strain level ever reached. In the nonlocal damage theory, the damage is driven by the nonlocal equivalent strain  $\bar{\varepsilon}_{eq}$  instead of the local one. In the elasticity-based integral-type nonlocal

model,  $\bar{\varepsilon}_{eq}$  is defined as (Pijaudier-Cabot and Bažant, 1987)

$$\bar{\varepsilon}_{eq}(\mathbf{x}) = \int_{\tilde{\Omega}} \alpha(\|\mathbf{x} - \mathbf{y}\|) \varepsilon_{eq}(\mathbf{y}) d\Omega , \quad (3.42)$$

where the weight function  $\alpha(\|\mathbf{x} - \mathbf{y}\|)$  determines the influence of the local strain at source point  $\mathbf{y}$  within the interacting volume  $\tilde{\Omega}$  on the nonlocal strain at the receiver point  $\mathbf{x}$ . The interacting volume is confined by the characteristic length  $l_c$  of the material. As pointed out by Jirasek et al. (2004), it is usually difficult to obtain such a characteristic length and one can only roughly estimate it to be of the same order of magnitude as the spacing of the dominant inhomogeneities (e.g. aggregates in concrete). It should be highlighted that small magnitudes of the length parameter  $l_c$  indicate that the mesh must be fine enough in order to resolve the localisation band with sufficient accuracy.

The implicit gradient enhanced damage model can be interpreted as an approximation to the integral-type nonlocal model characterised by Eq. (3.42) by assuming a particular Green's function (Peerlings et al., 2001). To derive the FE equations for the gradient enhanced damage model, we follow the classical work by Peerlings et al. (1996). The equilibrium equation given by Eq. (3.1a) is accompanied by a field equation of Helmholtz-type expressed according to Peerlings et al. (1996) as

$$\bar{\varepsilon}_{eq} - c \nabla^2 \bar{\varepsilon}_{eq} = \varepsilon_{eq} , \quad (3.43)$$

where  $c$  represents a positive parameter of the dimension length squared, determined by  $l_c$ .

To obtain an unique solution for  $\bar{\varepsilon}_{eq}$  of the partial differential equation (3.43), either the nonlocal equivalent strain  $\bar{\varepsilon}_{eq}$  itself or its normal derivative must be explicitly specified on the boundary of the problem domain. In the literature the homogeneous natural boundary condition is mostly adopted

$$\nabla \bar{\varepsilon}_{eq} \cdot \mathbf{n} = 0 , \quad (3.44)$$

with  $\mathbf{n}$  the unit normal vector to the external boundary.

### FE approximation:

The numerical implementation for the implicit gradient enhanced damage model has the character of a coupled problem. Recall the weak form of the balance of linear

momentum

$$\int_{\Omega} \boldsymbol{\sigma} : \delta \boldsymbol{\varepsilon} d\Omega = \int_{\Gamma_t} \bar{\mathbf{t}} \cdot \delta \mathbf{v} d\Gamma . \quad (3.45)$$

After employing the divergence theorem and inserting the natural boundary condition (3.44), the weak form of the Eq. (3.43) can be derived as

$$\int_{\Omega} \left( \delta \bar{\boldsymbol{\varepsilon}}_{eq} \bar{\boldsymbol{\varepsilon}}_{eq} + c \nabla \delta \bar{\boldsymbol{\varepsilon}}_{eq} \cdot \nabla \bar{\boldsymbol{\varepsilon}}_{eq} \right) d\Omega = \int_{\Omega} \delta \bar{\boldsymbol{\varepsilon}}_{eq} \boldsymbol{\varepsilon}_{eq} d\Omega . \quad (3.46)$$

From the above equation, it becomes clear that in this formulation a  $C^0$ -interpolation for  $\bar{\boldsymbol{\varepsilon}}$  suffices. The interpolation scheme for the displacement field is the same as usual. The nonlocal equivalent strain field  $\bar{\boldsymbol{\varepsilon}}_{eq}$  and its variation  $\delta \bar{\boldsymbol{\varepsilon}}_{eq}$  can be interpolated as

$$\bar{\boldsymbol{\varepsilon}}_{eq} = \bar{\mathbf{N}} \bar{\boldsymbol{\varepsilon}} , \quad \delta \bar{\boldsymbol{\varepsilon}}_{eq} = \bar{\mathbf{N}} \delta \bar{\boldsymbol{\varepsilon}} . \quad (3.47)$$

where  $\bar{\mathbf{N}}$  is the row vector of standard shape functions and the vector  $\bar{\boldsymbol{\varepsilon}}$  collects the degrees of freedom for the type of non-local equivalent strain at each node. Note that the displacement field and the nonlocal equivalent strain can be interpolated in different orders. In practice, identical interpolation functions are generally used.

Substituting Eq. (3.47) into Eq. (3.46) and requiring that the result holds for arbitrary  $\delta \bar{\boldsymbol{\varepsilon}}_{eq}$ , yields the discrete format of the Helmholtz equation

$$\int_{\Omega} \left( \bar{\mathbf{N}}^T \bar{\mathbf{N}} + c \bar{\mathbf{B}}^T \bar{\mathbf{B}} \right) \bar{\boldsymbol{\varepsilon}} d\Omega - \int_{\Omega} \bar{\mathbf{N}}^T \boldsymbol{\varepsilon}_{eq} d\Omega = \mathbf{0} , \quad (3.48)$$

where  $\bar{\mathbf{B}} = \nabla \bar{\mathbf{N}}$ . The discrete system to solve at iteration  $i$  in the Newton-Raphson method reads

$$\begin{bmatrix} \mathbf{K}_{aa} & \mathbf{K}_{a\varepsilon} \\ \mathbf{K}_{\varepsilon a} & \mathbf{K}_{\varepsilon\varepsilon} \end{bmatrix}^{i-1} \begin{bmatrix} d\mathbf{a} \\ d\bar{\boldsymbol{\varepsilon}} \end{bmatrix}^i = \begin{bmatrix} \mathbf{f}_{ext}^a \\ \mathbf{0} \end{bmatrix}^{i-1} - \begin{bmatrix} \mathbf{f}_{int}^a \\ \mathbf{f}_{int}^{\varepsilon} \end{bmatrix}^{i-1} , \quad (3.49)$$

The submatrices in the consistent Jacobian matrix on the LHS of Eq (3.49) and the internal nodal force vector  $\mathbf{f}_{int}^{\varepsilon}$  associated with the Helmholtz equation are derived in detail in the following.

#### Derivation detail:

We start the linearisation procedure by casting stress in rate form

$$\dot{\boldsymbol{\sigma}} = (1 - \omega) \mathbf{D} \dot{\boldsymbol{\varepsilon}} - \mathbf{D} \boldsymbol{\varepsilon} \dot{\omega} , \quad (3.50)$$

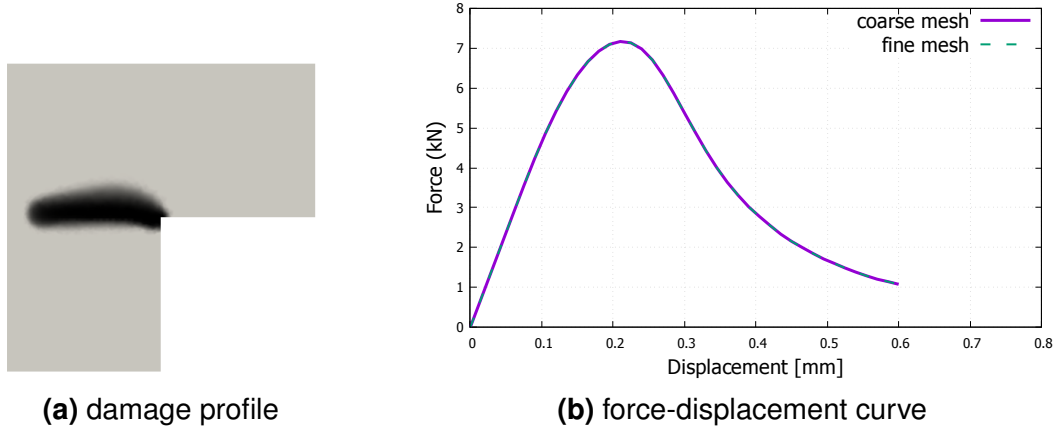


**Figure 3.5** L-shaped panel test (thickness 100 mm): (a) damage profile at the final load level and (b) force-displacement curves for two different mesh sizes (coarse and fine). The modified von Mises equivalent strain has been adopted.

where

$$\dot{\omega} = \frac{\partial \omega}{\partial \kappa} \frac{\partial \kappa}{\partial \bar{\varepsilon}_{eq}} \bar{\mathbf{N}} \dot{\bar{\boldsymbol{\varepsilon}}} . \quad (3.51)$$

Substituting the above equation into Eq. (3.50) and replacing  $\dot{\boldsymbol{\varepsilon}}$  by  $\mathbf{B}\dot{\mathbf{a}}$  results in

$$\dot{\boldsymbol{\sigma}} = (1 - \omega) \mathbf{D} \mathbf{B} \dot{\mathbf{a}} - \frac{\partial \omega}{\partial \kappa} \frac{\partial \kappa}{\partial \bar{\varepsilon}_{eq}} \mathbf{D} \boldsymbol{\varepsilon} \bar{\mathbf{N}} \dot{\bar{\boldsymbol{\varepsilon}}} . \quad (3.52)$$

Having this rate form of the constitutive equation, the linearisation of Eq. (3.45) at iteration  $i$  leads to

$$\mathbf{K}_{aa}^{i-1} \delta \mathbf{a}^i + \mathbf{K}_{a\varepsilon}^{i-1} \delta \bar{\boldsymbol{\varepsilon}}^i = (\mathbf{f}_{ext}^a)^{i-1} - (\mathbf{f}_{int}^a)^{i-1} , \quad (3.53)$$

where the matrices  $\mathbf{K}_{aa}$  and  $\mathbf{K}_{a\varepsilon}$  read

$$\begin{aligned} \mathbf{K}_{aa} &= \int_{\Omega} (1 - \omega) \mathbf{B}^T \mathbf{D} \mathbf{B} d\Omega \\ \mathbf{K}_{a\varepsilon} &= - \int_{\Omega} \frac{\partial \omega}{\partial \kappa} \frac{\partial \kappa}{\partial \bar{\varepsilon}_{eq}} \mathbf{B}^T \mathbf{D} \boldsymbol{\varepsilon} \bar{\mathbf{N}} d\Omega . \end{aligned} \quad (3.54)$$

In the same fashion, the linearisation of the Eq. (3.48) gives

$$\mathbf{K}_{\varepsilon a}^{i-1} \delta \mathbf{a}^i + \mathbf{K}_{\varepsilon \varepsilon}^{i-1} \delta \bar{\boldsymbol{\varepsilon}}^i = \int_{\Omega} \bar{\mathbf{N}}^T \boldsymbol{\varepsilon}_{eq}^{i-1} d\Omega - \mathbf{K}_{\varepsilon \varepsilon}^{i-1} \bar{\boldsymbol{\varepsilon}}^{i-1} = -(\mathbf{f}_{int}^{\varepsilon})^{i-1} , \quad (3.55)$$

where

$$\begin{aligned} \mathbf{K}_{\varepsilon a} &= - \int_{\Omega} \bar{\mathbf{N}}^T \left[ \frac{\partial \varepsilon_{eq}}{\partial \varepsilon} \right]^T \mathbf{B} d\Omega \\ \mathbf{K}_{\varepsilon \varepsilon} &= \int_{\Omega} (\bar{\mathbf{N}}^T \bar{\mathbf{N}} + c \bar{\mathbf{B}}^T \bar{\mathbf{B}}) d\Omega . \end{aligned} \quad (3.56)$$

As seen, the expressions for  $\mathbf{K}_{a\varepsilon}$  and  $\mathbf{K}_{\varepsilon a}$  exhibit a non-symmetry. This non-symmetry is caused by the damage formalism and not by the gradient enhancement. To demonstrate the working of the gradient enhance damage model, fracture testing of a L-shaped panel was performed numerically. It involves a mixed tension-compression curved cracking pattern (Unger et al., 2007). Figure 3.5a shows the numerical damage profile and Figure 3.5b plots the force-displacement curves for coarse and fine meshes. As can be seen from Figure 3.5b, the response is insensitive to the mesh size, demonstrating the efficacy of nonlocal regularisation.

### 3.3 Discontinuous crack approaches

#### Cohesive crack problem

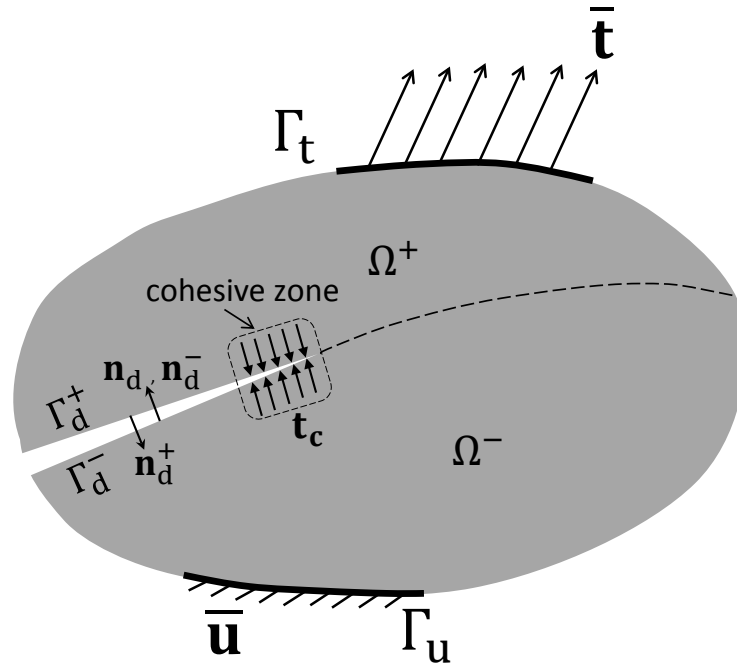


**Figure 3.6** A two-dimensional fracture problem. The cohesive crack behaviour is characterised by the cohesive zone model in the wake of the fictitious crack.

Before introducing different numerical approaches to fracture, the mathematical BVP should be first set up. Let us consider a cracked body denoted by  $\Omega$ , as shown in Figure 3.6. The crack and its virtual extension divide the whole domain into two non-overlapping subdomains  $\Omega^+$  and  $\Omega^-$ . The crack is assumed to include a traction-free portion and a cohesive zone. The nonlinear material behaviour due to various progressive damage mechanisms including microcracking, is idealised to be restricted to the cohesive zone, while the remaining bulk is assumed linear elastic. The governing equations comprise the balance of linear momentum, the essential and natural boundary conditions, and the traction continuity across the crack surfaces

$$\nabla \cdot \boldsymbol{\sigma} + \mathbf{b} = \mathbf{0} \quad \text{in } \Omega \quad (3.57a)$$

$$\boldsymbol{\sigma} \cdot \mathbf{n} = \bar{\mathbf{t}} \quad \text{on } \Gamma_t \quad (3.57b)$$

$$\mathbf{u} = \bar{\mathbf{u}} \quad \text{on } \Gamma_u \quad (3.57c)$$

$$-\boldsymbol{\sigma} \cdot \mathbf{n}_d^+ = \boldsymbol{\sigma} \cdot \mathbf{n}_d^- = \mathbf{t}_c \quad \text{on } \Gamma_d \quad (3.57d)$$

where  $\mathbf{t}_c$  is the cohesive traction vector across the crack  $\Gamma_d$  with the unit normal vector  $\mathbf{n}_d$  ( $\mathbf{n}_d = \mathbf{n}_d^- = -\mathbf{n}_d^+$ ).

Using the principle of virtual work, the weak form corresponding to the strong form of the cohesive crack problem Eq. (3.57) is derived as

$$\int_{\Omega} \boldsymbol{\sigma} : \boldsymbol{\varepsilon}(\delta \mathbf{v}) d\Omega + \int_{\Gamma_d} \mathbf{t}_c \cdot \delta \llbracket \mathbf{v} \rrbracket d\Gamma_d = \int_{\Omega} \mathbf{b} \cdot \delta \mathbf{v} d\Omega + \int_{\Gamma_t} \bar{\mathbf{t}} \cdot \delta \mathbf{v} d\Gamma \quad \forall \delta \mathbf{v} \in \mathcal{V} \quad (3.58)$$

where  $\mathcal{V}$  is the functional space of admissible virtual displacements defined previously in Eq. (3.3b). The operator  $\llbracket \cdot \rrbracket$  represents the jump of a variable across the crack surfaces. For example,  $\llbracket \mathbf{u} \rrbracket$  denotes the displacement jump of the crack. The cohesive traction  $\mathbf{t}_c$  is an explicit function of the displacement jump  $\llbracket \mathbf{u} \rrbracket$ , determined by a defined cohesive law.

There are two classes of cohesive law models namely (a) initially elastic cohesive laws (*intrinsic model*) and (b) initially rigid cohesive laws (*extrinsic model*) (Needleman, 1987, Camacho and Ortiz, 1996, Kubair and Geubelle, 2003). Two typical representatives of those traction-separation law models are illustrated in Figure 3.7. It should be mentioned that the initiation criterion is inherently considered in the intrinsic model, whereas in the extrinsic model a separate initiation criterion is essential for starting the fracture process.

The cohesive zone model can be represented by cohesive elements, XFEM or

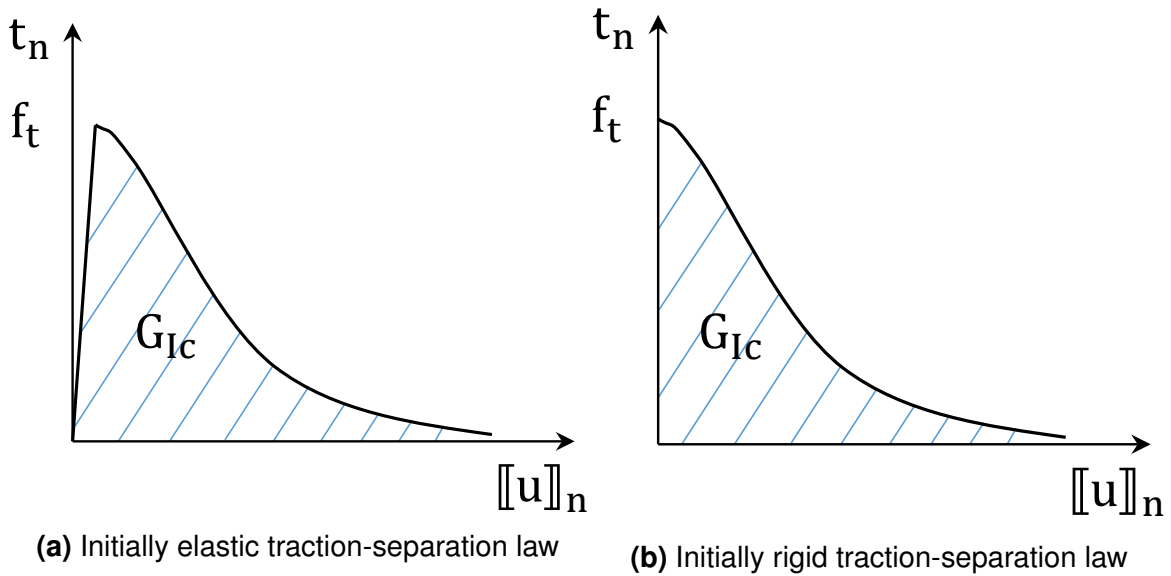


**Figure 3.7** Schematic of two types of traction-separation laws.

meshless methods. In the following, we will discuss the cohesive elements and XFEM method.

### 3.3.1 Cohesive elements

Cohesive elements (or called interface elements) are extensively utilised to address interface problems, such as composite delamination and interface debonding. At the same time, cohesive elements are also used when capturing complex fracture mechanisms such as crack branching and crack coalescence, where they are explicitly inserted *a priori* along any potential cracking path in the continuum. In this section, the four-node  $1D$  linear cohesive elements with initially elastic cohesive laws (see Figure 3.7a) are described. Cohesive elements are inserted before the simulation starts and the cohesive law consists of an initial elastic branch with a rather high artificial stiffness.

#### Kinematics of cohesive elements

The bulk is discretised by continuum elements and the crack is discretised by cohesive elements which are one dimension less than the continuum elements, see Figure 3.8. Each cohesive element has two characteristic faces, the upper and lower faces, used to model the difference in the displacements at the attached sides of the continuum elements.

With the nodal displacements given for a four-node cohesive element, the global

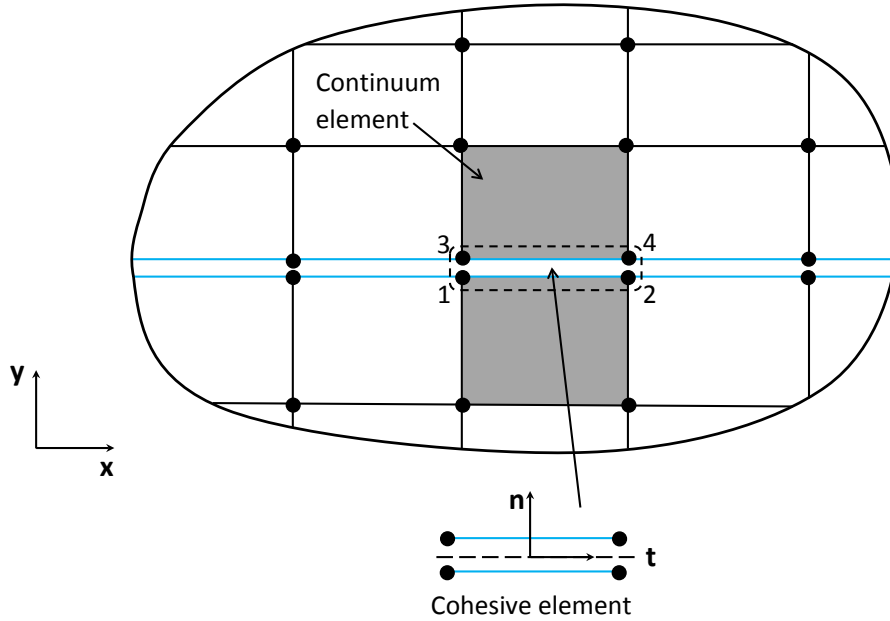


**Figure 3.8** 1D linear cohesive elements are embedded between continuum elements to model the crack. Global coordinates and local coordinates are denoted by  $(x, y)$  and  $(t, n)$ , respectively. The nodes for the typical cohesive element are ordered 1, 2, 3, 4.

displacements of the upper face (marked by sign +) and lower face (marked by sign -) of the cohesive element are interpolated as

$$\begin{aligned} \mathbf{u}^+ &= N_1 \mathbf{u}_3 + N_2 \mathbf{u}_4 \\ \mathbf{u}^- &= N_1 \mathbf{u}_1 + N_2 \mathbf{u}_2, \end{aligned} \quad (3.59)$$

where  $N_1, N_2$  are the shape functions of the two-node line elements, and  $(\mathbf{u}_3, \mathbf{u}_4)$  and  $(\mathbf{u}_1, \mathbf{u}_2)$  are the upper-face and the lower-face global nodal displacements, respectively.

The global displacement jump (separation) for the typical crack segment represented by the cohesive element under consideration is then expressed as

$$[[\mathbf{u}]] = \mathbf{u}^+ - \mathbf{u}^- = \mathbf{N}_{int} \begin{bmatrix} \mathbf{u}_3 - \mathbf{u}_1 \\ \mathbf{u}_4 - \mathbf{u}_2 \end{bmatrix}, \quad (3.60)$$

with  $\mathbf{N}_{int}$  being the shape function matrix of the cohesive element,

$$\mathbf{N}_{int} = \begin{bmatrix} N_1 & 0 & N_2 & 0 \\ 0 & N_1 & 0 & N_2 \end{bmatrix}, \quad (3.61)$$

where the subscript “int” has been added to distinguish from that of the continuum elements. Eq. (3.60) can be modified by introducing a separation-displacement relation matrix  $\mathbf{L}_s$

$$\mathbf{L}_s = \begin{bmatrix} -1 & 0 & 0 & 0 & 1 & 0 & 0 & 0 \\ 0 & -1 & 0 & 0 & 0 & 1 & 0 & 0 \\ 0 & 0 & -1 & 0 & 0 & 0 & 1 & 0 \\ 0 & 0 & 0 & -1 & 0 & 0 & 0 & 1 \end{bmatrix}, \quad (3.62)$$

such that

$$[[\mathbf{u}]] = \mathbf{N}_{int} \mathbf{L}_s [\mathbf{u}_1, \mathbf{u}_2, \mathbf{u}_3, \mathbf{u}_4]^T. \quad (3.63)$$

To diminish the effect of rigid rotations of cohesive elements, the global coordinate system  $(x, y)$  should be transformed to a local coordinate system  $(t, n)$  aligned with the midplane of the cohesive element, see Figure 3.9. The midplane  $AB$  connecting midside points of the cohesive element, defines the local tangential direction  $t$ . The normal (thickness) axis direction  $n$  is then obtained as the cross product of the out-of-plane and tangent directions.

To change between the local and global displacements, a orthogonal rotational

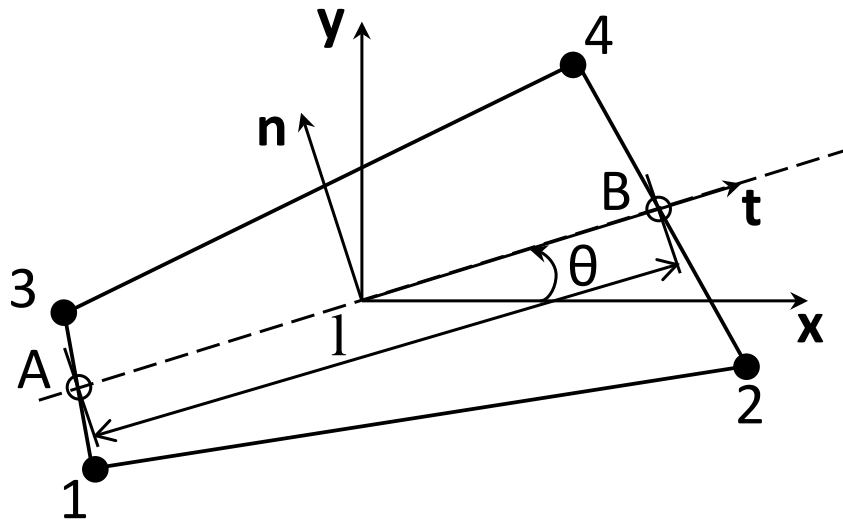


**Figure 3.9** Definition of the local axes  $(t, n)$ , midplane  $AB$  and rotation angle  $\theta$  in a cohesive element.

matrix  $\mathbf{Q}$  is introduced

$$\mathbf{Q} = \begin{bmatrix} \cos \theta & \sin \theta \\ -\sin \theta & \cos \theta \end{bmatrix}, \quad (3.64)$$

where  $\theta$  is the rotation angle with respect to the global axes and defined as (see Figure 3.9)

$$\begin{aligned}\theta &= \arccos\left(\frac{x_B - x_A}{l}\right) \\ l &= \sqrt{(x_B - x_A)^2 + (y_B - y_A)^2} .\end{aligned}\tag{3.65}$$

Accordingly, the local separation  $[[\mathbf{u}]]^l$  is obtained by the application of the transformation matrix onto the global separation  $[[\mathbf{u}]]$

$$[[\mathbf{u}]]^l = \mathbf{Q}[[\mathbf{u}]] .\tag{3.66}$$

Once the local separation is defined, the local cohesive traction field  $\mathbf{t}_c^l$  can be derived through the traction-separation law that describes the crack behaviour. The rate form of the cohesive crack constitutive equation can be symbolised as

$$\dot{\mathbf{t}}_c^l = \mathbf{T}[[\dot{\mathbf{u}}]]^l ,\tag{3.67}$$

where  $\mathbf{T}$  is the cohesive (material) tangent matrix whose precise form relies on the adopted traction-separation law. The global cohesive traction field  $\mathbf{t}_c$  is transformed from the local cohesive traction field  $\mathbf{t}_c^l$  using the transformation matrix  $\mathbf{Q}$

$$\mathbf{t}_c = \mathbf{Q}^T \mathbf{t}_c^l = \mathbf{Q}^T \mathbf{T} \mathbf{Q} [[\dot{\mathbf{u}}]] = \mathbf{Q}^T \mathbf{T} \mathbf{Q} \mathbf{N}_{int} \mathbf{L}_s \mathbf{L}_e \mathbf{U} .\tag{3.68}$$

where use of Eqs. (3.67,3.66,3.63,3.6a) was made in sequence in the above derivation.

### Cohesive elements formulation

With the (discretised) approximation for the displacement jumps at hand and recalling Eq. (3.4) for the displacement approximation of the continuum elements, considering their variational forms, Eq. (3.58) can be discretised as

$$\mathbf{f}_{int} + \mathbf{f}_{coh} = \mathbf{f}_{ext}\tag{3.69}$$

with

$$\begin{aligned}
 \mathbf{f}_{int} &= \sum_{e=1}^{n_{bulk}} \mathbf{L}_e^T \int_{\Omega_e} \mathbf{B}_e^T \boldsymbol{\sigma}_e d\Omega \\
 \mathbf{f}_{coh} &= \sum_{e=1}^{n_{int}} \mathbf{L}_e^T \mathbf{L}_s^T \int_{\Gamma_d} \mathbf{N}_{int}^T \mathbf{t}_c d\Gamma_d \\
 \mathbf{f}_{ext} &= \sum_{e=1}^{n_{bulk}} \mathbf{L}_e^T \left( \int_{\Omega_e} \mathbf{N}_e^T \mathbf{b}_e d\Omega + \int_{\Gamma_e} \mathbf{N}_e^T \bar{\mathbf{t}}_e d\Gamma \right),
 \end{aligned} \tag{3.70}$$

where the internal force vector  $\mathbf{f}_{int}$  and external force vector  $\mathbf{f}_{ext}$  are computed from contributions of  $n_{bulk}$  continuum elements, whereas  $\mathbf{f}_{int}$  is assembled from  $n_{int}$  cohesive elements.

The linearisation of the (global) cohesive force vector in Eq. (3.70), as with the procedure discussed in Section 3.1.2, results in the cohesive tangent stiffness matrix. For a cohesive element, the cohesive tangent stiffness matrix is written as

$$\mathbf{K}_e^{int} = \mathbf{L}_s^T \int_{\Gamma_d} \mathbf{N}_{int}^T \mathbf{Q}^T \mathbf{T} \mathbf{Q} \mathbf{N}_{int} \mathbf{L}_s d\Gamma_d, \tag{3.71}$$

which is a  $8 \times 8$  matrix for four-node linear cohesive elements and it is then assembled to the appropriate locations by the element location matrix  $\mathbf{L}_e$ . The tangent stiffness matrix of standard continuum elements is expressed the same as in Eq. (3.11) in Section 3.1.2.

[Nguyen \(2014\)](#) presented an automatic preprocessing procedure for inserting cohesive elements into places where possible crack initiation and propagation are permitted to occur. This increases the flexibility for using cohesive elements in the whole domain for simulation. Figure 3.10 shows a numerical example with cohesive elements only inserted along the mid-plane of a compact-tension specimen.

**Remark 8** *An alternative implementation of the cohesive zone concept allocates discrete point-wise spring elements at FE node pairs on the intended crack surface or interface ([Xie and Waas, 2006](#), [Xie et al., 2006](#)). It makes use of a discrete cohesive zone model that engages a force-separation relation. Traction distributed on the interface are explicitly lumped to point-wise spring elements instead of their surface contribution being accounted for through performing numerical integration as in the cohesive elements just described.*

### Mixed-mode cohesive laws

When describing progressive separation processes in materials, a variety of cohesive (traction-separation) laws of can be considered. These cohesive laws generally

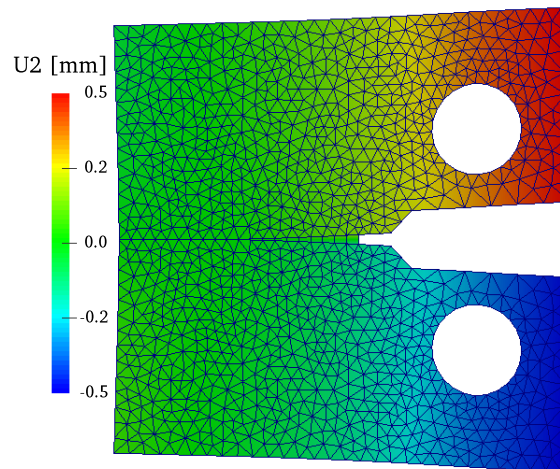


**Figure 3.10** Deformed configuration of a compact-tension specimen under mode-I fracture with the crack modelled with cohesive elements.  $U_2$  represents the vertical displacement.

have distinct shapes for quasi-brittle and ductile materials, depending on the intrinsic nature of materials. Since mixed-mode loading scenarios are frequently encountered in engineering practice, a mixed-mode cohesive law formulation is necessary. In the literature, two main categories of cohesive law formulations exist, namely potential-based formulations (Needleman, 1987, Tvergaard and Hutchinson, 1993, Ortiz and Pandolfi, 1999, Park et al., 2009) and non-potential-based formulations (Xie and Waas, 2006, Camanho et al., 2003, Geubelle and Baylor, 1998, Turon et al., 2006).

In the first family of formulations, a potential function is first constructed, perhaps using a one-dimensional generalised relationship between the equivalent traction and separation as in (Ortiz and Pandolfi, 1999). Normal and tangential cohesive laws are merely the derivatives of this potential function with respect to the corresponding normal and tangential separations.

In the second family of formulations, normal and tangential cohesive laws under mixed-mode conditions are not required to be related through a potential function. Their interaction may be governed through extra criteria such as the well known power law criterion for crack growth (Xie and Waas, 2006). In a distinct setting in which each traction component is a function of both normal and tangential separations, a single effective law and a constant scaling factor have been used to treat mixed-mode crack propagation in (Geubelle and Baylor, 1998). It is noteworthy that some of the non-potential-based implementations encounter a critical issue that non-zero tractions on the crack surface can be found in the final failure state (Nguyen and Waas, 2016). To address this issue, an incremental mixed-mode evolution law

was developed in (Joseph et al., 2018) where the energy remaining to be dissipated is estimated at each load increment following an assumption that the ratio of energy remaining to be dissipated for the individual modes is proportional to the ratio of energy dissipated by the individual modes so far. Nguyen and Waas (2016) examined different cohesive formulations and proposed a novel mixed-mode cohesive formulation where the mode-II cohesive law is scaled to the mode-I cohesive law, and an effective separation is defined for the scaled law. In this way, physically realistic and numerically stable results were obtained.

In the following, a mixed-mode cohesive formulation following the work by Turon et al. (2006) is described in the two-dimensional setting, where an equivalent displacement jump  $[[u]]_{eq}$  is defined as

$$[[u]]_{eq} = \sqrt{\langle [[u]]_n \rangle^2 + [[u]]_s^2}, \quad (3.72)$$

with  $[[u]]_n$  and  $[[u]]_s$  being the normal and shear (tangential) components of displacement jump in the local coordinate system, respectively. For a bilinear shape of the softening law, two essential equivalent displacement jump parameters need to be determined at which damage is considered to be initiated and completed. These two equivalent displacement jump parameters are not unique and recognised to depend on the relation between the normal and shear components at the interface. This relation may be captured by the following mode-mixity parameter  $\beta$  (Turon et al., 2006)

$$\beta = \frac{|[[u]]_s|}{\langle [[u]]_n \rangle + |[[u]]_s|}, \quad (3.73)$$

For the detailed treatment of damage initiation criterion, damage evolution law and tangent stiffness matrix, interested readers refer to (Turon et al., 2006).

## Drawbacks of intrinsic cohesive elements

### 1. Artificial compliance

Cohesive elements with an intrinsic cohesive law are not very effective when used for modelling bulk cracking. One major reason is that cohesive elements have to be *a priori* present along all the shared edges of the continuum elements, leading to artificial compliance at the same time. To keep the unnecessary opening to a minimum in the elastic regime, sufficiently high artificial stiffness has to be considered. This may lead to an issue of spurious traction oscillations, as discussed in the literature (Schellekens and De Borst, 1993b). A widely used strategy to mitigate oscillations is by means of reduced Lobatto integration (Schellekens and De Borst,

1993b, Simone, 2004). Svenning (2016) attributed traction oscillations to the violation of the inf–sup condition and suggested a weak penalty formulation for the intrinsic cohesive elements. Based on a traction approximation that fulfils the inf–sup condition, oscillation free response is expected without the need to modify cohesive zone laws or introduce additional unknowns.

## 2. Small element sizes

To fully resolve the cohesive tractions with accuracy and seek the stable post-peak response at each load increment, the size of cohesive elements has to be sufficiently small compared to the characteristic length  $l_{cz}$  of the cohesive zone model (Camacho and Ortiz, 1996, Falk et al., 2001, Turon et al., 2007). Note that the length  $l_{cz}$  is defined as the distance from the crack tip to the point of maximum cohesive traction. The number of elements  $N_e^{cz}$  used in the cohesive zone can be defined as

$$N_e^{cz} = \frac{l_{cz}}{l_e}, \quad (3.74)$$

where  $l_e$  is the typical element size in the propagation direction of cracks. Note that  $l_{cz}$  can have varied definitions in the literature (Dugdale, 1960, Hillerborg et al., 1976).

Small values of cohesive element size would typically result in considerable computational burden, since the size of the cohesive zone of materials is normally small compared to the whole structure. Falk et al. (2001) used  $N_e^{cz}$  between 2 and 5 elements in the cohesive zone in their simulations. Turon et al. (2007) proposed to adjust the maximum interfacial strength in the computations with coarse meshes. By reducing the maximum interfacial strength, the cohesive zone length  $l_{cz}$  can be enlarged such that the cohesive zone is able to comprise more elements. Zander et al. (2017) proposed a multilevel  $hp$ -adaptivity approach for cohesive fracture where the computational burden was significantly reduced while allowing for an accurate resolution of the cohesive zone.

## 3. Convergence issues

Alfano and Crisfield (2003) proposed a local arc-length method combined with line-search techniques to alleviate convergence issues when using cohesive elements in their delamination analysis. A poor convergence rate or even divergence can be manifested by local elastic snap-backs on the global load-displacement diagram

under displacement loading control (Gao and Bower, 2004, Zander et al., 2017). The standard Newton-Raphson method cannot capture such snap-backs as the convergence radius is no longer existent. Another interpretation of the convergence problem is the appearance of several zero or negative eigenvalues in stiffness matrices of damaging elements, thereby resulting in the ill-conditioning of the global discrete system (Liu and Zheng, 2010). To make the solution procedure more robust, Chaboche et al. (2001) and Gao and Bower (2004) proposed viscous regularisation techniques. Yu et al. (2016) applied such techniques to the numerical study of hydrogen embrittlement under constant displacement condition.

From the energy point of view, the surplus energy released during creation of new free surfaces can appear in other forms, such as kinetic energy or viscous energy. The cohesive traction during separation is adjusted by the rate of separation and the additional energy dissipation by viscosity is thereby dependent on the rate of separation. For small enough step increments, a positive definite tangent stiffness for the cohesive constitutive model can be expected, which should result in reasonable numerical convergence.

Following the viscous regularisation technique by Gao and Bower (2004), a small viscous term is added to the cohesive traction-separation relation. This technique is quite straightforward in practical applications. Let us take a one-dimensional cohesive law in terms of traction  $t$  and separation  $\delta$  for example. The modified traction  $t_\mu$  can be expressed as

$$t_\mu(\delta) = t(\delta) + \eta \cdot \frac{t_f \dot{\delta}}{\delta_f}, \quad (3.75)$$

where  $\eta$  stands for the viscosity parameter;  $t_f$  and  $\delta_f$  are the maximum cohesive strength and the separation corresponding to total failure. In this manner, the dependence of cohesive traction on the rate of separation is explicitly considered. Another alternative is to introduce a viscous constant through controlling the evolution rate of damage variable (Abaqus, 2012), by which the increase in damage is slowed down.

Caution should be exercised in choosing the appropriate viscosity parameter, since too high damping may significantly affect the accuracy of solutions, while for low values, convergence may not be attained (Zander et al., 2017). Obtaining an optimal value for the viscosity parameter is a manual process that requires trial and error until the change in response is insignificant.

### 3.3.2 The eXtended finite element method

The XFEM is a widespread numerical technique for modelling discontinuous and moving interfaces. It is based on the concept of a *partition of unity* and can be viewed as a special case of the partition of unity method (PUM) (Babuška and Melenk, 1997). In the literature, a quite similar method to the XFEM is known as the Generalized Finite Element Method (GFEM) (Strouboulis et al., 2001).

For any arbitrary field function  $f(\mathbf{x})$ , the following equality always holds

$$\sum_{i=1}^n \varphi_i(\mathbf{x}) f(\mathbf{x}) = f(\mathbf{x}), \quad \text{if } \sum_{i=1}^n \varphi_i(\mathbf{x}) = 1. \quad (3.76)$$

In this case, functions  $\varphi_i(\mathbf{x})$  are said to form a partition of unity.

A typical example is the standard finite element method where the shape functions form a partition of unity. The underlying idea of the PUM is that the standard finite element approximation space is enriched by products of the partition-of-unity functions and deliberately selected functions. These selected functions are the so-called *enrichments* and are usually constructed on the basis of *a priori* knowledge of the solution of the original physical problem. In this manner, the crucial characteristics of the problem are captured by the enriched approximation, which would otherwise be difficult or even impossible by the piecewise polynomial approximation in the standard FEM.

One remarkable feature of the PUM is the local compact support of the enriched functions, which is achieved by multiplying the enrichment functions with the standard nodal shape functions that take place of  $\varphi_i(\mathbf{x})$  in Eq. (3.76); thus the resulting global stiffness matrix remains sparse. The enrichment functions can be recovered exactly within regions of interest due to the property of partition of unity of the standard shape functions. To avoid linear dependency, the enriched functions should not come from the span of the partition of unity functions.

Whenever particular characteristics are required, additional degrees of freedom are added to the nodes within the enriched regions. Therefore, the mesh topology can be preserved without the need to update for conforming to the interface geometry. This property is quite powerful especially for evolving internal interfaces (e.g., cracks) (Moës et al., 1999, Chessa et al., 2002, Sukumar et al., 2003). In the following, a curved crack that has been approximated with piecewise straight crack segments will be discussed.

The dominant features of the solution to a brittle fracture problem are that the crack

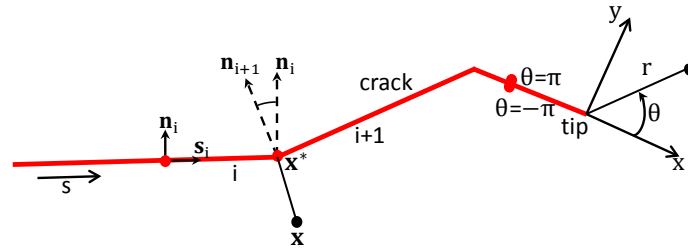


**Figure 3.11** A crack with kinks to approximate a smooth curved crack with a local polar coordinate system at the crack tip.  $x^*$  is the closest point to  $x$  on the crack.

is discontinuous in displacements (i.e., crack opening) and the stresses and strains are singular at the crack tip. To capture the highly nonlinear displacement field and the singularity at the crack tip, the branch functions obtained from the exact near-tip asymptotic displacement field are taken as the enrichment functions (Dolbow et al., 2001)

$$B_\alpha(r, \theta) \equiv \left\{ \sqrt{r} \sin \frac{\theta}{2}, \sqrt{r} \cos \frac{\theta}{2}, \sqrt{r} \sin \frac{\theta}{2} \sin \theta, \sqrt{r} \cos \frac{\theta}{2} \sin \theta \right\}, \quad (3.77)$$

where  $(r, \theta)$  are the local polar coordinates defined at the crack tip; see Figure 3.11. The local polar coordinates  $r$  and  $\theta$  can be evaluated from the local Cartesian coordinates  $x$  and  $y$

$$r(x, y) = \sqrt{x^2 + y^2}, \quad \theta(x, y) = \text{sgn}(y) \arccos \frac{x}{\sqrt{x^2 + y^2}}. \quad (3.78)$$

From the above equation, the range of  $\theta$  is  $[-\pi, \pi]$ , where  $-\pi$  and  $\pi$  correspond to points on the bottom surface and top surface of the crack segment on which the crack tip is located. It is realised that the first function  $\sqrt{r} \sin \frac{\theta}{2}$  in Eq. (3.77) is discontinuous across the crack segment with the crack tip while the remaining three functions are continuous.

The nodes whose support is entirely bisected by the crack, see Figure 3.12, are enriched with the Heaviside (step) function  $H(\mathbf{x})$  shifted on the crack path. The crack is for simplicity often explicitly described by a polyline that can be parametrised by the crack length  $s$ , as in Figure 3.11. The Heaviside function reads

$$H(\mathbf{x}) = \begin{cases} 1 & \text{for } (\mathbf{x} - \mathbf{x}^*) \cdot \mathbf{n}_i > 0, \\ 0 & \text{for } (\mathbf{x} - \mathbf{x}^*) \cdot \mathbf{n}_i < 0, \end{cases} \quad (3.79)$$

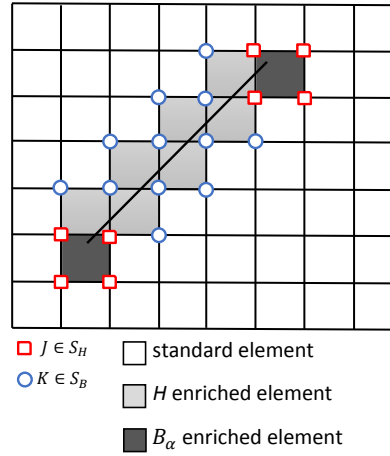


**Figure 3.12** A typical FE mesh with a crack. The circled nodes are enriched with the Heaviside function, and the squared nodes are enriched with near-tip asymptotic fields.

where  $\mathbf{x}^*$  is the closest point on the  $i$ -th crack segment to the point  $\mathbf{x}$  and  $\mathbf{n}_i$  is the unit normal to the current crack segment through the point  $\mathbf{x}^*$  such that  $\mathbf{s}_i \times \mathbf{n}_i = \mathbf{e}_z$  with  $\mathbf{e}_z$  is the unit vector normal to and pointing out of the page.  $\mathbf{s}_i$  is the tangential unit vector parallel to the  $i$ -th crack segment where  $\mathbf{x}^*$  locates. In the case where no unique normal but a cone of normals is defined at  $\mathbf{x}^*$ ,  $H(\mathbf{x}) = 1$  if the vector  $(\mathbf{x} - \mathbf{x}^*)$  belongs to the cone of normals at  $\mathbf{x}^*$  and otherwise 0. By using the Heaviside function, the character of displacement discontinuity along the entire crack is captured exactly where it needs to be identified.

In summary, the approximate displacement field for the body with a linear elastic crack by exploiting the PUM is

$$\mathbf{u}(\mathbf{x}) = \sum_{I \in S} N_I(\mathbf{x}) \mathbf{a}_I + \sum_{J \in S_H} N_J(\mathbf{x}) H(\mathbf{x}) \mathbf{b}_J + \sum_{K \in S_B} N_K(\mathbf{x}) \sum_{\alpha=1}^4 B_\alpha(\mathbf{x}) \mathbf{b}_K^\alpha, \quad (3.80)$$

where nodes in set  $S_H$  are such that their support is split by the crack and nodes in  $S_B$  belong to the elements that contain a crack tip. The nodes in these two different sets are enriched with the Heaviside function  $H(\mathbf{x})$  in Eq. (3.79) and the branch functions  $B_\alpha(\mathbf{x})$  in Eq.(3.77), respectively. The number of enriched degrees of freedom per node is equal to the number of terms in the enriched basis multiplied by the spatial dimension.

Following the Bubnov-Galerkin procedure, the discrete equation  $\mathbf{K}\mathbf{d} = \mathbf{f}$  is obtained corresponding to the weak form of the XFEM formulation. Special care is needed for the integration of the weak form since the enrichment functions are discontinuous or even singular within the elements. The standard approach for the numerical

integration in the XFEM is to split the crack intersected elements into integration subcells (normally triangles) (Khoei, 2014). In practice, this is performed according to the geometrical data of the element nodes, intersection points of the crack path with element edges, and the crack tip.

### Cohesive crack with XFEM

To deal with cohesive cracks with the XFEM formulation, we follow the work presented by Wells and Sluys (2001b). To allow displacement discontinuities within continuum elements, the Heaviside function defined in Eq. (3.79) is used. The approximated displacement field can be represented as

$$\mathbf{u} = \mathbf{N}\mathbf{a} + H_{\Gamma_d}\mathbf{N}\mathbf{b} , \quad (3.81)$$

where  $\mathbf{N}$  is the matrix of the standard finite element shape functions; the subscript  $\Gamma_d$  has been added to  $H$  to indicate that the Heaviside function is centred along the discontinuity  $\Gamma_d$ ; the vector  $\mathbf{a}$  contains the regular degrees of freedom and the vector  $\mathbf{b}$  contains the enriched degrees of freedom. The displacement jump at the discontinuity can be interpolated as

$$[[\mathbf{u}]] = \mathbf{N}\mathbf{b} . \quad (3.82)$$

By taking the symmetric gradient of Eq. (3.81), the strain field in enriched elements can be expressed as

$$\boldsymbol{\varepsilon} = \mathbf{B}\mathbf{a} + H_{\Gamma_d}\mathbf{B}\mathbf{b} + (\delta_{\Gamma_d}\bar{\bar{\mathbf{n}}})\mathbf{N}\mathbf{b} , \quad (3.83)$$

where  $\delta_{\Gamma_d}$  is the Dirac delta distribution as a result of the differentiation of the discontinuous Heaviside function; the matrix  $\bar{\bar{\mathbf{n}}}$  (not explicitly given here) contains the normal components to the discontinuity.

Inserting the strain expression from Eq. (3.83) into the weak form Eq. (3.2) without considering the body forces leads to

$$\int_{\Omega} \nabla^s \delta \hat{\mathbf{v}} : \boldsymbol{\sigma} d\Omega + \int_{\Omega} H_{\Gamma_d} \nabla^s \delta [[\mathbf{v}]] : \boldsymbol{\sigma} d\Omega + \int_{\Gamma_d} \mathbf{t}_c \cdot \delta [[\mathbf{v}]] d\Gamma_d = \int_{\Gamma_t} \bar{\mathbf{t}} \cdot \delta \hat{\mathbf{v}} d\Gamma , \quad (3.84)$$

where  $\delta \hat{\mathbf{v}}$  and  $\delta [[\mathbf{v}]]$  are separate admissible displacement variations;  $\mathbf{t}_c$  are the cohesive tractions acting on the discontinuity. The integration property of the Dirac delta distribution and Cauchy's stress theorem were used in the derivation of the third term in Eq. (3.84). Note that the external force contributions, that is the RHS

of Eq. (3.84), do not involve  $\delta[[\mathbf{v}]]$  related terms in order to simplify in practice the application of traction and displacement boundary conditions.

After deriving the variational formulation as Eq. (3.84), the next step is to derive the discrete FE equations. The variations  $\delta\hat{\mathbf{v}}$  and  $\delta[[\mathbf{v}]]$  can be expressed in terms of variations  $\delta\mathbf{a}$  and  $\delta\mathbf{b}$  of nodal degrees of freedom  $\mathbf{a}$  and  $\mathbf{b}$  in Eq. (3.81)

$$\delta\hat{\mathbf{v}} = \mathbf{N}\delta\mathbf{a}, \quad \delta[[\mathbf{v}]] = \mathbf{N}\delta\mathbf{b}. \quad (3.85)$$

Accordingly, the corresponding gradients of the variations  $\delta\hat{\mathbf{v}}$  and  $\delta[[\mathbf{v}]]$  are

$$\nabla^s \delta\hat{\mathbf{v}} = \mathbf{B}\delta\mathbf{a}, \quad \nabla^s \delta[[\mathbf{v}]] = \mathbf{B}\delta\mathbf{b}. \quad (3.86)$$

Inserting these variations into the variational formulation Eq. (3.84) and taking variations in turn  $\delta\hat{\mathbf{v}}$  and  $\delta[[\mathbf{v}]]$  while fixing the other result in

$$\int_{\Omega} \mathbf{B}^T \boldsymbol{\sigma} d\Omega = \int_{\Gamma_t} \mathbf{N}^T \bar{\mathbf{t}} d\Gamma, \quad (3.87a)$$

$$\int_{\Omega^+} H_{\Gamma_d} \mathbf{B}^T \boldsymbol{\sigma} d\Omega + \int_{\Gamma_d} \mathbf{N}^T \mathbf{t}_c d\Gamma_d = \mathbf{0}. \quad (3.87b)$$

Note that the integration domain of the first integral in Eq. (3.87b) is  $\Omega^+$  (Figure 3.6), for which  $\delta[[\mathbf{v}]]$  is non-zero. From Eq. (3.87), the equivalent internal nodal forces relating to the regular degrees of freedom  $\mathbf{a}$  and to the enriched degrees of freedom  $\mathbf{b}$  are written as

$$\mathbf{f}_a^{int} = \int_{\Omega} \mathbf{B}^T \boldsymbol{\sigma} d\Omega, \quad (3.88a)$$

$$\mathbf{f}_b^{int} = \int_{\Omega^+} H_{\Gamma_d} \mathbf{B}^T \boldsymbol{\sigma} d\Omega + \int_{\Gamma_d} \mathbf{N}^T \mathbf{t}_c d\Gamma_d. \quad (3.88b)$$

As can be seen from Eq. (3.88), the internal force vector  $\mathbf{f}_a^{int}$  is of the usual form for finite elements, and the internal force vector  $\mathbf{f}_b^{int}$  must be zero as indicated by Eq. (3.87b), which imposes traction continuity in a weak sense.

The global stiffness matrix can be obtained as by linearising Eq. (3.88)

$$\mathbf{K}_{xfem} = \begin{bmatrix} \mathbf{K}_{aa} & \mathbf{K}_{ab} \\ \mathbf{K}_{ba} & \mathbf{K}_{bb} \end{bmatrix}, \quad (3.89)$$

where the constituting components are

$$\begin{aligned}
\mathbf{K}_{aa} &= \int_{\Omega} \mathbf{B}^T \mathbf{D} \mathbf{B} d\Omega , \\
\mathbf{K}_{ab} &= \mathbf{K}_{ba} = \int_{\Omega^+} H_{\Gamma_d} \mathbf{B}^T \mathbf{D} \mathbf{B} d\Omega , \\
\mathbf{K}_{bb} &= \int_{\Omega^+} H_{\Gamma_d} \mathbf{B}^T \mathbf{D} \mathbf{B} d\Omega + \int_{\Gamma_d} \mathbf{N}^T \mathbf{Q}^T \mathbf{T} \mathbf{Q} \mathbf{N} d\Gamma_d ,
\end{aligned} \tag{3.90}$$

where the generic rate form of the bulk constitutive model  $\dot{\boldsymbol{\sigma}} = \mathbf{D} : \dot{\boldsymbol{\varepsilon}}$  and the generic rate form of the cohesive constitutive model posed in Eq. (3.67), have been taken into account. The integration of the discontinuity term in Eq. (3.87b) over the discontinuity is straightforward. In the case of a two-dimensional implementation, the discontinuity, represented by a set of connected straight line segments, can be integrated using a one-dimensional integration scheme. The implementation of the cohesive XFEM in an existing FE code needs extra modifications in order to find the elements affected by the cracks and to modify the element stiffness matrices of these enriched elements.

In the numerical implementation, when Dirichlet boundary conditions are applied at the enriched nodes, the shifted basis enrichment scheme is suggested such that the enrichment term vanishes at the nodes and thus the blending elements problem is avoided (Zi and Belytschko, 2003).

One should notice that in Eq. (3.81) there is no enrichment term for the crack tip equivalent to the last term in Eq (3.80). In this case, the crack tip has to be located on the element edge in order to ensure that the crack tip keeps closed, leading to a fully cracked element.

The initiation or propagation of the discontinuity is governed by a fracture criterion. One commonly adopted criterion is the criterion of maximum principal tensile stress (Wells and Sluys, 2001b). If the maximum principal tensile stress at any integration point in the element ahead of the crack exceeds the tensile strength of materials, a new discontinuity is introduced or the existing discontinuity is extended with a predefined length. After reaching equilibrium at each time step, we need to check whether or not the fracture criterion is violated at any integration point. If so, we extend the current discontinuity and then recompute the time step for the equilibrium of the system; otherwise we commit the solution and enter the next time step. The reason for the recomputation of the time step is that the just converged nonlinear solution no longer corresponds to an equilibrium state for the modified topology of extending cracks under the same load level.

Due to jumps in the approximated stresses, it may happen that existing crack tips do not extend, but rather new cracks initiate one or two elements away from these tips. In fact, it is often the case that only one main crack will propagate and recently initiated cracks will close. However, the opening and closure of several cracks at the same time can adversely affect the convergence. To this end, new cracks are only permitted to initiate outside a neighbourhood of the existing crack tip. This neighbourhood can be defined as a circle centred at the crack tip of radius equal to three to five times element characteristic length. This often provides reasonable results in practice, since new cracks at very small distances cause little extra energy dissipation.

### 3.4 Path following strategy

In nonlinear finite element analyses, load control cannot handle the limit points in a load-displacement diagram. This is because the global tangent stiffness matrix at these points becomes singular and more importantly the prescribed load magnitude is likely to overshoot or undershoot the limit points (De Borst et al., 2012). This issue can be addressed with displacement control. However, this type of loading control fails when facing the snap-back phenomenon, which is characterised by the change in the sign of the displacement increment. A typical situation when snap-back can occur is strain localisation in a structure which is long enough in the loading direction.

To handle snap-through or snap-back instabilities, arc-length methods can be employed as a robust solution procedure. These methods can be dated back to the work by Riks (1979) and have been adapted by several researchers (De Borst, 1987, May and Duan, 1997, Alfano and Crisfield, 2003, Gutiérrez, 2004, May et al., 2016). The basic idea underlying arc-length methods is to introduce a load factor  $\lambda$  as an additional unknown governed by a constrained equation  $\phi(\mathbf{a}, \lambda) = 0$ , which is also known as control function. Hence, the enlarged system of equations to be solved reads

$$\begin{bmatrix} \mathbf{f}_{int}(\mathbf{a}) - \lambda \mathbf{q} \\ \phi(\mathbf{a}, \lambda) \end{bmatrix} = \begin{bmatrix} \mathbf{0} \\ 0 \end{bmatrix}, \quad (3.91)$$

where  $\mathbf{q}$  is the unit load vector.

As a result of the second law of thermodynamics, the rate of dissipation must be non-negative. Therefore, the rate of energy dissipation is appropriate to be taken as the basis of a constraint equation. Following the work by Gutiérrez (2004) and

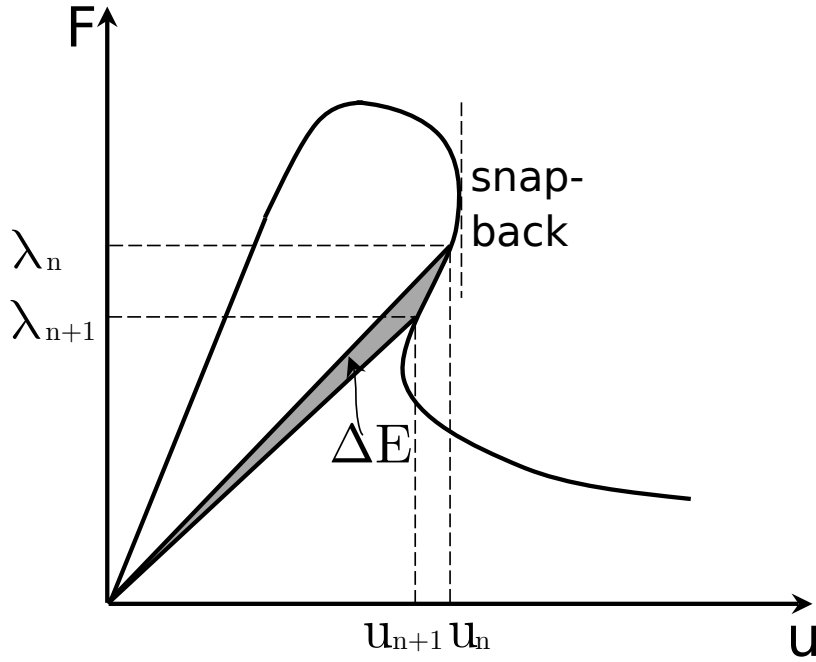


**Figure 3.13** Energy dissipation based arc-length control of equilibrium path with a snap back. The energy dissipation increment  $\Delta E$  is prescribed for time step from  $t_n$  to  $t_{n+1}$ .

Verhoosel et al. (2009), the constraint equation can be defined as

$$\phi(\mathbf{a}, \lambda) = \frac{1}{2} (\lambda_0 \Delta \mathbf{a}^T \mathbf{q} - \Delta \lambda \mathbf{a}_0^T \mathbf{q}) - \Delta E, \quad (3.92)$$

where  $\Delta E$  is the prescribed amount of energy dissipation during the current time step and the subscript 0 signifies values from the last converged time step. Figure 3.13 illustrates a representative load increment based on the incremental dissipation energy in the equilibrium path for a single degree of freedom.

Assuming that the solution at the  $i$ -th iteration and at the  $n+1$ -th increment is known for  $\mathbf{a}_{n+1}^i$  and  $\lambda_{n+1}^i$ , the linearisation of Eq. (3.91) using a Taylor series expansion about  $\mathbf{a}_{n+1}^i$  and  $\lambda_{n+1}^i$  results in

$$\mathbf{K}_T(\mathbf{a}_{n+1}^i, \lambda_{n+1}^i) \begin{bmatrix} \mathbf{a} - \mathbf{a}_{n+1}^i \\ \lambda - \lambda_{n+1}^i \end{bmatrix} = \begin{bmatrix} \mathbf{r} \\ -\phi(\mathbf{a}, \lambda) \end{bmatrix}_{n+1}^i, \quad (3.93)$$

with the tangential stiffness matrix defined as

$$\mathbf{K}_T(\mathbf{a}, \lambda) = \begin{bmatrix} \mathbf{K} & \mathbf{q} \\ \mathbf{v}^T & w \end{bmatrix}, \quad (3.94)$$

where

$$\mathbf{r} = \lambda \mathbf{q} - \mathbf{f}_{int}(\mathbf{a}), \quad \mathbf{K} = \frac{\partial \mathbf{f}_{int}}{\partial \mathbf{a}}, \quad \mathbf{v} = \frac{\partial \phi}{\partial \mathbf{a}}, \quad w = \frac{\partial \phi}{\partial \lambda}. \quad (3.95)$$

In the end, the solution of Eq. (3.91) for  $(\mathbf{a}_{n+1}^{i+1}, \lambda_{n+1}^{i+1})$  at the  $i + 1$ -th iteration at the  $n + 1$ -th increment can be obtained by solving

$$\begin{bmatrix} \mathbf{a} \\ \lambda \end{bmatrix}_{n+1}^{i+1} = \begin{bmatrix} \mathbf{a} \\ \lambda \end{bmatrix}_{n+1}^i + \mathbf{K}_T^{-1} \Big|_{n+1}^i \cdot \begin{bmatrix} \mathbf{r} \\ -\phi(\mathbf{a}, \lambda) \end{bmatrix}_{n+1}^i. \quad (3.96)$$

The above iterative procedure is repeated until some norm of the residual  $\mathbf{r}$  and  $\phi$  individually satisfy the predefined convergence criteria.

In order to save computational time for the solution, the inverse of the tangential stiffness matrix  $\mathbf{K}_T$  can be evaluated utilising the Sherman-Morrison formula (Verhoosel et al., 2009). By defining the following vectors

$$\mathbf{a}_I = \mathbf{K}^{-1} \mathbf{r}, \quad \mathbf{a}_{II} = \mathbf{K}^{-1} \mathbf{q}, \quad (3.97)$$

the final form for the solution at the  $i + 1$ -th iteration can be reached

$$\begin{bmatrix} \mathbf{a} \\ \lambda \end{bmatrix}_{n+1}^{i+1} = \begin{bmatrix} \mathbf{a} \\ \lambda \end{bmatrix}_{n+1}^i + \left\{ \begin{bmatrix} \mathbf{a}_I \\ 0 \end{bmatrix} - \frac{\mathbf{v}^T \mathbf{a}_I + \phi}{\mathbf{v}^T \mathbf{a}_{II} + w} \begin{bmatrix} \mathbf{a}_{II} \\ 1 \end{bmatrix} \right\}_{n+1}^i, \quad (3.98)$$

where the expression in the braces is the correction term to the unknowns at iteration  $i + 1$ .

One remarkable feature of the energy dissipation control is that it does not require information on the local failure patterns of the structure, since incremental energy dissipation can be expressed in terms of global quantities. One should notice that the energy dissipation control may fail when the amount of incremental dissipated energy is quite limited. Potential situations include hardening or reloading in the equilibrium path after passing the peak load, leading to the singularity of the enlarged system of algebraic equations.

For highly nonlinear and complicated fracture processes such as composite laminate failure, the analysis usually cannot be completed without a robust time (load) stepping strategy to follow the entire equilibrium path. The adaptive increment strategy proposed in (Van der Meer, 2012) offers a good option for enhancing the robustness of the solution procedure. This strategy involves the adaptive selection of step size and switching of increment type if necessary. Interested readers refer to (Van der Meer, 2012) for more details.

## 3.5 Summary

In this chapter, the main focus is on the FE formulation and algorithmic aspects of several existing numerical approaches for strain localisation or fracture in the literature. Also, their merits and drawbacks have been discussed.

Isotropic continuum damage models and cohesive traction-separation laws were presented as constitutive models for describing failure or fracture of materials. In order to trace snap-backs in structural response, the energy dissipation based arc-length solution technique has been detailed.

The following remarks concerning this chapter are highlighted:

- As a continuum approach, the local smeared crack approach is partially regularised and the simulated solution typically suffers from spurious mesh bias dependence. However, the implicit gradient enhanced damage model recovers the ellipticity of governing equations and then results in a well-posed quasi-static mechanical problem.
- When representing discontinuities in displacements, the XFEM is preferred in most situations over cohesive elements, because, compared to cohesive elements, XFEM allows a crack to transverse continuum elements; a small number of new degrees of freedom are added when a crack needs to be extended, indicating that the scale of resultant enlarged global systems is not increased too much and high artificial stiffnesses can be avoided. However, it is worth noting that XFEM cannot easily handle complex crack topologies, like branching and intersections, especially in three dimensions.
- The nonlinear response induced by damage or fracture may need a robust path following strategy in order to trace the equilibrium path.



# Chapter 4

## Multiscale Failure Modelling based on Macro-discontinuity Enhanced $FE^2$

Macroscale mesh sensitivity and RVE size dependence are the two major issues that make the conventional homogenisation technique incapable of modelling the softening behaviour of materials. In this chapter, a new continuous-discontinuous multiscale modelling approach to failure is presented. Inspired by the classical crack band model of Bazant and Oh (1983), this approach is built upon a new computational homogenisation (CH) scheme that is referred to as *the macro-discontinuity enhanced  $FE^2$*  from now on.

The outline of this chapter follows. Section 4.1 and 4.2 introduce the fundamentals of the conventional first-order CH scheme. Emphasis is placed on the weakly periodic boundary conditions, which will be adopted in the microscopic failure modelling. Section 4.3 reproduces the failure zone averaging scheme proposed in the literature illustrated with numerical examples. The macro-discontinuity enhanced  $FE^2$  approach is introduced in Section 4.4, followed by the algorithmic details for the presented multiscale failure modelling approach in Section 4.5. Several numerical examples are provided in Section 4.6 to demonstrate the effectiveness of the proposed multiscale failure approach. Conclusions are summarised in the last section.

## 4.1 Preliminaries

For the mechanical characterisation of heterogeneous material behaviour at large scales, the use of effective quantities (e.g. density, strain and stress) is fundamental. These effective quantities incorporate the statistical features and interactions between constituents of microstructures. In the literature, computational homogenisation (CH) has been proposed for the identification of effective quantities for different applications.

In this section, the standard first-order CH for continuous bulk materials is introduced in detail. Averaging theorems are first presented and followed by the Hill-Mandel condition. Then, emphasis is placed on several types of boundary conditions often used in multiscale modelling with some numerical implementation aspects provided. To assess the performance of these different boundary conditions, a linear elastic RVE problem is studied.

The semi-concurrent multiscale methods implemented within the FE setting are usually formulated based on the technique of CH known as FE<sup>2</sup> in the literature (Miehe et al., 1999, Feyel and Chaboche, 2000). The CH scheme is built upon the concept of an RVE. This family of methods provides an effective and flexible tool for analysing a wide range of heterogeneous materials possessing complex microstructures with moderately or highly nonlinear behaviour such as plasticity, damage and softening. A schematic illustration for the standard first-order CH applied to materials under infinitesimal strains is provided in Figure 4.1.

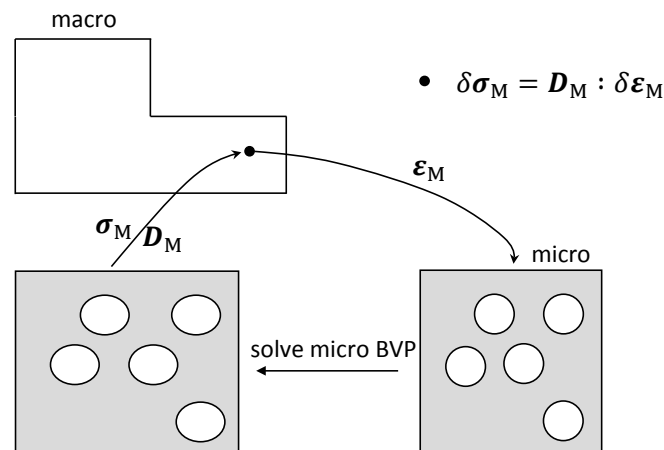


**Figure 4.1** Schematic of the first-order CH.

### 4.1.1 Principle of separation of scales

In the literature, there exist multiple definitions for an RVE. Hill (1963) defined the RVE as a sample of a heterogeneous material that: "is entirely typical of the whole mixture on average", and "contains a sufficient number of inclusions for the apparent properties to be independent of the surface values of traction and displacement, so long as these values are macroscopically uniform". A more practical definition that can be used is "the RVE is defined as the minimum volume of a laboratory scale specimen, such that the results obtained from this specimen can still be regarded as representative for a continuum" (Van Mier, 2017).

According to Hashin (1983), to be statistically representative, size of the RVE should be larger than the characteristic length of the microstructure; for accuracy, size of the RVE should be smaller than the characteristic length of the macroscopic body. To define an RVE, the principle of separation of scales should be satisfied in essence. According to (Geers et al., 2010), the principle of separation of scales is stated as follows: "The microscopic length scale  $l_m$  is assumed to be much smaller than the characteristic length  $l_M$  over which the macroscopic loading varies in space". In expression,

$$l_m \ll l_M, \quad (4.1)$$

which indicates that the characteristic length of the RVE has to be sufficiently small compared to the macroscopic length scale.

### 4.1.2 Averaging theorems

For an arbitrary field  $\rho_m$  at the microscale, the corresponding effective quantity  $\rho_M$  is its unweighted volume (area in 2D) average

$$\rho_M(\mathbf{X}_M) \equiv \langle \rho_m(\mathbf{X}_m) \rangle = \frac{1}{|\Omega_m|} \int_{\Omega_m} \rho_m(\mathbf{X}_m) d\Omega_m, \quad (4.2)$$

where  $|\bullet|$  and  $\langle \bullet \rangle$  represent the measure of the microscale domain and averaging operator respectively;  $\mathbf{X}$  denotes the position vector in the reference configuration. The subscripts  $M$  and  $m$  are employed to refer to macroscale and microscale quantities.

## Averaging strain theorem

The macroscale strain tensor  $\varepsilon_M$  at a macroscopic material point can be defined as the average of the microscale strain field  $\varepsilon_m$  over the RVE associated with that point. To compute the macroscale strain tensor, the following averaging strain theorem (the right most term) will be most helpful

$$\varepsilon_M = \langle \varepsilon_m \rangle = \frac{1}{|\Omega_m|} \int_{\Omega_m} \varepsilon_m(\mathbf{X}_m) d\Omega_m = \frac{1}{|\Omega_m|} \int_{\Gamma_m} \mathbf{u}_m \otimes^s \mathbf{n}_m d\Gamma_m, \quad (4.3)$$

where  $\mathbf{u}_m$  is the microscale displacement vector and  $\mathbf{n}_m$  the microscale outward normal to the RVE boundary. In the third equality, the infinitesimal strain definition and divergence theorem have been applied to transform the volume integral to the boundary integral. Thus, the effective macroscale strain can be enforced over the RVE in terms of the boundary displacements.

**Remark 9** *The third equality in Eq. (4.3) holds true only when there are no internal discontinuities anywhere in the RVE model (the microstructure is perfectly bonded).*

## Averaging stress theorem

Likewise, the macroscale stress tensor  $\sigma_M$  at a macroscopic material point is defined as the average of the microscale stress field  $\sigma_m$  over the RVE associated with that point. The averaging stress theorem (the right most term) is stated as

$$\sigma_M = \langle \sigma_m \rangle = \frac{1}{|\Omega_m|} \int_{\Omega_m} \sigma_m(\mathbf{X}_m) d\Omega_m = \frac{1}{|\Omega_m|} \int_{\Gamma_m} \mathbf{t}_m \otimes \mathbf{x}_m d\Gamma_m, \quad (4.4)$$

where  $\mathbf{t}_m = \sigma_m \cdot \mathbf{n}_m$  is the microscale traction vector on the RVE boundary. In the derivation of the last equality, the observation  $\nabla \cdot (\sigma_m \otimes \mathbf{x}_m) = \nabla \cdot \sigma_m \otimes \mathbf{x}_m + \sigma_m$ , the equilibrium equation, and the divergence theorem have been used sequentially. The above transformation of the volume integral to the boundary integral enables us to prescribe the effective stress over the RVE just in terms of the boundary tractions. This can be used in practice to derive the microscopic finite element analysis or to extract the effective stress from the microscale.

**Remark 10** *The above used integral transformation remains true when there are no body forces.*

### 4.1.3 Hill-Mandel condition

So far, strain and stress averaging have been presented. They provide the connection between macroscale strain and stress, and their microscale counterparts. However, the energetic equivalence between the two scales has not yet been described.

The Hill-Mandel condition (Hill, 1963), also termed as the macrohomogeneity condition, states that the local stress power at a macroscopic material point should be equal to the average of the stress power at the microscale

$$\boldsymbol{\sigma}_M : \dot{\boldsymbol{\varepsilon}}_M = \langle \boldsymbol{\sigma}_m : \dot{\boldsymbol{\varepsilon}}_m \rangle. \quad (4.5)$$

The boundary conditions enforced on the RVE boundary are used to pass the macroscale information ( $\boldsymbol{\varepsilon}_M$  or  $\boldsymbol{\sigma}_M$ ) and generate strain and stress fields in the RVE. Nonetheless, for arbitrary pairs of computed microscale stress and strain fields, the above equivalence is generally not satisfied. To demonstrate this, split the microscale stress and strain fields as

$$\boldsymbol{\sigma}_m = \langle \boldsymbol{\sigma}_m \rangle + \tilde{\boldsymbol{\sigma}}_m, \quad (4.6a)$$

$$\boldsymbol{\varepsilon}_m = \langle \boldsymbol{\varepsilon}_m \rangle + \tilde{\boldsymbol{\varepsilon}}_m, \quad (4.6b)$$

where  $\tilde{\boldsymbol{\sigma}}_m$  and  $\tilde{\boldsymbol{\varepsilon}}_m$  are the fluctuation components, complementary to the averages. Applying the above decompositions to the Hill-Mandel condition Eq. (4.5) results in

$$\boldsymbol{\sigma}_M : \dot{\boldsymbol{\varepsilon}}_M = \langle \boldsymbol{\sigma}_m : \dot{\boldsymbol{\varepsilon}}_m \rangle + \langle \tilde{\boldsymbol{\sigma}}_m : \dot{\tilde{\boldsymbol{\varepsilon}}}_m \rangle. \quad (4.7)$$

The term  $\langle \tilde{\boldsymbol{\sigma}}_m : \dot{\tilde{\boldsymbol{\varepsilon}}}_m \rangle$  in the above equation does not vanish in general. This necessitates appropriate types of boundary conditions to conserve energy across scales so that the stress and strain averaging (homogenisation) make sense.

Further algebraic manipulations on this term lead to

$$\langle \tilde{\boldsymbol{\sigma}}_m : \dot{\tilde{\boldsymbol{\varepsilon}}}_m \rangle = \frac{1}{|\Omega_m|} \int_{\Gamma_m} \tilde{\mathbf{t}}_m \cdot \dot{\tilde{\mathbf{u}}}_m d\Gamma_m, \quad (4.8)$$

in which the displacement fluctuation vector  $\tilde{\mathbf{u}}_m$  and boundary traction fluctuation vector  $\tilde{\mathbf{t}}_m = \tilde{\boldsymbol{\sigma}}_m \cdot \mathbf{n}_m$  at the microscale have been introduced.

Using the first-order homogenisation scheme for which macroscale deformation is

homogeneous on the RVE, we have the following relation

$$\mathbf{u}_M = \boldsymbol{\varepsilon}_M \cdot (\mathbf{X}_m - \mathbf{X}_{m,r}), \quad \forall \mathbf{X}_m \in \Omega_m, \quad (4.9)$$

with  $\mathbf{X}_{m,r}$  as a reference point.

**Remark 11** *As proved in (de Souza Neto and Feijóo, 2006), the Hill-Mandel condition is equivalent to requiring that body forces and surface traction in the RVE be purely reactive, which means they are reactions to the chosen kinematic constraints, and cannot be prescribed independently.*

## 4.2 Boundary conditions on RVE

There are two obvious ways to fulfil the requirement that the average in Eq. (4.8) vanish, either set the displacement or traction fluctuation field on the boundary to zero. The first yields the so-called linear displacement boundary conditions and the latter the so-called uniform traction boundary conditions in the literature. Because the analysis of RVE models under consideration is displacement driven, in the sequel we only focus on the kinematical types of boundary conditions (BCs).

### 4.2.1 Linear displacement BCs

As the name indicates, the displacement of the RVE boundary is linear and given by

$$\mathbf{u}_m = \boldsymbol{\varepsilon}_M \cdot \mathbf{X}_m \quad \forall \mathbf{X}_m \in \Gamma_m. \quad (4.10)$$

It is easy to verify that the linear displacement boundary conditions satisfy the average strain assumption, therefore we omit the proof details here. Due to  $\tilde{\mathbf{u}}_m = 0$  on the boundary, it is concluded from Eq. (4.8) that the Hill-Mandel condition holds true. Note that in this case, since the RVE problem is deformation driven, the average stress assumption needs to be derived from the Hill-Mandel condition. The numerical implementation of this type of BCs is quite straightforward such that it is not provided here.



decomposed into two parts  $\Gamma_m^-$  and  $\Gamma_m^+$  such that  $\Gamma_m = \Gamma_m^- \cup \Gamma_m^+$  and  $\Gamma_m^- \cap \Gamma_m^+ = \emptyset$ . In the periodic BCs, except the corner vertex 3, each point  $\mathbf{X}_m^+$  on the boundary  $\Gamma_m^+$  is mapped to its unique corresponding point  $\mathbf{X}_m^-$  on the boundary  $\Gamma_m^-$  according to the mapping  $\varphi_{per}$

$$\begin{aligned} \mathbf{X}_m^- &= \varphi_{per}(\mathbf{X}_m^+), \\ \varphi_{per} : (L_m, Y_p) &\rightarrow (0, Y_p) \text{ or } (X_p, L_m) \rightarrow (X_p, 0), \end{aligned} \quad (4.13)$$

where  $X_p$  and  $Y_p$  refer to X-axis and Y-axis coordinate values of arbitrary point p. Note the corner vertex 3 has two pairing points (corners), vertex 2 and vertex 4. With these preliminaries, the periodic BCs are defined as

$$\llbracket \mathbf{u} \rrbracket_{\Gamma_m} = \mathbf{u}_m^+ - \mathbf{u}_m^- = \boldsymbol{\varepsilon}_M \cdot (\mathbf{X}_m^+ - \mathbf{X}_m^-), \quad \mathbf{t}_m^+ = -\mathbf{t}_m^-, \quad (4.14)$$

where use of the notation  $(\cdot)^+ = (\cdot)|_{\mathbf{x}^+}$  with  $\mathbf{X}^+ \in \Gamma_m^+$  and  $(\cdot)^- = (\cdot)|_{\mathbf{x}^-}$  with  $\mathbf{X}^- \in \Gamma_m^-$  has been made of. The second sub-equation in the above equation (4.14) implies the anti-periodicity character of boundary tractions.

For the sake of completeness, let us check the equality between the (given) macroscale strain and the averaged microscale strain,

$$\begin{aligned} \langle \boldsymbol{\varepsilon}_m \rangle &= \frac{1}{|\Omega_m|} \left( \int_{\Gamma_m^+} \mathbf{u}_m^+ \otimes^s \mathbf{n}_m^+ d\Gamma_m + \int_{\Gamma_m^-} \mathbf{u}_m^- \otimes^s \mathbf{n}_m^- d\Gamma_m \right) \\ &= \frac{1}{|\Omega_m|} \int_{\Gamma_m^+} (\mathbf{u}_m^+ - \mathbf{u}_m^-) \otimes^s \mathbf{n}_m^+ d\Gamma_m \\ &= \frac{1}{|\Omega_m|} \boldsymbol{\varepsilon}_M \cdot \int_{\Gamma_m^+} (\mathbf{X}_m^+ - \mathbf{X}_m^-) \otimes^s \mathbf{n}_m^+ d\Gamma_m \\ &= \boldsymbol{\varepsilon}_M, \end{aligned} \quad (4.15)$$

wherein the fact that  $\mathbf{n}_m^+ = -\mathbf{n}_m^-$  has been used twice. It is not difficult to observe the satisfaction of the Hill-Mandel condition from the fact that the expression Eq. (4.8) vanishes, due to the point-wise periodicity of the boundary displacement fluctuations and point-wise anti-periodicity of boundary traction fluctuations.

#### 4.2.3.1 Hybrid BCs

The hybrid BCs proposed in (Hirschberger et al., 2008, 2009) and adopted in (Verhoosel et al., 2010, Nguyen et al., 2011a), are a combination of linear displacement BCs and periodic BCs, as shown in Figure 4.3. Along the tangential direction of a material interface or crack, periodic fluctuations are assumed. Macroscopic

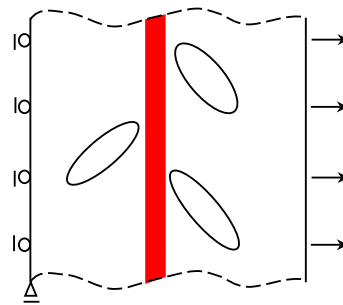


**Figure 4.3** Schematic representation of hybrid BCs for tensile failure mode, in which periodic constraints are applied on the top and bottom edges and linear displacement constraints on the left and right edges.

deformations, such as macroscale interface opening  $[[\mathbf{u}]]_M$ , are enforced by linear displacement BCs acting on the RVE edges that are not across the interface or crack.

#### 4.2.4 Weakly periodic BCs

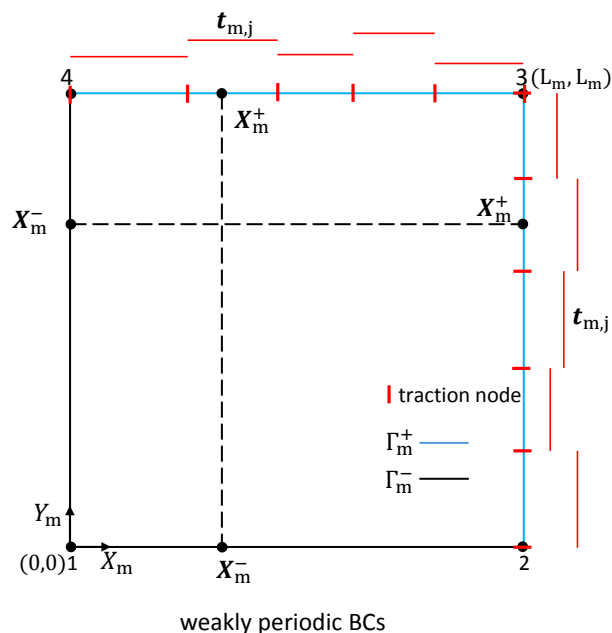


**Figure 4.4** Illustration of weakly periodic BCs with periodicity along the horizontal direction. Piecewise constant boundary traction discretisation has been adopted.

The weakly periodic BCs in Figure 4.4 can be regarded in an integral sense as a weak implementation of the strong periodic BCs that are applied pointwise. In the

weak setting, the weakly periodic BCs can be expressed as (Larsson et al., 2011)

$$\int_{\Gamma_{m,i}^+} \delta \mathbf{t}_m \cdot \llbracket \tilde{\mathbf{u}} \rrbracket_{\Gamma_m} d\Gamma_m = \mathbf{0} , \quad (4.16)$$

where  $\delta \mathbf{t}_m$  can be regarded a test function and interpreted as the weighted boundary traction vector which is unknown at the moment;  $i = 1, 2$ . The condition (4.16) is equivalent to the following form

$$\int_{\Gamma_{m,i}^+} \delta \mathbf{t}_m \cdot \llbracket \mathbf{u} \rrbracket_{\Gamma_m} d\Gamma_m = \int_{\Gamma_{m,i}^+} \delta \mathbf{t}_m \cdot \boldsymbol{\varepsilon}_M \cdot (\mathbf{X}_m^+ - \mathbf{X}_m^-) d\Gamma_m . \quad (4.17)$$

The detail of showing that the weakly periodic BCs respect the Hill-Mandel condition (4.5) is given as follows

$$\begin{aligned} \langle \boldsymbol{\sigma}_m : \delta \boldsymbol{\varepsilon}_m \rangle &= \frac{1}{|\Omega_m|} \left( \int_{\Omega_m} \boldsymbol{\sigma}_m : \delta \nabla \mathbf{u}_M d\Omega_m + \int_{\Omega_m} \boldsymbol{\sigma}_m : \delta \nabla \tilde{\mathbf{u}}_m d\Omega_m \right) \\ &= \frac{1}{|\Omega_m|} \int_{\Omega_m} \boldsymbol{\sigma}_m : \delta \nabla \mathbf{u}_M d\Omega_m + \frac{1}{|\Omega_m|} \int_{\Gamma_m} \mathbf{t}_m \cdot \delta \tilde{\mathbf{u}}_m d\Gamma_m \\ &= \boldsymbol{\sigma}_M : \delta \boldsymbol{\varepsilon}_M + \frac{1}{|\Omega_m|} \int_{\Gamma_m^+} \mathbf{t}_m \cdot \delta \llbracket \tilde{\mathbf{u}} \rrbracket_{\Gamma_m} d\Gamma_m \\ &= \boldsymbol{\sigma}_M : \delta \boldsymbol{\varepsilon}_M , \end{aligned} \quad (4.18)$$

where the equilibrium equation of RVE and the divergence theorem, the anti-periodicity of boundary tractions  $\mathbf{t}_m$  and Eq. (4.16) have been used in sequence. The condition (4.17) can be implemented in the context of FE by means of introducing Lagrange multipliers into the system.

The weak form of the BVP of the RVE model after enforcing boundary conditions through Eq. (4.16) or (4.17) (Larsson et al., 2011) leads to

$$\int_{\Omega_m} \boldsymbol{\sigma}_m : \delta \nabla \mathbf{u}_m d\Omega_m - \int_{\Gamma_m^+} \mathbf{t}_m \cdot \delta \llbracket \mathbf{u} \rrbracket_{\Gamma_m} d\Gamma_m = 0 . \quad (4.19)$$

The homogenised stress  $\boldsymbol{\sigma}_M$  is straightforward, which is just

$$\boldsymbol{\sigma}_M = \frac{1}{|\Omega_m|} \int_{\Gamma_m^+} \mathbf{t}_m \otimes \llbracket \mathbf{x} \rrbracket_m d\Gamma_m , \quad (4.20)$$

where Eq. 4.4 was recalled. Note that the boundary traction field  $\mathbf{t}_m$  has been known after solving the augmented system that arises from the combination of Eq. (4.19) and (4.17).

### Construction of the Traction Mesh

To numerically implement the weakly periodic BCs, an independent discretisation for the weighted boundary traction unknown  $t_m$  is necessary. The traction mesh with a piecewise constant interpolation for tractions is constructed following the procedure in (Larsson et al., 2011). Note that there is no strict requirement on the regularity of tractions. To fulfil the inf-sup (LBB) condition when making use of the piecewise constant traction approximation, there must be at least one displacement node inside each traction element, refer to (Svenning et al., 2016) for more details.

To create the traction mesh for interpolating boundary tractions, firstly all the boundary displacement nodes are projected onto the boundary  $\Gamma_m^+$ . This forms an initial pool of candidate traction nodes for further selection. The intersection points of discrete cracks with the boundary are also incorporated into this node pool. A selection criterion needs to be defined. Such a criterion can be preserving the minimum number of displacement nodes lying between two neighbouring traction nodes or eliminating candidate traction nodes that are too close to each other. Note that the traction nodes at end points of  $\Gamma_m^+$  have to be kept. Traction elements are created by just connecting neighbouring traction nodes that remain after selection, as shown in Figure 4.4.

The weakly periodic BCs have been further extended to tackle boundary crossed discrete cracks (Svenning et al., 2016) and also strong strain localisation problems of testing (Svenning et al., 2017a), of numerical samples (RVEs). A work similar to the weakly periodic BCs was presented in (Goldmann et al., 2018) for applying to strain localisation problems.

To handle strain localisation phenomena occurring on the RVE, the weakly periodic BCs are required to be modified to align with the localisation direction provided that the localisation direction is known as proposed by Svenning et al. (2017a). To this end, the mapping function in (4.13) needs to be redefined such that the points on the boundary  $\Gamma_m^+$  are mapped onto  $\Gamma_m^-$  along lines that are parallel to the localisation direction. Interested readers refer to the article (Svenning et al., 2017a).

#### 4.2.4.1 FE discretisation

The RVE boundary traction field  $t_m$  can be approximated as

$$t_m = \mathbf{N}_t t_a, \quad (4.21)$$

where the matrix  $\mathbf{N}_t$  comprises shapes functions for the traction approximation and the vector  $\mathbf{t}_a$  collects all the nodal tractions of the traction mesh.

Let us consider there is  $nt$  traction nodes in the traction mesh. Regarding the computer implementation, Voigt representation for the homogenised stress  $\{\boldsymbol{\sigma}_M\}$  is employed here. According to Eq. (4.20), the discrete form for the variation of homogenised stress  $\delta\{\boldsymbol{\sigma}_M\}$  can be represented as

$$\delta\{\boldsymbol{\sigma}_M\} = \underbrace{\frac{1}{|\Omega_m|} \int_{\Gamma_m^+} \mathbf{P} \mathbf{N}_t d\Gamma_m}_{\mathbf{M}_p} \delta \mathbf{t}_a, \quad (4.22)$$

with the coefficient matrix  $\mathbf{P} = [\mathbf{P}_1 \dots \mathbf{P}_i \dots \mathbf{P}_{nt}]$ . A typical matrix  $\mathbf{P}_i$  has the following form

$$\mathbf{P}_i = \begin{bmatrix} \llbracket x \rrbracket_{\Gamma_m} & 0 \\ 0 & \llbracket y \rrbracket_{\Gamma_m} \\ \frac{1}{2} \llbracket y \rrbracket_{\Gamma_m} & \frac{1}{2} \llbracket x \rrbracket_{\Gamma_m} \end{bmatrix}.$$

The homogenised tangent stiffness  $\mathbf{D}_M$  is obtained through a static condensation procedure once the global FE tangent stiffness matrix is assembled from the RVE model. Let us represent the augmented discrete system that arises from the FE discretisation of Eq. (4.19) and (4.17). The converged discrete system can be partitioned into blocks associated with displacement dofs and boundary traction dofs

$$\begin{bmatrix} \mathbf{K}_{uu} & -\mathbf{K}_{ut} \\ -\mathbf{K}_{tu} & \mathbf{0} \end{bmatrix} \begin{bmatrix} \delta \mathbf{u} \\ \delta \mathbf{t}_a \end{bmatrix} = \begin{bmatrix} \mathbf{0} \\ -\delta \mathbf{f}_{ext}^t \end{bmatrix}, \quad (4.23)$$

where  $\mathbf{K}_{tu} = \int_{\Gamma_m^+} \mathbf{N}_t^T \mathbf{N}_u^\pm d\Gamma_m$  and  $\mathbf{K}_{uu}$  is just the standard tangent stiffness term. In Eq. (4.23),  $\delta \mathbf{f}_{ext}^t$  is written as

$$\delta \mathbf{f}_{ext}^t = \underbrace{\frac{1}{|\Omega_m|} \int_{\Gamma_m^+} \mathbf{N}_t^T \mathbf{P}^T d\Gamma_m}_{\mathbf{M}_p^T} \delta \{\boldsymbol{\varepsilon}_M\}. \quad (4.24)$$

From (4.23), we can condense out the displacement field  $\delta \mathbf{u}$  to derive  $\delta \mathbf{t}_a$  as

$$\delta \mathbf{t}_a = (\mathbf{K}_{tu} \mathbf{K}_{uu}^{-1} \mathbf{K}_{ut})^{-1} \delta \mathbf{f}_{ext}^t. \quad (4.25)$$

Inserting the above equation into Eq. (4.22) and considering the expression (4.24), we have

$$\delta\{\sigma_M\} = \underbrace{\left(\mathbf{M}_p(\mathbf{K}_{tu}\mathbf{K}_{uu}^{-1}\mathbf{K}_{ut})^{-1}\mathbf{M}_p^T\right)}_{\mathbf{D}_M} \delta\{\epsilon_M\}, \quad (4.26)$$

where  $\mathbf{D}_M$  is the sought-for homogenised tangent stiffness.

### 4.2.5 Comparison of BCs

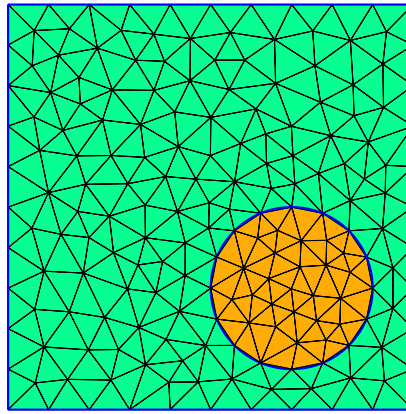


**Figure 4.5** BC comparison test: mesh for the used unit cell.

This subsection aims to compare the performance of different BCs for a linear elastic problem of a square unit cell. The unit cell of length 1 comprises a stiff elastic particle with elastic modulus  $1 \times 10^5$  embedded in one corner of the matrix with elastic modulus  $1 \times 10^4$ . The same Poisson's ratio 0.2 is taken for both constituents. The mesh for the unit cell is given by Figure 4.5 with global element size 0.1. The increasing sizes of RVE are obtained by a periodic repetition of the unit cell. Plane stress condition is assumed and a macroscale strain vector  $\{\epsilon_M\} = [1 \times 10^{-4}, 0, 0]$  is prescribed. The computed homogenised normal stress  $\sigma_{xx}$  is used to measure the performance of different BCs discussed previously. Four different RVE sizes measured by the number of unit cells in both periodic directions are considered, namely  $1 \times 1$ ,  $2 \times 2$ ,  $4 \times 4$ ,  $8 \times 8$  unit cells by unit cells. When producing the traction mesh for the weakly periodic BCs, each traction line element contains one displacement node that can be projected on its interior.

The deformed shapes for different RVE sizes are displayed in Figure 4.7. The curve of homogenised stress  $\sigma_{xx}$  versus RVE size is shown in Figure 4.6 for different BCs. The trend of convergence of the effective response is shown in Figure

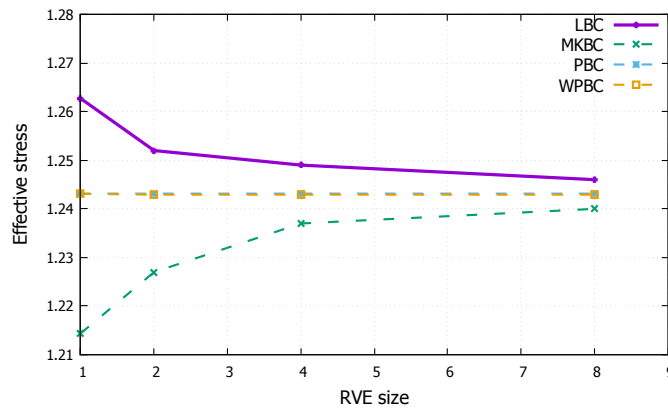


**Figure 4.6** BC comparison test: effective stress-RVE size curves. LBC: linear BC, MKBC: minimal kinematic BC, PBC: periodic BC and WPBC: weakly periodic BC.

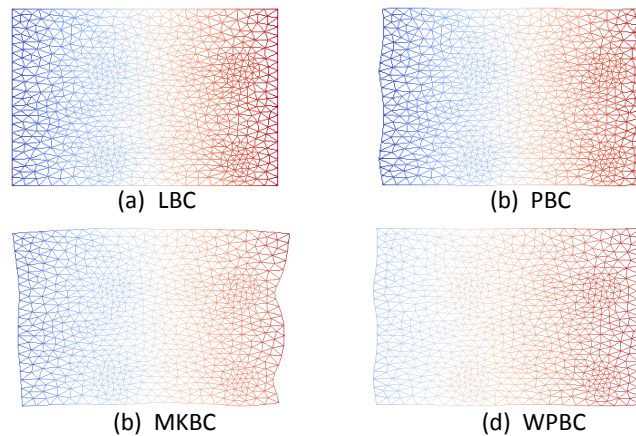


**Figure 4.7** BC comparison test: deformed configurations (magnified by 5000) obtained with different boundary conditions for the RVE made of  $2 \times 2$  unit cells.

4.6. It is found that the linear BCs give the stiffest response whereas the minimal kinematic BCs result in the softest response when the RVE size is small. This is because the linear BCs and the minimal kinematic BCs correspond to the most and the least kinematic constraints over the boundary, respectively, thus leading to unreasonable constraining effects, as can be observed from Figure 4.7. However, these undesirable effects on the effective response are diminishing as the RVE size is increasing, see Figure 4.6. The periodic BCs and its weak version, the weakly periodic BCs, take into account the influence of the neighbouring microstructure by means of respecting the periodic fluctuations in the deformation of boundary (Figure 4.7). Thus, the computed effective responses show no apparent sensitivity to the variation of RVE size, see Figure 4.6.

### 4.3 Failure zone averaging

Let us specify the microscale problem domain in 2D as a rectangle (typically square)  $\Omega_m$  with dimensions  $w_m \times h_m$ , see Figure 4.8. As loading increases, microscale damage in form of voids or cracks will coalesce and form a weak band while its length is comparable to the domain's length scale. At this stage, this solid block loses its material stability; however, it may still be able to carry some load.

The failure zone averaging scheme devised in (Nguyen et al., 2010), as its name

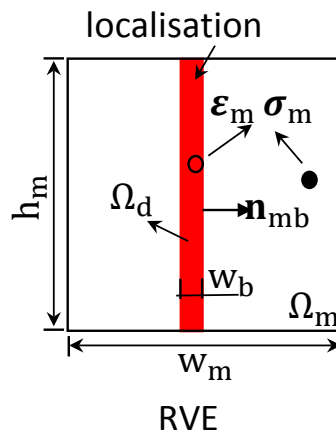


**Figure 4.8** Square RVE with a vertical localisation band across the boundary.

indicates, is to average the mechanical fields (e.g., stress and strain) over the active damage domain after strain localisation instead of over the entire RVE domain. This scheme can be used to extract from the RVE analysis a stress-strain response that is independent of the selected RVE size.

Let us denote the active damaged domain as  $\Omega_d$ , see Figure 4.8. According to the continuum damage model, this domain is identified as the collective region that comprises integration patches, mastered by Gauss points that are still experiencing damage loading. The homogenised stresses and strains are defined as the volume averages of the microscopic stresses and strains, respectively, over  $\Omega_d$  (Nguyen et al., 2010)

$$\begin{aligned} \langle \boldsymbol{\sigma} \rangle_{dam} &= \frac{1}{|\Omega_d|} \int_{\Omega_d} \boldsymbol{\sigma}_m d\Omega_d \\ \langle \boldsymbol{\varepsilon} \rangle_{dam} &= \frac{1}{|\Omega_d|} \int_{\Omega_d} \boldsymbol{\varepsilon}_m d\Omega_d . \end{aligned} \quad (4.27)$$

This averaging scheme filters out the linear contribution which makes the stress-strain curves not unique (Gitman et al., 2007). It merely extracts only the inelastic response from the RVE, thus leading to an RVE-size insensitive response. Note that this *ad hoc* averaging scheme should be used only after the development of a strain localisation band on the RVE.

### 4.3.1 Traction-separation law

For simulating a macroscopic cohesive crack, an essential ingredient is the identification of the traction-separation law. This goal can be achieved by transforming the homogenised stress-strain response just mentioned from the microscale (Nguyen et al., 2011a).

When employing continuum damage models, the displacements due to damage can be defined as the projection of the average damage strain tensor onto the crack plane (Nguyen et al., 2011a)

$$\mathbf{u}_{dam} = \langle \boldsymbol{\varepsilon} \rangle_{dam} \cdot (w_b \mathbf{n}_{mb}) , \quad (4.28)$$

where  $w_b$  stands for the average width of the localisation band (estimated as  $|\Omega_d|/h_m$  when considering a vertical microscale localisation band, see Figure 4.8 for clarity), and the unit vector  $\mathbf{n}_{mb}$  denotes the normal direction to the microscopic localisation band. To obtain an initially rigid traction-opening relation for the macroscale crack, a shift is applied, resulting in

$$[[\mathbf{u}]]_M = \mathbf{u}_{dam} - \dot{\mathbf{u}}_{dam} , \quad (4.29)$$

where  $\dot{\mathbf{u}}_{dam}$  corresponds to the damage opening/displacement at the maximum traction point.

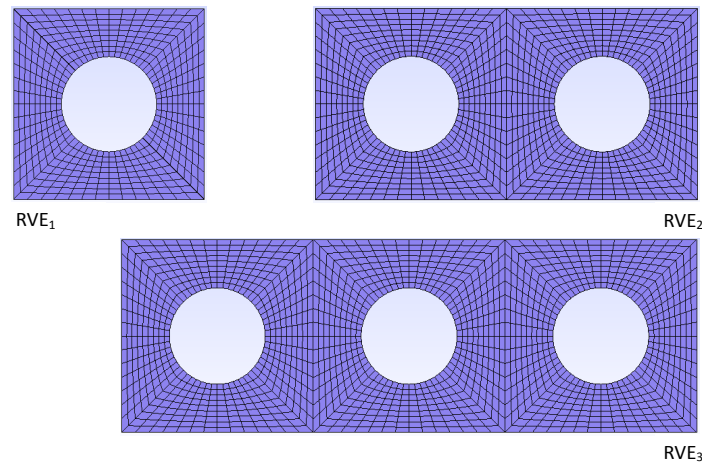
### 4.3.2 Numerical examples

Firstly, we replicate the numerical example of samples with voids presented in the paper (Nguyen et al., 2010), but instead use the weakly periodic BCs to prescribe the macroscale deformation over the RVE boundary. Although it is not quite novel, for the sake of completeness, it is demonstrated here the validity of the failure zone averaging scheme when overcoming the non-existence issue of RVE under the condition of material softening. The adopted weakly periodic BCs can minimise

the effect of boundary conditions on the development of strain localisation and thus ensure a more realistic overall response. Secondly, the failure zone averaging scheme is applied to complex microstructures, taking concrete as an example.

### Voided samples in Section 4.3.2

The geometries of three RVEs are shown in Figure 4.9. The dimensions of RVE<sub>1</sub> (unit cell) are  $10 \times 10$  and the central hole diameter is 5, while RVE<sub>2</sub> and RVE<sub>3</sub> are just periodic repetitions of RVE<sub>1</sub> in the horizontal direction. All the length units are in mm. An isotropic damage model with exponential softening is used to simulate the material degradation process, with  $\kappa_0$  being the damage initiation strain and  $\kappa_f$  a parameter controlling the ductility. The equivalent strain  $\varepsilon_{eq}$  is defined in terms of the positive principal strain components (Mazars and Pijaudier-Cabot, 1989). The gradient enhanced damage model proposed in (Peerlings et al., 1996) is used to regularise the strain localisation induced by softening, thus leading to a mesh-independent response. The parameter  $c$  in the gradient enhanced damage model has the dimension of length squared. The material constants are listed in Table 4.1.

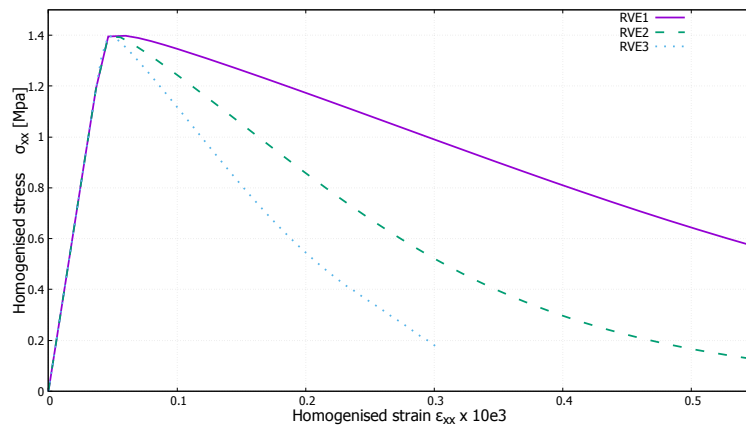


**Figure 4.9** Three meshed RVE configurations of different sizes with holes. They are identified with RVE<sub>1</sub>, RVE<sub>2</sub> and RVE<sub>3</sub>.

The results in terms of effective stress  $\sigma_{xx}$  versus effective strain  $\varepsilon_{xx}$  for the classical first-order homogenisation scheme are plotted in Figure 4.10. It is evident that the mechanical responses coincide with each other before strong strain localisation occurs; however, the response after the peak load is becoming more brittle as the RVE size increases. It is worth noting that strength size effect does not exist for the

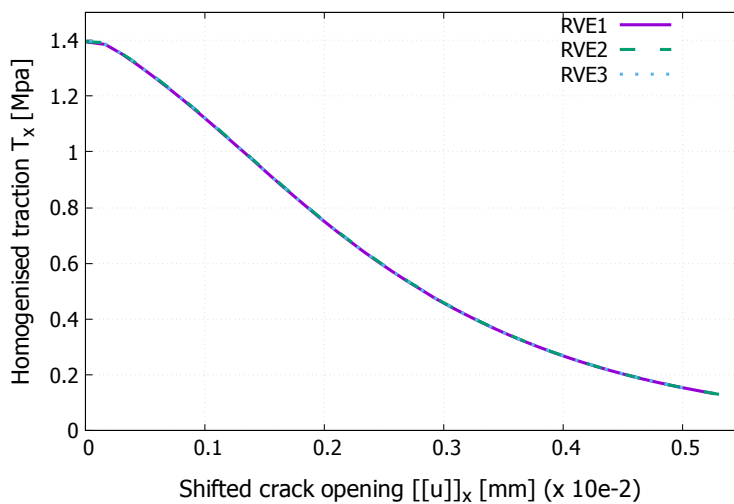
**Table 4.1** Material constants for the voided microstructure.

$E_m$ [MPa]	$\nu_m$	$\kappa_0$	$\kappa_f$	$C$ [mm <sup>2</sup> ]
$5 \times 10^4$	0.2	$5 \times 10^{-5}$	$2 \times 10^{-3}$	0.2

**Figure 4.10** Homogenised stress-strain responses of three voided samples under uniaxial tensile loading, using the standard first-order computational homogenisation scheme.

classical homogenisation scheme, as evidenced by the coincident peak points in the homogenised stress–strain diagrams.

The homogenised traction-separation diagrams for three RVE sizes, obtained with

**Figure 4.11** Homogenised cohesive responses of three voided samples under tensile loading, where the failure zone averaging scheme is employed. Note that the curves are already shifted to the left by an amount of the damage displacement at the onset of strain localisation.

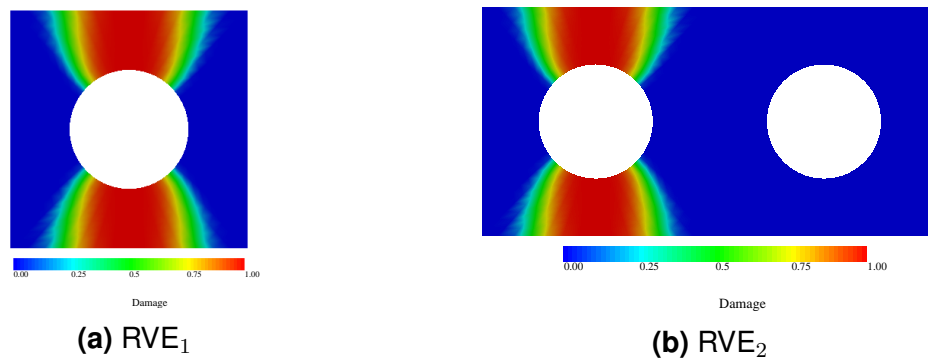


**Figure 4.12** Damage patterns at the end of analyses of two voided samples under tensile loading: (a)  $RVE_1$  and (b)  $RVE_2$ .

the failure zone averaging scheme are presented in Figure 4.11. It is obvious that these curves agree with each other. Therefore, when adopting the failure zone averaging scheme, the size-independent RVE definition does exist in the sense of an objective effective cohesive crack response. The damage patterns in terms of damage level at the end of simulations for  $RVE_1$  and  $RVE_2$  are displayed in the Figure 4.12 for illustration. The formed localisation bands with a finite thickness are the same in the morphology and damage distribution.

### Effect of parameter $c$

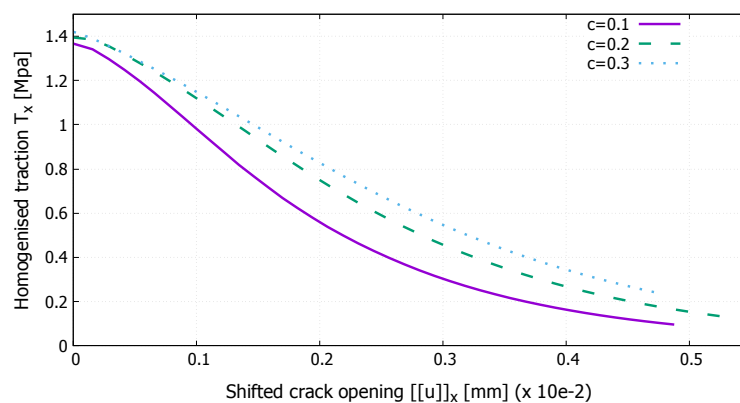


**Figure 4.13** Extracted cohesive laws with shifting for three different values of parameter  $c$  using a regular RVE of size  $10 \times 10 \text{ mm}^2$  with a central circular hole.

To show the influence of parameter  $c$ , using an RVE of size  $10 \times 10 \text{ mm}^2$  with a central circular hole, cohesive laws extracted for the different values  $c = 0.1, 0.2$  and  $0.3 \text{ mm}^2$  are displayed in Figure 4.13. A more ductile response is observed with an increasing

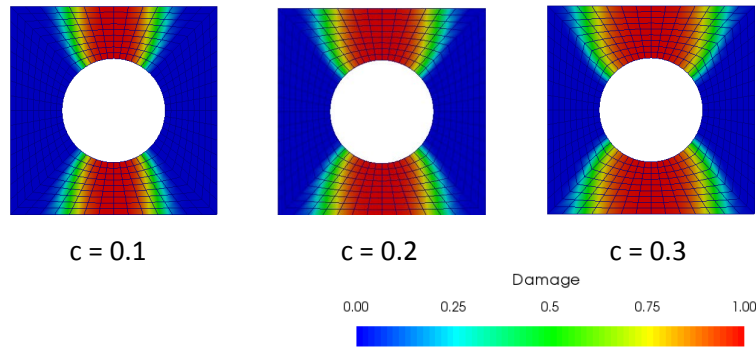


**Figure 4.14** Strain localisation bands for different values of parameter  $c$ .

value of  $c$  from the curves. This is caused by the larger width of the strain or damage localisation band, as displayed in Figure 4.14. The larger damage localisation region implies more dissipated energy.

### Mesoscopic concrete in Section 4.3.2

At a finer scale than the macroscale, plain concrete appears to be heterogeneous. It is typically described as a three-phase composite material consisting of the cement matrix, aggregates and interfacial transition zones (ITZ) surrounding the aggregates (Van Mier, 2012), see Figure 4.15. According to Gitman et al. (2007), aggregates can be assumed circular with diameters ranging from 2.5 mm to 5 mm with a uniformly random distribution and the interface width is set to 0.25 mm, namely 10% of the smallest diameter of the aggregates. Four sample sizes  $10 \times 10 \text{ mm}^2$ ,  $15 \times 15 \text{ mm}^2$ ,  $20 \times 20 \text{ mm}^2$  and  $30 \times 30 \text{ mm}^2$  are studied. The aggregate density  $\rho = 40\%$  is chosen to simplify the process of random packing of the aggregates. The randomness of the aggregate distribution is considered by simulating three random realisations for each sample size.

Making reference to (Gitman et al., 2007, Nguyen et al., 2010), the material constants for each phase are summarised in Table 4.2. When generating samples for simulation, periodicity of the material is kept by preventing “wall effects”, as suggested by Gitman et al. (2007). The elements size in the interfaces and matrix should be small enough to to adequately capture the modes of high strain localisation. However, the aggregates in concrete are not allowed to experience damage by assigning a rather high value to  $\kappa_0$ , and coarse elements can be used for meshing aggregate regions.

For these four sizes of concrete samples under tensile loading, the homogenised

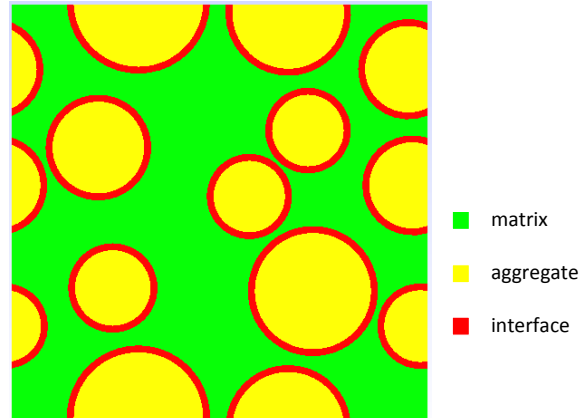


**Figure 4.15** Idealisation of material composition of plain concrete at the mesoscale.

**Table 4.2** Material constants of the heterogeneous three-phase concrete material.

Constituent	$E_m$ [MPa]	$\nu_m$	$\kappa_0$	$\kappa_f$	$C$ [mm <sup>2</sup> ]
Aggregate	$3 \times 10^4$	0.2	0.5	1	0.2
Matrix	$2.5 \times 10^4$	0.2	$5 \times 10^{-6}$	$7.5 \times 10^{-4}$	0.2
ITZ	$2 \times 10^4$	0.2	$3 \times 10^{-6}$	$7.5 \times 10^{-4}$	0.2

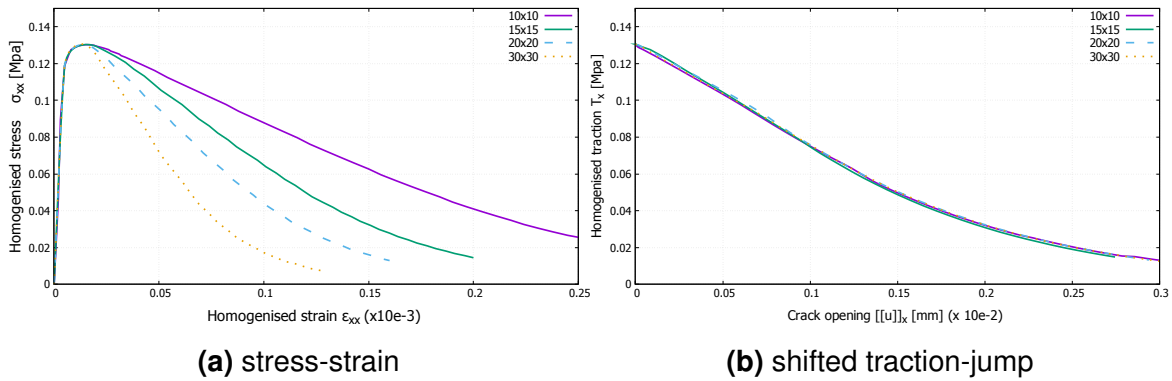


**Figure 4.16** Softening concrete RVEs in tension: standard averaging (a) vs. failure zone averaging (b).

responses in terms of the stress and strain relation using the standard averaging scheme are displayed in Figure 4.16a. Obviously, the objectivity of the measured response with respect to the RVE size is not retained after entering the post-peak softening regime. This obstructs the definition of an RVE for softening materials, see

(Gitman et al., 2007). The responses in terms of the extracted traction and crack opening (displacement jump) with the failure zone averaging scheme of Nguyen et al. (2010) are shown in Figure 4.16b. As can be seen, these diagrams show good agreement (almost overlapping each other), which demonstrates the capability of the failure zone averaging for overcoming the RVE size dependence issue induced by material softening. Note that these cohesive response diagrams in Figure 4.16b have shifted to the left, by an amount of the damage displacement at the peak, along the crack opening axis to eliminate the pre-peak portion. This is quite useful when incorporating this extracted cohesive law in the XFEM or EFEM framework for describing the crack behaviour of progressive separation.

The localisation patterns in terms of damage level for one realisation of each size

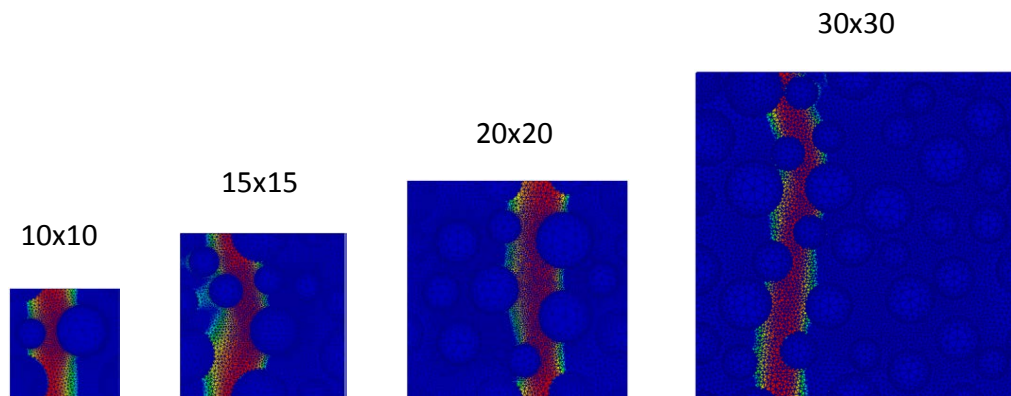


**Figure 4.17** Damage patterns of concrete RVEs ( $\rho = 40\%$ ) of five sizes:  $10 \times 10$ ,  $15 \times 15$ ,  $20 \times 20$ ,  $30 \times 30$  from left to right (unit of length is mm).

are illustrated in Figure 4.17. A vertical straight localisation band, developed due to tension, is observed with similar width in each case.

The slight difference in the effective cohesive traction-jump diagrams in Figure 4.16b, can be explained by two possible reasons. The first is the RVE realisation pool size (three) is very small so that the statistical character (randomness) cannot be guaranteed. Figure 4.18 gives the extracted cohesive responses from three realisations for the sample sizes  $10 \times 10$  and  $15 \times 15$ , where minor differences are found on the curves. When employing more realisations and then repeating the simulation and averaging procedure, it is reasonable to anticipate a smoother and more coincident response. The second reason is that the localisation band width is an approximate value, which might affect the crack opening estimation. Figure 4.19 shows the damage patterns at the end of simulation for three different realisations of size 15 mm, where the band width seems slightly different.

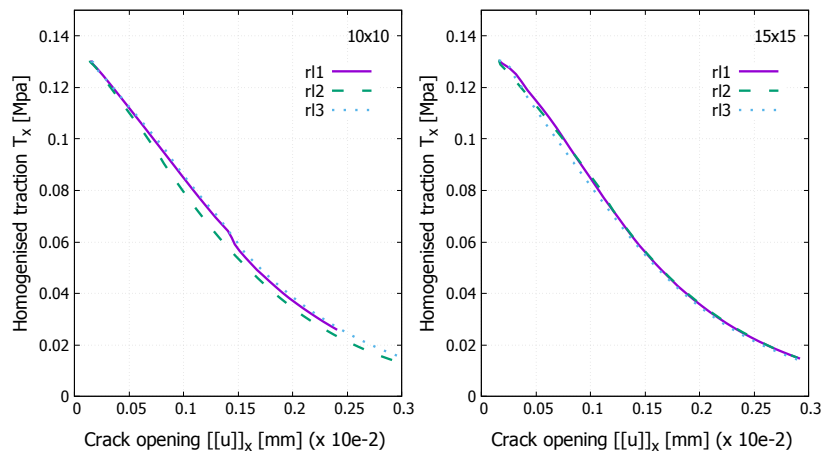


**Figure 4.18** Cohesive responses (unshifted) of three realisations of concrete RVEs ( $\rho = 40\%$ ): size  $10 \times 10$  (left) and size  $15 \times 15$  (right).

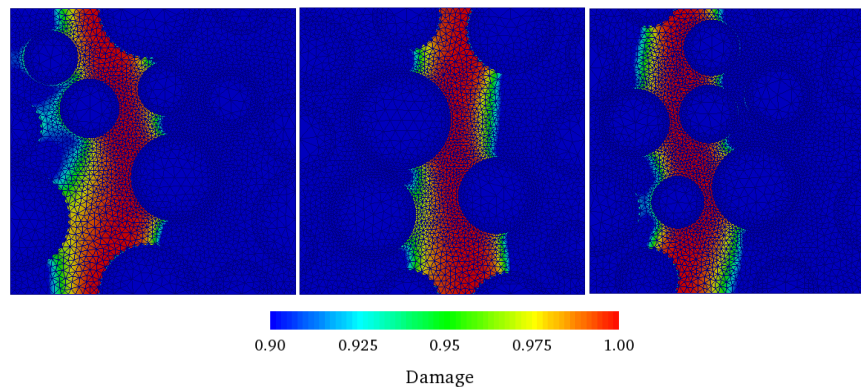


**Figure 4.19** Damage patterns of three different realisations of concrete RVEs of size 15 mm ( $\rho = 40\%$ ).

## 4.4 Macro-discontinuity enhanced FE<sup>2</sup>

This section aims to present a new multiscale failure model based on the first-order CH. The coupling relations between the macro- and microscale are firstly introduced, which is followed by the proof of energetic equivalence between the two scales, employing the variational principle. The implementation details will be given in the next section.

### 4.4.1 Macro-micro coupling

For a cohesive fracture problem, the macroscale domain can be categorised into two sets of material points, those with stable and unstable mechanical responses. In

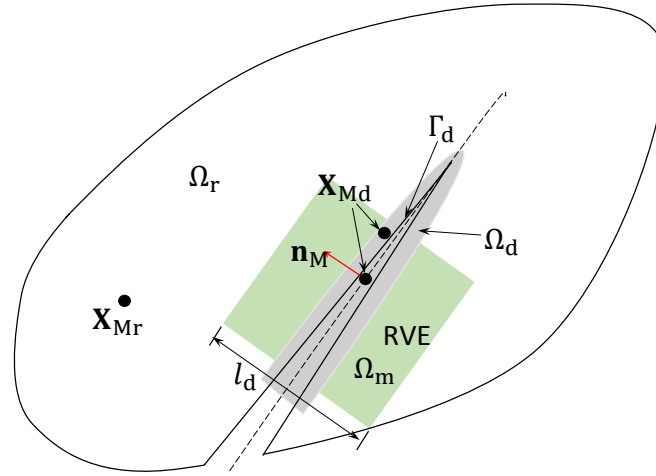


**Figure 4.20** Macroscale domain with a macroscale crack  $\Gamma_d$  corresponding to a strain localisation band  $\Omega_d$ . Also given is the an rotated RVE that coincides with the crack normal direction  $\mathbf{n}_M$ . The RVE with microstructural details is used to simulate material responses, including strain localisation.

view of the localisation, stable and unstable responses correspond to different stages of the deformation process. We use  $\Omega_r$  and  $\Omega_d$  to denote the separate macroscale regions made of stable  $\mathbf{X}_{Mr}$  and unstable material points  $\mathbf{X}_{Md}$ , as shown in Figure 4.20. Indeed,  $\Gamma_{Md}$  is a crack surface when considering strong discontinuities in displacement.  $\Gamma_{Md}$  can be regarded as a consequence of strain localisation.

The definition of an RVE exists for the stable material points  $\mathbf{X}_{Mr}$  that are experiencing uniform deformations at the macroscale. The microscale displacement field for such an RVE can be described as an addition of two displacement fields

$$\mathbf{u}_m = \mathbf{u}_M + \tilde{\mathbf{u}}_m, \quad (4.30)$$

where  $\mathbf{u}_M$  is, according to the first-order deformation assumption, expressed as (reusing Eq. (4.9))

$$\mathbf{u}_M = \boldsymbol{\varepsilon}_M \cdot (\mathbf{X}_m - \mathbf{X}_{Mr}), \quad \forall \mathbf{X}_m \in \Omega_m, \quad (4.31)$$

and the unknown field  $\tilde{\mathbf{u}}_m$  is strongly dependent on the microstructural details. Note that  $\boldsymbol{\varepsilon}_M$  is merely the macroscale strain at each stable point  $\mathbf{X}_{Mr}$ .

For the unstable material points  $\mathbf{X}_{Md}$ , the definition of an RVE is questioned in terms of an effective response that is not sensitive to the RVE size. This requires modifications to the standard first-order CH. To this end, one possibility is to incorporate

the kinematics corresponding to the macroscale crack into the RVE domain. Note that for points on the crack surface, the displacement field is discontinuous and the resulting infinite strain does not make sense when considering  $\varepsilon_M$ . Considering the equivalence between a strong discontinuity and a smeared weak discontinuity, we may smear the strong discontinuity jump over a certain dimension along the normal direction to the localisation band that emerges within the RVE. This is very similar to the concept of the crack band model of [Bažant and Oh \(1983\)](#). Hence, the kinematics to distribute over the RVE may be represented as ([Kolymbas, 2009](#), [Nguyen et al., 2012a](#))

$$\varepsilon_M = \varepsilon_{M0} + \frac{1}{l_d} (\llbracket \mathbf{u} \rrbracket_M \otimes^s \mathbf{n}_M) . \quad (4.32)$$

where  $\varepsilon_{M0}$  represents the effective bulk strain of the material in the vicinity of the macroscale crack,  $\llbracket \mathbf{u} \rrbracket_M$  and  $\mathbf{n}_M$  denote the discontinuity jump across the crack surface and the normal direction to the crack surface, and  $l_d$  is the so-called smearing width. It is obvious that the homogeneous strain term  $\varepsilon_{M0}$  can be neglected when its magnitude is negligible compared with the term  $\frac{1}{l_d} \llbracket \mathbf{u} \rrbracket_M \otimes^s \mathbf{n}_M$ . Eq. (4.32) states that the average strain is equivalent to the sum of the strain contributions due to the bulk and the macroscale crack.

For the case where the square RVE ( $w_m = h_m$ ) is aligned with the global coordinate system, for an inclined localisation band, the parameter  $l_d$  can be estimated as

$$l_d = \frac{|\Omega_m|}{l_{eff}} = \frac{|\Omega_m|}{w_m \cdot |\mathbf{n}_M(1)| \text{ or } w_m \cdot |\mathbf{n}_M(2)|} , \quad (4.33)$$

where  $l_{eff}$  denotes the effective band length along the tangent direction orthogonal to  $\mathbf{n}_M$ .

The homogeneous bulk strain  $\varepsilon_{M0}$  near the macroscale crack can be approximated in the numerical implementation as

$$\varepsilon_{M0} = \lim_{\delta \rightarrow 0} \frac{1}{2} (\varepsilon(\mathbf{X}_{Md} + \delta \cdot \mathbf{n}_M) + \varepsilon(\mathbf{X}_{Md} - \delta \cdot \mathbf{n}_M)) , \quad (4.34)$$

which is the averaged strain between bulk strains at two points that are approaching the crack surface.

**Remark 12** *The current treatment for coupling discontinuities between two scales shares some similarities with the idea presented by [Svenning et al. \(2017b\)](#). The authors there also considered a smeared macro-to-micro discontinuity transition*

but in the framework of variationally consistent homogenisation. In their work, the macroscale crack is implicitly governed by the microscale response.

With the enriched kinematics  $\varepsilon_M$  at hand, the microscale displacement field for an RVE coupled with an unstable material point can be thereby described as

$$\mathbf{u}_m = \mathbf{u}_M + \tilde{\mathbf{u}}_m = \varepsilon_M \cdot (\mathbf{X}_m - \mathbf{X}_{mr}) + \tilde{\mathbf{u}}_m. \quad (4.35)$$

Eq. (4.35) has the same form as Eq. (4.30) except the definition for  $\varepsilon_M$  is different. In addition, the displacement fluctuations here  $\tilde{\mathbf{u}}_m$  are affected not only by the microstructure, but also by the emerged strain localisation band in the RVE.

#### 4.4.2 Energetic equivalence

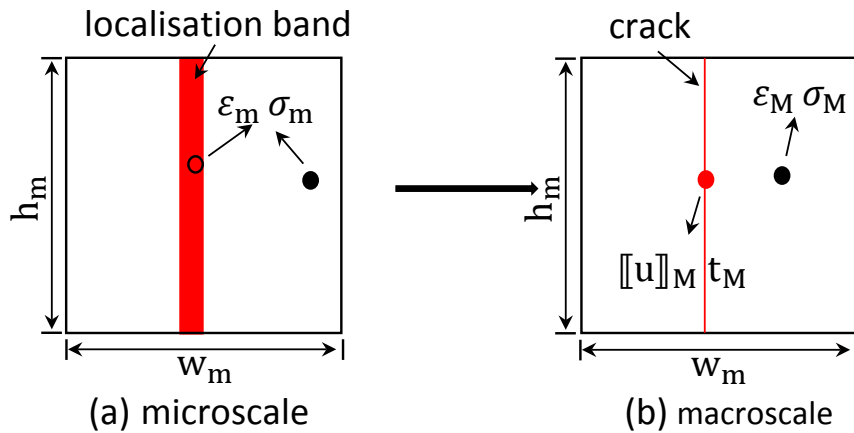


**Figure 4.21** Equivalent macroscopic crack: mechanical quantities of interest at (a) microscale and (b) macroscale.

After determining the connection between the microscale kinematics and the macroscale displacement jump, the next step is to work out the effective cohesive traction. To this end, let us consider the energetic equivalence between two problem setups, as shown in Figure 4.21.

Taking Eq. (4.35) into the expression for internal virtual work of the whole RVE and considering the definition of  $\mathbf{u}_M$  by Eq. (4.32) and  $l_d = w_m$  in this case, it follows that

$$\begin{aligned} \mathcal{W}_m &= \int_{\Omega_m} \boldsymbol{\sigma}_m : \delta \boldsymbol{\varepsilon}_m d\Omega_m \\ &= \int_{\Omega_m} \boldsymbol{\sigma}_m : \delta \boldsymbol{\varepsilon}_{M0} d\Omega_m + \frac{1}{w_m} \int_{\Omega_m} \boldsymbol{\sigma}_m \cdot \mathbf{n}_M \cdot \delta [[\mathbf{u}]]_M d\Omega_m + \int_{\Omega_m} \boldsymbol{\sigma}_m : \nabla^s \delta \tilde{\mathbf{u}}_m d\Omega_m. \end{aligned} \quad (4.36)$$

The virtual work  $\mathcal{W}_M$  performed by the macroscopic body with an equivalent crack to the strain localisation band in the RVE can be expressed as

$$\mathcal{W}_M = w_m h_m \boldsymbol{\sigma}_M : \delta \boldsymbol{\varepsilon}_{M0} + h_m \mathbf{t}_M \cdot \delta [[\mathbf{u}]]_M . \quad (4.37)$$

The RHS in Eq. (4.37) consists of two types of virtual work contributions, the change in internal energy corresponding to the bulk material and the work performed by the equivalent cohesive crack.

Equating  $\mathcal{W}_m$  to  $\mathcal{W}_M$  and making use of the variational principle, we can derive the expression for the effective cohesive traction

$$\begin{aligned} \mathbf{t}_M &= \frac{1}{w_m h_m} \int_{\Omega_m} \boldsymbol{\sigma}_m \cdot \mathbf{n}_M d\Omega_m \\ &= \langle \boldsymbol{\sigma}_m \rangle \cdot \mathbf{n}_M = \boldsymbol{\sigma}_M \cdot \mathbf{n}_M , \end{aligned} \quad (4.38)$$

and the expression for the variational form of the microscale equilibrium problem

$$\int_{\Omega_m} \boldsymbol{\sigma}_m : \nabla^s \delta \tilde{\mathbf{u}}_m d\Omega_m = 0 . \quad (4.39)$$

Note that an approximation between the virtual bulk work in  $\mathcal{W}_m$  and that in  $\mathcal{W}_M$  has been made after assuming statistical homogeneity in the material on the both sides of the crack. As can be seen from the Eq. (4.38), the expression for the effective traction is just the the projection of the macroscopic Cauchy stress on the macroscopic crack plane, the same as was postulated in (Hirschberger et al., 2009, Verhoosel et al., 2010).

Eq. (4.39) represents the weak form of the microscale equilibrium problem that needs to be solved for unknown displacement fluctuation field  $\tilde{\mathbf{u}}_m$ .

The extended CH for characterising the cohesive crack behaviour can be illustrated in the Figure 4.22.

Any of those boundary conditions discussed in Section 4.2 might be chosen. However, the enforced boundary conditions should respect the localisation band to ensure a realistic localisation mode and to give an accurate effective mechanical response. Therefore, after the localisation is detected, the localisation aligned weakly periodic BCs presented by Svenning et al. (2017a) are adopted.

The cohesive tangent stiffness matrix  $\mathbf{T}_M$  can be obtained by performing the linearisation of the cohesive traction given by Eq. (4.38) over the macroscale displacement

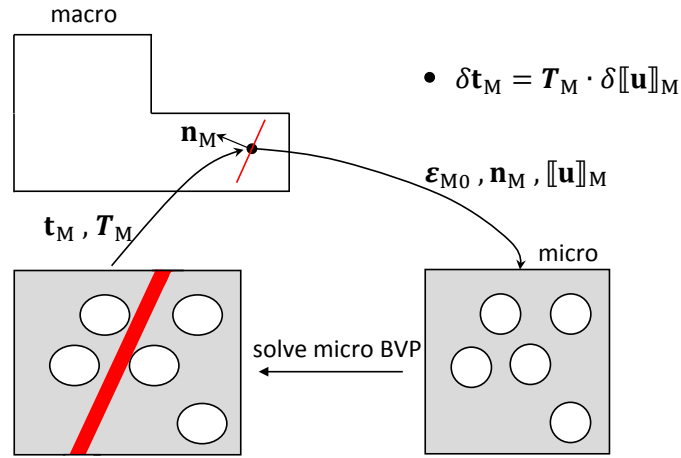


**Figure 4.22** Extended computational homogenisation for the multiscale constitutive model of cohesive cracks.

jump  $[[\mathbf{u}]]_M$ . The derivation process is given as follows

$$\begin{aligned}
 \mathbf{T}_M &= \frac{\delta \mathbf{t}_M}{\delta [[\mathbf{u}]]_M} \\
 &= \frac{\delta \boldsymbol{\sigma}_M}{\delta \boldsymbol{\varepsilon}_M} \frac{\delta \boldsymbol{\varepsilon}_M}{\delta [[\mathbf{u}]]_M} \cdot \mathbf{n}_M \\
 &= \frac{1}{l_d} \mathbf{n}_M \cdot \mathbf{D}_M \cdot \mathbf{n}_M,
 \end{aligned} \tag{4.40}$$

where Eqs. (4.32) and (4.38) have been used and the minor symmetry of the homogenised stiffness  $\mathbf{D}_M = \frac{\delta \boldsymbol{\sigma}_M}{\delta \boldsymbol{\varepsilon}_M}$  has been assumed. Note that  $\mathbf{D}_M$  may have different explicit forms for different boundary conditions prescribed on the RVE. When the weakly periodic BCs are employed,  $\mathbf{D}_M$  has the expression form as shown in Eq. (4.26).

## 4.5 Computational implementation

Discrete cracks at the macroscale are represented with the XFEM. To numerically simulate a discrete crack, two necessary ingredients need to be specified: when the crack is allowed to emerge (initiation criterion) and the direction along which the crack is about to extend with a predefined length (propagation criterion).

### 4.5.1 Initiation and propagation criterion of macroscale cracks

The discrete crack is a consequence of strain localisation. The strain localisation relates to the loss of ellipticity of stress governing equations. In the multiscale setting, the localisation detection at the macroscopic scale can be based on singularity of the acoustic tensor associated with the homogenised bulk tangent stiffness (Massart et al., 2007, Belytschko et al., 2008, Coenen et al., 2012a, Toro et al., 2014) and on negative eigenvalues of the homogenised bulk tangent stiffness (Svenning et al., 2019). Another option is to identify strain localisation based on the stress field at the macroscale (Verhoosel et al., 2010, Nguyen et al., 2011a).

The singularity condition of the acoustic tensor from the bifurcation analysis in FE<sup>2</sup> reads

$$\det(\mathbf{Q}) = 0, \quad \mathbf{Q} = \mathbf{n} \cdot \mathbf{D}_M \cdot \mathbf{n}, \quad (4.41)$$

where  $\mathbf{Q}$  is the so-called acoustic tensor (localisation tensor),  $\mathbf{n}$  denotes the normal direction to the localisation band or the strain discontinuity surface, and  $\mathbf{D}_M$  is the homogenised tangent stiffness tensor of the bulk material.

Another alternative to the condition (4.41) is to identify whether the minimum eigenvalue of the homogenised bulk tangent stiffness  $\mathbf{D}_M$  is non-positive

$$\lambda_{D_M}^{min} \leq 0. \quad (4.42)$$

It should be noticed that an additional algorithm is required to compute the localisation direction when the limit point criterion defined by (4.42) is violated. A choice for this purpose was mentioned in the work by Svenning et al. (2019). The minimisation procedure is summarised as follows:

1. Compute the eigenstrain  $\tilde{\boldsymbol{\varepsilon}}$  corresponding to  $\lambda_{D_M}^{min}$ ;
2. Minimise the problem defined as  $\|\tilde{\boldsymbol{\varepsilon}} - \boldsymbol{\gamma} \otimes^s \mathbf{n}\|$ ;
3. The vector  $\mathbf{n}$  that satisfies the minimisation is the sought strain localisation direction, namely the direction of the newly inserted crack segment.

Another choice for determining crack propagation direction is the maximum principal stress criterion which assumes that the crack will propagate in a direction perpendicular to the maximum principal stress. To improve the accuracy of prediction, the nonlocal stress tensor  $\hat{\boldsymbol{\sigma}}$  at the crack tip is computed (Wells and Sluys, 2001b). This is performed by weighted averaging of stresses located within the half circle patch

$\Omega_T$  ahead of the crack tip ( see Figure 4.23 )

$$\hat{\sigma}(\mathbf{x}_{tip}) = \frac{\sum_{i=1}^{N_{GP}} \alpha(\|\mathbf{x}_i - \mathbf{x}_{tip}\|) \boldsymbol{\sigma}(\mathbf{x}_i) \Delta V_i}{\sum_{i=1}^{N_{GP}} \alpha(\|\mathbf{x}_i - \mathbf{x}_{tip}\|) \Delta V_i} \quad (4.43)$$

$$\alpha(r) = \frac{1}{(2\pi)^{3/2} l^3} \exp\left(-\frac{r^2}{2l^2}\right),$$

where a Gaussian-type weight function is selected for  $\alpha$ ;  $\mathbf{x}_{tip}$  and  $\mathbf{x}_i$  represent the global coordinates of the crack tip and the Gauss point  $i$  located in  $\Omega_T$  respectively;  $N_{GP}$  is the total number of Gauss points in  $\Omega_T$ ;  $\Delta V_i$  denotes the geometrical volume corresponding to the Gauss point  $i$ . The parameter  $l$  determines how quickly the weight function decays away from the crack tip and is usually taken as three times the characteristic length of elements.

In the current work, the limit point criterion given by (4.42) is used as the crack initiation criterion and the normal direction to the start segment is determined by the minimisation procedure mentioned previously. The start segment can be specified to pass through either the cracked Gauss point or element centre. Here, we mean by the cracked Gauss point the macroscale Gauss point where strain localisation has been detected on the RVE coupled with that Gauss point. For the treatment of crack propagation, we choose the combination of the limit point criterion and the maximum principal stress criterion with the nonlocal stress at the crack tip. The former addresses when the crack propagates and the latter how the crack propagates. The use of the maximum principal stress criterion is because large elements at the macroscale are normally favoured in practice to reduce computational burden; the accuracy of predicting propagation direction is critical in obtaining an accurate global response. The existing cracks propagate in an element-by-element manner, indicating that the crack tip must be always located on an element edge. The propagation length can be one element wide or several elements wide. This needs to be manually specified as an input.

At every converged state of the macroscale problem, homogenised bulk tangent stiffness needs to be checked for condition (4.42) at each GP of each macroscale element. Once the condition (4.42) is violated, a new crack segment is about to be introduced. However, as mentioned in Chapter 3, multiple Gauss points may violate the condition (4.42) at the same time. This makes the solution procedure unstable. Also, allowing new crack initiation near the existing crack results in a crack path that is not continuous, as is the case in the embedded discontinuity approach ( EFEM ). Therefore, to ensure a continuous crack path, the propagation criterion is first



localisation. Therefore, the initial states for these Gauss points are required to be set once created.

In the work by Souza and Allen (2011), the initial state of the cohesive ( localised ) RVEs was built by standard cloning from the original Gauss point, only one for the constant triangular element. Nguyen et al. (2012c) proposed a new cloning operation, called load control cloning, where the new cohesive RVE states were defined by loading an RVE from an undeformed state to the maximum strength of the RVE. This allows the use of different RVE configurations (e.g. size and morphology) for describing the behaviour of cohesive cracks. To integrate the cohesive traction contribution accurately, at least two cohesive Gauss points for an enriched element are necessary, see Figure 4.23, since the displacement jump along the cohesive segment is approximated by a linear interpolation function provided by the XFEM. Simultaneously, this signifies that at least two cohesive RVEs are required for each enriched element. In this work, the initial state of cohesive RVEs associated with cohesive Gauss points in the fractured element comes from the localised RVE associated with the cracked Gauss point located in the same element, as illustrated in the Figure 4.24.

In the current implementation, three Gauss points, as shown in Figure 4.23, are

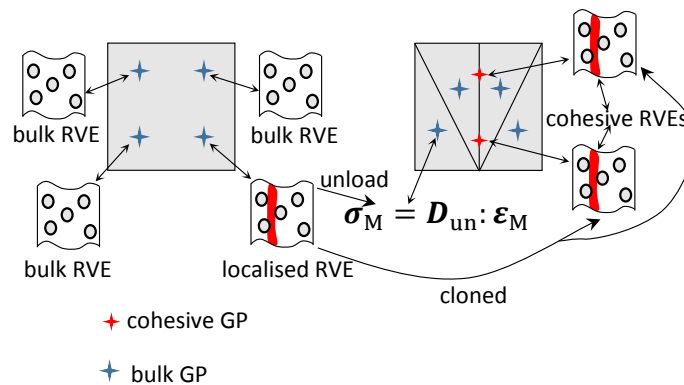


**Figure 4.24** Multiscale failure modelling: at the beginning, four bulk RVEs are coupled to the four bulk GPs in a quadrilateral element. When strain localisation emerges in one of the bulk RVEs, a macroscale crack segment is inserted (in this case, it goes through the element centre). The two cohesive GPs are coupled to cohesive RVEs with their initial state copied from the localised RVE. The bulk GPs of the fractured element behave elastically with the elastic stiffness matrix  $D_{un}$  from unloading the localised RVE.

chosen for each subdivided triangle to calculate the Jacobian matrix and the internal forces for the fractured elements. Hence, it is necessary to remap the internal and state variables ( e.g. damage, strain and stress ) from the existing to the new Gauss

points (Jirásek, 2004, Bobiński and Tejchman, 2016). To enhance the accuracy of state variable mapping, the classical super-convergent patch recovery proposed by Zienkiewicz and Zhu (1987) might be considered. However, in the  $FE^2$  setting, RVEs coupled with old Gauss points in a fractured element may exhibit perhaps different microstructures and damage or crack profiles, as noted in (Svenning et al., 2019); thus it is not practicable to interpolate between RVEs.

In the current work, the bulk Gauss points of a fractured macroscale element are assumed to behave linear elastically and to no longer be coupled to any RVEs. The elastic constants of these bulk Gauss points are obtained by means of unloading the cohesive RVE that is associated with the cracked Gauss point in the fractured element under consideration, see Figure 4.24. Another choice is to unload the RVE that is closest to the bulk Gauss point of interest. This helps save the computational cost and more importantly facilitates the bifurcation of material behaviour commonly observed in experiments on quasi-brittle materials. However, according to our numerical experience, the adoption of an unloading stiffness may lead to compliant responses (global unloading) when inserting a cohesive segment by XFEM. This is because the unloading moment may be not accurate, thus leading to an underestimation of unloading elastic moduli. This is worth further investigation.

The procedure for introducing a new crack or propagating cracks is summarised in Box 4.1.

**Box 4.1.** Treatment for inserting a new crack segment.

After obtaining a converged time step, check whether there is any existing crack about to propagate according to propagation criterion:

1. If yes, propagate it with predefined length and recompute the current time step with the last converged solution as initial guess;
2. Else, check whether there is any new crack about to initiate:
  - (a) If yes, initiate it with predefined length and recompute the current time step with the last converged solution as initial guess;
  - (b) Else, commit the state for macroscale model and the states for all RVE models.

The treatment of a newly fractured macroscale element  $e$  is given as follows:

1. Unload the RVE that has experienced strain localisation; Compute the (homogenised) secant elastic matrix  $D_{un}$  by static condensation.
2. Divide element  $e$  into sub-triangles and assign new GPs for them. These bulk GPs have elastic behaviour characterised by elastic moduli  $D_{un}$ .
3. Determine the line segment between intersection points of the crack with the element edges and assign two cohesive GPs on it. Two cohesive RVEs with their initial state copied from the localised RVE are dispatched to the two cohesive GPs.

### 4.5.3 Recursive sub-stepping

In the FE<sup>2</sup> setting, the stress update at the macroscale involves the solution of an incremental equilibrium BVP that is probably highly nonlinear. Therefore, the macroscale incremental time (load) step size once nonlinearities of some degree appear, should be chosen sufficiently small to ensure that all RVE models subsequently converge within a specified maximum number of Newton iterations. However, such small macroscale step increments will largely increase the computational time in cases when a significant number of RVEs are involved in the overall analysis. This motivates the use of a sub-stepping strategy during the computation of RVEs in order to support large macroscale time step sizes. A guide on sub-stepping has been provided in (Sommer et al., 2009, Reis and Pires, 2013) in the context of multiscale

modelling.

Let us consider an RVE, driven by a macroscopic displacement gradient  $\epsilon_M$ , for which an equilibrium state has been found at time  $t_n$ . An iterative process is started for time step  $[t_n, t_{n+1}]$  to seek a converged solution  $\mathbf{u}_{n+1}$  at time  $t_{n+1}$ . Denote  $\Delta\epsilon_M = \epsilon_M^{n+1} - \epsilon_M^n$ . Assuming such a typical time step fails to converge within a reasonable number of iterations, the procedure of the sub-stepping strategy in infinitesimal strain regime can be summarised as follows:

0. Initialise  $\epsilon_M^{fail} = \epsilon_M^{n+1}$ ,  $\Delta\epsilon_M^{fail} = \epsilon_M^{fail} - \epsilon_M^n$  and  $\epsilon_M^{pre} = \epsilon_M^n$ ;
1. Split the step  $\Delta\epsilon_M^{fail}$  into two equally sized sub-steps such that an intermediate configuration can be defined corresponding to  $\epsilon_M^{int} = \epsilon_M^{pre} + \Delta\epsilon_M^{fail}/2$ ;
2. Use  $\mathbf{u}_{pre}$  as an initial guess for the Newton-Raphson scheme to find  $\mathbf{u}_{int}$ , that is, the solution of the RVE equilibrium problem at the intermediate configuration corresponding to  $\epsilon_M^{int}$ ;
3. Once the solution step  $\epsilon_M^{int}$  is converged, use the intermediate solution  $\mathbf{u}_{int}$  as an initial guess to find the solution of the RVE equilibrium problem at  $\epsilon_M^{fail}$ ;
4. If the above step 2 or 3 fails to converge, reset the values for  $\epsilon_M^{pre}$ ,  $\epsilon_M^{fail}$ , and  $\Delta\epsilon_M^{fail}$  entering a new sub-stepping block, and then the sub-stepping steps 1-3 are applied recursively, until the sought configuration at  $\epsilon_M^{n+1}$  is achieved.

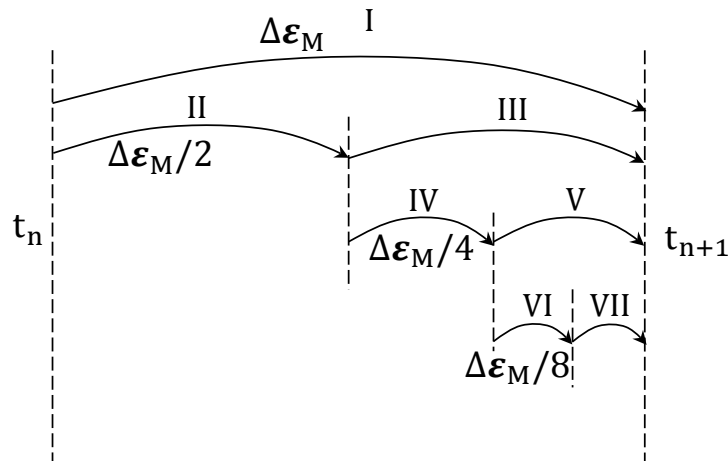


**Figure 4.25** Recursive sub-stepping for a typical failed step  $[t_n, t_{n+1}]$  in solving the RVE equilibrium problem. Reproduced with permission from (Somer et al., 2009), © 2009, Elsevier.

As can be seen from the above recursive sub-stepping procedure, the sub-increments are defined by the constant bisection of the macroscopic displacement gradient increment. A schematic illustration for the sub-stepping procedure is presented in Figure 4.25.

#### **4.5.4 finite element procedure**

The Box 4.2 summarises the finite element procedure for the two-scale failure model.

**Box 4.2.** Flowchart for solving the macro-discontinuity enhanced multiscale failure model.

Initialisation

Loop over time steps:

1. at the current time step, do
  1. Loop over macroscale elements
    - (A) For a nonfractured element in the coupled region, do
      - (i) At each bulk GP, prescribe macroscale strain  $\varepsilon_M$  by means of weakly periodic BCs for associated bulk RVE, then solve microscale BVP
      - (ii) Calculate effective stress  $\sigma_M$  using Eq. (4.22) and effective tangent stiffness  $D_M$  by Eq. (4.26)
      - (iii) Assemble the element Jacobian matrix and internal force vector
    - (B) For a fractured element, do
      - (i) For bulk GPs, use  $\sigma_M = D_{un} : \varepsilon_M$
      - (ii) Loop over cohesive cracks belonging to this element
      - (iii) At each cohesive GP, do
        - (iv) (a) Compute displacement jump  $[[u]]_M$  and  $\varepsilon_{M0}$
        - (b) Calculate  $\varepsilon_M$  according to Eq. (4.32) with known  $l_d$  and  $\mathbf{n}_M$ ; prescribe  $\varepsilon_M$  over the cohesive RVE by means of localisation aligned weakly periodic BCs
        - (c) Solve BVP defined by Eq. (4.39) for the cohesive RVE; If solution procedure diverges, perform the sub-stepping technique in Subsection 4.5.3 until the solution gets converged or the maximum sub-stepping number is reached
        - (d) Compute cohesive traction  $t_M$  using Eq. (4.38) and cohesive tangent  $\mathbf{T}_M$  using Eq. (4.40)
      - (v) Assemble the element Jacobian matrix and internal force vector
  2. Solve the macroscale linear system of algebraic equations
  3. Check for convergence. If met, perform actions in Box 4.1; Else, reduce current time step and then goto procedure 1
2. Proceed to next time step

## 4.6 Numerical studies

In this section, several numerical tests are performed to verify the ability of the continuous-discontinuous multiscale failure model. In 4.6.1, adhesive layer failure is simulated by means of the multiscale failure model in comparison to the Direct Numerical Simulation (DNS) results. In 4.6.2, a series of mode-I cohesive crack examples are illustrated, including the case of inclined cracks. In 4.6.3, multiscale crack propagation in a concrete beam under three-point bending is analysed with the multiscale failure model, compared with the DNS solution.

### 4.6.1 Adhesive layer failure

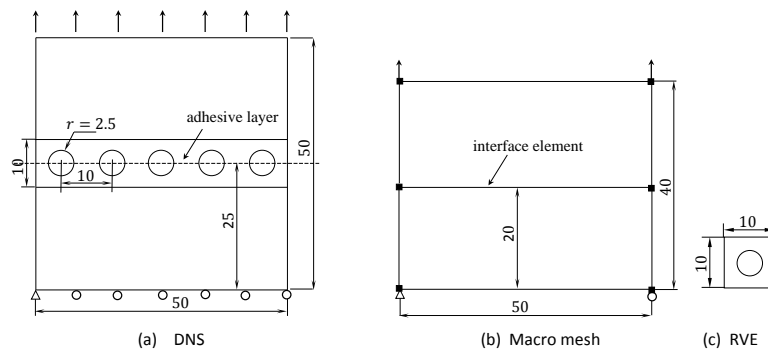


**Figure 4.26** Adhesive layer failure (Example 4.6.1): DNS model - (a) geometry and boundary conditions; Multiscale failure model - (b) macroscale geometry meshed with 2 quadrilateral elements and 1 interface element, and (c) RVE geometry. All units are in mm.

Adhesive bonding is recognised as a promising substitute to the traditional fastening methods in a wide range of industrial applications. The adhesive layer can be treated as an adhesive crack with pre-peak response. The macroscopic deformation mode of the adhesive layer  $[[\mathbf{u}]]_M$  is transferred to the RVE model through boundary conditions. No lateral effect is considered here for the adhesive layer.

In this example, we numerically examine tensile failure of an adhesive layer which has circular holes. The geometry of the structure with thickness 1 mm is shown in Figure 4.26. Plane stress condition is assumed.

The mesh for the DNS analysis is shown in Figure 4.27(a) for illustration. For the multiscale simulation, at the macroscale, the adhesive layer is modelled by a zero-thickness interface element with initially elastic response obtained from the computation of RVE models. The Gaussian integration scheme is adopted for the

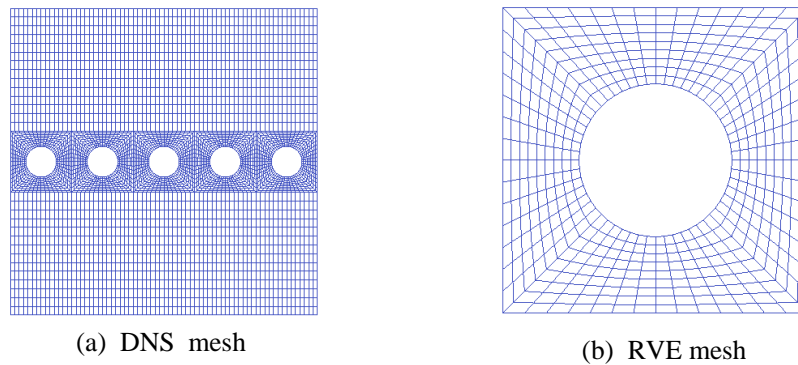


**Figure 4.27** Adhesive layer failure (Example 4.6.1: (a) mesh for the DNS model and (b) mesh for the RVE representing the adhesive layer.

interface element. The effective elastic constants for the adherends are Young's modulus  $5 \times 10^4$  MPa and Poisson's ratio 0.2. At the microscale, the square RVE has the same height as the adhesive layer thickness, that is, 10 mm. The mesh for the RVE is shown in 4.27(b) and material properties in Table 4.1 are used.

As output, the response from the multiscale simulation in terms of the force versus displacement is plotted in Figure 4.28, with the DNS solution as the reference solution. The agreement in response confirms that the multiscale failure modelling approach is effective in capturing the pre- and post-peak behaviour for an adhesive structure.

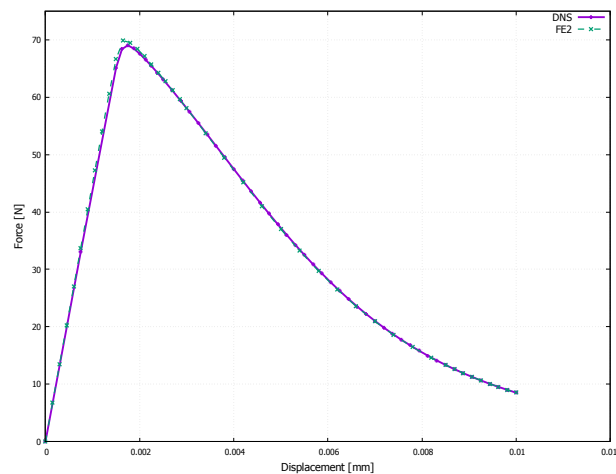


**Figure 4.28** Comparison between results from the DNS and multiscale failure simulation in the Example 4.6.1.

## 4.6.2 Uniaxial tension test

In this numerical study, we simulated cohesive cracks under the simplest loading scenario, namely uniaxial tensile loading. All the numerical tests are performed with the macro-discontinuity enhanced FE<sup>2</sup> scheme. We first explore the initiation and evolution of a macroscopic crack that is aligned with the global coordinate system. Then, inclined macroscopic cracks are studied.

### 4.6.2.1 Horizontal cracks

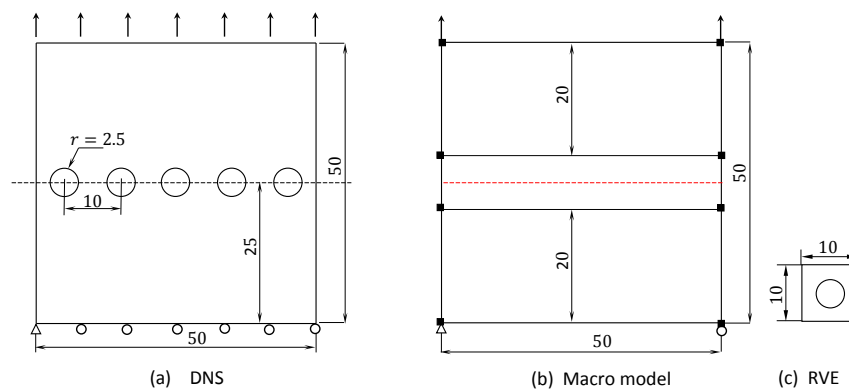


**Figure 4.29** Uniaxial tension test on a plate with holes: DNS model - (a) geometry and boundary conditions; Multiscale failure model - (b) macroscale geometry meshed with 3 quadrilateral elements and boundary conditions and (c) RVE geometry. All units are in mm.

The geometry and boundary conditions of the structure under investigation are shown in Figure 4.29(a). For the multiscale simulation, three bilinear XFEM elements are used at the macroscale with dimensions shown in Figure 4.29(b). However, only the middle one is coupled to RVEs and the remaining are equipped with effective material constants of Young's modulus  $5 \times 10^4$  MPa and Poisson's ratio 0.2. The crack is assumed to initiate across the middle element centre. The geometry of used RVEs is displayed in Figure 4.29(c). The same RVE with assigned material properties from Table 4.1 is employed for all coupled Gauss points.

As can be seen from Figure 4.30, the DNS and FE<sup>2</sup> present crack initiation at the same displacement as indicated by the highest point. Furthermore, the load-displacement responses obtained by these methods agree with each other, which verifies the effectiveness of the current multiscale failure model. At the end of analysis corresponding to  $u_y = 0.01$ , the damage pattern given by the DNS and the multiscale results for the macroscale displacement field  $u_y$  and damage pattern of two cohesive RVEs are displayed in Figure 4.31.

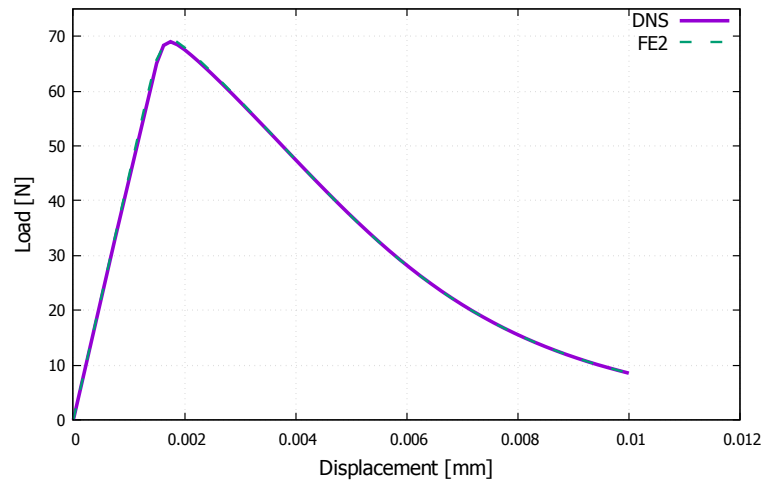


**Figure 4.30** Uniaxial tension test (Example 4.6.2.1): load-displacement curves obtained by DNS and multiscale failure model, with various microstructures.

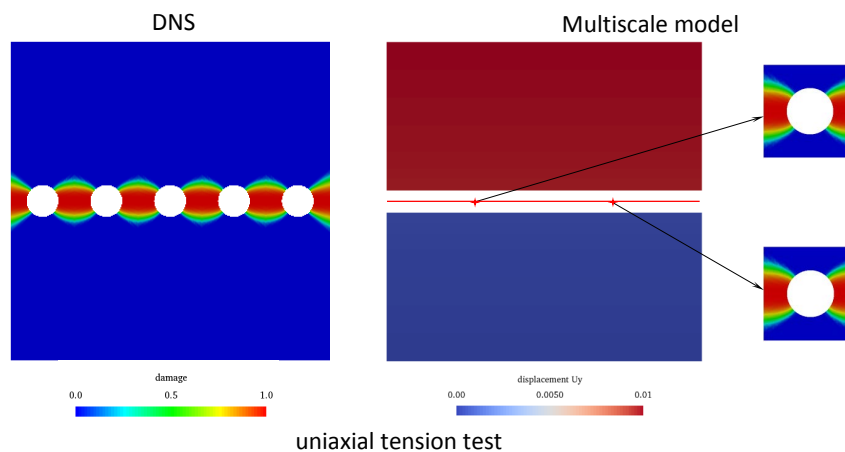


**Figure 4.31** Uniaxial tension test (Example 4.6.2.1): damage profile obtained by DNS (left) and (right)  $y$ -direction displacement contour at the macroscale and damage profiles of cohesive RVEs, obtained by multiscale failure model, with various microstructures.

### Handling Snap-backs

Snap-back phenomena are common in structural mechanics. An example of handling snap-backs in the case of multiscale failure modelling is illustrated here. Similar demonstrations of handling dissipative equilibrium paths or snap-backs in the multiscale setting can be found in (Kaczmarczyk et al., 2010b, Nguyen et al., 2012b).

To introduce snap-backs in the simulation, the numerical example just presented is reused except that the height of the structure is increased to 500 mm and the horizontal displacements on the left and right faces of the structure are fixed. The energy

dissipation based arc-length control explained in Chapter 3 is employed to follow the unstable equilibrium path that cannot otherwise be handled by direct solution control strategies. When the dissipated energy of the macro model reaches a specified threshold, the solution control strategy is switched from the direct displacement to the arc-length control. This switch energy is taken as  $5 \times 10^{-4}$  Nmm in this example. For comparison purposes, two values 0.01 Nmm and 0.015 Nmm for the maximum dissipated energy increment  $\Delta E_{max}$  are chosen.

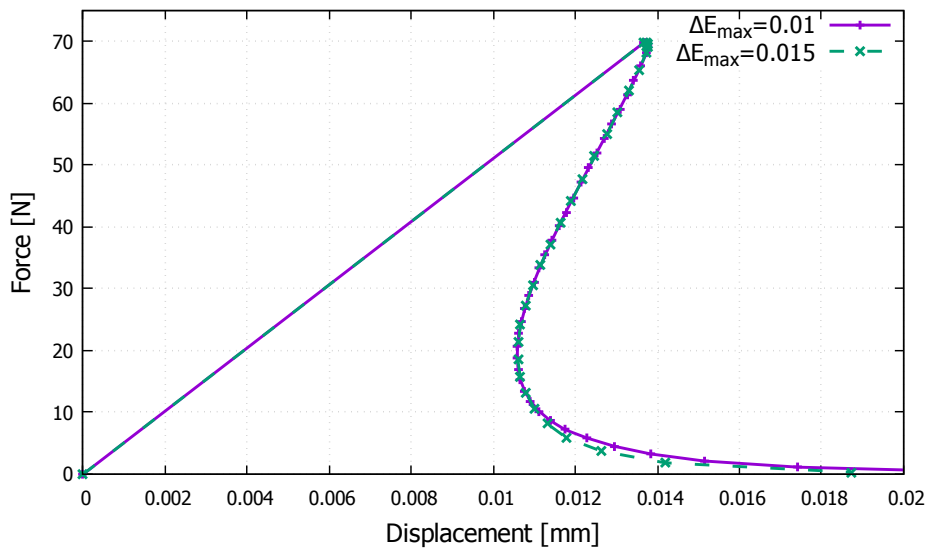


**Figure 4.32** Handling snap-back test: two different values for maximum dissipated energy increment  $\Delta E_{max}$  are chosen for comparison. Marked points except the origin on the curves denote the time steps at which the energy dissipation based arc-length control is used.

It is evident from Figure 4.32 that a snap-back event occurs just after the creation of the macroscale crack. During the simulation, it was observed that in order to attain a converged solution for the RVE model, the sub-stepping scheme was called multiple times in the late stages of analysis for  $\Delta E = 0.015$  Nmm. However, no sub-stepping was required for  $\Delta E_{max} = 0.01$  Nmm. This is because the macroscale displacement jump, determined by the dissipated energy increment, is too large especially at the final stages of loading, so that the RVE model cannot find a converged solution within several iterations. To make sure the macro model and all RVE models can attain convergence within a reasonable number of iterations, small values for  $\Delta E_{max}$  are suggested.

### 4.6.2.2 Inclined cracks

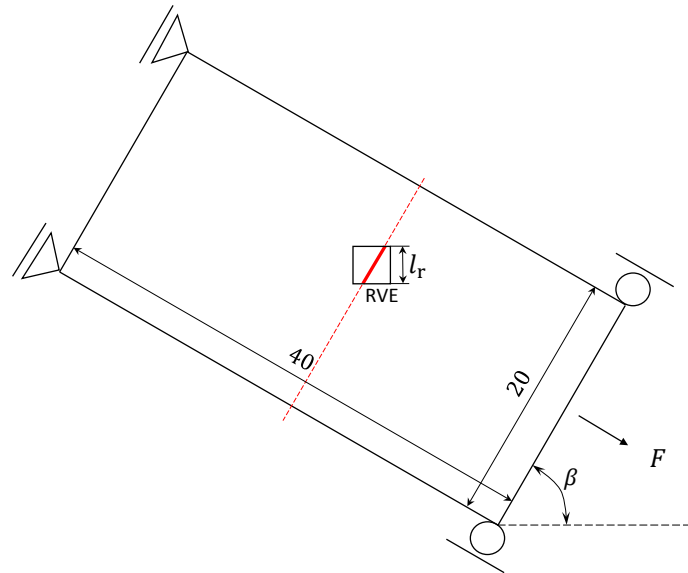


**Figure 4.33** Multiscale inclined crack problem: geometry of the macroscopic structure and boundary and loading conditions; RVE with an inclined microscopic crack modelled with cohesive elements. The angle  $\beta$  characterises the crack direction and loading direction.

To show the capability of the current multiscale failure model in handling inclined cracks, a simple numerical example under tension is given. The geometry of the macroscopic structure and its boundary and loading conditions are displayed in Figure 4.33, where  $\beta$  defines the angle between the right edge and the horizontal direction. The thickness for the structure is 1 mm and plane stress condition is assumed.

The Young's modulus and Poisson's ratio are  $1 \times 10^5$  MPa and 0.2 for the bulk material. The failure mechanism at the microscale is represented by an inclined crack that traverses through the centre of the RVE. Such an inclined crack is modelled with intrinsic cohesive elements with fracture energy 0.05 Nmm and tensile strength 10 MPa. The initial elastic stiffness for cohesive elements is assigned as  $1 \times 10^8$  MPa/mm. Owing to tension, only pure normal fracture mode is taken into account for these cohesive elements. Localisation aligned periodic BCs are adopted to diminish the boundary effects on the microcrack opening. For comparison purposes, four different values for  $\beta$  are taken, that is,  $30^\circ$ ,  $45^\circ$ ,  $60^\circ$  and  $90^\circ$ . Two square RVEs of side length 1 mm and 2 mm are used.

As can be seen from Figure 4.34, good agreement in the displacement versus applied force curves is achieved for different loading directions, which demonstrates

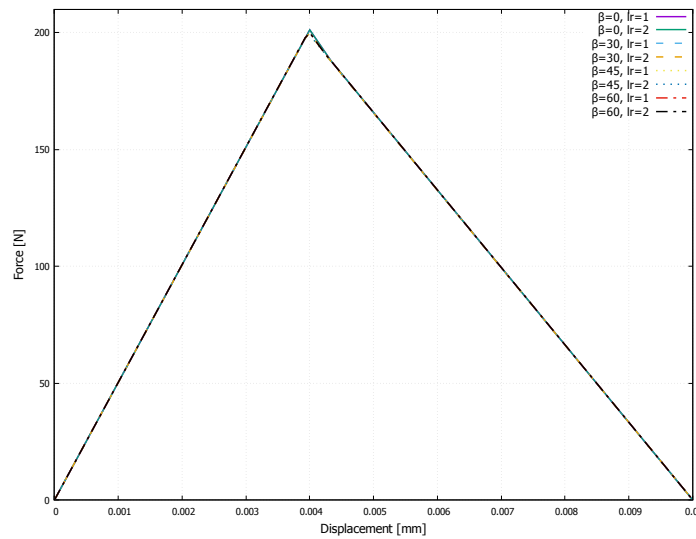


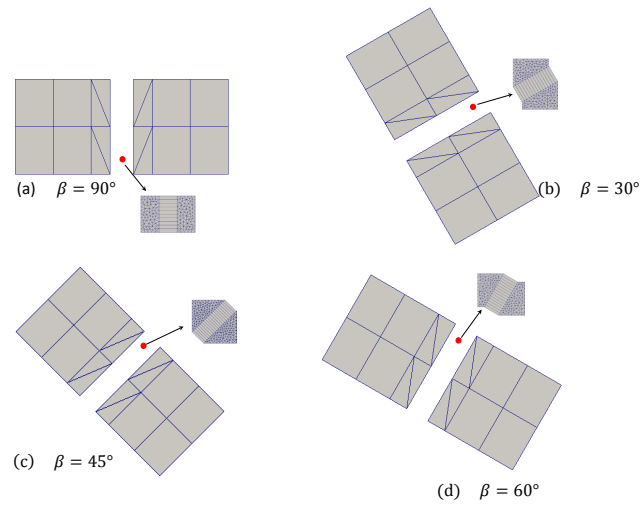
**Figure 4.34** Multiscale inclined crack problem: simulation results of force versus displacement at the right edge for different loading directions determined by  $\beta$ .

the ability of the current FE<sup>2</sup> in handling inclined crack problems. Note that the use of localisation aligned periodic BCs was critical for adequately capturing the opening mode of the cohesive microcracks (Svenning et al., 2017a, Coenen et al., 2012b, Goldman et al., 2018). The deformed configurations of the overall structure and RVE at total loss of load bearing capacity of the structure for different crack normal directions are displayed in Figure 4.35.

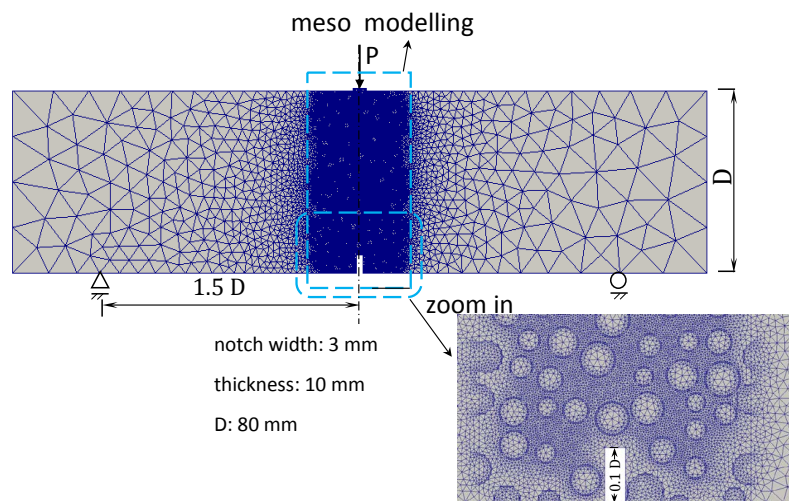
### 4.6.3 Three-point bending test

In order to assess the performance of the presented multiscale failure model for crack propagation, a simply supported three-point bending specimen of concrete is simulated.

The geometry and boundary conditions for the DNS model are displayed in Figure 4.36. Plane stress condition is assumed. To minimise computation time, only the central region of finite width is resolved with explicit mesostructural features. The volume fraction of aggregates is assigned 30%. To mitigate stress concentrations at the loading position, the applied load is distributed on a rigid loading platen glued on the top surface. In the DNS model, the whole domain is discretised with 49250 constant strain triangles. The damage model is regularised with the implicit gradient formulation. Material properties listed in Table 4.2 are used for characterising the behaviour of constituents at the mesoscale. The effective Young's modulus for the (

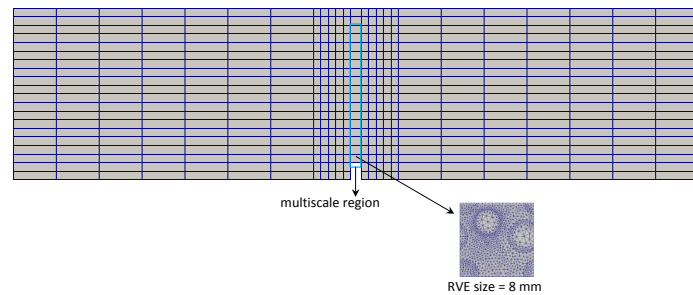


**Figure 4.35** Multiscale inclined crack problem: deformed configurations of the macroscopic structure (magnified by a factor of 500) and the  $1 \times 1$  RVE (magnified by a factor of 50) for different crack angles with the horizontal direction,  $30^\circ$ ,  $45^\circ$ ,  $60^\circ$  and  $90^\circ$ , at total loss of the strength.



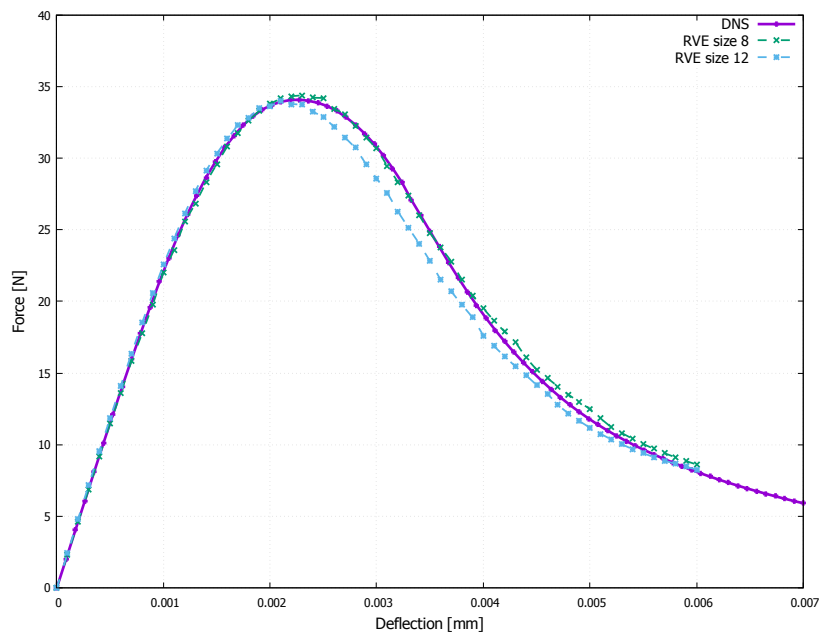
**Figure 4.36** Three-point bending test in Example 4.6.3. DNS model: geometry, boundary and loading conditions. The central region is resolved with explicit mesostructural details with aggregate volume fraction as 30%.

isotropic) concrete material is  $2.57 \times 10^4$  MPa, obtained by a standard homogenisation process before starting the simulation. For the multiscale simulations, the macro domain is discretised with 498 bilinear quadrilateral elements and a typical RVE of size  $8 \text{ mm} \times 8 \text{ mm}$  is meshed with 1892 constant strain triangles, shown in Figure



**Figure 4.37** Three-point bending test in Example 4.6.3: macroscale mesh and  $8\text{ mm} \times 8\text{ mm}$  RVE mesh.

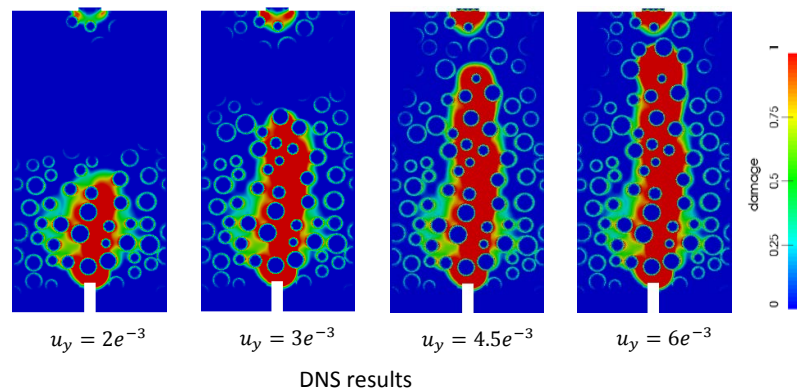
4.37. Note that only the lower 16 elements across the midspan are coupled to RVEs, such that the total number of employed RVEs is 64 at the beginning of analysis.



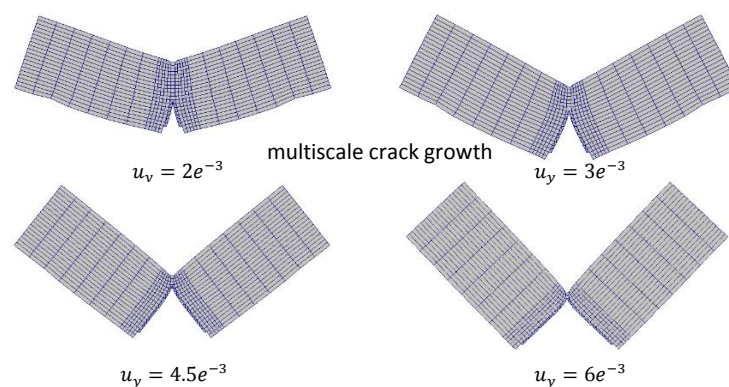
**Figure 4.38** Three-point bending test in Example 4.6.3: comparison of load versus midspan deflection curves for the DNS approach and the multiscale failure approach.

Figure 4.38 compares the load-deflection curves obtained from the DNS ( a reference ) and multiscale failure simulations. As evidenced from the figure, before the peak load, the responses are in good agreement. After the peak load, the curves for multiscale model with RVE size  $8\text{ mm} \times 8\text{ mm}$  and DNS seem to coincide with each other. Also, the curve for multiscale model with RVE size  $12\text{ mm} \times 12\text{ mm}$  has a softer response compared to the DNS. However, we have reasons to believe that this realisation of the DNS model gives a stiffer response than the real response

since the central line of the strain localisation band is deviating from the midspan and diffuse damage is occurring in regions near the strain localisation band, as evidenced in Figure 4.39 below. This requires more numerical comparisons with enlarged RVEs and different realisations of the DNS model. Compared to the DNS results, the curves from the multiscale failure simulations are not quite smooth since the macroscopic time increments are large and the macroscale mesh is coarse. As output from the simulations, we also choose to monitor the resulting strain localisation or crack pattern. For comparison and illustration purposes, Figure 4.39 and Figure 4.40 respectively show the strain localisation profiles and propagating macroscale crack geometries at four different deflection distances.



**Figure 4.39** Three-point bending test in Example 4.6.3: localisation patterns of the DNS model at four different deflection magnitudes.



**Figure 4.40** Three-point bending test in Example 4.6.3: propagating macroscale crack at four different deflection magnitudes.

## 4.7 Concluding remarks

A continuous-discontinuous multiscale failure modelling approach based on the macro-discontinuity enhanced CH scheme has been presented in this chapter. The enhanced CH scheme employs the notion of the crack band model and extends the capability of the conventional CH to the softening regime of materials. When employing this approach, there is no need for explicit assumptions about the constitutive behaviour of bulk materials and cohesive cracks at the macroscale. Therefore, details on microstructure and its evolution can be incorporated. Several numerical examples have been performed to illustrate the performance of the continuous-discontinuous multiscale failure model.

Only one dominant strain localisation band on the RVE has been studied. We should pay attention to the fact that the (unloading) elastic stiffness has been assumed for describing the bulk behaviour after inserting a cohesive segment in one element in order to save computational costs. However, this may result in inaccurate responses when continuous damage loading can occur in directions other than the localisation direction.

Although attractive, the presented multiscale failure model does not preserve the mechanical consistency in discontinuity kinematics and energy dissipation across two scales in a softening material in a strict manner. Consideration of such consistency may be of great importance for a number of reasons. Firstly, on physical grounds a macroscale cohesive crack undergoing progressive degradation is strongly subject to strain and damage localisation evolution within the material microstructure. Secondly, it is desirable for accuracy and reliability when developing and using multiscale failure simulation packages. To this end, we will introduce a new multiscale failure framework in next chapter.

# Chapter 5

## Multiscale Failure Modelling based on Failure-Oriented Multiscale Variational Formulation

### 5.1 Introduction

In some particular engineering situations, such as hydraulic fracture, it is critical in preserving the consistency of physical phenomena across scales in terms of kinematics, kinetics and energy. In this chapter, we are interested in an existing multiscale theoretical framework, which has been called Failure-Oriented Multiscale Variational Formulation (FOMVF) in the literature. Unlike the preceding work in Chapter 4 that does not strictly enforce the kinematical consistency and ensure the same energy dissipation between the macroscopic crack and microscopic strain localisation band, this framework is capable of precisely defining scale transitions in a variationally consistent manner for multiscale failure problems. Relevant work on the theoretical basis of FOMVF includes ([Sánchez et al., 2013](#), [Toro et al., 2014](#), [2016a](#), [Blanco et al., 2016](#)). Like other CH based methods, the FOMVF based multiscale methods build upon the Representative Volume Element (RVE) concept. One of the main features of this formulation is its full variational consistency. Specifically, as the theoretical foundation, the FOMVF employs the notion of kinematic admissibility and the principle of virtual power that can be regarded as a generalisation of the conventional Hill-Mandel condition.

To address the multiscale failure problem, the FOMVF comprises two submodels, a Classical Multiscale Model (ClMM) for stable macroscopic material response and

a generalised new Cohesive Multiscale Model (CohMM) for macroscopic cohesive crack response. The former is employed for the stable regime, whereas the latter for the unstable regime of macroscopic material response.

The novelty in the work presented in this chapter is two-fold. Firstly, the XFEM is adopted to simulate the cohesive crack at the macroscale, instead of the EFEM approach (finite elements with embedded strong discontinuities) used in (Toro et al., 2014, 2016a). This choice is aimed at guaranteeing the continuity of crack path across element boundaries. Secondly, the computer implementation aspects are detailed and several numerical examples are demonstrated to assess the performance of the current FOMVF based multiscale failure approach.

### Multiscale failure problem

The multiscale failure problem specification as shown in Figure 5.1 is the similar

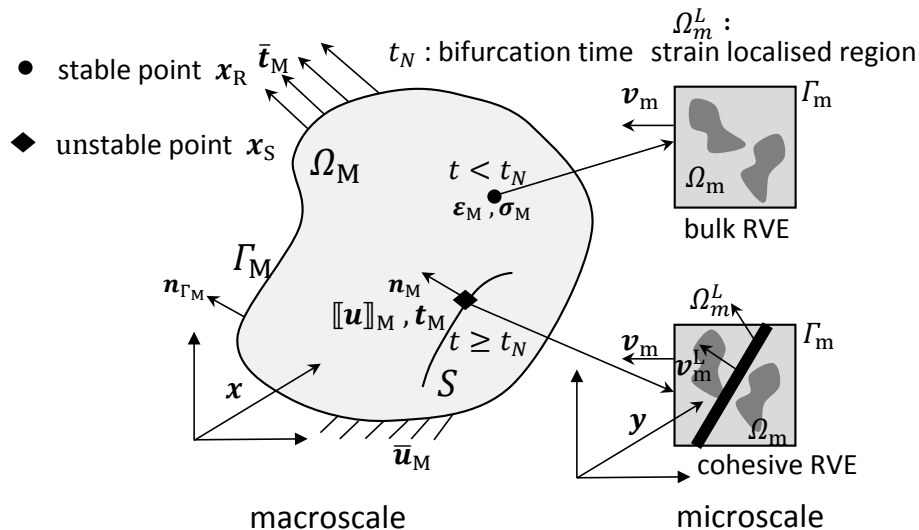


**Figure 5.1** Schematic illustration of the multiscale failure model built upon the failure-oriented multiscale variational formulation. Two material states that are stable and unstable are distinguished, signified by the bifurcation time  $t_N$ .

to that in the preceding Chapter 4, except the scale transition scheme is different. At the macroscale, the material at the stable or regular point  $x_R$  in the domain  $\Omega_M$  is represented by the bulk RVE model, for which the CiMM formulation is adopted to extract a stress-strain constitutive law. When bifurcation occurs at time  $t_N$  due to material instability at a material point signified by  $x_S$ , it is implied that either a new crack initiates or the existing crack denoted by  $S$  propagates. Therefore, a discrete

crack segment modelled with the XFEM method is introduced into the geometrical configuration. We call the RVE after bifurcation as a cohesive RVE, for which the CohMM formulation has to be adopted to extract a traction-separation constitutive law.

The microscale problem is formulated in terms of an RVE containing the microstructural details. The reference material configuration of the RVE is denoted by  $\Omega_m$  with a piecewise smooth boundary  $\Gamma_m$ , see Figure 5.1. A specific reference system is introduced at the microscale with points identified by  $y$ . Macroscopic fields depend on  $\mathbf{x}$ , whereas those at the microscale depend on  $y$ . The subscripts  $(\cdot)_M$  and  $(\cdot)_m$  refer to variables defined at the macroscale and microscale, respectively. In the sequel, we will describe the Classical Multiscale variational Model (Clamm) formulation and then the Cohesive Multiscale variational Model (CohMM) formulation.

Before starting to present the multiscale formulations, let us recall the enriched kinematics for a macroscopic body with a crack, which has been explained in Chapter 3. The displacement field for a cracked body  $\mathbf{u}_M$  can be decomposed into

$$\mathbf{u}_M(\mathbf{x}) = \mathbf{u}_R(\mathbf{x}) + H_s \llbracket \mathbf{u}(\mathbf{x}) \rrbracket_M, \quad (5.1)$$

where  $\mathbf{u}_R$  and  $\llbracket \mathbf{u} \rrbracket_M$  represent the regular and enriched components respectively, and  $H_s$  is the Heaviside function centred at the crack  $S$ . By taking the gradient of Eq. (5.1), the corresponding strain field can be expressed as

$$\boldsymbol{\varepsilon}_M = \underbrace{\nabla_x^s \mathbf{u}_R + H_s \nabla_x^s \llbracket \mathbf{u} \rrbracket_M}_{\boldsymbol{\varepsilon}_R, \text{ bounded}} + \underbrace{\delta_s (\llbracket \mathbf{u} \rrbracket_M \otimes^s \mathbf{n}_M)}_{\text{unbounded}}, \quad (5.2)$$

where  $\boldsymbol{\varepsilon}_R$  is the regular strain,  $\mathbf{n}_M$  denotes the crack normal vector and  $\delta_s$  is the Dirac-delta distribution centred at the crack  $S$ . It can be easily seen from Eq. (5.2) that the first two RHS terms are bounded, whereas the third RHS term is unbounded due to the occurrence of displacement jump.

Next, let us recall from the literature (Rice, 1976, Ruesson et al., 1991) that the bifurcation condition to admit a non-uniform deformation mode can be stated as

$$\det(\mathbf{Q}) = 0, \quad \mathbf{Q} = \mathbf{n} \cdot \mathbf{D} \cdot \mathbf{n}, \quad (5.3)$$

where  $\mathbf{Q}$  is the so-called acoustic tensor (localisation tensor),  $\mathbf{n}$  denotes the normal direction (see Figure 5.2) to the localisation band, and  $\mathbf{D}$  is the material tangent stiffness tensor. When  $\mathbf{D}$  exhibits major symmetries, the solution of Eq. (5.3) has

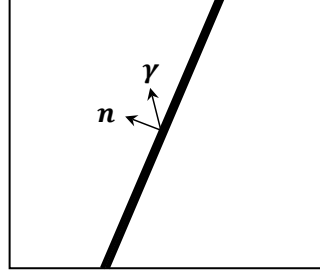


**Figure 5.2** A mixed-mode strain localisation band signified by the normal  $\mathbf{n}$ . The direction pointed by  $\gamma$  coincides with the initial opening velocity direction.

two conjugate eigenvectors  $\mathbf{n}$  and  $\gamma$  (Oliver et al., 2010), where  $\gamma$  coincides with the initial opening velocity direction.

## 5.2 Classical Multiscale variational Model (ClAMM) formulation

This formulation is used for characterising the stable response at a stable or regular material point  $\mathbf{x}_R$  within the sub-domain  $\Omega_M \setminus \mathcal{S}$ .

### 5.2.1 Kinematic admissibility

Let  $\epsilon_M$  as usual denote the macroscale strain at the point  $\mathbf{x}_R$ . In this case,  $\epsilon_M = \epsilon_R$ , see Eq. (5.2). We can decompose the total microscale strain field  $\epsilon_m$  as the sum of two contributions

$$\epsilon_m = \mathcal{I}_y(\epsilon_M) + \tilde{\epsilon}_m, \tag{5.4}$$

where the first RHS term is the so-called *Insertion Operator* (Blanco et al., 2016) that is used to distribute the macroscale deformation or macroscale strain into the RVE and the second RHS term is the microscale strain fluctuation field, defined as  $\tilde{\epsilon}_m = \nabla_y^s \tilde{\mathbf{u}}_m$  with  $\tilde{\mathbf{u}}_m$  the microscale displacement fluctuation field that accounts for the contribution of heterogeneities.

The insertion operator  $\mathcal{I}_y(\cdot)$  distributes its argument into the RVE domain. It maps a constant symmetric second-order tensor, defined at the macroscale, into a symmetric second-order tensor field at the microscale. In addition,  $\mathcal{I}_y(\cdot)$  is a linear operator, thus it can be expressed as

$$\mathcal{I}_y(\cdot) \equiv \mathbf{I}(y)(\cdot), \tag{5.5}$$

with  $\mathbf{I}(\mathbf{y})$  being a fourth-order microscale tensor field. With the linear property of  $\mathcal{I}_{\mathbf{y}}(\cdot)$ , as shown in Eq. (5.5), the total microscale strain form Eq. (5.4) can be alternatively replaced by the incremental form

$$d\boldsymbol{\varepsilon}_m = \mathbf{I}(\mathbf{y})d\boldsymbol{\varepsilon}_M + \nabla_y^s d\tilde{\mathbf{u}}_m . \quad (5.6)$$

The microscale strain increments  $d\boldsymbol{\varepsilon}_m$  are said to be “*Kinematically Admissible*” in  $\Omega_m$  (Sánchez et al., 2013), if the following property is satisfied

$$\int_{\Omega_m} d\boldsymbol{\varepsilon}_m d\Omega_m = \int_{\Omega_m} \mathbf{I}(\mathbf{y})d\boldsymbol{\varepsilon}_M d\Omega_m . \quad (5.7)$$

In the ClaMM that is first-order, the insertion operator is defined as the fourth-order identity operator, which means that the macroscale strain increment  $d\boldsymbol{\varepsilon}_M$  is uniformly inserted into the RVE domain  $\Omega_m$ . As a consequence, Eq. (5.6) becomes

$$d\boldsymbol{\varepsilon}_m = d\boldsymbol{\varepsilon}_M + \nabla_y^s d\tilde{\mathbf{u}}_m , \quad (5.8)$$

and Eq. (5.7) yields

$$d\boldsymbol{\varepsilon}_M = \frac{1}{|\Omega_m|} \int_{\Omega_m} d\boldsymbol{\varepsilon}_m d\Omega_m , \quad (5.9)$$

with  $|\Omega_m|$  being the area or volume of  $\Omega_m$ .

### 5.2.2 Hill-Mandel variational principle

The Hill-Mandel variational principle requires the virtual internal power at the macroscale to be equal to the volume average of the virtual internal power performed at the microscale

$$\boldsymbol{\sigma}_M : \delta\boldsymbol{\varepsilon}_M = \frac{1}{|\Omega_m|} \int_{\Omega_m} \boldsymbol{\sigma}_m : \delta\boldsymbol{\varepsilon}_m d\Omega_m . \quad (5.10)$$

where the variations  $\delta\boldsymbol{\varepsilon}_M$  and  $\delta\boldsymbol{\varepsilon}_m$  come from the appropriate kinematically admissible variational spaces. Considering the above equality holds throughout the entire loading history and writing  $\boldsymbol{\sigma}_M$  and  $\boldsymbol{\sigma}_m$  in their incremental forms, Eq. (5.10) can be expressed in an equivalent way as

$$d\boldsymbol{\sigma}_M : \delta\boldsymbol{\varepsilon}_M = \frac{1}{|\Omega_m|} \int_{\Omega_m} d\boldsymbol{\sigma}_m : \delta\boldsymbol{\varepsilon}_m d\Omega_m . \quad (5.11)$$

Inserting Eq. (5.6) into Eq. (5.11) and conducting some mathematical manipulations, the Hill-Mandel variational principle becomes

$$\left[ d\boldsymbol{\sigma}_M - \frac{1}{|\Omega_m|} \int_{\Omega_m} (\mathbf{I}(\mathbf{y}))^\top d\boldsymbol{\sigma}_m d\Omega_m \right] : \delta\boldsymbol{\varepsilon}_M - \frac{1}{|\Omega_m|} \int_{\Omega_m} d\boldsymbol{\sigma}_m : \nabla_y^s \delta\tilde{\mathbf{u}}_m d\Omega_m = 0, \quad (5.12)$$

$$\forall \delta\boldsymbol{\varepsilon}_M \text{ and } \delta\tilde{\mathbf{u}}_m \in \mathcal{V}_m,$$

where  $(\mathbf{I}(\mathbf{y}))^\top$  denotes the transpose of the insertion tensor, defined as the fourth-order identity tensor in this ClaMM formulation.

### 5.2.3 Homogenised mechanical response

Taking arbitrary variations of  $\delta\boldsymbol{\varepsilon}_M$  but zero variation of  $\delta\mathbf{u}_m$  in Eq. (5.12), the first consequence of Hill-Mandel principle is derived as

$$d\boldsymbol{\sigma}_M = \frac{1}{|\Omega_m|} \int_{\Omega_m} d\boldsymbol{\sigma}_m d\Omega_m, \quad (5.13)$$

where the property of the fourth-order identity tensor dot product any second-order tensor returning the original second-order tensor has been used. The expression (5.13) furnishes the macroscopic stress at a generic material point and behaves like macroscopic constitutive functional.

**Remark 13** *The insertion operator  $\mathcal{I}_y(\cdot)$  plays a fundamental role in the procedure of stress homogenisation as argued in (Sánchez et al., 2013). Any change in the  $\mathcal{I}_y(\cdot)$  might furnish a different homogenised stress in order to hold the Hill-Mandel condition.*

### 5.2.4 Microscale equilibrium problem

Alternatively, taking arbitrary variations of  $\delta\mathbf{u}_m$  but zero variation of  $\delta\boldsymbol{\varepsilon}_M$  in Eq. (5.12), the second consequence of Hill-Mandel principle is derived as

$$\int_{\Omega_m} d\boldsymbol{\sigma}_m : \nabla_y^s \delta\tilde{\mathbf{u}}_m d\Omega_m = 0, \quad \forall \delta\tilde{\mathbf{u}}_m \in \mathcal{V}_m, \quad (5.14)$$

which characterises the microscale equilibrium problem in a variational form. This equation provides a self-equilibrated microscale stress field as a mechanical reaction to prescribed kinematical boundary conditions.

### 5.2.5 Constitutive models at the microscale

To solve the quasi-static microscale equilibrium problem Eq. (5.14), material constitutive laws that characterise the mechanical behaviours of microstructural constituents are required to be provided *a priori*. Theoretically, any inviscid phenomenological material models can be employed, depending on the physical nature of underlying materials. For a pseudo-time interval  $[t^n, t^{n+1}]$ , the history-dependent inelastic constitutive functional of the strain history can be symbolically represented in an incremental setting as

$$\boldsymbol{\sigma}_m^{n+1}(\mathbf{y}) = \mathcal{F}_y(\boldsymbol{\varepsilon}_m^{n+1}; \mathbf{q}_m^n), \quad (5.15)$$

where  $t$  is a pseudo-time needed to track the deformation history and  $\mathbf{q}_m$  is a set of internal variables of state that are introduced to account for the dissipative processes occurring in the internal microstructure. The subscript  $y$  is used to clarify that  $\mathcal{F}_y$  determines the constitutive response at point  $y$ . Note that the constitutive model may vary from point to point of the RVE.

### 5.2.6 Homogenised constitutive tangent tensor

The homogenised constitutive tangent tensor, denoted as  $\mathbf{D}_M$ , defines the linearised relation between the macroscopic stress and macroscopic strain. It can be obtained by means of a linearisation process of the (incremental) homogenised constitutive response given in Eq. (5.13). To derive such a constitutive tangent tensor, we follow the details presented in the reference (de Souza Neto and Feijóo, 2006).

Consider the total derivative of the homogenised stress with respect to the macroscopic strain

$$\mathbf{D}_M = \left. \frac{D\boldsymbol{\sigma}_M}{D\boldsymbol{\varepsilon}_M} \right|_{\boldsymbol{\varepsilon}_M} = \left. \frac{Dd\boldsymbol{\sigma}_M}{Dd\boldsymbol{\varepsilon}_M} \right|_{\boldsymbol{\varepsilon}_M}, \quad (5.16)$$

where the symbol  $\frac{D}{D\boldsymbol{\varepsilon}_M}(\cdot)$  represents the total derivative with respect to  $\boldsymbol{\varepsilon}_M$ . Considering the explicit dependence of  $\boldsymbol{\sigma}_M$  on  $\boldsymbol{\sigma}_m$  through Eq. (5.13), the dependence of microscale stresses  $\boldsymbol{\sigma}_m$  on the microscale strain through Eq. (5.15) and the definition of the microscale strain  $\boldsymbol{\varepsilon}_m$  via Eq. (5.8), the expression (5.37) can be rewritten as

$$\begin{aligned} \mathbf{D}_M &= \left. \frac{Dd\boldsymbol{\sigma}_M}{Dd\boldsymbol{\varepsilon}_M} \right|_{\boldsymbol{\varepsilon}_M} = \frac{1}{|\Omega_m|} \int_{\Omega_m} \mathbf{D}_m d\Omega_m + \frac{1}{|\Omega_m|} \int_{\Omega_m} \mathbf{D}_m : \frac{\partial d\tilde{\boldsymbol{\varepsilon}}_m}{\partial d\boldsymbol{\varepsilon}_M} d\Omega_m \\ &= {}^{\text{Taylor}} \mathbf{D}_M + \tilde{\mathbf{D}}_M, \end{aligned} \quad (5.17)$$

where  $\mathbf{D}_m = \frac{\partial d\sigma_m}{\partial d\varepsilon_m} \Big|_{\varepsilon_M}$  denotes constitutive tangent tensor at the microscale. It is realised that the expression (5.17) consists of two contributions to the homogenised constitutive tangent tensor. The first one is called the Taylor contribution  ${}^{\text{Taylor}}\mathbf{D}_M$  and the second one the fluctuation contribution  $\tilde{\mathbf{D}}_M$ .  ${}^{\text{Taylor}}\mathbf{D}_M$  is just the volume average of the microscale constitutive tangent tensor, but the determination of the fluctuation counterpart  $\tilde{\mathbf{D}}_M$  that involves the tangential relation between the histories of  $\tilde{\varepsilon}_m$  and  $\varepsilon_M$  needs extra elaboration.

To ease the derivation of the yet unknown term  $\frac{\partial d\tilde{\varepsilon}_m}{\partial d\varepsilon_M}$  in Eq. (5.17), let us first introduce a new notation  $\mathcal{E}$  for representing below the functional relation between the histories of  $\tilde{\varepsilon}_m$  and  $\varepsilon_M$

$$\tilde{\varepsilon}_m^{n+1} = \nabla_y^s \tilde{\mathbf{u}}_m^{n+1} = \mathcal{E}(\varepsilon_M^{n+1}) . \quad (5.18)$$

We then proceed to explore the directional derivative of the functional  $\mathcal{E}$ . Consider the microscale displacement fluctuation function perturbed in the direction of  $\Delta\tilde{\mathbf{u}}_m^{n+1}$

$$\tilde{\mathbf{u}}_\varepsilon^{n+1} \equiv \tilde{\mathbf{u}}_m^{n+1} + \varepsilon \Delta\tilde{\mathbf{u}}_m^{n+1} , \quad \forall \Delta\tilde{\mathbf{u}}_m^{n+1} \in \mathcal{V}_m , \quad (5.19)$$

where  $\varepsilon$  is a scalar infinitesimal perturbation factor.

Substituting Eq. (5.19) into the expression (5.18) and meanwhile perturbing the RHS of the expression (5.18) gives

$$\nabla_y^s \tilde{\mathbf{u}}_m^{n+1} + \varepsilon (\nabla_y^s \Delta\tilde{\mathbf{u}}_m^{n+1}) = \mathcal{E}(\varepsilon_M^{n+1}) + \varepsilon \mathbf{D}^{\mathcal{E}}(\varepsilon_M^{n+1})[\Delta\varepsilon_M^{n+1}] + \mathcal{O}(\varepsilon) , \quad (5.20)$$

where  $\mathbf{D}^{\mathcal{E}}(\varepsilon_M^{n+1})[\Delta\varepsilon_M^{n+1}]$  represents the directional derivative of the functional  $\mathcal{E}$  in the direction of  $\Delta\varepsilon_M^{n+1}$  evaluated at  $\varepsilon_M^{n+1}$ . The first two terms on the RHS of Eq. (5.20) define the linearisation of functional  $\mathcal{E}(\varepsilon_M)$  about  $\varepsilon_M^{n+1}$ . As it can be seen,  $\mathbf{D}^{\mathcal{E}}$  maps the increments of macroscopic strain linearly into the increments of microscale strain fluctuation.

The linearisation of the microscale equilibrium problem defined by Eq. (5.14) at an admissible pair  $\{\varepsilon_M^{n+1}, \tilde{\mathbf{u}}_m^{n+1}\}$  as  $\varepsilon = 0$  contributes to a new problem, that is, for a given function  $\Delta\varepsilon_M^{n+1}$ , find the field  $\Delta\tilde{\mathbf{u}}_m^{n+1} \in \mathcal{V}_m$  such that

$$\int_{\Omega_m} \mathbf{D}_m : \nabla_y^s \Delta\tilde{\mathbf{u}}_m^{n+1} : \nabla_y^s \delta\tilde{\mathbf{u}}_m = - \int_{\Omega_m} \mathbf{D}_m : \Delta\varepsilon_M^{n+1} : \nabla_y^s \delta\tilde{\mathbf{u}}_m , \quad \forall \delta\tilde{\mathbf{u}}_m \in \mathcal{V}_m , \quad (5.21)$$

where Eq. (5.8) has been used. The above equation defines the linear mapping operator  $\mathbf{D}^{\mathcal{E}}$ .

## 5.3 Cohesive Multiscale variational Model (CohMM) formulation

When a material point loses its stability in the sense that strain bifurcation occurs at the macroscale, the ClaMM scheme detailed in the last section is no longer reasonable. This necessitates the development of an extended multiscale variational formulation. This new formulation which aims to deal with the unstable material points has been called the Cohesive Multiscale variational Model (CohMM) in a series of papers (Sánchez et al., 2013, Toro et al., 2014, 2016a). Like most other multiscale approaches to fracture (e.g. the work in (Rudraraju et al., 2012b)), a cohesive crack segment or surface is required to be inserted through unstable points  $\mathbf{x}_s$  at the macroscale to circumvent the numerical difficulties related to mesh sensitivity confronted when modelling failure with the conventional FEM. The constitutive behaviour of the cohesive crack is obtained from an extended homogenisation procedure involving the computation of microscopic models with softening.

### 5.3.1 Kinematics of the RVE

Let us focus on the kinematics of the RVE linked to an unstable macroscopic point  $\mathbf{x}_s$ . The macroscopic strain increment (we keep using the incremental forms for mechanical state variables to facilitate the mathematical development of the CohMM) at  $\mathbf{x}_s$  is characterised by three macroscopic variables, that is, the increment of the regular strain counterpart  $d\boldsymbol{\varepsilon}_R$ , the displacement jump increment vector  $d[[\mathbf{u}]]_M$  of the macroscopic crack at  $\mathbf{x}_s$  and the normal vector  $\mathbf{n}_M$  to the crack surface at  $\mathbf{x}_s$ . They are collected in a triad as  $\{d\boldsymbol{\varepsilon}_R, d[[\mathbf{u}]]_M, \mathbf{n}_M\}$ . In the same manner as the strain decomposition given by Eq. (5.4) in the ClaMM, the microscale strain increment field of the RVE after strain localisation can be decomposed as

$$d\boldsymbol{\varepsilon}_m = \mathcal{I}_y^*(d\boldsymbol{\varepsilon}_R, d[[\mathbf{u}]]_M) + d\tilde{\boldsymbol{\varepsilon}}_m, \quad (5.22)$$

where  $\mathcal{I}_y^*(d\boldsymbol{\varepsilon}_R, d[[\mathbf{u}]]_M)$  defines a new insertion strategy to distribute the generalised macroscopic strain components from  $\mathbf{x}_s$  into each RVE point  $y$  and  $d\tilde{\boldsymbol{\varepsilon}}_m$  denotes the microscale strain fluctuation accounting for the contribution of heterogeneities including microscale localisation bands.

In (Sánchez et al., 2013, Toro et al., 2014), this new insertion strategy has two aspects. The first assumes that the component  $d\boldsymbol{\varepsilon}_R$  is distributed uniformly over

the entire RVE domain including those strain localising elements. The second one postulates that the macroscale discontinuity mode, characterised by  $\{d[[\mathbf{u}]]_{\mathbf{M}}, \mathbf{n}_{\mathbf{M}}\}$ , is uniformly inserted into a subdomain  $\Omega_m^L$ , instead of being uniformly distributed into the entire RVE as employed in the work of Chapter 4. The subdomain  $\Omega_m^L$  denotes the region where microscale strains intensively localise, and is to be determined and then fixed once the macroscopic strain localisation is detected. Therefore, the expression Eq. (5.22) can be rewritten as

$$d\boldsymbol{\varepsilon}_m = d\boldsymbol{\varepsilon}_R + \mathcal{I}_y^L(d[[\mathbf{u}]]_{\mathbf{M}}) + \nabla_y^s d\tilde{\mathbf{u}}_m, \quad (5.23)$$

where the *Failure Insertion Operator*  $\mathcal{I}_y^L(\cdot)$  reads

$$\mathcal{I}_y^L(d[[\mathbf{u}]]_{\mathbf{M}}) = \phi_m^L(\mathbf{y}) \frac{d[[\mathbf{u}]]_{\mathbf{M}} \otimes^s \mathbf{v}_m^L}{l_{\mathbf{M}}}; \quad \phi_m^L(\mathbf{y}) = \begin{cases} \frac{|\Omega_m|}{|\Omega_m^L|} = \frac{l_{\mathbf{M}}}{l_m} & \forall \mathbf{y} \in \Omega_m^L \\ 0 & \text{otherwise} \end{cases} \quad (5.24)$$

where  $\phi_m^L(\mathbf{y})$  is a collocation function and  $l_m$  denotes the thickness of a typical localisation band simulated at the microscale, which may have a different value along the band.  $l_{\mathbf{M}}$  plays the role of macroscopic localisation bandwidth, but actually behaves like a fictitious quantity that is introduced to simplify the mathematical development. However,  $l_m$  plays a crucial role so that a physically objective formulation is guaranteed. When smeared crack approaches are adopted for modelling cracks at the microscale,  $l_m$  is the characteristic element length that is used to regularise the softening process, whereas when zero-thickness interface elements are used,  $l_m$  vanishes.

The microscale kinematics is said “*kinematically admissible*”, if the following two constraints hold (Sánchez et al., 2013)

$$\int_{\Omega_m} d\boldsymbol{\varepsilon}_R + \mathcal{I}_y^L(d[[\mathbf{u}]]_{\mathbf{M}}) d\Omega_m = \int_{\Omega_m} d\boldsymbol{\varepsilon}_m d\Omega_m; \quad (5.25)$$

$$\int_{\Omega_m^L} d\boldsymbol{\varepsilon}_R + \mathcal{I}_y^L(d[[\mathbf{u}]]_{\mathbf{M}}) d\Omega_m^L = \int_{\Omega_m^L} d\boldsymbol{\varepsilon}_m d\Omega_m^L. \quad (5.26)$$

After considering (5.24), the above two equations can be transformed to become

$$d\boldsymbol{\varepsilon}_R + \frac{1}{|\Omega_m|} \int_{\Omega_m} \frac{d[[\mathbf{u}]]_{\mathbf{M}} \otimes^s \mathbf{v}_m^L}{l_{\mathbf{M}}} d\Omega_m = \frac{1}{|\Omega_m|} \int_{\Omega_m} d\boldsymbol{\varepsilon}_m d\Omega_m, \quad (5.27)$$

$$d\boldsymbol{\varepsilon}_R + \frac{1}{|\Omega_m^L|} \int_{\Omega_m^L} \frac{d[[\mathbf{u}]]_{\mathbf{M}} \otimes^s \mathbf{v}_m^L}{l_m} d\Omega_m^L = \frac{1}{|\Omega_m^L|} \int_{\Omega_m^L} d\boldsymbol{\varepsilon}_m d\Omega_m^L. \quad (5.28)$$

The assumptions of *kinematic admissibility* of the microscale displacement incre-

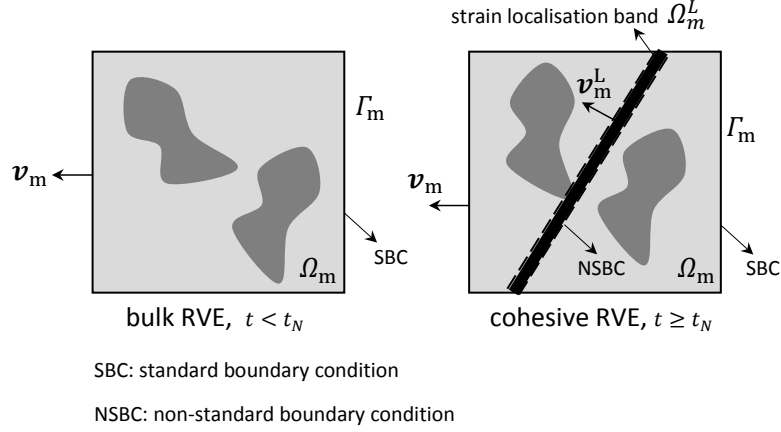


**Figure 5.3** Prescription of boundary conditions on the bulk RVE and cohesive RVE models.

ment field imply that the integrals of the microscale strain fluctuation increments over  $\Omega_m$  and  $\Omega_m^L$  are zero. These kinematical constraints, derived from (5.27) and (5.28), are expressed respectively in integral forms

$$\int_{\Gamma_m} d\tilde{\mathbf{u}}_m \otimes^s \mathbf{v}_m d\Gamma_m = \mathbf{0} , \quad (5.29)$$

and

$$\int_{\Gamma_m^L} d\tilde{\mathbf{u}}_m \otimes^s \mathbf{v}_m^L d\Gamma_m^L = \mathbf{0} , \quad (5.30)$$

where  $\Gamma_m$  is the external boundary of the RVE and  $\mathbf{v}_m$  denotes its outward unit normal vector;  $\Gamma_m^L$  constitutes the boundary of  $\Omega_m^L$  and  $\mathbf{v}_m^L$  is its outward unit normal vector, see Figure 5.3. Conditions (5.29) and (5.30) are to be prescribed on the specific domains of the RVE under strain localisation in order to ensure that the macro-to-micro kinematical transition is properly accomplished. To help distinguish these two boundary conditions, from now on, we call the boundary condition (5.29) the standard boundary condition (SBC) because it is the same type of boundary condition arisen in the ClMM, and the boundary condition (5.30) the non-standard boundary condition (NSBC), following the names coined in (Sánchez et al., 2013). The combination of Eqs. (5.29) and (5.30) defines the vector space of kinematically admissible microscale displacement fluctuation increments in the RVE  $\Omega_m$ :  $\mathcal{U}_m^L$ . The

microscale field  $d\tilde{\mathbf{u}}$  is kinematically admissible if (Sánchez et al., 2013)

$$\mathcal{U}_m^L \equiv \left\{ d\tilde{\mathbf{u}} \mid d\tilde{\mathbf{u}} \in \mathbf{H}^1(\Omega_m), \int_{\Gamma_m} d\tilde{\mathbf{u}}_m \otimes^s \mathbf{v}_m d\Gamma_m = \mathbf{0} \text{ and } \int_{\Gamma_m^L} d\tilde{\mathbf{u}}_m \otimes^s \mathbf{v}_m^L d\Gamma_m^L = \mathbf{0} \right\}. \quad (5.31)$$

Following the Bubnov–Galerkin method, the vector space  $\mathcal{V}_m^L$  of virtual kinematically admissible microscale displacement fluctuation actions is taken as

$$\mathcal{V}_m^L \equiv \left\{ \delta\tilde{\mathbf{u}} \mid \delta\tilde{\mathbf{u}} \in \mathbf{H}^1(\Omega_m), \int_{\Gamma_m} \delta\tilde{\mathbf{u}}_m \otimes^s \mathbf{v}_m d\Gamma_m = \mathbf{0} \text{ and } \int_{\Gamma_m^L} \delta\tilde{\mathbf{u}}_m \otimes^s \mathbf{v}_m^L d\Gamma_m^L = \mathbf{0} \right\}. \quad (5.32)$$

It obviously follows that  $\mathcal{V}_m^L \subset \mathcal{V}_m$ , where  $\mathcal{V}_m$  has been defined in the ClaMM.

The virtual kinematically admissible microscale strain  $\delta\epsilon_m$  can be chosen according to (Sánchez et al., 2013) as

$$\delta\epsilon_m = \phi_m^L(\mathbf{y}) \frac{\delta[[\mathbf{u}]]_M \otimes^s \mathbf{v}_m^L}{l_M} + \nabla_y^s \delta\tilde{\mathbf{u}}_m, \quad \forall \delta[[\mathbf{u}]]_M \text{ and } \forall \delta\tilde{\mathbf{u}}_m \in \mathcal{V}_m^L, \quad (5.33)$$

where  $\delta[[\mathbf{u}]]_M$  is a virtual kinematically admissible macroscopic displacement jump vector. Comparing Eq. (5.33) with Eq. (5.23), it is noticed that the virtual action for  $d\epsilon_R$  is not included since  $t > t_N$ .

### 5.3.2 Energetic consistency across scales

We are now in a position to introduce the Hill-Mandel variational principle to guarantee the energetic consistency between virtual work preformed by the macroscopic crack and that by the microscale failure mechanisms (e.g., smeared cracks or interface elements) after the strain localisation is detected at the macroscale. The Hill-Mandel variational principle for the post-critical dissipation process ( $t > t_N$ ) can be specialised to

$$\mathbf{t}_M \cdot \delta[[\mathbf{u}]]_M = \frac{l_M}{|\Omega_m|} \int_{\Omega_m} \boldsymbol{\sigma}_m : \delta\epsilon_m d\Omega_m, \quad (5.34)$$

where the LHS term represents the macroscopic internal virtual work per unit area of the macroscopic crack and the RHS term characterises the microscopic internal virtual work performed by a unit average characteristic surface, representative of the microscale strain localisation subdomain in  $\Omega_m$ . This characteristic surface is orthogonal to the vector  $\mathbf{v}_m^L$  and the length of it is given by  $\frac{|\Omega_m|}{l_M}$ .

Taking into account that the variational statement Eq. (5.34) is satisfied at previous loading steps, the definition of virtual microscale strain given by (5.33), the total form

of the Hill-Mandel variational principle (5.34) can be transformed to the incremental form

$$\left[ dt_M - \frac{1}{|\Omega_m^L|} \int_{\Omega_m^L} d\boldsymbol{\sigma}_m \cdot \mathbf{v}_m^L d\Omega_m^L \right] \cdot \delta[[\mathbf{u}]]_M - \frac{l_M}{|\Omega_m|} \int_{\Omega_m} d\boldsymbol{\sigma}_m : \nabla_y^s \delta \tilde{\mathbf{u}}_m d\Omega_m = 0, \quad (5.35)$$

$$\forall \delta[[\mathbf{u}]]_M \text{ and } \forall \delta \tilde{\mathbf{u}}_m \in \mathcal{V}_m^L, t > t_N,$$

where  $l_M$  has been cancelled out in the second term of the square brackets.

By standard variational arguments on Eq. (5.35), two consequences can be obtained, which will be presented in the next two following sub-sections.

### 5.3.3 Homogenised mechanical response: macroscopic cohesive traction

Taking arbitrary variations of  $\delta[[\mathbf{u}]]_M$ , but zero variation of  $\delta \tilde{\mathbf{u}}_m$  in the variational expression (5.35), the macroscopic cohesive traction increment is derived

$$dt_M = \frac{1}{|\Omega_m^L|} \int_{\Omega_m^L} d\boldsymbol{\sigma}_m \cdot \mathbf{v}_m^L d\Omega_m^L, \quad t > t_N. \quad (5.36)$$

It is worth remarking that Eq. (5.36) does not arise from an *a priori* definition, but a consequence of the adopted admissible kinematics defined through  $\mathcal{I}_y^L(\cdot)$  and the Hill-Mandel variational principle. As it can be seen, the traction homogenisation procedure in an incremental form is only performed for the microscale stress increment distribution times  $\mathbf{v}_m^L$  in the strain localisation subdomain in the RVE. This guarantees an objective mechanical response of macroscopic cohesive tractions with respect to the RVE size, provided  $[[\mathbf{u}]]_M$ .

The homogenised cohesive tangent for the macroscale cohesive crack can be obtained in different ways. One straightforward way is by means of adding an infinitesimal perturbation in the direction of macroscale displacement jump increments. This implies that two auxiliary RVE models are demanded to solve for a cohesive Gauss point at each iteration. Another way is to linearise the homogenised cohesive traction  $t_M$  with respect to the macroscale displacement jump  $[[\mathbf{u}]]_M$  in analogy to the method for the derivation of homogenised bulk tangent stiffness in 5.2.6. Considering

Eqs. (5.36) and (5.23), the following can be derived

$$\begin{aligned} \mathbf{T}_M &= \frac{D\mathbf{t}_M}{D[\mathbf{u}]_M} \Big|_{[\mathbf{u}]_M} \\ &= \frac{1}{|\Omega_m^L|l_m} \int_{\Omega_m^L} \mathbf{v}_m^L \cdot \mathbf{D}_m \cdot \mathbf{v}_m^L d\Omega_m^L + \frac{1}{|\Omega_m^L|l_m} \int_{\Omega_m^L} \mathbf{v}_m^L \cdot \mathbf{D}_m \cdot \left( \mathbf{I} : \frac{\partial \tilde{\boldsymbol{\varepsilon}}_m}{\partial [\mathbf{u}]_M} \right) d\Omega_m^L, \end{aligned} \quad (5.37)$$

where  $\frac{\partial \tilde{\boldsymbol{\varepsilon}}_m}{\partial [\mathbf{u}]_M}$  can be computed by considering the implicit functional dependence  $d\tilde{\mathbf{u}}_m(d\boldsymbol{\varepsilon}_R, d[\mathbf{u}]_M)$ . It can be found by solving two microscale equilibrium problems.

### 5.3.4 Microscale equilibrium problem

Taking arbitrary variations of  $\delta\tilde{\mathbf{u}}_m$ , but zero variation of  $\delta[\mathbf{u}]_M$  in the variational expression (5.35), the following microscale equilibrium problem is derived in variational form: given the history of the generalised macroscopic strain characterised by  $\{\boldsymbol{\varepsilon}_R^n, [\mathbf{u}]_M^n\}$  and kinematically admissible increments  $\{d\boldsymbol{\varepsilon}_R, d[\mathbf{u}]_M\}$ , find the microscale displacement fluctuation increment field  $d\tilde{\mathbf{u}}_m \in \mathcal{V}_m^L$  such that

$$\int_{\Omega_m} d\boldsymbol{\sigma}_m : \nabla_y^s \delta\tilde{\mathbf{u}}_m d\Omega_m = 0, \forall \delta\tilde{\mathbf{u}}_m \in \mathcal{V}_m^L, t > t_N. \quad (5.38)$$

The solution of the above variational equilibrium problem determines the microscale strain field, and then the microscale stress field via material models. This stress field can be regarded as the reaction to the imposed generalised macroscopic strain increment characterised by  $\{d\boldsymbol{\varepsilon}_R, d[\mathbf{u}]_M\}$ . Moreover, notice that the variational equilibrium problem is subjected to two kinematical boundary conditions (5.29) and (5.30), which are consistent with the two strain homogenisation procedures given in (5.27) and (5.28).

Time continuity when using discrete cohesive zone modelling techniques is an important requirement as discussed in (Papoulia et al., 2003). In a multiscale setting, this issue has been mentioned in (Verhoosel et al., 2010, Nguyen et al., 2011a), where the authors have chosen  $\sigma_I \geq \alpha\sigma_{ult}$ ,  $\alpha \approx 1.0$  as the macroscopic crack initiation criteria to make sure that the solution procedure for the microscale models will not diverge. The symbol  $\sigma_I$  denotes the calculated maximum principal stress and  $\sigma_{ult}$  is the ultimate tensile strength of the microscale model. The artificial parameter  $\alpha$  defines the moment of introducing fractured points and coupled cohesive RVEs. In the present work, the transition from the ClaMM scheme to the CohMM scheme

at the macroscale bifurcation instant  $t_N$  requires time continuity of the macroscopic tractions in the crack  $S$ , expressed as follows

$$\mathbf{t}_M^{\text{ClaMM}} = \mathbf{t}_M^{\text{CohMM}}, \text{ for } t = t_N \quad (5.39)$$

where  $\mathbf{t}_M^{\text{ClaMM}}$  is the traction vector evaluated through the ClaMM formulation

$$\mathbf{t}_M^{\text{ClaMM}} = \frac{1}{|\Omega_m|} \int_{\Omega_m} \boldsymbol{\sigma}_m d\Omega_m \cdot \mathbf{n}_M, \quad (5.40)$$

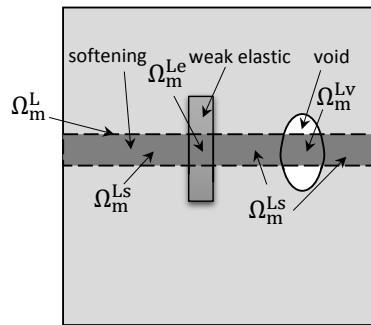
and  $\mathbf{t}_M^{\text{CohMM}}$  is the traction vector evaluated through the CohMM formulation

$$\mathbf{t}_M^{\text{CohMM}} = \frac{1}{|\Omega_m^L|} \int_{\Omega_m^L} \boldsymbol{\sigma}_m \cdot \mathbf{v}_m^L d\Omega_m^L. \quad (5.41)$$

This time-continuity requirement calls for an elaborate treatment of the detection of the strain localisation subdomain  $\Omega_m^L$  as mentioned in (Sánchez et al., 2013, Toro et al., 2014), which will be discussed in the following section.

### 5.3.5 Detection of the localisation subdomain $\Omega_m^L$

Once macroscopic bifurcation is detected, the localisation subdomain  $\Omega_m^L$  and its boundary  $\Gamma_m^L$  need to be identified in order to prescribe the NSBC and perform the traction homogenisation for the newly inserted macroscopic cohesive crack. A sensitivity analysis is performed for this purpose as in (Sánchez et al., 2013, Toro et al., 2014). This detection procedure starts with the prescription of an infinitesimal



strain localisation region:

$$\Omega_m^L = \Omega_m^{Ls} \cup \Omega_m^{Le} \cup \Omega_m^{Lv}$$

**Figure 5.4** Definition of strain localisation region  $\Omega_m^L$  for a complex microstructure. It includes softening material  $\Omega_m^{Ls}$  and traverses a weak elastic inclusion  $\Omega_m^{Le}$  and a void inclusion  $\Omega_m^{Lv}$ .

uniform macroscopic strain increment  $\Delta\gamma_M \otimes^s \mathbf{n}_M$  to the entire RVE domain, where  $\gamma$  is the initial direction of the macroscopic crack. Then, the strain field  $d\epsilon_m$  is computed based on the solution from the variational equilibrium problem (5.14). The criterion for selection of such a domain is based on the projection of  $d\epsilon_m(\mathbf{y})$  at a point  $\mathbf{y}$  of interest in the direction of  $\Delta\gamma_M \otimes^s \mathbf{n}_M$

$$\mathbf{y} \in \Omega_m^L, \text{ iff } d\epsilon_m(\mathbf{y}) : (\Delta\gamma_M \otimes^s \mathbf{n}_M) > 0 \quad \text{when } t = t_N, \quad (5.42)$$

where  $d\epsilon_m(\mathbf{y})$  is the microscale strain fluctuation increment defined in Eq. (5.4). Note that this detection method is totally different from the damage loading criterion mentioned in (Nguyen et al., 2010). It is based on a pure kinematical criterion and does not consider any specific constitutive response of points in  $\Omega_m^L$ . This has the benefit of flexible identification of the strain localisation subdomain  $\Omega_m^L$  for a range of distinctive material configurations of the RVE, as illustrated in Figure 5.4. In this figure, three types of material points are distinguished to describe the composition of the strain localisation band as discussed in (Sánchez et al., 2013). The softening material points are signified by superindex “s”, weak elastic material points by superindex “e” and void interior points by superindex “v”. Note that in the numerical implementation, voids must be considered as an extremely soft elastic material, with Young’s modulus approaching zero. The strain localisation domain  $\Omega_m^L$ , indicated by the shaded dark gray area in Figure 5.4, is just a union of those points that fulfil the criterion (5.42), wherever the point is located. Mathematically,  $\Omega_m^L$  can be expressed as  $\Omega_m^L = \Omega_m^{Ls} \cup \Omega_m^{Le} \cup \Omega_m^{Lv}$ .

## 5.4 Computational implementation

The computational treatment of the multiscale failure model based on the FOMVF resembles that in Chapter 4, except that the implementation details for the macro-to-micro transition and the homogenisation scheme in the CohMM model are different. At the start of analysis, Gauss points (GP) in the elements located within the multiscale coupling region are coupled to bulk RVEs, which may exhibit a different geometry or material composition. The ClaMM formulation is adopted for the bulk RVE models. After solving the bulk RVE models with  $\epsilon_M$  prescribed through a selected type of boundary conditions, the Eq. (5.13) or other equivalent forms are adopted to compute the homogenised stress tensor.

At the end of each converged time step, the bifurcation condition (5.3) needs to

be checked at any coupled stable bulk GP. To this end, at a bulk GP of interest, the homogenised tangent stiffness tensor is first computed using the method in 5.2.6, then a sweep algorithm is performed over a range of angles  $[0, \Delta\theta, \pi)$ , with  $\Delta\theta$  as an angle increment. The two angles that verify the bifurcation condition (5.3) determine the unit vectors  $\mathbf{n}_M$  and  $\gamma_M$ , and simultaneously signify the bifurcation occurrence. Once the bifurcation is detected at a bulk GP, a new crack initiates with the normal direction  $\mathbf{n}_M$  through the GP if there is no existing crack nearby; otherwise the nearby crack extends from the current tip a predefined length in the direction  $\mathbf{n}_M$ . The insertion of a new crack segment is achieved by employing the XFEM in order to allow the crack to travel through the element interiors. The transition from the bulk RVE model to the cohesive RVE model requires the detection of the localisation subdomain  $\Omega_m^L$ , provided  $\mathbf{n}_M$  and  $\gamma_M$ , by the method discussed in 5.3.5. This facilitates the enforcement of the NSBC on the boundary of the strain localisation subdomain  $\Omega_m^L$  in the CohMM. A SBC is applied on the external boundary of the cohesive RVE. The crack behaviour is simulated with a homogenised traction  $t_M$  versus separation  $[[\mathbf{u}]]_M$  law computed from the RVE model. After solving the BVP of a cohesive RVE, the cohesive traction homogenisation formula displayed in Eq. (5.36) is used to compute the homogenised cohesive traction vector. The formula in (5.37) is used to compute the homogenised cohesive tangent stiffness.

In the XFEM, a number of bulk GPs in the fractured element are necessary to accurately integrate bulk relevant elemental integrals present in the weak form. In order to save computational cost, such bulk GPs are not coupled to any RVEs; instead, they are assumed to behave linear elastic with the effective material constants computed after unloading the localised cohesive RVE in the same element upon bifurcation.

## 5.5 Numerical verification

In this section, emphasis is given to the numerical assessment of the present multi-scale failure model. Firstly, a series of fine-scale numerical tests for examining the validity and accuracy of the CohMM is performed. These tests include homogeneous strain localisation band situations in 5.5.1 and inhomogeneous strain localisation band situations in 5.5.2, and a loading-unloading-reloading scheme in 5.5.3. The primary aim is to demonstrate the objectivity of the homogenised constitutive response especially in the post-critical regime with respect to the RVE size. Secondly, a fully coupled two-scale failure simulation for a uniaxial tensile specimen is presented in 5.5.4.

## Preliminary

Except for the fully coupled two-scale failure analyses, the incremental generalised macroscopic strains  $\{d\boldsymbol{\varepsilon}_R, \mathcal{I}_y^L(d[\mathbf{u}]_M)\}$  inserted into the RVE are parameterised as follows

$$d\boldsymbol{\varepsilon}_R = df_1(t)(\boldsymbol{\Lambda} \otimes^s \boldsymbol{\eta}) , \quad \boldsymbol{\Lambda} = [\cos(\Lambda); \sin(\Lambda)] , \quad (5.43)$$

$$\boldsymbol{\eta} = [\cos(\eta); \sin(\eta)] ,$$

$$\mathcal{I}_y^L(d[\mathbf{u}]_M) = \phi_m^L(\mathbf{y}) \frac{d[\mathbf{u}]_M \otimes^s \mathbf{n}_M}{l_M} \quad (5.44)$$

$$d[\mathbf{u}]_M = df_2(t)\boldsymbol{\beta} , \quad \boldsymbol{\beta} = [\cos(\beta); \sin(\beta)] ,$$

where  $\Lambda, \eta, \beta$  are arbitrary angles to be defined in advance in each testing example. The coefficients  $df_1(t)$  and  $df_2(t)$  define the magnitudes of the macroscopic regular strain increment and macroscopic jump increment, respectively. The vector  $\mathbf{n}_M$  is the unit vector normal to the macroscopic cohesive crack, which can be determined by taking one of eigenvectors of the acoustic tensor at the bifurcation time or taken as  $\mathbf{n}_M = [-\sin(\theta); \cos(\theta)]$  with the angle  $\theta$  between the middle line of the predefined localisation band on the RVE and the horizontal direction.  $\phi_m^L(\mathbf{y})$  is the collocation function specified in Eq. (5.24).

A scalar isotropic elastic damage model is employed in all the simulations for modelling the failure mechanism in the RVE model. The material constants of interest are a Young's modulus  $E_m$ , Poisson's ratio  $\nu_m$ , uniaxial tensile strength  $\sigma_{mf}$ , and fracture energy  $G_m$ . Either linear or exponential softening evolution law is used. Conventional implicit schemes are used for integration of such damage models. The softening modulus is regularised based on the concept of smeared crack approach according to the fracture energy and the element characteristic length to overcome the issue of inherent mesh dependence.

### 5.5.1 RVEs with homogeneous strain localisation bands

The first case study is focused on RVEs which have pre-induced homogeneous strain localisation bands embedded in them. A single macroscopic material point is taken into account. The geometries of RVEs of different sizes are displayed in Figure 5.5. Three RVE configurations are considered, identified as  $RVE_1$ ,  $RVE_2$  and  $RVE_3$ .

A set of material properties for each constituent is displayed in Table 5.1. The identifiers  $M_1$  and  $M_2$  are introduced to represent the bulk material and the damageable

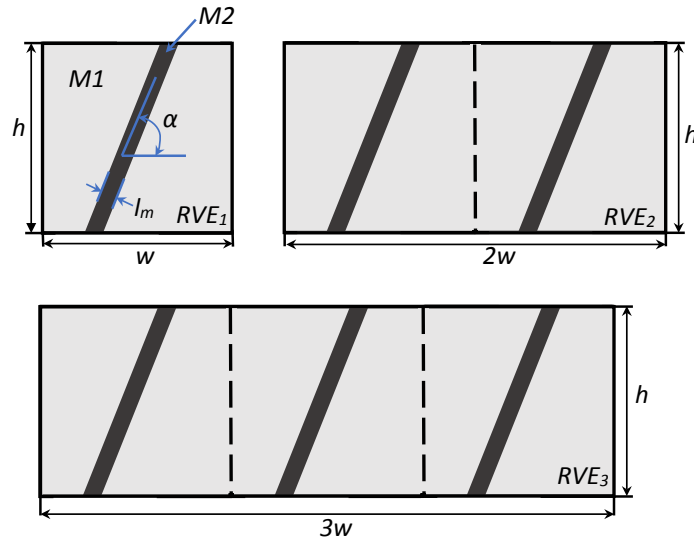


**Figure 5.5** Three RVE configurations with different sizes and different numbers of homogeneous damageable localisation bands. Each localisation band of thickness  $l_m$  forms an angle  $\alpha$  with the horizontal line.

material in the localisation band, respectively. The bulk material  $M_1$  is modelled with a linear elastic law whereas the material  $M_2$  is modelled with the isotropic elastic damage model with a linear or exponential strain softening branch. Each localisation band is homogeneous which means there is no any obstacle or void inside the localisation band. The bandwidth  $l_m$  is chosen in advance. However, it should be

**Table 5.1** Material parameters of two phases of the heterogeneous material used in Section 5.5.1.

Material	$E_m$ [MPa]	$\nu_m$	$\sigma_{mf}$ [MPa]	$G_m$ [MPa·mm]
$M_1$	$2 \times 10^4$	0.2	—	—
$M_2$	$2 \times 10^3$	0.2	25	0.4

noted that this parameter should be calculated according to the evaluation of the strain localisation subdomain  $\Omega_m^L$  in a fully coupled two-scale analysis. In numerical tests of this section,  $l_m$  is set to  $0.05w$  and  $w = h = 1$  mm. The plane stress condition is assumed.

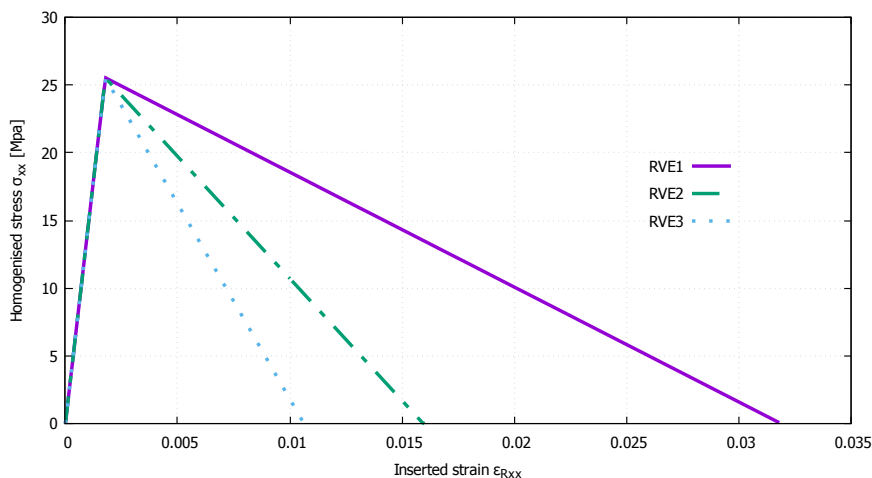
### A vertical localisation band

We first consider a vertical localisation band corresponding to  $\alpha = 90^\circ$ . Two loading conditions are studied: laterally constrained uniaxial tension in Case 1 and pure shear in Case 2.

#### Case 1: laterally constrained uniaxial tension

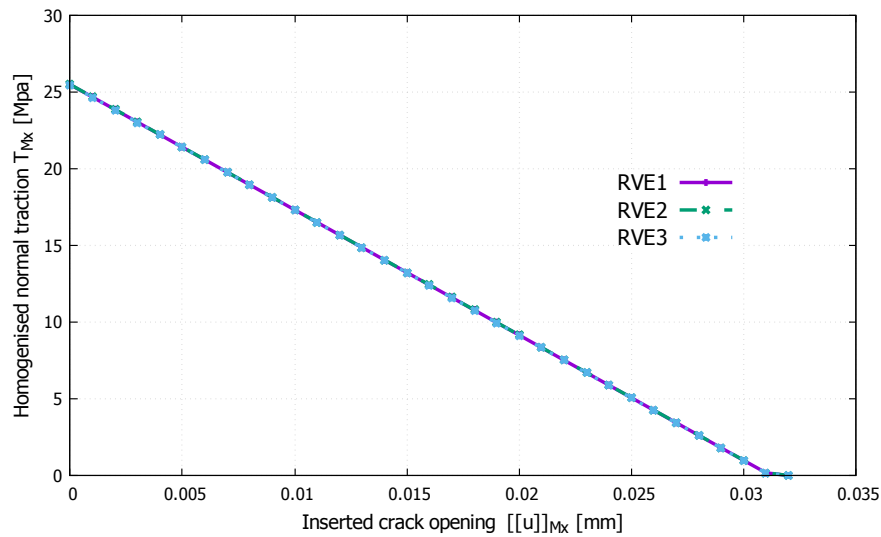
The first loading condition is laterally constrained uniaxial tension, defined by  $\Lambda = \eta = 0^\circ$ . Figure 5.6 plots the homogenised responses in terms of the stress-strain relationship ( $\sigma_{xx}$  vs.  $\varepsilon_{Rxx}$ ) that are obtained with the ClaMM approach. It is obvious that from this figure, during the pre-peak regime, the macroscopic homogenised responses are identical for the three RVE sizes under consideration. However, with the ClaMM approach, a considerable difference in the post-peak mechanical response is observed after the highest point is passed, as shown by descending branches. Also, as can be seen in Figure 5.6, with the RVE size increased, the homogenised response becomes more brittle, leading to a lower predicted fracture energy.

Figure 5.7 plots the homogenised cohesive responses ( $T_{Mx}$  vs.  $[[u]]_{Mx}$ ) obtained with



**Figure 5.6** Homogenised stress-strain curves for three different RVE sizes: the ClaMM is adopted during the whole simulation.

the CohMM approach after the macroscopic bifurcation is detected, that is, when  $t > t_N$ . Note that to make the solution procedure more stable, one of bands in the  $RVE_2$  and  $RVE_3$  needs to be slightly weakened in the thickness or tensile strength, compared to others. From the Figure 5.7, it is evident that the homogenised traction-separation curves fully coincide with each other. The estimated fracture energy can be obtained by integrating the area of the traction-separation curve. The calculated



**Figure 5.7** Homogenised cohesive response ( $T_x$  vs.  $[[u]_{Mx}$ ) resulted from the CohMM scheme adopted after the strain localisation is detected on the RVE: a linear softening law is taken.

fracture energy value is  $0.4 \text{ MPa}\cdot\text{mm}$ , which matches well with the fracture energy  $0.4 \text{ MPa}\cdot\text{mm}$  of the damageable material  $M_2$  chosen in the band. The above two observations verifies the effectiveness of employing the CohMM scheme after strain localisation to overcome the shortcomings of the first-order ClaMM.

The deformed RVEs corresponding to the fluctuation field at the end of analyses are given in Figure 5.8.

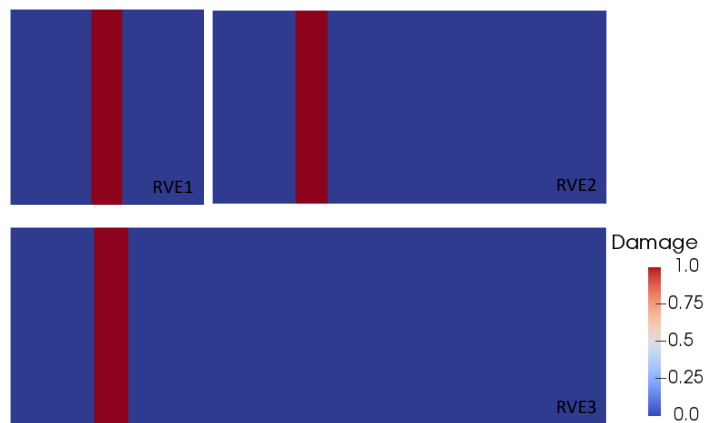


**Figure 5.8** The deformed RVEs with a vertical softening band: the red colour identifies the location of the damaging zone modelled with the smeared crack approach. Amplification factor is set to 200.

**Case 2: pure shear**

We next examine a pure shear deformation mode. Before macroscopic bifurcation, the generalised macroscale strain, inserted into the RVE, is characterised by  $\Lambda = 90^\circ$  and  $\eta = 0^\circ$ . After macroscopic bifurcation, the loading history is fixed for the material  $M_1$ , but a continuous loading with  $df_2(t) > 0$  is enforced to the domain occupied by the material  $M_2$ . Figure 5.9 shows the homogenised cohesive response ( $T_{My}$  vs.  $[[u]]_{My}$ ) obtained with the CohMM approach. The analysis reveals that a physically objective solution is computed for three RVE sizes undergoing pure shear. Due to the selected equivalent strain definition, the calculated fracture energy from the area under each curve, is 0.8 MPa·mm, two times the fracture energy of the material  $M_2$ .

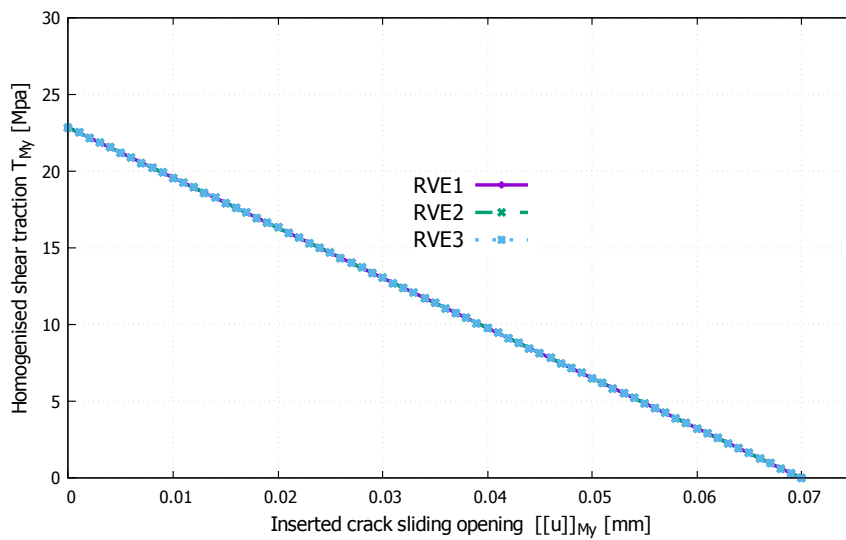


**Figure 5.9** Homogenised cohesive response ( $T_{My}$  vs.  $[[u]]_{My}$ ) resulted from the CohMM scheme adopted after the strain localisation is detected on the RVE: a linear softening law is taken.

**An inclined localisation band**

An inclined localisation band with  $\alpha = 60^\circ$  is chosen here. Before macroscopic bifurcation, the generalised macroscale strain inserted into the RVE is characterised by  $\Lambda = 150^\circ$  and  $\eta = 150^\circ$ . After bifurcation, we turn to using the CohMM scheme:  $d\epsilon_R$  is fixed, and we set  $df_2(t) = 5 \times 10^{-4}$  and  $\beta = 150^\circ$ . The normal direction  $\mathbf{n}_M$  will be derived from the localisation analysis based on the acoustic tensor criterion. This set-up gives a Mode-I fracture which has separations normal to the crack plane. The expected fracture energy should be 0.4 MPa·mm, namely, the fracture energy of the

material  $M_2$ .

For the material  $M_2$  with linear softening, Figure 5.10 displays the homogenised traction vector versus the inserted crack opening in the global coordinate system. The mechanical responses match each other well, demonstrating that the CohMM can overcome the issue of the RVE size dependency. The (effective) fracture energy is the addition of the areas under curves  $T_{Mx} - \llbracket u \rrbracket_{Mx}$  and  $T_{My} - \llbracket u \rrbracket_{My}$ , which equals to 0.4 MPa·mm. This value agrees with the fracture energy for the material  $M_2$ . In addition, the predicted localisation angle  $\theta$  is  $150^\circ$ .

Figure 5.11 displays the homogenised traction vector versus the inserted crack

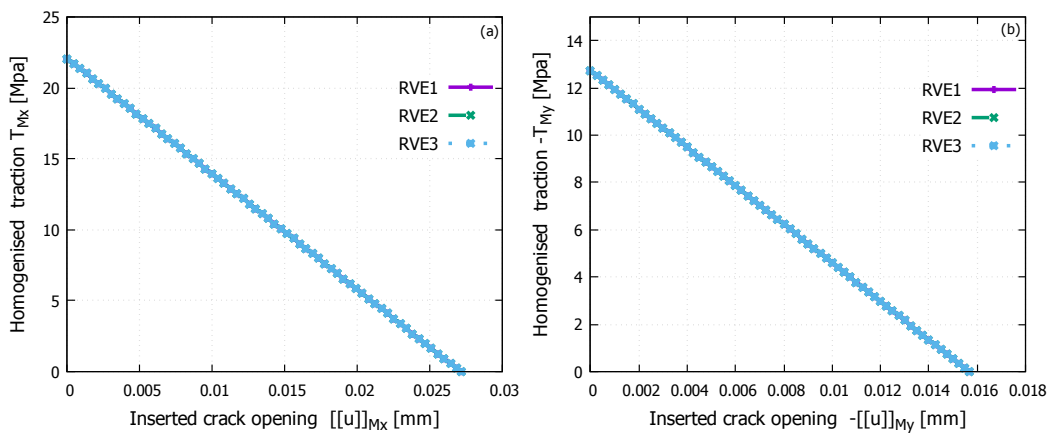


**Figure 5.10** Homogenised cohesive response using the CohMM after the strain localisation: (a)  $T_{Mx}$  vs.  $\llbracket u \rrbracket_{Mx}$  and (b)  $-T_{My}$  vs.  $-\llbracket u \rrbracket_{My}$ . A linear softening damage law is adopted. (Note that a negative sign is added before the  $y$ -components to ease the display. )

opening in the global coordinate system for the material  $M_2$  with strain softening of exponential form.

### 5.5.2 RVEs with inhomogeneous strain localisation bands

In reality, the strain localisation band is likely to contain voids or hard inclusions, instead of being a homogeneous material as in the Section 5.5.1. These voids or inclusions never exhibit any softening behaviour and do not contribute to energy dissipation. Therefore, in these situations, it is inappropriate to identify the region  $\Omega_m^L$  by checking the points which still undergo damage loading when macroscale bifurcation is detected. To verify identification procedure based on the kinematical criterion detailed in 5.3.5, two numerical tests are designated, whose RVEs are shown in Figure 5.12. The material parameters are tabulated in Table 5.2.

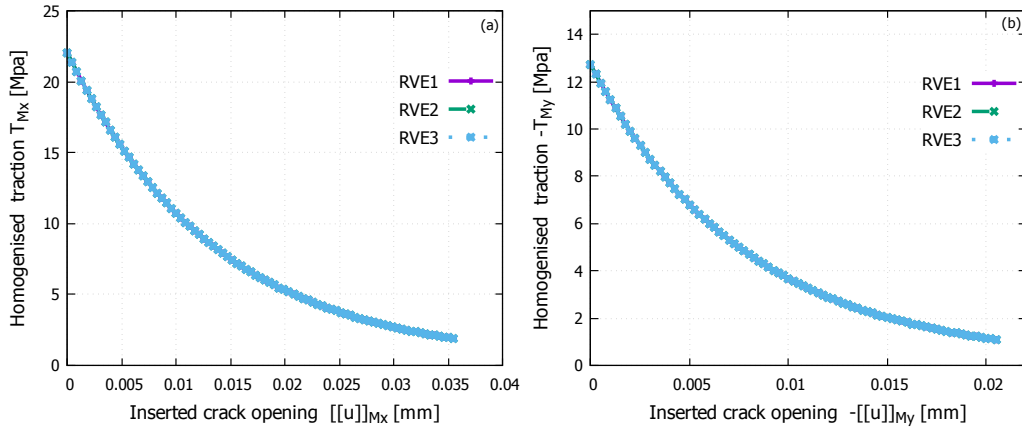


**Figure 5.11** Homogenised cohesive response using the CohMM after the strain localisation: (a)  $T_{Mx}$  vs.  $[[u]]_{Mx}$  and (b)  $-T_{My}$  vs.  $-[[u]]_{My}$ . An exponential softening damage law is adopted. (Note that a negative sign is added before the  $y$ -components to ease the display. )

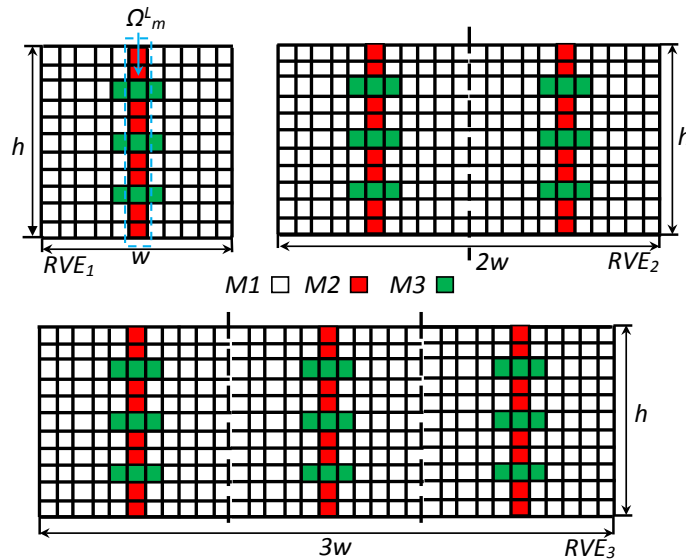


**Figure 5.12** Three RVE configurations of different sizes and their material composition: each RVE domain is meshed into quadrilateral elements with lengths  $1/11w$  and  $1/11h$ ; material model of  $M_1$  is linear elastic, material model of  $M_2$  is isotropic elastic damage and material  $M_3$  represents void or hard inclusion.

### Case a: localisation band with hard elastic inclusions

In this case, the green region in Figure 5.12 is composed of linear elastic material  $M_3$ . The expected localisation domain, as illustrated in Figure 5.12,  $\Omega_m^L$ , consists of the red region of  $M_2$  and a portion of the green region of  $M_3$ . The results in terms of homogenised cohesive response are given in Figure 5.13. It is observed that

**Table 5.2** Material parameters of three phases of the heterogeneous material used in Section 5.5.2.

Material	$E_m$ [MPa]	$\nu_m$	$\sigma_{m,f}$ [MPa]	$G_m$ [MPa·mm]
$M_1$	$2 \times 10^4$	0.2	–	–
$M_2$	$2 \times 10^3$	0.2	25	0.4
$M_3$ (Case a)	$1 \times 10^2$	0.2	–	–
$M_3$ (Case b)	$1 \times 10^{-3}$	0.2	–	–

the response is RVE size independent when using the CohMM after macroscale bifurcation. Due to the composition of the microstructure and material properties of constituents, there is a transition point  $T$  from energy dissipation states to elastic states hereafter, see Figure 5.13. The homogenised cohesive law is made of two adjoining branches, a linear softening (descending) and a linear elastic (ascending) one. Also, there is a strain hardening portion (not drawn in Figure 5.13) in the pre-peak regime, characterised by low levels of damage of material  $M_2$ . The macroscopic bifurcation is attained until enough damage is accumulated; then the CohMM scheme is used in the post-peak regime to guarantee a size independent cohesive response.

### Case b: localisation band with voids

In this case, the green region in Figure 5.12 is void ( $M_3$ ) modelled with vanishing Young's modulus. The expected localisation domain, as illustrated in Figure 5.12,  $\Omega_m^L$ , consists of the red region of  $M_2$  and a portion of the green region of  $M_3$ . The results in terms of homogenised cohesive response are given in Figure 5.14, with results from homogeneous localisation bands shown for reference. It is evident that the response is RVE size independent when using the CohMM after macroscale bifurcation. More importantly, when compared with the reference solution, the response is rather brittle in terms of the peak traction and fracture energy, which is the area under the curve. This is because the strain localisation domain  $\Omega_m^L$ , identified with the kinematical criterion, includes void sub-domains, leading to a softer response.

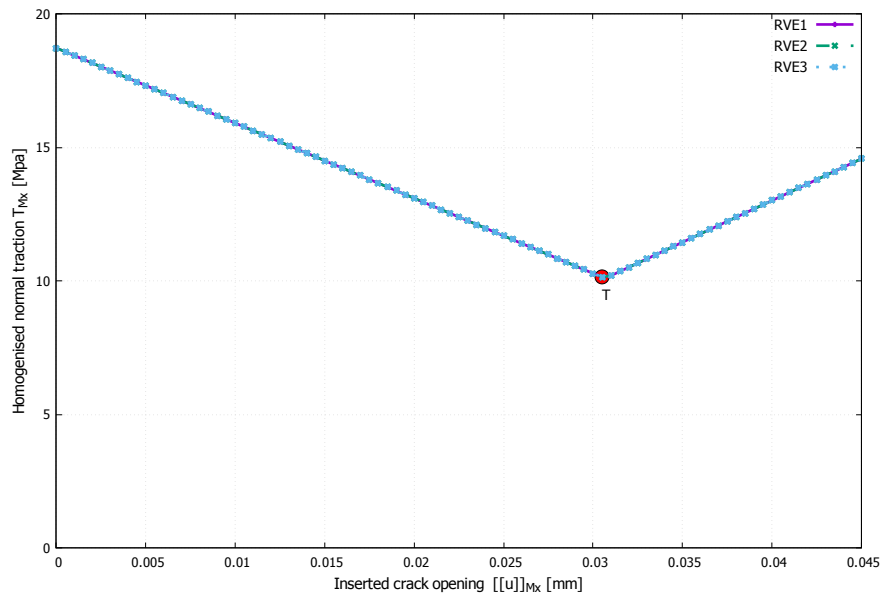


**Figure 5.13** Homogenised cohesive responses ( $T_x$  vs.  $[[u]]_{Mx}$ ) of RVEs with inhomogeneous localisation bands in Case a, resulted from the CohMM scheme. The red shaded circle (labelled  $T$ ) marks the transition from energy dissipation states to elastic states hereafter.

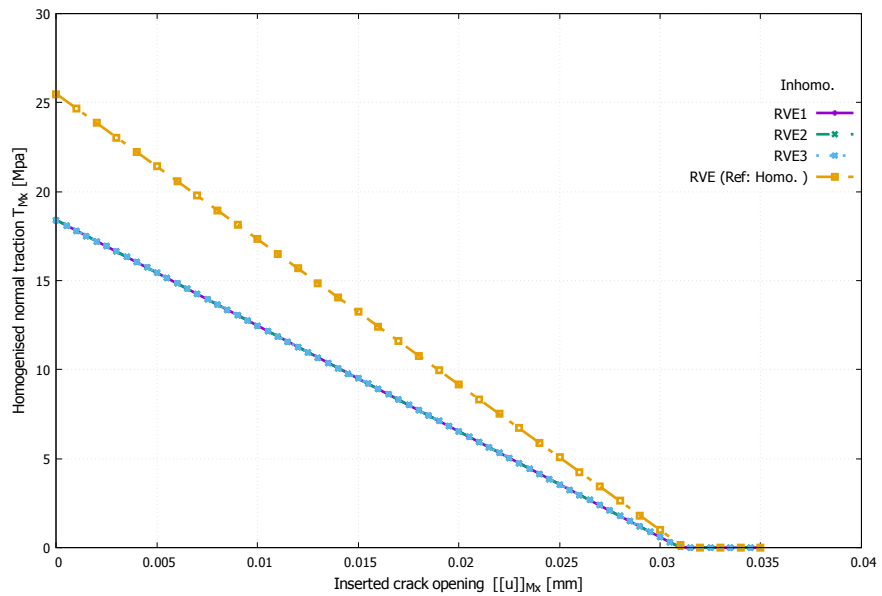


**Figure 5.14** Homogenised cohesive responses ( $T_x$  vs.  $[[u]]_{Mx}$ ) of RVEs with inhomogeneous localisation bands in Case b, resulted from the CohMM scheme. The solution from RVE with a homogeneous band is selected as reference.

### 5.5.3 RVEs subjected to loading/unloading

In this study, the behaviour of RVEs experiencing a process of “loading, unloading and reloading” is studied. A proportional unloading and reloading process is specified beforehand.

To demonstrate the unloading process is size dependent, the RVE configuration

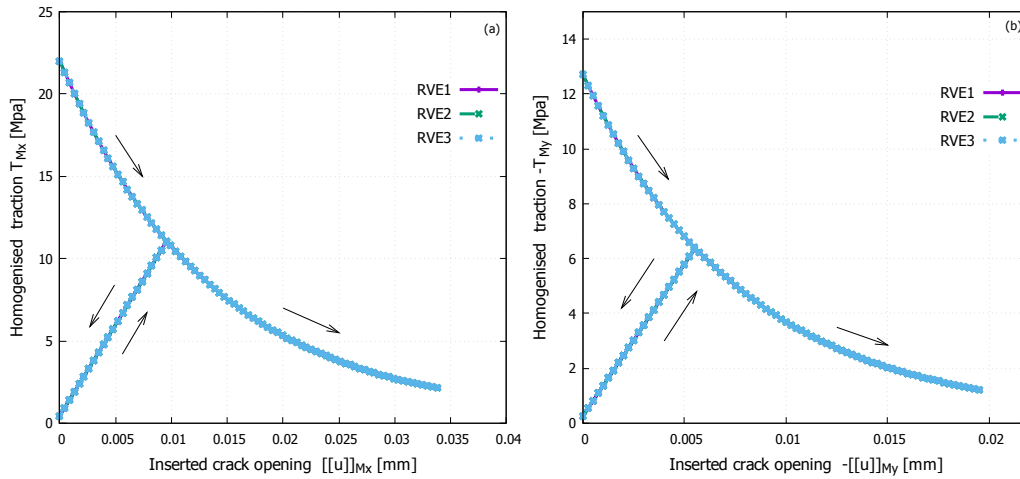


**Figure 5.15** An unloading and reloading process is inserted to the equilibrium path. Homogenised cohesive response using the CohMM after the strain localisation: (a)  $T_{Mx}$  vs.  $[[u]]_{Mx}$  and (b)  $-T_{My}$  vs.  $-[[u]]_{My}$ .

in Section 5.5.1 is considered. Three RVEs with increasing size are used, labeled as  $RVE_1$ ,  $RVE_2$  and  $RVE_3$ . RVEs comprise inclined bands with the material  $M_2$ , equipped with exponential strain softening induced by damage. Plane stress condition is assumed.

At a certain moment within the post-peak regime, the RVEs are unloaded by letting  $df_2 < 0$ . Also, the previously accumulated macroscale regular strain component  $\varepsilon_R$  is removed to simulate a sudden regular unloading mechanism at the macroscale. The homogenised cohesive responses, in terms of cohesive traction and crack opening components in the global Cartesian coordinate frame, obtained with the CohMM are illustrated in Figure 5.15. Unloading branches are featured with reduced elastic moduli, caused from the damage occurring in the localisation band. Note that RVEs do not perfectly unload to the origin (0, 0) in those curves, due to the existence of remaining deformations of quite small magnitude.

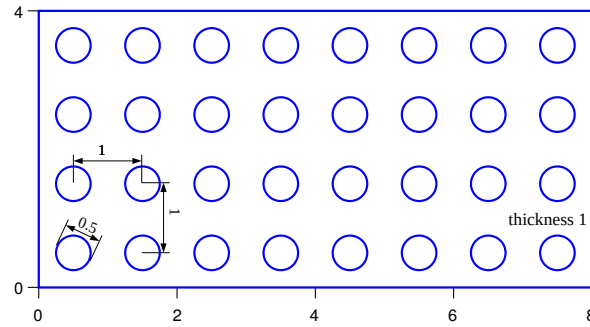


**Figure 5.16** Geometry of the uniaxial tensile test in 5.5.4 with full resolution (unit of length: mm).

### 5.5.4 A fully coupled two-scale failure simulation

This numerical experiment is designed to show the performance of the current multiscale failure approach consisting of two submodels (Clamm and CohMM) through the fully coupled macro-micro failure simulation of a simple tensile test. The specimen with the dimensions of height of 4 mm, length of 8 mm and thickness of 1 mm, illustrated in Figure 5.16 shows a regular arrangement of voids with a diameter of 0.5 mm and a spacing between the neighbouring centres of 1 mm in the microstructure. The left end of the specimen is fixed in the horizontal direction while its right end is stretched with a monotonically increasing horizontal displacement. The material is modelled with the isotropic damage model regularised with the local smeared crack approach. The Young's modulus, Poisson's ratio, tensile strength and the fracture energy are  $2 \times 10^4$  MPa, 0.2, 2 MPa and  $5 \times 10^{-3}$  N/mm, respectively.

For the DNS, the whole domain is meshed with constant strain triangles. For the multiscale simulation, the macroscale domain is meshed with one bilinear quadrilateral element that allows the enrichment for representing the crack. Square RVE models are used and two sizes of 1 mm and 2 mm, corresponding to one void and four voids respectively, are considered to show the RVE size independence. Constant strain triangles are used to mesh each RVE geometry. Note that the voids regions in each RVE are also meshed with elements in order to facilitate the detection of the inhomogeneous strain localisation subdomain  $\Omega_m^L$  as mentioned in 5.3.5. It is conceivable that a macroscale crack will emerge at a certain loading level and afterwards evolve towards a wide-open crack with a progressive degrading behaviour dictated by the evolution of strain localisation in the RVE model.

The load-displacement diagrams for the uniaxial tensile test are displayed in Figure

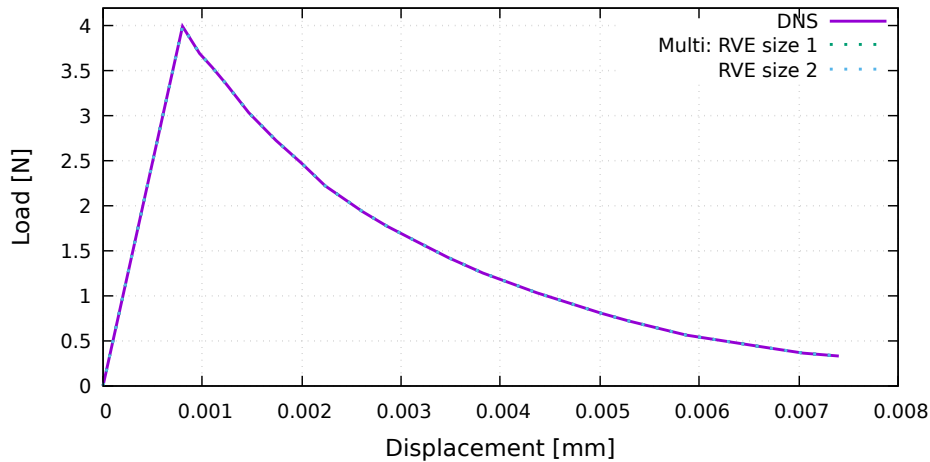


**Figure 5.17** Load-displacement diagrams of the uniaxial tensile test in 5.5.4 with the DNS and multiscale failure simulation.

5.17. As can be seen in this figure, the results from the multiscale simulation are unchanged with varying RVE sizes and match well with the DNS solution. This highlights that the current multiscale failure approach is capable to adequately describe material failure processes across two length scales within an RVE-based multiscale setting.

## 5.6 Summary

In this chapter, a multiscale failure modelling approach based on the Failure-Oriented Multiscale Variational Formulation (FOMVF) proposed in the literature has been presented. Several numerical examples were provided to show its effectiveness in overcoming the issues present in the standard CH based multiscale approach when addressing material softening.

This current multiscale approach is derived from the kinematic admissibility requirement and the principle of multiscale virtual power. The kinematic compatibility requirement between the two scales is met by defining a proper kinematic insertion operator especially for the case of strain localisation. As a result, two types of BCs that need to be enforced upon strain localisation are derived. In the CohMM, the macroscale cohesive traction and the microscale equilibrium are two direct consequences of applying the principle of multiscale virtual power. Although more involved in terms of the numerical implementation, this multiscale approach is superior to that

presented in the preceding chapter in that it strictly enforces kinematic consistency between the macroscopic crack and the microscopic strain localisation band.

# Chapter 6

## Application of Multiscale Modelling to Cortical Bone Fracture

Bone fractures can have significant health, economic and social outcomes. Studies of the interactions between the underlying structure of cortical bone and its mechanical response, particularly failure behaviour, enable us to develop technical strategies for the prevention of fracture risks, especially those related to skeletal fragility caused by aging and disease, and to choose optimal treatment schemes for healing bone fractures. From the perspective of material design, unravelling the fracture toughening mechanisms in cortical bone and the role played by structural hierarchy helps us tailor novel bio-inspired materials with advantageous high stiffness and toughness properties.

As a preliminary study, this chapter aims to apply the multiscale failure modelling technique to numerically investigate fracture mechanisms in cortical bone tissue. This chapter is outlined as follows. The first section 6.1 provides a brief review of the hierarchical nature of bone structure (6.1.1), toughening mechanisms (6.1.2), and fracture toughness assessment methods both experimentally and numerically (6.1.3). In Section 6.2, the multiscale failure study of cortical bone is presented, including the extraction of effective cohesive laws as well as the investigation of the effects of cement lines fracture properties on the effective cohesive laws (6.2.1), and a fully coupled multiscale failure analysis of the three-point bending test of cortical bone (6.2.2) by means of the multiscale failure model introduced in Chapter 4.

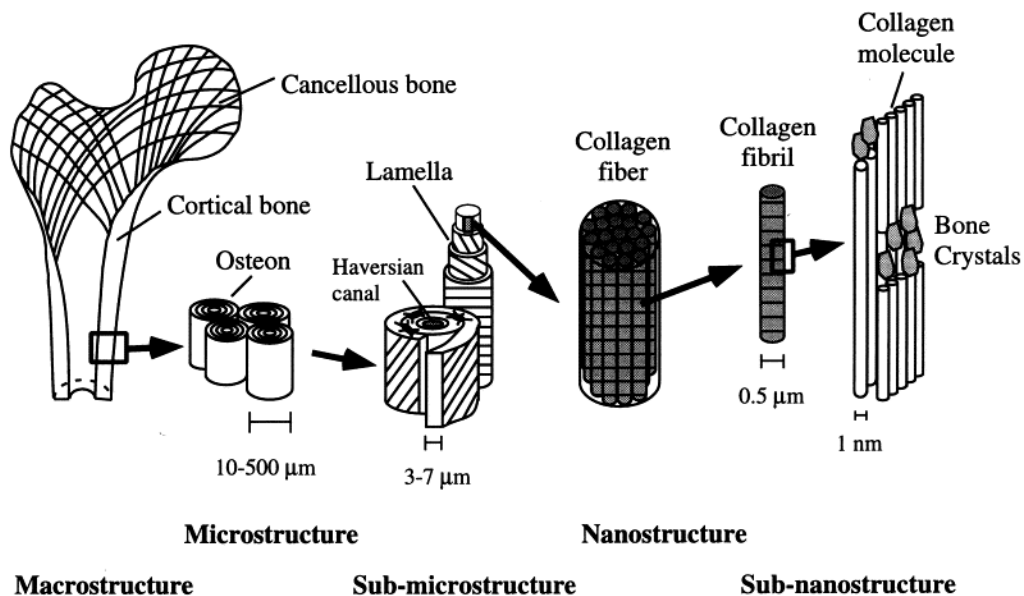


**Figure 6.1** Hierarchical structural organisation of bone. Reprinted from (Rho et al., 1998) with permission granted from Elsevier.

## 6.1 Bone hierarchy and fracture toughness

Before investigating bone fracture or failure by means of experimental testing or numerical simulations, it is first necessary to have some basic knowledge of bone structure and material composition. Then, toughening mechanisms and fracture toughness assessment methods for cortical bone are presented in sequence. These aspects will furnish a foundation for further numerical studies of fracture problems in cortical bone tissue.

### 6.1.1 Architecture of cortical bone tissue

Bones in the skeletal system support the entire human body, carry the daily static or dynamic mechanical loads, protect internal organs and transmit muscle forces between different parts. Bones also serve as reservoirs of minerals like calcium and sodium, and contribute to extracellular mineral ion homeostasis. Furthermore, they produce blood and some fat cells in the marrow.

Bone modelling and remodelling are two bone-related dynamic physiological processes (US Department of Health and Human Services, 2004). Bone modelling occurs during childhood and adolescence and contributes to bone growth and re-

forming. Bone remodelling involves the removal and replacement of old or damaged bone. During bone remodelling, osteoclast cells (responsible for bone resorption) and osteoblast cells (responsible for bone production) work sequentially in the same bone remodelling unit.

Bone shows a hierarchical organisation in its structure (Rho et al., 1998, Launey et al., 2010), which results in different mechanical properties at various length scales of observation. The bone characteristic length scales can be roughly categorised into three levels, the structural level with order of magnitude 1 cm, microscopic level ranging from submicrons to hundreds of microns and nanoscopic level around nanometres.

### The structural level

At this scale, the bone structure is distinguishable between the outer cortical (compact) bone tissue that is hard and dense, and the interior cancellous (trabecular) bone that is porous and sponge-like. The cancellous bone is more permeable and is remodelled more often than the cortical bone. In cortical bone, the mechanical properties are influenced greatly by several factors, including the porosity (Haversian canals and lacunae), the mineralisation degree and the osteon fraction in the interstitial matrix.

### The microscopic level

At this scale, cortical bone consists of densely packed secondary osteons that are embedded in an highly mineralised interstitial matrix. Near the surface of the cortical bone, circumferential lamellae are arranged parallel to the surface. The osteons are assembled in concentric lamellar sheets. Haversian (central) canals, located inside the osteons, allow blood vessels and nerves to travel through them and build connection with bone cells through canaliculi that are microscopic canals between the lacunae of ossified bone. The interstitial matrix consists of remnants of old osteons that were partially resorbed during bone remodelling. Between the secondary osteon and interstitial bone are the cement lines which are a key feature in the Haversian system. Secondary osteons have a circular-to-ellipsoidal shape with a  $100 - 300 \mu\text{m}$  diameter in the cross section and are  $1 - 2 \text{ mm}$  long. The cement line is approximately  $1 - 5 \mu\text{m}$  thick.

There are two types of Haversian-system, primary and secondary osteons. Primary

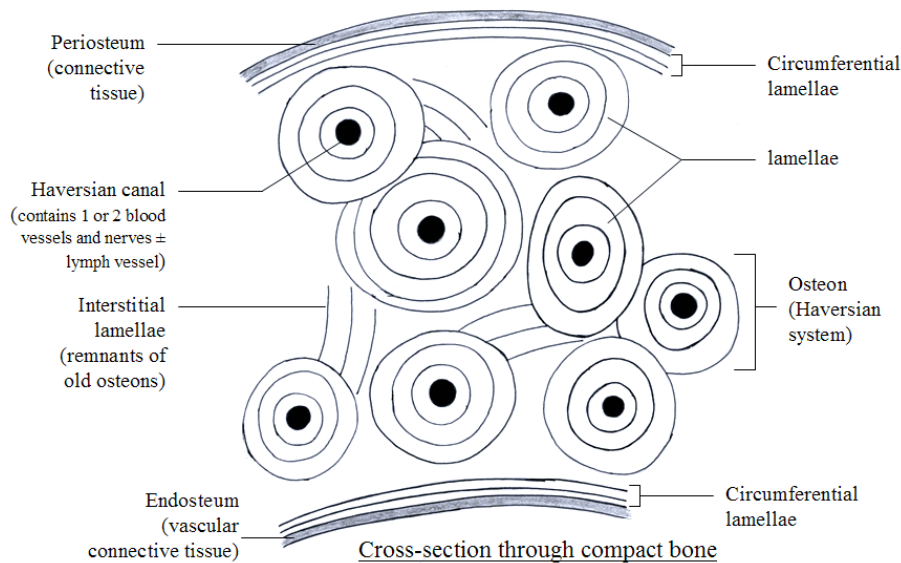


**Figure 6.2** Schematic microstructure of cortical bone (cross-sectional view). The osteons with Haversian canals are distributed within the interstitial matrix, separated by cement lines (not shown). The outer are the circumferential lamellae.

osteons are firstly formed around an existing blood vessel on the surface of bone. Over time, the primary osteons may be replaced by secondary osteons by remodelling process. The primary osteons do not contain as many lamellae as secondary osteons. Also, the vascular channels within primary osteons tend to be smaller than secondary osteons.

## The nanoscopic level

The principal mineral in cortical bone tissue is carbonated hydroxyapatite and its amount is usually thought to determine the stiffness of the material. Approximately 30% of the total mass of bone is composed of organics, of which 90% is collagen fibres and the remaining 10% a mixture of non-collageneous proteins (Wang et al., 2001, Rho et al., 1998). We should note that bone modifies its material composition and structure to accommodate loads by adaptive modelling and remodelling.

### 6.1.2 Multiple toughening mechanisms

Fractures in bone can be identified as either stress or fragility fractures. Stress fractures primarily happen in those individuals who are often exposed to intense

rates and magnitudes of loading, e.g. athletes or military recruits (Daffner and Pavlov, 1992). On the other hand, fragility fractures can happen even with minor trauma and are attributed to deficient repairs to accumulated microdamage or microcracks (Schaffler et al., 1995) and loss of bone mass (Seeman and Delmas, 2006) in the elderly.

Mineralised biomaterials, like bone and dentin, show some natural advantages in exceptional fracture toughness through various toughening mechanisms. There is a strong desire to enhance the performance of synthetic materials by understanding such toughening mechanisms. Cortical bone derives its resistance to fracture primarily from extrinsic mechanisms during crack growth, whereas crack initiation resistance to fracture, which is related to intrinsic damage mechanisms, is relatively low (Vashishth, 2004, Koester et al., 2008). Fracture in cortical bone can be regarded as a mutual competition between intrinsic damage mechanisms, which act ahead of the crack tip to promote cracking, and extrinsic toughening mechanisms, which act primarily in the crack wake to shield the crack from the applied driving force in order to inhibit further cracking (Ritchie et al., 2005, Koester et al., 2008).

Cortical bone exhibits multiple extrinsic mechanisms to resist crack growth (Launey

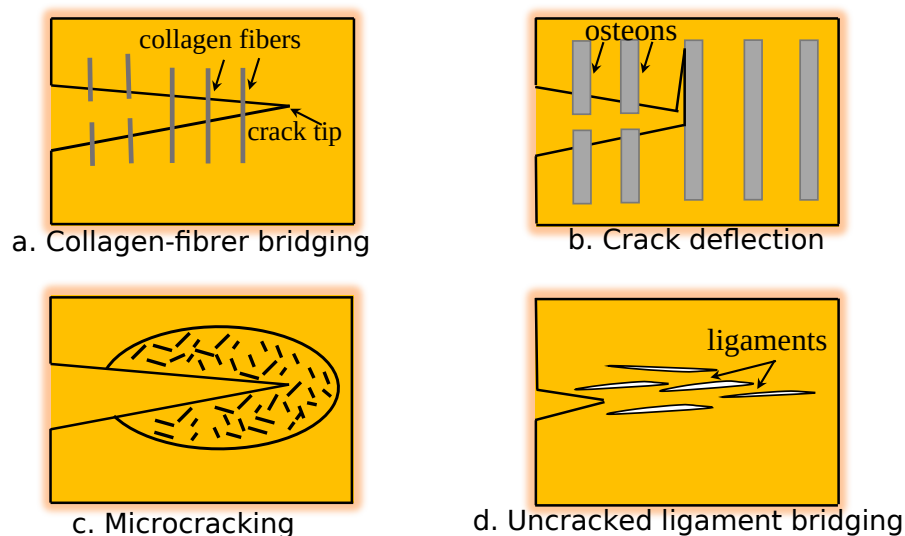


**Figure 6.3** Schematic illustration of extrinsic toughening mechanisms possible in cortical bone. a. Crack bridging by collagen fibres, b. crack deflection by osteons, c. constrained microcracking, and d. uncracked-ligament bridging.

et al., 2010). These include constrained microcracking, crack path deflection and twist, uncracked ligament bridging, osteon pullout, and interface delamination. Figure 6.3 gives a schematic representation of several dominant toughening mechanisms.

Extrinsic mechanisms are created primarily by the interaction of growing cracks with the osteonal structures. [Vashishth et al. \(2000\)](#) reported that microcracking was the primary reason for the occurrence of rising branch in R-curves. [Nalla et al. \(2004, 2005\)](#) attributed toughening for crack propagation in the longitudinal direction mostly to uncracked ligament bridging in the crack wake. Compared with crack propagation in the longitudinal direction, crack propagation in the transverse direction is more clinically relevant ([Behiri and Bonfield, 1989](#)). SEM observation by [An et al. \(2011\)](#) showed that the uncracked ligament bridging was the main toughening mechanism in the longitudinal fracture, while crack deflection and bifurcation were found when cracks propagated in the transverse direction, leading to an ultimate fracture toughness corresponding to stable propagation that was twice the crack initiation toughness.

Aging-related loss of bone quality, corresponding to degradation in fracture strength and toughness, has been suggested as a great contributor to bone fragility. Aging will adversely affect the bone fracture toughness by altering material and structural properties of cortical bone. This is reflected in an increase in the fraction of highly mineralised bone ([Simmons Jr et al., 1991](#)) and the modification of collagen by denaturation ([Wang et al., 2001](#)) or non-enzymatic glycation. Besides, the elderly tends to have increasing size and porosity of Haversian canals, and a higher osteon density ([Zimmermann et al., 2011](#)). [Zioupou and Currey \(1998\)](#) reported that the propensity of older human bone to form linear microcracks over diffuse damage was the major reason in aging-related bone fragility. [Chan et al. \(2009\)](#) showed that young bone was more effective in deflecting cracks into cement lines, but most of cracks in older bone tended to cross osteons. [Budyn et al. \(2008\)](#) investigated the effect of aging on structural and mechanical properties of human cortical bone by employing 3D FEM unit cells.

### 6.1.3 Fracture toughness evaluation

Traditionally, fracture resistance of cortical bone is evaluated by its bone mineral density (BMD) ([Seeman and Delmas, 2006](#)). However, the fracture risk can differ among individuals with the same BMD, indicating that other factors besides BMD need to be considered in clinically evaluating bone fracture risk. Nowadays, an increasing number of studies reveal that microstructural morphology and material composition are decisive factors influencing bone failure or fracture. Similar to other quasi-brittle materials, such as concrete, ceramics, rocks and ice, excessive microdamage ac-

cumulation is a strong signal that the bone structure will be compromised and may even break. In cortical bone, the remodelling process constantly repairs fatigue microdamage to keep the amount of microdamage at a low level. If remodelling is abnormal or deficient due to genetic disorders, aging or disease, there will be an increased risk that the bone suffers from fragility fracture.

Two common damage morphologies, linear microcracks and diffuse damage, can be found in the microstructure of cortical bone. Linear microcracks can be viewed as sharp micron dimension cracks mainly distributed within the bone matrix, whereas the diffuse damage is described as a patch of multiple submicron cracks. Linear microcracks more likely form under compressive loading in the interstitial bone tissue and stop at osteonal boundaries (Boyce et al., 1998). In contrast, diffuse damage forms under tensile loading (Boyce et al., 1998) as submicroscopic cracks in the interstitial bone.

As a mineralised tissue, cortical bone exhibits superior fracture-resistant behaviour, though it is composed of inferior building blocks (mainly collagen molecules and mineral crystals) at the nanoscale. In nature, some other biological materials such as dentin, nacre and diatoms also reveal remarkable defect tolerance (Sen and Buehler, 2011).

### 6.1.3.1 Quantitative fracture toughness measurement

There are several experimental approaches to assess the toughness of cortical bone tissue. This is usually conducted macroscopically by fracture testing and then analysing the data. The fracture specimens (Figure 6.4c) can be prepared by a series of manual machining operations, including cutting, drilling, milling and polishing after transversely sectioning long bones (Figure 6.4a) and removing soft tissues. They are then labelled according to their cortex positions in order to differentiate fracture toughness along different directions, as illustrated in Figure 6.4(b). In some situations, high resolution cameras are attached to a microscope in order to track the crack propagation length and the crack mouth opening displacement.

The oldest and once widely used approach for quantifying bone fracture toughness is the work-of-fracture method (Currey, 1979, Zioupos and Currey, 1998). The fracture toughness value is simply obtained by dividing the area under the load-displacement curve, representing the fracture work, by twice the nominal cracked ligament area. However, this calculation is often specimen-size dependent (size effect). Differences in the energy consumed during the tensile or flexural testing of materials were pointed out by Zioupos (1998).

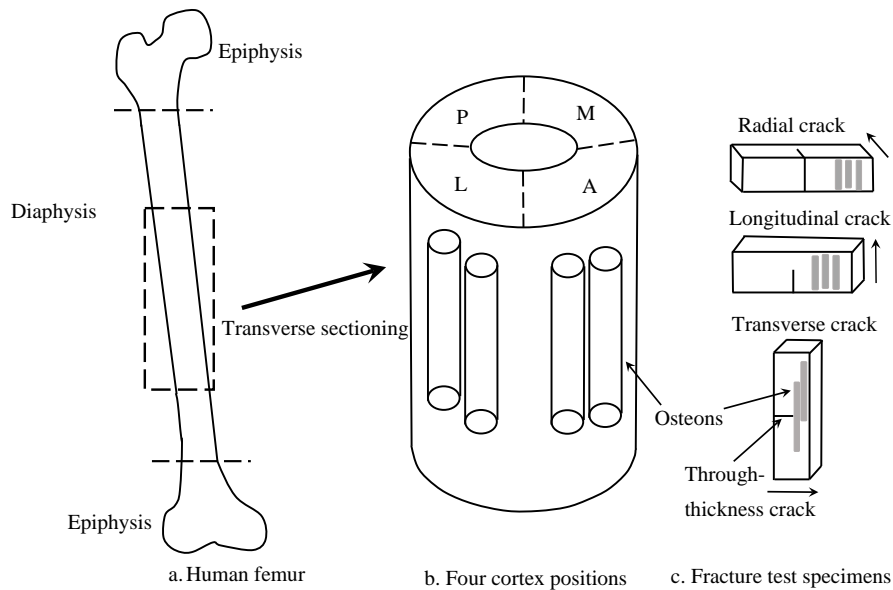


**Figure 6.4** Schematic illustration of: a. a long human femur; b. cortex positions in anatomical terms (letters A, P, M and L stand for anterior, posterior, medial and lateral respectively); c. fracture specimens fabricated for testing radial, longitudinal, transverse fracture toughness. Arrows point towards the anticipated crack propagation direction.

Other approaches are based on linear or nonlinear fracture mechanics theories. The fracture toughness can be measured by critical stress intensity factors ( $K_c$ ), critical fracture energy ( $G_c$ ), and the  $J$  integral (Anderson, 2017). Note that these are fracture mode dependent, but here we ignore the subindex for brevity. The former two concepts are often adopted in the context of fracture of brittle materials and used to give a single-parameter characterisation. They are meaningful only for fracture events where there is no or a rather small fracture process zone (e.g. yield zone for metals); in this situation  $G_c$  is equivalent to the  $J$  integral. However,  $K_c$  and  $G_c$  are not suitable to quantify the magnitude of fracture resistance and they are incapable of representing the multiple fracture toughening mechanisms concentrated in the fracture process zone in cortical bone. This deficiency may be overcome by the introduction of cohesive zone models or the use of crack growth resistance-curves ( $K$  based or  $J$  based R-curves) to take into account the extra energy dissipation contribution to the ultimate fracture toughness of materials. The R-curve reflects the increasing driving force required to advance further a unit crack growth. For cortical bone fracture, a rising portion can be observed in the R-curve. This rising trend reflects extrinsic toughening mechanisms that primarily appear in the wake of the dominant crack and play a remarkable role in toughening cortical bone.

The authors [Wright and Hayes \(1977\)](#), [Behiri and Bonfield \(1989\)](#), [Norman et al. \(1991\)](#) used a single-parameter fracture toughness measure determined from the experimental testing of compact specimens to assess cortical bone fracture toughness. Later on, other researchers noticed that cortical bone principally derives its toughness during the crack growth phase, and the evaluation of fracture toughness in terms of  $K$  based R-curves with crack growth length as the independent variable becomes more appropriate ([Vashishth, 2004](#), [Nalla et al., 2005](#)). Some researchers, such as [Peterlik et al. \(2006\)](#), [Yan et al. \(2007\)](#), [Koester et al. \(2008\)](#), [Fletcher et al. \(2014\)](#), applied elastoplastic fracture mechanics ( $J$  integral) that considers the contribution from plasticity to the fracture toughness, to evaluate the fracture toughness of cortical bone. Cohesive zone models are classical nonlinear fracture models widely chosen for incorporating large-scale fracture processes in quasi-brittle materials. For example, owing to extensive fibre bridging experimentally observed in triaxially braided carbon fibre composites, simulations incorporating a discrete cohesive zone model to characterise the fracture process zone has been undertaken, resulting in well replicated structural responses ([Xie et al., 2006](#)). [Yang et al. \(2006a,b\)](#), [Cox and Yang \(2007\)](#) used such a fracture model to account for toughening and damage behaviour both ahead and behind the crack tip. They demonstrated that utilising cohesive zone models could explain the disagreement in fracture toughness data in the literature measured via LEFM and also provided a consistent nonlinear fracture model that could be well matched with different experimental toughness values for a variety of small crack sizes in bone toughness tests. In other words, the cohesive model is able to capture the specimen size effect on nominal strength and fracture energy in fracture tests in cases where fracture process zone can not be ignored compared to the crack length.

Interestingly, [Willett et al. \(2017\)](#) measured the size of characteristic fracture process zone at maximum load as approximately  $550 \mu m$  for the transverse fracture of bovine cortical bone. Also, using laser scanning confocal microscopy, they observed flames that might be similar to tunnelling observed in other materials during fracture. This fracture process zone size may provide valuable information for the calibration of the numerical fracture models, especially when using cohesive zone models.

In summary, in order to explore bone failure mechanisms experimentally, in the literature there have already existed several alternative fracture toughness notions (parameters), multiple experimental fracture test setup standards and also abundant experimental data at different anatomical cortices for a wide range of bone tissues (e.g. human femura, human tibia, bovine femura, deer antler). At the same time, a

variety of types of equipment (e.g. fluorescence microscope, scanning electron microscope, digital image correlation, backscattered, micro-CT) and image processing software (e.g. ImageJ) have been employed to monitor and analyse the distribution and number of internal microdamage or microcracks.

### 6.1.3.2 FEM simulations for bone fracture toughness

Though experiments on bone are indispensable and constitute a crucial part of researching bone failure, they are not always the best option to conduct parametric studies and predict fracture events in bone. Parametric studies are beneficial when studying the factors that are crucial and responsible for aging-related or disease-related reduction in bone fracture toughness. These factors may involve porosity ratio, osteon size, compositional heterogeneity, collagen denaturation, damage severity, cement line properties etc.. Parametric studies are also effective in eliminating the confounding factors that exist in experimental studies in order to identify the direct influence of an individual factor.

What is also important is the development of robust numerical tools to furnish accurate predictions of fracture risks for groups like the elderly and patients with osteoporosis. This is not an easy objective to achieve due to the hierarchical organisation of bone, the continuous remodelling process, the anisotropic mechanical properties and the substantial variety in bone material composition.

In the existing literature, several numerical experiments have been conducted to reveal the role of osteons and cement lines in the fracture toughness in bone. [Najafi et al. \(2007\)](#) studied the crack propagation path in cortical bone with a two-dimensional micromechanical fibre reinforced composite materials model, under tension and compression, in the framework of FEM. Their results showed bone microstructural heterogeneity greatly influenced fracture parameters and osteons acted as barriers to microcrack growth and high osteonal density could depress crack growth, which seemed to agree with previous experimental measurements by [O'Brien et al. \(2005\)](#). These last authors stated that for a large majority of cracks, osteons acted as barriers to growth, but for a few long cracks (larger than  $300\ \mu\text{m}$ ) that broke through the cement line and split through a Haversian canal, osteons might act as a weakness site promoting crack propagation, likely leading to eventual failure of specimens.

As classical fracture models frequently adopted in computational fracture mechanics, cohesive crack models have been introduced in the study of bone fracture using cohesive or interface elements as described in Chapter 3 ([Ural and Vashishth,](#)

2006, Ural, 2011, Mischinski and Ural, 2013, Ural and Mischinski, 2013). Interface elements have special advantages in dealing with crack initiation, multiple crack propagation and crack branching or intersecting. More importantly, they are easier to implement into an existing FE code, compared to other numerical techniques like XFEM. The justification for the use of cohesive crack models is the existence of a fracture process zone. Ural and her co-workers employed cohesive interface elements in an attempt to find the influence of microscopic factors on bone fracture-resistance performance. Ural and Mischinski (2013) showed that in their simulations the microscopic fracture toughening was most effective when the cement line had a lower strength than the surrounding bone, reducing the tendency to fracture at the macroscale.

The XFEM described in Chapter 3 has also been used to study the crack initiation and propagation in the cortical bone due to its merit in the incorporation of cracks anywhere and allowing propagation without conforming to mesh topologies. Budyn and her collaborators performed a series of studies on fracture strength assessment of cortical bone with XFEM. In their models, cortical bone was considered as a four-phase composite with osteons, interstitial matrix, Haversian canals and cement lines. The osteons were idealised as non-touching circles or ellipses. Budyn and Hoc (2007), Budyn et al. (2008) modelled multiple crack growth with XFEM in human cortical bone under tension in order to investigate the influence of changes in microstructure morphology and mechanical parameters. Using the XFEM, Budyn and Hoc (2010), Jonvaux et al. (2012) investigated the influence of different parameters such as morphology, porosity, aging and osteoporosity on stress and strain fields, failure and fracture of bone. Abdel-Wahab et al. (2012), Li et al. (2014) studied the effect of microstructure and material properties of bone on crack growth employing XFEM implemented within the commercial software ABAQUS.

Most previous XFEM based simulation work studying the crack propagation in cortical bone has been based on the maximum tangential stress (MTS) crack propagation criterion, commonly used and suitable for homogeneous materials. As argued in (Marco et al., 2018), the predicted crack path was determined based on MTS thresholds without detecting the presence of heterogeneities such as the cement lines. Therefore, osteons were crossed most probably due to the use of a propagation criterion that is not suitable for heterogeneous materials. Thus, inspired by interface damage prediction in composites, Marco et al. (2018) proposed a new crack orientation criterion considering the material heterogeneity, which was able to reproduce realistic fracture paths in cortical bone microstructure, as evidenced by Figure 6.5.

The majority of the strength and fracture modelling methods only consider one

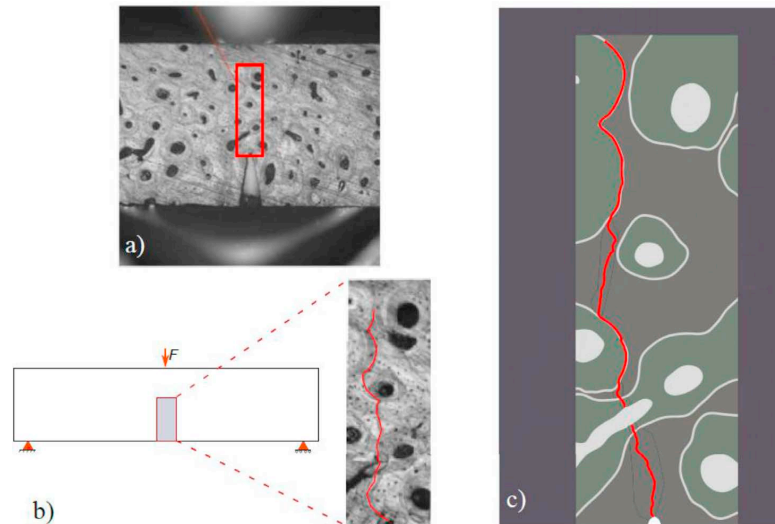


**Figure 6.5** Satisfactory prediction (right) of crack path around osteons without penetration using a new crack orientation criterion, in good agreement with experimental evidence (left) by Budyn et al. (Budyn and Hoc, 2010). Reprinted from (Marco et al., 2018) with permission from Elsevier.

size scale, rather than multiple size scales. There have been few studies based on multiscale modelling methods. In this regard, to explore the hierarchical nature of the cortical and trabecular bone in rats, Oftadeh et al. (2015) used a variety of analytical techniques to characterise the structural and compositional properties of cortical and trabecular bone, as well as to determine the best mathematical model for the prediction of the mechanical properties of the bone tissue. Hamed and Jasiuk (2013) employed a cohesive zone model for the prediction of the effective elastic moduli and strength of lamellar bone at three different scales. Moreover, a multiscale model incorporating the cohesive FEM approach was also utilised to simulate bone fracture both at the microscale and macroscale (Ural and Mischinski, 2013).

## 6.2 Multiscale failure study of cortical bone

The present study focuses on the radial fracture of cortical bone. Quasi-brittle loading and plane strain conditions were assumed. Plasticity was not considered and thus

no permanent deformation occurred. The morphological data and mechanical properties for each microscopic constituent were collected from the literature. A significant number of micromechanics simulation studies have been carried out in the past (Heinrich et al., 2012, Pineda et al., 2013, D'Mello and Waas, 2019, Bhuiyan et al., 2020) to name a few, mostly with an emphasis on the failure development in fibre reinforced composites. A series of questions have been looked at, for example, the influence of random packing on the residual stress build-up during the curing process and on the transverse tensile response; the influence of unit cell size on the details of crack path, overall strength and overall stiffness; and the influence of morphological variability on the transverse elastic and fracture properties. We believe that the modelling techniques, numerical issues and simulation results presented in these works can provide useful insights into failure and fracture simulations of the cortical bone tissue.

### Geometrical description

In the following studies, each RVE was idealised to feature osteons, cement lines, Haversian canals and interstitial bone matrix, as in (Budyn and Hoc, 2007, Budyn et al., 2008). The cement lines act as the interfaces between the osteons and the interstitial matrix. Due to the abundance in available experimental measurements in the literature, the geometric parameters for bovine cortical bone are referenced. According to (Budyn and Hoc, 2007), the distributions of the diameters of the osteons and the Haversian canals each follow a Gaussian distribution. The volumetric fraction of osteons is approximately 60%. The average diameters for the Haversian canals and osteons are  $35 \mu\text{m}$  and  $140 \mu\text{m}$ , respectively. However, based on experimental measurements in (Abdel-Wahab et al., 2012), the average diameters of osteons and Haversian canals are  $99.89 \mu\text{m}$  and  $23.1 \mu\text{m}$ , different from those data of Budyn and Hoc (2007). The thickness of the cement line is measured as  $5 \mu\text{m}$  (Budyn and Hoc, 2007, Abdel-Wahab et al., 2012).

In the current numerical study, the diameter of each osteon was randomly selected in the range  $[100 \mu\text{m} \ 250 \mu\text{m}]$ . The osteons were not allowed to intersect. The diameter of each canal was fixed to  $50 \mu\text{m}$ . The thickness of the cement line was taken as  $5 \mu\text{m}$ . The volume fraction of osteons with canals was specified as 45%. A typical square sample of size  $0.8 \text{ mm}$  is illustrated in Figure 6.6.

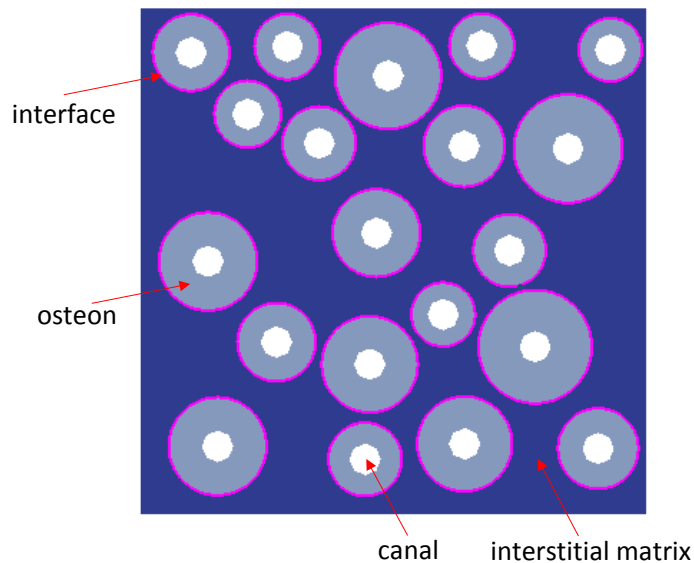


**Figure 6.6** A typical mesoscopic sample for cortical bone tissue.

### Mechanical properties

The Young's modulus for the osteons was  $1.2 \times 10^4$  MPa taken from (Rho et al., 1999). The interstitial matrix was assumed to have a stiffness  $1.44 \times 10^4$  MPa, which is 20% higher than the osteons according to (Li et al., 2014) since that the interstitial matrix is composed of remnants of highly mineralised old osteons. There is no consensus in the literature on whether the stiffness of the cement line should be higher or lower than that of osteons. However, this material constant is not of interest in the current study since interface elements were used to model the failure process. Poisson's ratio was assumed as 0.3 for all the constituents based on (Gustafsson et al., 2019). The fracture properties of osteons were not collected due to the assumption that osteons were not allowed to experience fracture. The critical strength 57.6 MPa of the interstitial matrix was derived by the product of its stiffness and the damage initiation strain  $4 \times 10^{-3}$  by reference to (Budyn and Hoc, 2007). The critical strength (normal or shear) of the cement line was taken as 30 MPa, lower than that of the interstitial matrix. The critical fracture energy was assumed equal for fracture energy and Mode II fracture. The critical fracture energy of the interstitial matrix was taken as 0.2 N/mm (Gustafsson et al., 2019). The critical fracture energy for the cement line was specified as 0.163 N/mm (Giner et al., 2017).

The above material constants are summarised in Table 6.1.

**Table 6.1** Material constants of the mesoscopic constituents in cortical bone.

phase	$E_m$ [MPa]	$\nu_m$	$\sigma_{mf}$ [MPa]	$G_m$ [N/mm]
osteon	$1.2 \times 10^4$	0.3	–	–
matrix	$1.44 \times 10^4$	0.3	57.6	0.2
cement line	–	–	30	0.163

### 6.2.1 Extracted macroscopic cohesive laws

The numerical simulations of micro samples for cortical bone were carried out with intrinsic interface elements approach described in Chapter 3. Zero-thickness interface elements embedded between continuum elements were used to simulate the fracture process in the microstructure. They were only used in the regions of the cement lines and interstitial matrix. An interface damage model with linear softening as in (Turon et al., 2006, Cid Alfaro et al., 2010) was adopted to model the mixed-mode fracture behaviour by means of defining a mode-mixity parameter. To quantify the fracture properties of cortical bone at the macroscale of millimetres, the method presented in (Verhoosel et al., 2010) was employed to extract the homogenised or effective cohesive laws that characterise the traction-separation behaviour for a cohesive crack. The fundamental idea of this method is to separate the nonlinear response from the linear elastic response for an RVE model under strain localisation. It should be noted that this method and the failure zone averaging scheme mentioned in Chapter 4 share a similar idea. We employed the limit point criterion to mark the instant of strain localisation or material instability in the microscale model.

For simplicity we have only focused on the mode I fracture behaviour for cortical bone. For a single mode cohesive law, the most important fracture parameters are cohesive strength and fracture toughness (critical fracture energy). The effective cohesive strength and the effective fracture toughness defined at the macroscale were computed from the extracted effective cohesive law. In the following, these two quantities are denoted as  $\sigma_{eff}$  and  $G_{eff}$  respectively.

#### RVE size determination

As mentioned in Chapter 4, the RVE size should be large enough in order to be statistically representative of the mechanical behaviour of microstructure. This size may need to be larger particularly in cases where cracking and strain localisation

occur. To better capture the interaction between the microcracks and the Haversian microstructure, the minimal numerical sample size  $l_s$  was restricted to 0.3 mm, which indicated at least 3 osteons were included. Four different sizes,  $l_s = 0.3, 0.6, 0.8$  and 1.2 mm, were considered and for each size, five different realisations were simulated. The material constants in Table 6.1 were used. The average continuum element size was 0.01 mm considering the currently available computational power. It is important to realise that when using the cohesive element approach the mesh density will have a significant impact on the predicted crack path and effective fracture properties (Cid Alfaro et al., 2010, Ballard and Whitcomb, 2017). However, this is not the main concern of the current study.

A laterally constrained uniaxial tensile loading was applied to the micro samples. During simulations, it was likely found that the convergence failed using the full Newton-Raphson iterations around the peak strength point. To circumvent this convergence difficulty, once lack of convergence was identified, the use of tangent stiffness was converted to the use of secant stiffness. After attaining convergence (with a large number of iterations), tangent stiffness was reinstated.

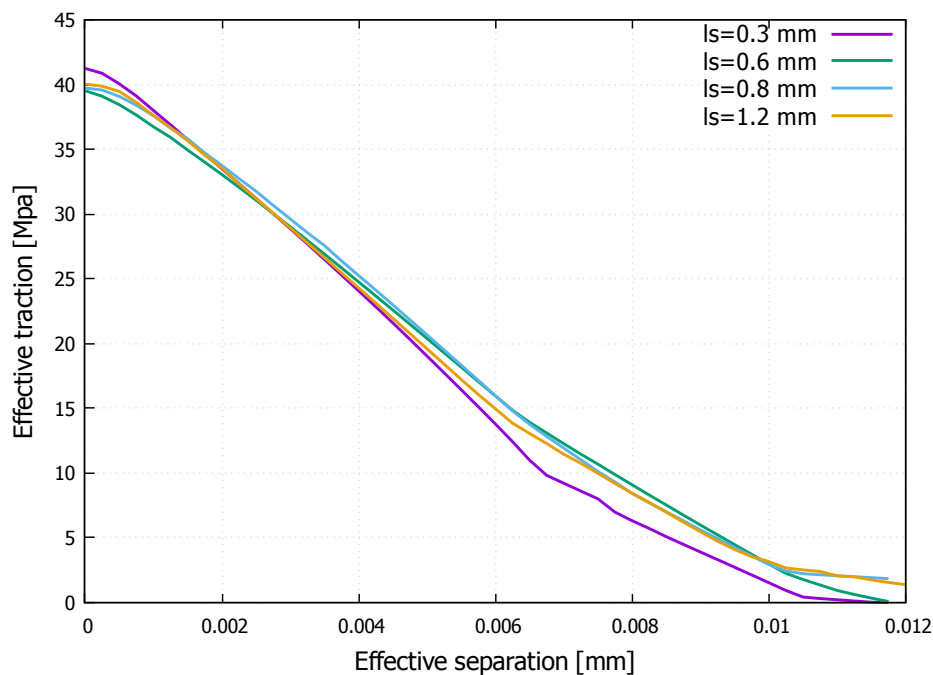


**Figure 6.7** Effective traction-separation laws for different sample sizes of cortical bone, obtained by averaging over five realisations.

The mean extracted cohesive laws after averaging are shown in Figure 6.7 for

different sample sizes. As evidenced from the figure, the sample size 0.3 mm appears to largely deviate from the remaining three mean curves that are almost identical.

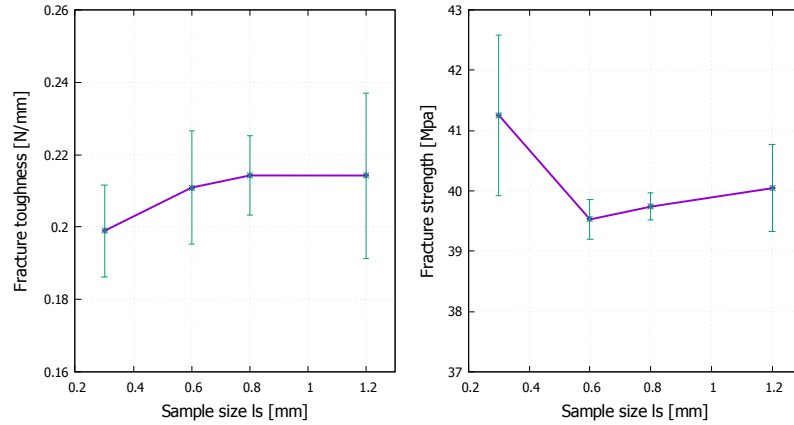


**Figure 6.8** Computed effective fracture properties (Mode I) for cortical bone tissue. The error bars represent the standard deviations.

To further look at the differences, the effective cohesive strength  $\sigma_{eff}$  and the effective fracture toughness  $G_{eff}$  obtained by numerically integrating the area under the cohesive law are shown in Figure 6.8 for each tested sample size. It is concluded from comparing these values that the size 0.3 mm might be slightly small and it is not suitable to be considered as an RVE size employed for extracting effective cohesive laws or adopted in multiscale failure analysis.

For purposes of illustration, the final crack paths for different tested sample sizes at the end of analyses are displayed in Figure 6.9. An almost vertical crack path can be observed for each sample size. This is because an uniaxial tensile loading was applied. It is observed that the interface debonding constitutes a large portion of the final crack path. In Figure 6.9, the local bridging zones located on crack paths are highlighted which explains the long tails of some cohesive law curves (see Figure 6.7).

### Effect of fracture properties of cement line

Cement lines acting as an interface play an important role in failure or fracture in cortical bone. To assess the effect of the fracture properties of cement line, a parametric study was conducted. The size for the numerical micro samples was specified as 0.6 mm which contained about 10 osteons. This size was considered representative of cortical bone microstructure based on the work in the last subsection. The values

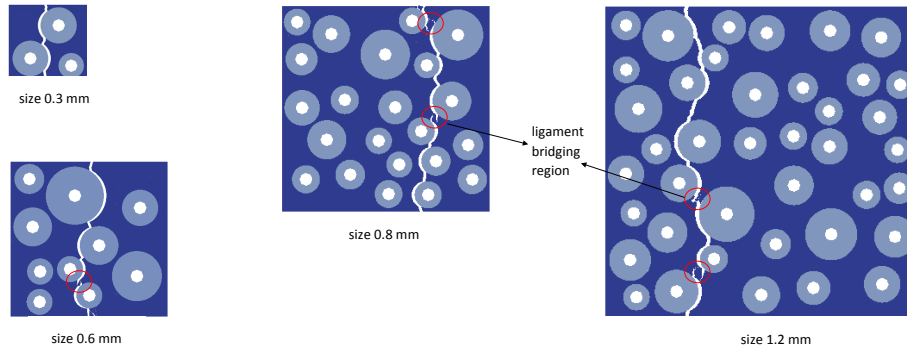


**Figure 6.9** Final crack paths for bone samples of different sizes. Red circles highlight local bridging zones located on crack paths.

$\sigma_{cl0}$  and  $G_{cl0}$  of fracture strength and fracture toughness (critical fracture energy) for cement line in Table 6.1 were chosen as the control case.

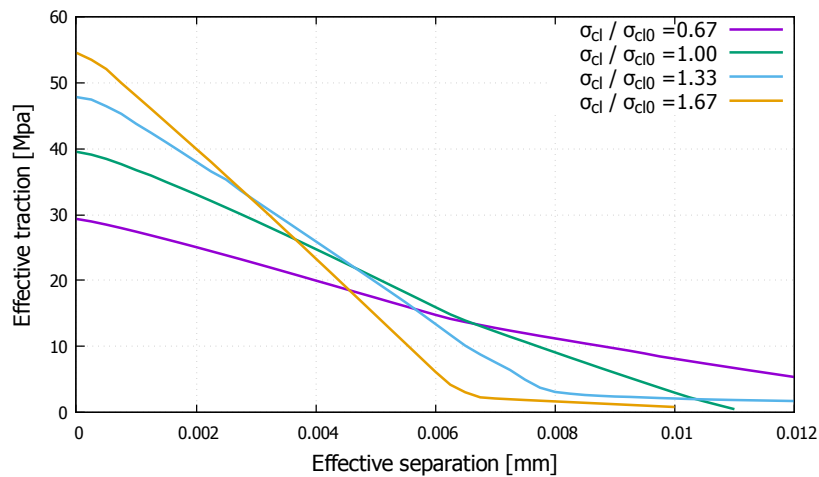


**Figure 6.10** Parametric study of fracture strength  $\sigma_{cl}$  of cement line: effective traction-separation laws.

Firstly, the effect of the fracture strength of cement line was investigated by solely varying the value for  $\sigma_{cl}$  but fixing the remaining material constants including  $G_{cl}$ . Values selected for  $\sigma_{cl}$  in this study were  $0.67 \sigma_{cl0}$ ,  $1.33 \sigma_{cl0}$  and  $1.67 \sigma_{cl0}$ . For each value, five different realisations of microstructure were simulated. The mean curves representing the extracted macroscopic cohesive response are plotted in Figure 6.10 for different values of the fracture strength  $\sigma_{cl}$  of cement line. From the figure, with an increase in fracture strength of cement line, the sample exhibits a reduced fracture displacement at near zero strength. It is interesting to notice that from the outputs of damage distribution, increased values for  $\sigma_{cl}$  result in more matrix cracking in a

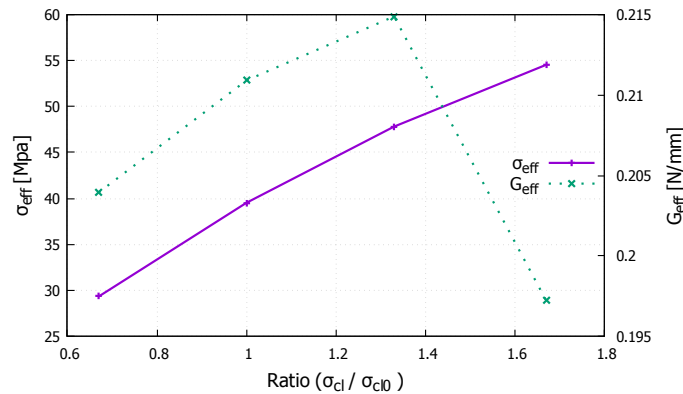


**Figure 6.11** Parametric study of fracture strength  $\sigma_{cl}$  of cement line: computed effective fracture properties (Mode I),  $\sigma_{eff}$  and  $G_{eff}$ .

diffuse manner prior to localised deformation. This corresponds to more energy dissipation in the hardening regime.

The trends in the computed effective fracture properties (mean values) are shown in Figure 6.11. From Figure 6.11, an approximately linear relationship is found between the effective fracture strength and the fracture strength ratio for cement line. A possible explanation for this could be that the relative length ratio of the debonding section to the total crack path does not change significantly. In addition, the effective fracture toughness value does not vary much (8.5%) since the critical energy of cement line  $G_{cl}$  was kept constant for all cases.

Secondly, the effect of critical fracture energy of cement line was investigated by solely varying the value for  $G_{cl}$  but fixing the remaining material constants including  $\sigma_{cl}$ . Values selected for  $G_{cl}$  in this study were  $0.75 G_{cl0}$  and  $1.25 G_{cl0}$ . For each value, five different realisations of microstructure were simulated. The mean curves representing the extracted macroscopic cohesive response are plotted in Figure 6.12 for different values of the critical fracture energy  $G_{cl}$  of cement line. The trends in the computed effective fracture properties (mean values) are shown in Figure 6.13. From the figure, with an increase in the critical fracture energy of cement line, the sample shows an increased fracture displacement at near zero strength.

From Figure 6.13, an approximately linear relationship is found between the effective fracture toughness and the critical fracture energy ratio for cement line. This could be explained by account of roughly constant debonding proportion in the total crack path. In addition, the effective fracture strength value does not vary much (1.0%) since the fracture strength of cement line  $G_{cl}$  was kept constant for all cases.

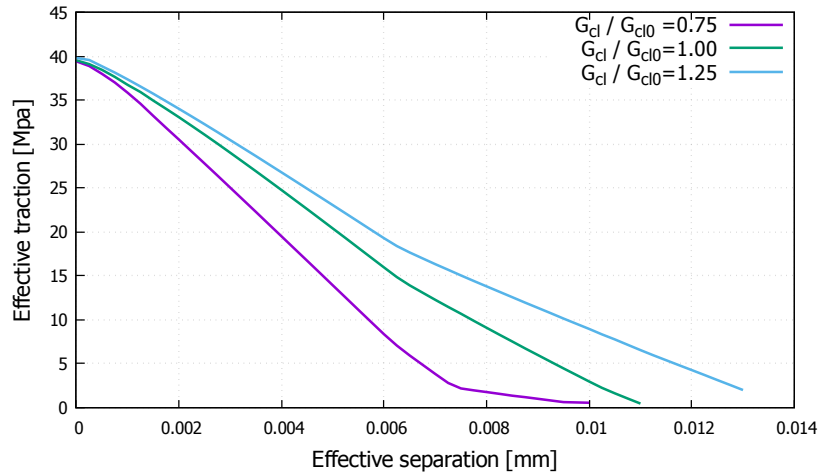


**Figure 6.12** Parametric study of critical fracture energy  $G_{cl}$  of cement line: effective traction-separation laws.

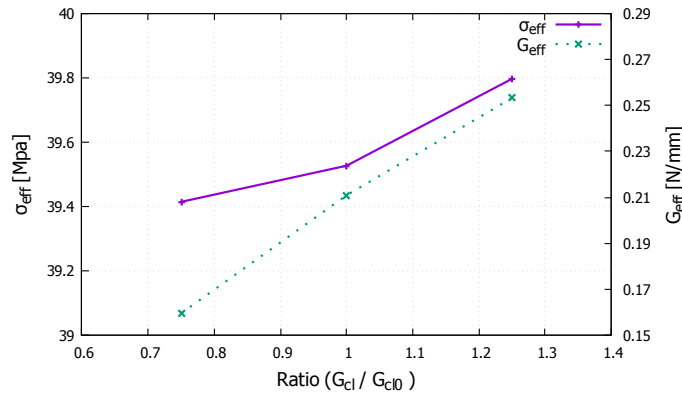


**Figure 6.13** Parametric study of critical fracture energy  $G_{cl}$  of cement line: computed effective fracture properties (Mode I),  $\sigma_{eff}$  and  $G_{eff}$ .

**Discussion**

The fracture process in an RVE model can be summarised as follows. Debonding occurs first at multiple cement lines at a certain level of loading, due to the lower fracture strength of cement line compared to that of interstitial matrix. As loading increases, diffuse matrix cracks (Figure 6.3c) are found primarily emanating from or initiating close to the cement lines that are undergoing further debonding. At a certain stage, the neighbouring matrix cracks coalesce, which finally leads to an *effective single* crack path that is slightly tortuous across the whole RVE (Figure 6.9). The effective single crack path is composed of debonding interfaces and matrix cracks. It is highlighted that the word “single” here does not mean the effective crack

path can be ideally defined as a continuous curve. However, crack bridging (Figure 6.3d) may be present as shown in Figure 6.9. Roughly speaking, the formation of the effective single crack path corresponds to reaching the ultimate RVE (tensile) strength and the occurrence of instability or strain localisation at a macroscale material point. This also identifies the instant when the numerical scheme in (Verhoosel et al., 2010) is employed to extract an effective cohesive law. After strain localisation, the effective crack experiences continuous damage, while the bulk material on both sides of the effective single crack undergoes elastic unloading.

Cortical bone has a heterogeneous microstructure at the scale of osteons. This heterogeneity is the primary reason for having multiple extrinsic toughening mechanisms in cortical bone. The extrinsic toughening mechanisms of interface debonding, diffuse matrix cracking and ligament bridging have been observed in most experiments on radial fracture in the literature (O'Brien et al., 2007, Launey et al., 2010, Budyn and Hoc, 2010, Li et al., 2014). These mechanisms have been well reproduced on a transverse section of osteons in our numerical simulations. Also the tortuous crack path observed in the simulations is evidence for the toughening mechanism of slight crack deflections. However, severe crack deflections are not observed because of the configuration of the problem and since uniaxial loading is applied.

Two major limitations of the current study are (i) the effects of plasticity on the fracture process are not incorporated, and (ii) cracking in osteons is not taken into account. These are worth further investigation.

### 6.2.2 Multiscale failure analysis of bone fracture

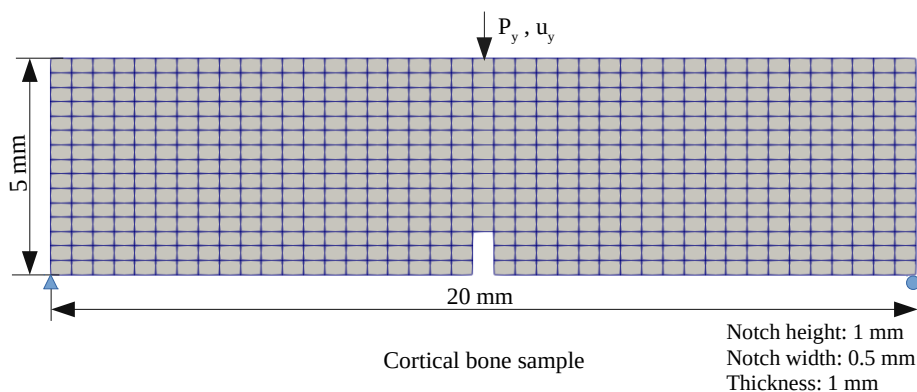


**Figure 6.14** Three-point bending test of cortical bone: geometry, boundary and loading conditions.

To study the interaction between the external loading and microstructural evolution, multiscale failure modelling is necessary. The three-point bending test is widely used to experimentally investigate fracture properties and mechanisms of cortical bone (Ritchie et al., 2008). In this subsection, the three-point bending test of cortical bone was numerically simulated using the multiscale failure model described in Chapter 4. The specimen geometry and loading conditions for the three-point bending test are shown in Figure 6.14. A traction-free finite-width notch was introduced instead of a crack in the middle of the bottom side. Plane stress condition was assumed due to the geometry and loading setup. The simulation was performed with displacement control. To reduce the computational effort, the set of bilinear quadrilateral elements in the mid-span was selected as multiscale elements with RVEs associated with them. To further reduce the computational effort, an RVE size of 0.3 mm was chosen, though it was not considered as an adequate RVE size in the case of strain softening according to the previous RVE size analysis. The behaviour of the remaining macroscale elements was assumed isotropic linear elastic with effective Young's modulus 10.15 GPa and effective Poisson's ratio 0.264. As a comparison, two values for the ultimate strength of the cement line in the cortical bone microstructure, a reduced value  $0.67 \sigma_{cl0}$  and a reference value  $\sigma_{cl0}$ , were used in order to study the interaction between the global mechanical response and the evolving microstructure.

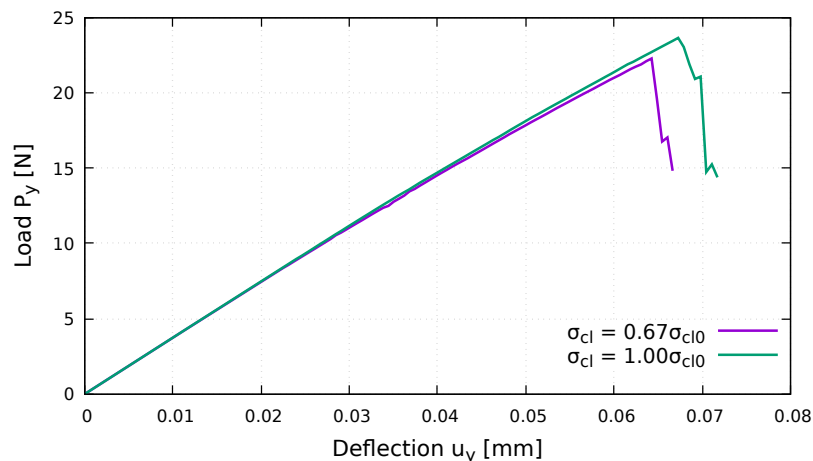


**Figure 6.15** Three-point bending test of cortical bone: load versus deflection curves for two different cement line strengths (reduced and reference) using a multiscale failure approach.

As expected, in the specimen a crack arises from the notch tip and propagates vertically along the mid-span (see Figure 6.16). The resulting load-deflection curves

are plotted in Figure 6.15. Since the macroscale mesh is too coarse to model crack growth accurately (crack growth is not continuous), a small number of sawtooth-like spikes are found in the post-peak response of these curves. A smoother curve could be expected by employing either a smaller macroscale element size or a crack-tip element formulation (the crack tip can stay inside elements) (Zi and Belytschko, 2003, Rabczuk et al., 2008). It is interesting to observe a sharp drop in the load at the peak in the load-deflection curves, which is different from the case of the more ductile transition in the three-point bending simulation for concrete performed in Chapter 4. This observation seems consistent with some experimental evidence such as in (Giner et al., 2017). From the modelling point of view, the sharp peak behaviour is caused by the brittleness of the effective cohesive law.

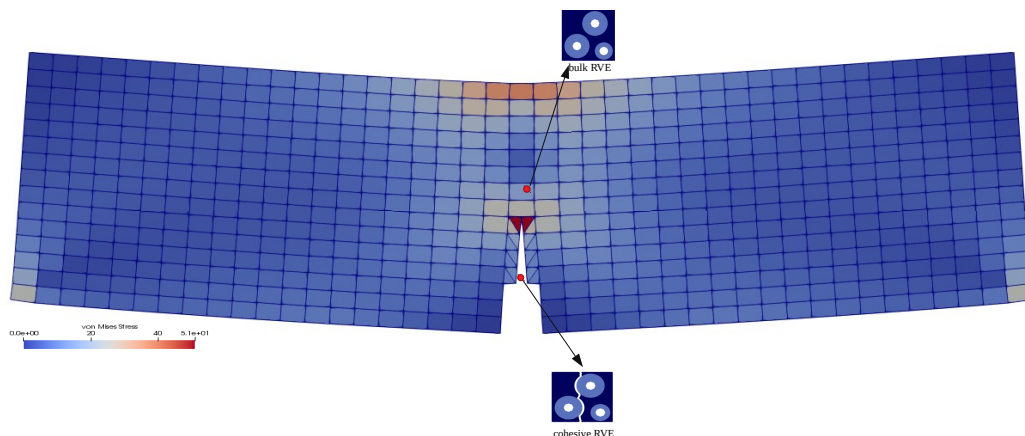


**Figure 6.16** Three-point bending multiscale simulation of cortical bone: macroscale deformation (x10), and typical bulk and cohesive RVE deformed configurations (magnified for visualisation purposes) at the final load step.

In Figure 6.15, the two curves are identical until roughly when the first bottom macroscale element is cracked. As expected, the case with  $0.67 \sigma_{cl0}$  gives a lower peak than the other case due to a reduced cement line strength. Note that the simulations were terminated when severe convergence issues occurred, which explains why the post-peak branches are short.

This current multiscale failure study for cortical bone demonstrates that the significant influences of mechanical properties of microscopic constituents in cortical bone on the overall response can be captured by means of multiscale failure modelling. This kind of multiscale failure modelling offers great potential in clinical practice to help

understand complicated bone failure and fracture mechanisms, and plan patient-specific treatment schemes.

### 6.3 Summary

In this chapter, a method in the literature has been employed to extract effective cohesive laws for cortical bone. The effective cohesive laws that are of mode I represent the crack separation behaviour in the normal direction at the macroscale. This method also helps quantify the effective fracture strength and the effective fracture toughness (mode I) for cortical bone, which is defined as the area under the curve of the effective cohesive law. To ensure that the effective cohesive laws are sufficiently accurate, the proper size for a valid RVE has been investigated. It was found that the minimum RVE size should be greater than 0.3 mm, though we did not know the exact value at the moment, due to only a limited number of tested RVE sizes. The effect of cement line on the effective fracture strength and toughness has been explored by means of a parametric study.

A three-point bending test has been simulated using the multiscale failure model established in Chapter 4. The interaction between microstructural evolution and external loads can be captured. This demonstrates that the multiscale failure modelling technique is advantageous in describing failure mechanisms at multiple length scales. The combination of multiscale simulation results with experimental observations and measurements can take us one step further in understanding the complex fracture mechanisms of bones. Therefore, this can help develop guidelines for the effective and trustworthy treatment and prevention of bone fracture in clinical practice.

Note that the developed multiscale failure model in Chapter 5 has not been applied to the fracture analyses for a structure made of cortical bone tissue in a fully-coupled two-way manner, since the current formulation and code implementation are limited to only the use of the local smeared crack approach at the microscale for the provision of microscopic damage onset and its evolution. However, the cohesive crack model approach implemented by interface elements was employed for representing failure mechanisms at the microscale. The extension to accounting for cohesive cracks at both the macroscale and microscale seems straightforward ([Toro et al., 2016a,b](#)); however it will require substantial additional coding effort and remains the subject of ongoing research.

# Chapter 7

## Conclusions and Perspective

### 7.1 Main Contributions

Modelling strain localisation is of great engineering interest particularly for large structures made of quasi-brittle materials. Strain localisation that results in a propagating macroscale crack is a physical phenomenon that involves the formation of extensive damage localisation starting from diffused damage inception. In this project, we aimed to develop new multiscale failure approaches that can be employed to simulate strain localisation and describe the failure processes at two different length scales, and then apply the multiscale failure modelling technique to investigate the fracture/failure mechanisms in cortical bone tissue. We first gave a comprehensive review of single or multi-scale computational approaches to fracture in the literature. Implementation details were given. Then, we developed two different multiscale failure frameworks that have distinct theoretical foundations. Both models are built upon the concept of cohesive cracks, and extended first-order computational homogenisation (CH) schemes in order to address RVE size dependence in the presence of strain localisation. Finally, we applied one of these proposed multiscale failure approaches to investigate the bone failure process. Three main contributions have been made:

1. A novel continuous-discontinuous multiscale failure modelling approach that is based on macro-discontinuity enhanced  $FE^2$  was proposed. One major advantage of this model is its simplicity as it does not require the knowledge of the evolution details of strain localisation bands at the microscale. In this model:

- (a) Bulk RVE models using the conventional CH are coupled to Gauss points located within the predefined critical regions of macroscopic structures at the beginning of analysis.
  - (b) Once a macroscale material point loses stability, a new crack segment is inserted for which cohesive RVE models using the extended CH and with copied initial states are coupled to crack integration points.
  - (c) The weakly periodic BCs that are aligned with the localisation direction are employed to minimise spurious boundary effects.
  - (d) In the extended CH, the homogenised or macroscale strain applied to the boundary of the cohesive RVE model is enriched with a macroscale discontinuity related term regularised with the effective length of the microscale localisation band. This alleviates the RVE size dependence of the homogenised cohesive response.
  - (e) The discrete crack at the macroscale is represented with the XFEM. The static condensation procedure is employed to derive the bulk and cohesive algorithmic tangent stiffnesses.
2. The previous approach does not strictly enforce the kinematic consistency between the macroscopic crack and microscopic strain localisation band. To this end, another multiscale failure modelling approach was developed on the basis of the Failure-Oriented Multiscale Variational Formulation (FOMVF) proposed in the literature. The FOMVF is built upon kinematic admissibility and the principle of multiscale virtual power. In this model:
- (a) The kinematic compatibility between two scales needs to be attained by defining a proper kinematical insertion operator especially for the case of strain localisation. As a result, two types of BCs to be enforced upon strain localisation are derived.
  - (b) In the extended CH, the macroscale cohesive traction expression and microscale equilibrium are two direct consequences of applying the principle of multiscale virtual power.
  - (c) The discrete crack at the macroscale is represented with the XFEM. The bulk and cohesive algorithmic tangent stiffnesses are derived by means of linearisation.
  - (d) The bifurcation condition is checked at the end of each load step so as to switch to the extended CH if necessary.

3. Multiscale failure modelling was then applied to explore the failure mechanisms of cortical bone tissue. The minimal RVE size in terms of ensuring a sufficiently accurate effective cohesive law was determined, which should be greater than 0.3 mm equal to about three times the average osteon diameter. The effects of fracture properties of cement line on the effective fracture strength and toughness were investigated. An approximately linear relationship was found when varying one fracture parameter while fixing the other for the cement line. The extrinsic toughening mechanisms observed in the RVE models were discussed. A three-point bending test was simulated with the first multiscale failure modelling approach just mentioned.

## 7.2 Plans for future work

As regards the future work, several potential research topics are listed below.

1. The proposed multiscale failure modelling approaches can be extended to the three-dimensional (3D) case. This calls for the 3D implementation of the XFEM with a robust tracking method for cracks. Also, the 3D version of weakly periodic boundary conditions needs to be implemented for the multiscale failure approach in Chapter 4. The multiscale failure approach presented in Chapter 5 can be extended to the situation where interface elements are employed for modelling failure mechanisms at the microscale. The interface elements can be inserted adaptively in order to significantly improve computational performance.
2. In general, multiscale failure approaches incur extreme computational costs, limiting their practical applicability. The application of reduced order modelling to microscale models could be very helpful. In addition, the parallel implementation of CH based multiscale approaches is straightforward, because each microscale BVP can be solved locally by a separate processor. An efficient load-balancing strategy for distributing the load to multiple processors may be a great concern.
3. The current work is confined to quasi-static loading scenarios. In practical engineering, impact-induced damage and fracture are prevalent such as in composite laminates. Therefore, the extension of the present multiscale failure approaches to impact loading conditions in order to simulate the dynamic fracture of heterogeneous materials is intriguing.

4. The multiscale failure approaches can be extended to incorporate multiphysics effects, such as coupled thermo-mechanical analyses for concrete and composites. This provides a promising avenue for studying complex material behaviour under loading and environmental conditions in a more accurate way.
5. Although the proposed multiscale failure approaches have been verified against direct numerical simulations, they have not been validated against experiments. When gradient enhanced damage models are employed at the microscale, the characteristic length parameter of materials needs to be calibrated, perhaps by an inverse analysis.
6. In the current microscopic failure modelling of cortical bone, the osteons were not allowed to fracture. This limitation can be simply resolved by inserting interface elements in the osteon regions. The mechanical and fracture properties were collected from the literature. These data can be obtained from performing experimental measurements to increase reliability. More numerical realisations for an RVE size can be simulated to reduce the errors in extracted effective cohesive laws. To better unveil the bone fracture and toughening mechanisms, a comprehensive comparison between numerical results and experimental observations is demanding. For example, fracture toughness and cohesive strength can be experimentally determined by coupon level tests. Both parameters can be used as material properties for prediction of crack growth in three-point bending simulations in a single scale setting. The obtained load-deflection responses will be compared against those from the multiscale failure simulations with microstructure details captured by imaging techniques.
7. Multiscale failure simulations can be integrated with statistical uncertainty quantification in order to capture inherent uncertainties in microstructure.

# References

- Abaqus (2012). Abaqus 6.12 theory manual. *Dassault Systèmes Simulia Corp., Providence, Rhode Island.*
- Abdel-Wahab, A. A., Maligno, A. R., and Silberschmidt, V. V. (2012). Micro-scale modelling of bovine cortical bone fracture: Analysis of crack propagation and microstructure using x-fem. *Computational Materials Science*, 52(1):128–135.
- Aifantis, E. C. (1984). On the microstructural origin of certain inelastic models. *Journal of Engineering Materials and technology*, 106(4):326–330.
- Alfaiate, J., Wells, G., and Sluys, L. (2002). On the use of embedded discontinuity elements with crack path continuity for mode-i and mixed-mode fracture. *Engineering fracture mechanics*, 69(6):661–686.
- Alfano, G. and Crisfield, M. (2001). Finite element interface models for the delamination analysis of laminated composites: mechanical and computational issues. *International journal for numerical methods in engineering*, 50(7):1701–1736.
- Alfano, G. and Crisfield, M. (2003). Solution strategies for the delamination analysis based on a combination of local-control arc-length and line searches. *International Journal for Numerical Methods in Engineering*, 58(7):999–1048.
- Alfano, M., Furguele, F., Leonardi, A., Maletta, C., and Paulino, G. (2009). Mode i fracture of adhesive joints using tailored cohesive zone models. *International journal of fracture*, 157(1-2):193.
- An, B., Liu, Y., Arola, D., and Zhang, D. (2011). Fracture toughening mechanism of cortical bone: An experimental and numerical approach. *Journal of the mechanical behavior of biomedical materials*, 4(7):983–992.
- Anderson, T. L. (2017). *Fracture mechanics: fundamentals and applications*. CRC press.
- Armero, F. and Garikipati, K. (1996). An analysis of strong discontinuities in multiplicative finite strain plasticity and their relation with the numerical simulation of strain localization in solids. *International Journal of Solids and Structures*, 33(20-22):2863–2885.
- Asferg, J. L., Poulsen, P. N., and Nielsen, L. O. (2007). A consistent partly cracked x-fem element for cohesive crack growth. *International Journal for Numerical Methods in Engineering*, 72(4):464–485.

- Ayachit, U. (2015). *The paraview guide: a parallel visualization application*. Kitware, Inc.
- Babuška, I. and Melenk, J. M. (1997). The partition of unity method. *International journal for numerical methods in engineering*, 40(4):727–758.
- Ballard, M. K. and Whitcomb, J. D. (2017). Effective use of cohesive zone-based models for the prediction of progressive damage at the fiber/matrix scale. *Journal of Composite Materials*, 51(5):649–669.
- Barenblatt, G. I. (1962). The mathematical theory of equilibrium cracks in brittle fracture. In *Advances in applied mechanics*, volume 7, pages 55–129. Elsevier.
- Bažant, Z. P. (2000). Size effect. *International Journal of Solids and Structures*, 37(1-2):69–80.
- Bažant, Z. P. and Jirásek, M. (2002). Nonlocal integral formulations of plasticity and damage: survey of progress. *Journal of Engineering Mechanics*, 128(11):1119–1149.
- Bažant, Z. P. and Oh, B. H. (1983). Crack band theory for fracture of concrete. *Matériaux et construction*, 16(3):155–177.
- Bazant, Z. P. and Planas, J. (1997). *Fracture and size effect in concrete and other quasibrittle materials*, volume 16. CRC press.
- Behiri, J. and Bonfield, W. (1989). Orientation dependence of the fracture mechanics of cortical bone. *Journal of biomechanics*, 22(8):863–867.
- Belytschko, T. and Black, T. (1999). Elastic crack growth in finite elements with minimal remeshing. *International journal for numerical methods in engineering*, 45(5):601–620.
- Belytschko, T., Fish, J., and Engelmann, B. E. (1988). A finite element with embedded localization zones. *Computer methods in applied mechanics and engineering*, 70(1):59–89.
- Belytschko, T., Gracie, R., and Ventura, G. (2009). A review of extended/generalized finite element methods for material modeling. *Modelling and Simulation in Materials Science and Engineering*, 17(4):043001.
- Belytschko, T., Liu, W. K., Moran, B., and Elkhodary, K. (2013). *Nonlinear finite elements for continua and structures*. John Wiley & sons.
- Belytschko, T., Loehnert, S., and Song, J.-H. (2008). Multiscale aggregating discontinuities: a method for circumventing loss of material stability. *International Journal for Numerical Methods in Engineering*, 73(6):869–894.
- Belytschko, T., Moës, N., Usui, S., and Parimi, C. (2001). Arbitrary discontinuities in finite elements. *International Journal for Numerical Methods in Engineering*, 50(4):993–1013.

- Belytschko, T., Xiao, S., and Parimi, C. (2003). Topology optimization with implicit functions and regularization. *International Journal for Numerical Methods in Engineering*, 57(8):1177–1196.
- Bhuiyan, F. H., Sanei, S. H. R., and Fertig III, R. S. (2020). Predicting variability in transverse effective elastic moduli and failure initiation strengths in ud composite microstructures due to randomness in fiber location and morphology. *Composite Structures*, page 111887.
- Blanco, P. J., Sánchez, P. J., de Souza Neto, E. A., and Feijóo, R. A. (2016). Variational foundations and generalized unified theory of rve-based multiscale models. *Archives of Computational Methods in Engineering*, 23(2):191–253.
- Bobiński, J. and Tejchman, J. (2016). A coupled constitutive model for fracture in plain concrete based on continuum theory with non-local softening and extended finite element method. *Finite Elements in Analysis and Design*, 114:1–21.
- Bonet, J. and Wood, R. D. (1997). *Nonlinear continuum mechanics for finite element analysis*. Cambridge university press.
- Borja, R. I. (2000). A finite element model for strain localization analysis of strongly discontinuous fields based on standard galerkin approximation. *Computer Methods in Applied Mechanics and Engineering*, 190(11-12):1529–1549.
- Borst, R. d., Remmers, J. J., Needleman, A., and Abellan, M.-A. (2004). Discrete vs smeared crack models for concrete fracture: bridging the gap. *International Journal for Numerical and Analytical Methods in Geomechanics*, 28(7-8):583–607.
- Bosco, E., Kouznetsova, V., and Geers, M. (2015). Multi-scale computational homogenization–localization for propagating discontinuities using x-fem. *International Journal for Numerical Methods in Engineering*, 102(3-4):496–527.
- Boyce, T. M., Fyhrie, D. P., Glotkowski, M. C., Radin, E. L., and Schaffler, M. B. (1998). Damage type and strain mode associations in human compact bone bending fatigue. *Journal of Orthopaedic Research*, 16(3):322–329.
- Brenner, S. and Scott, R. (2007). *The mathematical theory of finite element methods*, volume 15. Springer Science & Business Media.
- Budyn, É. and Hoc, T. (2007). Multiple scale modeling for cortical bone fracture in tension using x-fem. *European Journal of Computational Mechanics/Revue Européenne de Mécanique Numérique*, 16(2):213–236.
- Budyn, E. and Hoc, T. (2010). Analysis of micro fracture in human haversian cortical bone under transverse tension using extended physical imaging. *International Journal for Numerical Methods in Engineering*, 82(8):940–965.
- Budyn, E., Hoc, T., and Jonvaux, J. (2008). Fracture strength assessment and aging signs detection in human cortical bone using an x-fem multiple scale approach. *Computational Mechanics*, 42(4):579–591.

- Camacho, G. T. and Ortiz, M. (1996). Computational modelling of impact damage in brittle materials. *International Journal of Solids and Structures*, 33(20-22):2899–2938.
- Camanho, P. P., Davila, C. G., and De Moura, M. (2003). Numerical simulation of mixed-mode progressive delamination in composite materials. *Journal of Composite Materials*, 37(16):1415–1438.
- Cazes, F., Coret, M., Combescure, A., and Gravouil, A. (2009). A thermodynamic method for the construction of a cohesive law from a nonlocal damage model. *International Journal of Solids and Structures*, 46(6):1476–1490.
- Cervenka, V. (1995). Mesh sensitivity effects in smeared finite element analysis of concrete fracture. *FRAMCOS-2*, pages 1387–1396.
- Cervera, M. and Chiumenti, M. (2006a). Mesh objective tensile cracking via a local continuum damage model and a crack tracking technique. *Computer Methods in Applied Mechanics and Engineering*, 196(1-3):304–320.
- Cervera, M. and Chiumenti, M. (2006b). Smeared crack approach: back to the original track. *International journal for numerical and analytical methods in geomechanics*, 30(12):1173–1199.
- Cervera, M., Chiumenti, M., and Codina, R. (2010a). Mixed stabilized finite element methods in nonlinear solid mechanics: Part ii: Strain localization. *Computer Methods in Applied Mechanics and Engineering*, 199(37-40):2571–2589.
- Cervera, M., Pelà, L., Clemente, R., and Roca, P. (2010b). A crack-tracking technique for localized damage in quasi-brittle materials. *Engineering Fracture Mechanics*, 77(13):2431–2450.
- Chaboche, J. L., Feyel, F., and Monerie, Y. (2001). Interface debonding models: a viscous regularization with a limited rate dependency. *International journal of Solids and Structures*, 38(18):3127–3160.
- Chan, K. S., Chan, C. K., and Nicolella, D. P. (2009). Relating crack-tip deformation to mineralization and fracture resistance in human femur cortical bone. *Bone*, 45(3):427–434.
- Chen, B., Pinho, S., De Carvalho, N., Baiz, P., and Tay, T. (2014). A floating node method for the modelling of discontinuities in composites. *Engineering Fracture Mechanics*, 127:104–134.
- Chessa, J., Smolinski, P., and Belytschko, T. (2002). The extended finite element method (xfem) for solidification problems. *International Journal for Numerical Methods in Engineering*, 53(8):1959–1977.
- Cid Alfaro, M., Suiker, A., and De Borst, R. (2010). Transverse failure behavior of fiber-epoxy systems. *Journal of Composite Materials*, 44(12):1493–1516.

- Coenen, E., Kouznetsova, V., Bosco, E., and Geers, M. (2012a). A multi-scale approach to bridge microscale damage and macroscale failure: a nested computational homogenization-localization framework. *International Journal of Fracture*, 178(1-2):157–178.
- Coenen, E., Kouznetsova, V., and Geers, M. (2012b). Novel boundary conditions for strain localization analyses in microstructural volume elements. *International Journal for Numerical Methods in Engineering*, 90(1):1–21.
- Constantinides, G. and Ulm, F.-J. (2004). The effect of two types of csh on the elasticity of cement-based materials: Results from nanoindentation and micromechanical modeling. *Cement and concrete research*, 34(1):67–80.
- Cox, B. N. and Yang, Q. (2007). Cohesive zone models of localization and fracture in bone. *Engineering fracture mechanics*, 74(7):1079–1092.
- Currey, J. D. (1979). Mechanical properties of bone tissues with greatly differing functions. *Journal of biomechanics*, 12(4):313–319.
- Cuvilliez, S., Feyel, F., Lorentz, E., and Michel-Ponnelle, S. (2012). A finite element approach coupling a continuous gradient damage model and a cohesive zone model within the framework of quasi-brittle failure. *Computer methods in applied mechanics and engineering*, 237:244–259.
- Daffner, R. H. and Pavlov, H. (1992). Stress fractures: current concepts. *AJR. American journal of roentgenology*, 159(2):245–252.
- Daux, C., Moës, N., Dolbow, J., Sukumar, N., and Belytschko, T. (2000). Arbitrary branched and intersecting cracks with the extended finite element method. *International journal for numerical methods in engineering*, 48(12):1741–1760.
- De Borst, R. (1987). Computation of post-bifurcation and post-failure behavior of strain-softening solids. *Computers & Structures*, 25(2):211–224.
- de Borst, R., Crisfield, M. A., Remmers, J. J., and Verhoosel, C. V. (2012). *Nonlinear finite element analysis of solids and structures*. John Wiley & Sons.
- De Borst, R., Crisfield, M. A., Remmers, J. J., and Verhoosel, C. V. (2012). *Nonlinear finite element analysis of solids and structures*. John Wiley & Sons.
- De Borst, R. and Mühlhaus, H.-B. (1992). Gradient-dependent plasticity: formulation and algorithmic aspects. *International Journal for Numerical Methods in Engineering*, 35(3):521–539.
- De Borst, R., Sluys, L., Mühlhaus, H.-B., and Pamin, J. (1993). Fundamental issues in finite element analyses of localization of deformation. *Engineering computations*, 10(2):99–121.
- de Souza Neto, E. and Feijóo, R. (2006). Variational foundations of multi-scale constitutive models of solid: small and large strain kinematical formulation. *LNCC Research & Development Report*, 16.

- Dias-da Costa, D., Alfaiate, J., Sluys, L., and Júlio, E. (2009). Towards a generalization of a discrete strong discontinuity approach. *Computer Methods in Applied Mechanics and Engineering*, 198(47-48):3670–3681.
- Dolbow, J., Moës, N., and Belytschko, T. (2001). An extended finite element method for modeling crack growth with frictional contact. *Computer methods in applied Mechanics and engineering*, 190(51-52):6825–6846.
- Dufloy, M. (2007). A study of the representation of cracks with level sets. *International journal for numerical methods in engineering*, 70(11):1261–1302.
- Dugdale, D. S. (1960). Yielding of steel sheets containing slits. *Journal of the Mechanics and Physics of Solids*, 8(2):100–104.
- Dumstorff, P. and Meschke, G. (2007). Crack propagation criteria in the framework of x-fem-based structural analyses. *International Journal for Numerical and Analytical Methods in Geomechanics*, 31(2):239–259.
- D’Mello, R. J. and Waas, A. M. (2019). Influence of unit cell size and fiber packing on the transverse tensile response of fiber reinforced composites. *Materials*, 12(16):2565.
- Elices, M., Guinea, G., Gomez, J., and Planas, J. (2002). The cohesive zone model: advantages, limitations and challenges. *Engineering fracture mechanics*, 69(2):137–163.
- Falk, M. L., Needleman, A., and Rice, J. R. (2001). A critical evaluation of cohesive zone models of dynamic fracture. *Le Journal de Physique IV*, 11(PR5):Pr5–43.
- Feyel, F. and Chaboche, J.-L. (2000). Fe2 multiscale approach for modelling the elastoviscoplastic behaviour of long fibre sic/ti composite materials. *Computer methods in applied mechanics and engineering*, 183(3-4):309–330.
- Fletcher, L., Codrington, J., and Parkinson, I. (2014). Effects of fatigue induced damage on the longitudinal fracture resistance of cortical bone. *Journal of Materials Science: Materials in Medicine*, 25(7):1661–1670.
- Francfort, G. A. and Marigo, J.-J. (1998). Revisiting brittle fracture as an energy minimization problem. *Journal of the Mechanics and Physics of Solids*, 46(8):1319–1342.
- Fries, T.-P. and Belytschko, T. (2010). The extended/generalized finite element method: an overview of the method and its applications. *International journal for numerical methods in engineering*, 84(3):253–304.
- Gao, Y. and Bower, A. (2004). A simple technique for avoiding convergence problems in finite element simulations of crack nucleation and growth on cohesive interfaces. *Modelling and Simulation in Materials Science and Engineering*, 12(3):453.

- Garikipati, K. and Hughes, T. J. (1998). A study of strain localization in a multiple scale framework—the one-dimensional problem. *Computer methods in applied mechanics and engineering*, 159(3-4):193–222.
- Geers, M., De Borst, R., Brekelmans, W., and Peerlings, R. (1998). Strain-based transient-gradient damage model for failure analyses. *Computer methods in applied mechanics and engineering*, 160(1-2):133–153.
- Geers, M., Kouznetsova, V., and Brekelmans, W. (2001). Gradient-enhanced computational homogenization for the micro-macro scale transition. *Le Journal de Physique IV*, 11(PR5):Pr5–145.
- Geers, M. G., Kouznetsova, V. G., and Brekelmans, W. (2010). Multi-scale computational homogenization: Trends and challenges. *Journal of computational and applied mathematics*, 234(7):2175–2182.
- Geubelle, P. H. and Baylor, J. S. (1998). Impact-induced delamination of composites: a 2d simulation. *Composites Part B: Engineering*, 29(5):589–602.
- Geuzaine, C. and Remacle, J.-F. (2009). Gmsh: A 3-d finite element mesh generator with built-in pre-and post-processing facilities. *International journal for numerical methods in engineering*, 79(11):1309–1331.
- Giner, E., Belda, R., Arango, C., Vercher-Martínez, A., Tarancón, J. E., and Fuenmayor, F. J. (2017). Calculation of the critical energy release rate  $g_c$  of the cement line in cortical bone combining experimental tests and finite element models. *Engineering Fracture Mechanics*, 184:168–182.
- Gitman, I., Askes, H., and Sluys, L. (2007). Representative volume: existence and size determination. *Engineering fracture mechanics*, 74(16):2518–2534.
- Gitman, I., Askes, H., and Sluys, L. (2008). Coupled-volume multi-scale modelling of quasi-brittle material. *European Journal of Mechanics-A/Solids*, 27(3):302–327.
- Goldmann, J., Brummund, J., and Ulbricht, V. (2018). On boundary conditions for homogenization of volume elements undergoing localization. *International Journal for Numerical Methods in Engineering*, 113(1):1–21.
- Griffith, A. A. and Eng, M. (1921). Vi. the phenomena of rupture and flow in solids. *Phil. Trans. R. Soc. Lond. A*, 221(582-593):163–198.
- Guidault, P.-A., Allix, O., Champaney, L., and Navarro, J.-P. (2007). A two-scale approach with homogenization for the computation of cracked structures. *Computers & structures*, 85(17-18):1360–1371.
- Gustafsson, A., Khayyeri, H., Wallin, M., and Isaksson, H. (2019). An interface damage model that captures crack propagation at the microscale in cortical bone using xfm. *Journal of the mechanical behavior of biomedical materials*, 90:556–565.

- Gutiérrez, M. A. (2004). Energy release control for numerical simulations of failure in quasi-brittle solids. *Communications in Numerical Methods in Engineering*, 20(1):19–29.
- Hamed, E. and Jasiuk, I. (2013). Multiscale damage and strength of lamellar bone modeled by cohesive finite elements. *Journal of the mechanical behavior of biomedical materials*, 28:94–110.
- Hansbo, A. and Hansbo, P. (2004). A finite element method for the simulation of strong and weak discontinuities in solid mechanics. *Computer methods in applied mechanics and engineering*, 193(33-35):3523–3540.
- Hashin, Z. (1983). Analysis of composite materials-a survey. *Journal of applied mechanics*, 50(3):481–505.
- Heinrich, C., Aldridge, M., Wineman, A., Kieffer, J., Waas, A. M., and Shahwan, K. (2012). The influence of the representative volume element (rve) size on the homogenized response of cured fiber composites. *Modelling and simulation in materials science and engineering*, 20(7):075007.
- Hettich, T., Hund, A., and Ramm, E. (2008). Modeling of failure in composites by x-fem and level sets within a multiscale framework. *Computer Methods in Applied Mechanics and Engineering*, 197(5):414–424.
- Hill, R. (1963). Elastic properties of reinforced solids: some theoretical principles. *Journal of the Mechanics and Physics of Solids*, 11(5):357–372.
- Hillerborg, A., Modéer, M., and Petersson, P.-E. (1976). Analysis of crack formation and crack growth in concrete by means of fracture mechanics and finite elements. *Cement and concrete research*, 6(6):773–781.
- Hirschberger, C., Ricker, S., Steinmann, P., and Sukumar, N. (2009). Computational multiscale modelling of heterogeneous material layers. *Engineering Fracture Mechanics*, 76(6):793–812.
- Hirschberger, C. B., Sukumar, N., and Steinmann, P. (2008). Computational homogenization of material layers with micromorphic mesostructure. *Philosophical Magazine*, 88(30-32):3603–3631.
- Hughes, T. J., Feijóo, G. R., Mazzei, L., and Quincy, J.-B. (1998). The variational multiscale method-a paradigm for computational mechanics. *Computer methods in applied mechanics and engineering*, 166(1-2):3–24.
- Hund, A. and Ramm, E. (2007). Locality constraints within multiscale model for non-linear material behaviour. *International Journal for Numerical Methods in Engineering*, 70(13):1613–1632.
- Jäger, P., Steinmann, P., and Kuhl, E. (2008). Modeling three-dimensional crack propagation-a comparison of crack path tracking strategies. *International Journal for Numerical Methods in Engineering*, 76(9):1328–1352.
- Janert, P. K. (2010). *Gnuplot in action: understanding data with graphs*. Manning.

- Jirasek, M. (1998). Nonlocal models for damage and fracture: comparison of approaches. *International Journal of Solids and Structures*, 35(31-32):4133–4145.
- Jirásek, M. (2000). Comparative study on finite elements with embedded discontinuities. *Computer methods in applied mechanics and engineering*, 188(1-3):307–330.
- Jirásek, M. (2004). Modeling of localized inelastic deformation: Lecture notes. *Czech Technical University, Prague*.
- Jirásek, M. and Bauer, M. (2012). Numerical aspects of the crack band approach. *Computers & Structures*, 110:60–78.
- Jirasek, M., Rolshoven, S., and Grassl, P. (2004). Size effect on fracture energy induced by non-locality. *International Journal for Numerical and Analytical Methods in Geomechanics*, 28(7-8):653–670.
- Jirásek, M. and Zimmermann, T. (2001). Embedded crack model. part ii: Combination with smeared cracks. *International Journal for Numerical Methods in Engineering*, 50(6):1291–1305.
- Jonvaux, J., Hoc, T., and Budyn, E. (2012). Analysis of micro fracture in human haversian cortical bone under compression. *International journal for numerical methods in biomedical engineering*, 28(9):974–998.
- Joseph, A. P., Davidson, P., and Waas, A. M. (2018). Open hole and filled hole progressive damage and failure analysis of composite laminates with a countersunk hole. *Composite Structures*, 203:523–538.
- Ju, J. (1989). On energy-based coupled elastoplastic damage theories: constitutive modeling and computational aspects. *International Journal of Solids and structures*, 25(7):803–833.
- Kachanov, L. (2013). *Introduction to continuum damage mechanics*, volume 10. Springer Science & Business Media.
- Kaczmarczyk, Ł., Pearce, C. J., and Bićanić, N. (2008). Scale transition and enforcement of rve boundary conditions in second-order computational homogenization. *International Journal for Numerical Methods in Engineering*, 74(3):506–522.
- Kaczmarczyk, Ł., Pearce, C. J., and Bićanić, N. (2010a). Studies of microstructural size effect and higher-order deformation in second-order computational homogenization. *Computers & structures*, 88(23-24):1383–1390.
- Kaczmarczyk, Ł., Pearce, C. J., Bićanić, N., and de Souza Neto, E. (2010b). Numerical multiscale solution strategy for fracturing heterogeneous materials. *Computer Methods in Applied Mechanics and Engineering*, 199(17-20):1100–1113.
- Kanouté, P., Boso, D., Chaboche, J., and Schrefler, B. (2009). Multiscale methods for composites: a review. *Archives of Computational Methods in Engineering*, 16(1):31–75.

- Karamnejad, A. and Sluys, L. J. (2014). A dispersive multi-scale crack model for quasi-brittle heterogeneous materials under impact loading. *Computer Methods in Applied Mechanics and Engineering*, 278:423–444.
- Kerfriden, P., Paladim, D. A., García, J. J. R., and Bordas, S. P.-A. (2013). A posteriori error estimation for pod-based reduced order modelling with application in homogenisation.
- Khoei, A., Vahab, M., Haghghat, E., and Moallemi, S. (2014). A mesh-independent finite element formulation for modeling crack growth in saturated porous media based on an enriched-fem technique. *International Journal of Fracture*, 188(1):79–108.
- Khoei, A. R. (2014). *Extended finite element method: theory and applications*. John Wiley & Sons.
- Koester, K. J., Ager lli, J., and Ritchie, R. (2008). The true toughness of human cortical bone measured with realistically short cracks. *Nature materials*, 7(8):672.
- Kolymbas, D. (2009). Kinematics of shear bands. *Acta Geotechnica*, 4(4):315.
- Kouznetsova, V., Brekelmans, W., and Baaijens, F. (2001). An approach to micro-macro modeling of heterogeneous materials. *Computational mechanics*, 27(1):37–48.
- Kouznetsova, V., Geers, M., and Brekelmans, W. (2004). Multi-scale second-order computational homogenization of multi-phase materials: a nested finite element solution strategy. *Computer Methods in Applied Mechanics and Engineering*, 193(48-51):5525–5550.
- Kubair, D. V. and Geubelle, P. H. (2003). Comparative analysis of extrinsic and intrinsic cohesive models of dynamic fracture. *International Journal of Solids and Structures*, 40(15):3853–3868.
- Larsson, F., Runesson, K., Saroukhani, S., and Vafadari, R. (2011). Computational homogenization based on a weak format of micro-periodicity for rve-problems. *Computer Methods in Applied Mechanics and Engineering*, 200(1-4):11–26.
- Launey, M. E., Buehler, M. J., and Ritchie, R. O. (2010). On the mechanistic origins of toughness in bone. *Annual review of materials research*, 40:25–53.
- Lemaitre, J. (2012). *A course on damage mechanics*. Springer Science & Business Media.
- Li, S., Abdel-Wahab, A., Demirci, E., and Silberschmidt, V. V. (2014). Fracture process in cortical bone: X-fem analysis of microstructured models. In *Fracture Phenomena in Nature and Technology*, pages 43–55. Springer.
- Li, X. and Chen, J. (2017). An extended cohesive damage model for simulating arbitrary damage propagation in engineering materials. *Computer Methods in Applied Mechanics and Engineering*, 315:744–759.

- Lin, S., Nguyen, N., and Waas, A. M. (2019). Application of continuum decohesive finite element to progressive failure analysis of composite materials. *Composite Structures*, 212:365–380.
- Ling, D., Yang, Q., and Cox, B. (2009). An augmented finite element method for modeling arbitrary discontinuities in composite materials. *International journal of fracture*, 156(1):53–73.
- Liu, F. and Borja, R. I. (2008). A contact algorithm for frictional crack propagation with the extended finite element method. *International Journal for Numerical methods in engineering*, 76(10):1489–1512.
- Liu, P. and Zheng, J. (2010). Recent developments on damage modeling and finite element analysis for composite laminates: A review. *Materials & Design*, 31(8):3825–3834.
- Lloberas-Valls, O., Rixen, D., Simone, A., and Sluys, L. (2012). Multiscale domain decomposition analysis of quasi-brittle heterogeneous materials. *International Journal for Numerical Methods in Engineering*, 89(11):1337–1366.
- Loehnert, S. and Belytschko, T. (2007). A multiscale projection method for macro/microcrack simulations. *International Journal for Numerical Methods in Engineering*, 71(12):1466–1482.
- Marco, M., Belda, R., Miguélez, M. H., and Giner, E. (2018). A heterogeneous orientation criterion for crack modelling in cortical bone using a phantom-node approach. *Finite Elements in Analysis and Design*, 146:107–117.
- Massart, T., Peerlings, R., and Geers, M. (2007). An enhanced multi-scale approach for masonry wall computations with localization of damage. *International journal for numerical methods in engineering*, 69(5):1022–1059.
- MATLAB (2014). *version 7.10.0 (R2014b)*. The MathWorks Inc., Natick, Massachusetts.
- Matouš, K., Geers, M. G., Kouznetsova, V. G., and Gillman, A. (2017). A review of predictive nonlinear theories for multiscale modeling of heterogeneous materials. *Journal of Computational Physics*, 330:192–220.
- Matouš, K., Kulkarni, M. G., and Geubelle, P. H. (2008). Multiscale cohesive failure modeling of heterogeneous adhesives. *Journal of the Mechanics and Physics of Solids*, 56(4):1511–1533.
- May, I. and Duan, Y. (1997). A local arc-length procedure for strain softening. *Computers & structures*, 64(1-4):297–303.
- May, S., Vignollet, J., and de Borst, R. (2016). A new arc-length control method based on the rates of the internal and the dissipated energy. *Engineering Computations*, 33(1):100–115.
- Mazars, J. and Pijaudier-Cabot, G. (1989). Continuum damage theory-application to concrete. *Journal of Engineering Mechanics*, 115(2):345–365.

- Mergheim, J. (2009). A variational multiscale method to model crack propagation at finite strains. *International journal for numerical methods in engineering*, 80(3):269–289.
- Miehe, C., Schröder, J., and Becker, M. (2002). Computational homogenization analysis in finite elasticity: material and structural instabilities on the micro-and macro-scales of periodic composites and their interaction. *Computer Methods in Applied Mechanics and Engineering*, 191(44):4971–5005.
- Miehe, C., Schröder, J., and Schotte, J. (1999). Computational homogenization analysis in finite plasticity simulation of texture development in polycrystalline materials. *Computer methods in applied mechanics and engineering*, 171(3-4):387–418.
- Mischinski, S. and Ural, A. (2013). Interaction of microstructure and microcrack growth in cortical bone: a finite element study. *Computer methods in biomechanics and biomedical engineering*, 16(1):81–94.
- Moës, N., Dolbow, J., and Belytschko, T. (1999). A finite element method for crack growth without remeshing. *International journal for numerical methods in engineering*, 46(1):131–150.
- Najafi, A. R., Arshi, A. R., Eslami, M., Fariborz, S., and Moeinzadeh, M. H. (2007). Micromechanics fracture in osteonal cortical bone: A study of the interactions between microcrack propagation, microstructure and the material properties. *Journal of biomechanics*, 40(12):2788–2795.
- Nalla, R. K., Kruzic, J. J., Kinney, J. H., and Ritchie, R. O. (2005). Mechanistic aspects of fracture and r-curve behavior in human cortical bone. *Biomaterials*, 26(2):217–231.
- Nalla, R. K., Kruzic, J. J., and Ritchie, R. O. (2004). On the origin of the toughness of mineralized tissue: microcracking or crack bridging? *Bone*, 34(5):790–798.
- Needleman, A. (1987). A continuum model for void nucleation by inclusion debonding.
- Nemat-Nasser, S. and Hori, M. (2013). *Micromechanics: overall properties of heterogeneous materials*, volume 37. Elsevier.
- Nguyen, G. D., Einav, I., and Korsunsky, A. M. (2012a). How to connect two scales of behaviour in constitutive modelling of geomaterials. *Géotechnique Letters*, 2(3):129–134.
- Nguyen, N. and Waas, A. M. (2016). A novel mixed-mode cohesive formulation for crack growth analysis. *Composite structures*, 156:253–262.
- Nguyen, V. P. (2014). An open source program to generate zero-thickness cohesive interface elements. *Advances in Engineering Software*, 74:27–39.

- Nguyen, V. P., Lloberas-Valls, O., Stroeven, M., and Sluys, L. J. (2010). On the existence of representative volumes for softening quasi-brittle materials—a failure zone averaging scheme. *Computer Methods in Applied Mechanics and Engineering*, 199(45-48):3028–3038.
- Nguyen, V. P., Lloberas-Valls, O., Stroeven, M., and Sluys, L. J. (2011a). Homogenization-based multiscale crack modelling: from micro-diffusive damage to macro-cracks. *Computer Methods in Applied Mechanics and Engineering*, 200(9-12):1220–1236.
- Nguyen, V. P., Lloberas-Valls, O., Stroeven, M., and Sluys, L. J. (2012b). Computational homogenization for multiscale crack modeling. implementational and computational aspects. *International Journal for Numerical Methods in Engineering*, 89(2):192–226.
- Nguyen, V. P., Stroeven, M., and Sluys, L. J. (2011b). Multiscale continuous and discontinuous modeling of heterogeneous materials: a review on recent developments. *Journal of Multiscale Modelling*, 3(04):229–270.
- Nguyen, V. P., Stroeven, M., and Sluys, L. J. (2012c). An enhanced continuous–discontinuous multiscale method for modeling mode-i cohesive failure in random heterogeneous quasi-brittle materials. *Engineering Fracture Mechanics*, 79:78–102.
- Nguyen, V. P., Stroeven, M., and Sluys, L. J. (2012d). Multiscale failure modeling of concrete: micromechanical modeling, discontinuous homogenization and parallel computations. *Computer Methods in Applied Mechanics and Engineering*, 201:139–156.
- Norman, T. L., Vashishth, D., and Burr, D. (1991). Mode i fracture toughness of human bone. In *Winter Annual Meeting of the American Society of Mechanical Engineers*. Publ by ASME.
- O’Brien, F. J., Taylor, D., and Lee, T. C. (2005). The effect of bone microstructure on the initiation and growth of microcracks. *Journal of Orthopaedic Research*, 23(2):475–480.
- Oden, J. T. and Reddy, J. N. (2012). *An introduction to the mathematical theory of finite elements*. Courier Corporation.
- Oftadeh, R., Entezari, V., Spörri, G., Villa-Camacho, J. C., Krigbaum, H., Strawich, E., Graham, L., Rey, C., Chiu, H., Müller, R., et al. (2015). Hierarchical analysis and multi-scale modelling of rat cortical and trabecular bone. *Journal of The Royal Society Interface*, 12(106):20150070.
- Oliver, J. (1989). A consistent characteristic length for smeared cracking models. *International Journal for Numerical Methods in Engineering*, 28(2):461–474.
- Oliver, J. (1996). Modelling strong discontinuities in solid mechanics via strain softening constitutive equations. part 1: Fundamentals. *International journal for numerical methods in engineering*, 39(21):3575–3600.

- Oliver, J., Caicedo, M., Huespe, A. E., Hernández, J., and Roubin, E. (2017). Reduced order modeling strategies for computational multiscale fracture. *Computer Methods in Applied Mechanics and Engineering*, 313:560–595.
- Oliver, J., Caicedo, M., Roubin, E., Huespe, A. E., and Hernández, J. (2015). Continuum approach to computational multiscale modeling of propagating fracture. *Computer Methods in Applied Mechanics and Engineering*, 294:384–427.
- Oliver, J., Cervera, M., and Manzoli, O. (1999). Strong discontinuities and continuum plasticity models: the strong discontinuity approach. *International journal of plasticity*, 15(3):319–351.
- Oliver, J., Cervera, M., Oller, S., and Lubliner, J. (1990). Isotropic damage models and smeared crack analysis of concrete. In *Proc. SCI-C Computer Aided Analysis and Design of Concrete Structures*, volume 945958.
- Oliver, J., Dias, I., and Huespe, A. E. (2014). Crack-path field and strain-injection techniques in computational modeling of propagating material failure. *Computer Methods in Applied Mechanics and Engineering*, 274:289–348.
- Oliver, J. and Huespe, A. E. (2004). Continuum approach to material failure in strong discontinuity settings. *Computer Methods in Applied Mechanics and Engineering*, 193(30-32):3195–3220.
- Oliver, J., Huespe, A. E., Cante, J., and Diaz, G. (2010). On the numerical resolution of the discontinuous material bifurcation problem. *International journal for numerical methods in engineering*, 83(6):786–804.
- Oliver, J., Huespe, A. E., Pulido, M., and Chaves, E. (2002). From continuum mechanics to fracture mechanics: the strong discontinuity approach. *Engineering fracture mechanics*, 69(2):113–136.
- Oliver, J., Huespe, A. E., Samaniego, E., and Chaves, E. (2004). Continuum approach to the numerical simulation of material failure in concrete. *International Journal for Numerical and Analytical Methods in Geomechanics*, 28(7-8):609–632.
- Oliver, J., Huespe, A. E., and Sánchez, P. J. (2006). A comparative study on finite elements for capturing strong discontinuities: E-fem vs x-fem. *Computer methods in applied mechanics and engineering*, 195(37-40):4732–4752.
- Ortiz, M., Leroy, Y., and Needleman, A. (1987). A finite element method for localized failure analysis. *Computer methods in applied mechanics and engineering*, 61(2):189–214.
- Ortiz, M. and Pandolfi, A. (1999). Finite-deformation irreversible cohesive elements for three-dimensional crack-propagation analysis. *International journal for numerical methods in engineering*, 44(9):1267–1282.
- Otero, F., Oller, S., and Martinez, X. (2018). Multiscale computational homogenization: review and proposal of a new enhanced-first-order method. *Archives of Computational Methods in Engineering*, 25(2):479–505.

- O'Brien, F. J., Taylor, D., and Lee, T. C. (2007). Bone as a composite material: The role of osteons as barriers to crack growth in compact bone. *International Journal of Fatigue*, 29(6):1051–1056.
- Papoulia, K. D., Sam, C.-H., and Vavasis, S. A. (2003). Time continuity in cohesive finite element modeling. *International Journal for Numerical Methods in Engineering*, 58(5):679–701.
- Park, K., Paulino, G. H., and Roesler, J. R. (2009). A unified potential-based cohesive model of mixed-mode fracture. *Journal of the Mechanics and Physics of Solids*, 57(6):891–908.
- Patzák, B. (2012). Oofem-an object-oriented simulation tool for advanced modeling of materials and structures. *Acta Polytechnica*, 52(6).
- Peerlings, R., Geers, M., De Borst, R., and Brekelmans, W. (2001). A critical comparison of nonlocal and gradient-enhanced softening continua. *International Journal of Solids and Structures*, 38(44-45):7723–7746.
- Peerlings, R. d., De Borst, R., Brekelmans, W. d., and De Vree, J. (1996). Gradient enhanced damage for quasi-brittle materials. *International Journal for numerical methods in engineering*, 39(19):3391–3403.
- Peterlik, H., Roschger, P., Klaushofer, K., and Fratzl, P. (2006). From brittle to ductile fracture of bone. *Nature materials*, 5(1):52.
- Petracca, M., Pelà, L., Rossi, R., Oller, S., Camata, G., and Spacone, E. (2016). Regularization of first order computational homogenization for multiscale analysis of masonry structures. *Computational mechanics*, 57(2):257–276.
- Pijaudier-Cabot, G. and Bažant, Z. P. (1987). Nonlocal damage theory. *Journal of engineering mechanics*, 113(10):1512–1533.
- Pineda, E. J., Bednarczyk, B. A., Waas, A. M., and Arnold, S. M. (2013). Progressive failure of a unidirectional fiber-reinforced composite using the method of cells: Discretization objective computational results. *International Journal of Solids and Structures*, 50(9):1203–1216.
- Planas, J., Elices, M., and Guinea, G. (1993). Cohesive cracks versus nonlocal models: Closing the gap. *International Journal of Fracture*, 63(2):173–187.
- Prabhakar, P. and Waas, A. M. (2013). A novel continuum-decohesive finite element for modeling in-plane fracture in fiber reinforced composites. *Composites science and technology*, 83:1–10.
- Rabczuk, T., Zi, G., Gerstenberger, A., and Wall, W. A. (2008). A new crack tip element for the phantom-node method with arbitrary cohesive cracks. *International Journal for Numerical Methods in Engineering*, 75(5):577–599.
- Rashid, Y. (1968). Ultimate strength analysis of prestressed concrete pressure vessels. *Nuclear engineering and design*, 7(4):334–344.

- Reis, F. and Pires, F. A. (2013). An adaptive sub-incremental strategy for the solution of homogenization-based multi-scale problems. *Computer Methods in Applied Mechanics and Engineering*, 257:164–182.
- Remmers, J., de Borst, R., and Needleman, A. (2003). A cohesive segments method for the simulation of crack growth. *Computational mechanics*, 31(1-2):69–77.
- Rho, J., Zioupos, P., Currey, J., and Pharr, G. (1999). Variations in the individual thick lamellar properties within osteons by nanoindentation. *Bone*, 25(3):295–300.
- Rho, J.-Y., Kuhn-Spearing, L., and Zioupos, P. (1998). Mechanical properties and the hierarchical structure of bone. *Medical engineering & physics*, 20(2):92–102.
- Rice, J. R. (1976). The localization of plastic deformation.
- Riks, E. (1979). An incremental approach to the solution of snapping and buckling problems. *International journal of solids and structures*, 15(7):529–551.
- Ritchie, R., Koester, K., Ionova, S., Yao, W., Lane, N. E., and Ager Iii, J. (2008). Measurement of the toughness of bone: a tutorial with special reference to small animal studies. *Bone*, 43(5):798–812.
- Ritchie, R. O., Kinney, J. H., Kruzic, J. J., and Nalla, R. K. (2005). A fracture mechanics and mechanistic approach to the failure of cortical bone. *Fatigue & Fracture of Engineering Materials & Structures*, 28(4):345–371.
- Rots, J., Nauta, P., Kuster, G., and Blaauwendraad, J. (1985). Smearred crack approach and fracture localization in concrete.
- Rudraraju, S., Salvi, A., Garikipati, K., and Waas, A. M. (2012a). Experimental observations and numerical simulations of curved crack propagation in laminated fiber composites. *Composites science and technology*, 72(10):1064–1074.
- Rudraraju, S., Salvi, A., Garikipati, K., and Waas, A. M. (2012b). Predictions of crack propagation using a variational multiscale approach and its application to fracture in laminated fiber reinforced composites. *Composite structures*, 94(11):3336–3346.
- Rudraraju, S. S., Salvi, A., Garikipati, K., and Waas, A. M. (2010). In-plane fracture of laminated fiber reinforced composites with varying fracture resistance: Experimental observations and numerical crack propagation simulations. *International Journal of Solids and Structures*, 47(7-8):901–911.
- Runesson, K., Ottosen, N. S., and Dunja, P. (1991). Discontinuous bifurcations of elastic-plastic solutions at plane stress and plane strain. *International Journal of Plasticity*, 7(1-2):99–121.
- Saloustros, S., Cervera, M., and Pelà, L. (2018). Challenges, tools and applications of tracking algorithms in the numerical modelling of cracks in concrete and masonry structures. *Archives of Computational Methods in Engineering*, pages 1–45.

- Sánchez, P. J., Blanco, P. J., Huespe, A. E., and Feijóo, R. (2013). Failure-oriented multi-scale variational formulation: micro-structures with nucleation and evolution of softening bands. *Computer Methods in Applied Mechanics and Engineering*, 257:221–247.
- Schaffler, M., Choi, K., and Milgrom, C. (1995). Aging and matrix microdamage accumulation in human compact bone. *Bone*, 17(6):521–525.
- Schellekens, J. and De Borst, R. (1993a). A non-linear finite element approach for the analysis of mode-I free edge delamination in composites. *International Journal of Solids and Structures*, 30(9):1239–1253.
- Schellekens, J. and De Borst, R. (1993b). On the numerical integration of interface elements. *International Journal for Numerical Methods in Engineering*, 36(1):43–66.
- Seeman, E. and Delmas, P. D. (2006). Bone quality-the material and structural basis of bone strength and fragility. *New England journal of medicine*, 354(21):2250–2261.
- Sen, D. and Buehler, M. J. (2011). Structural hierarchies define toughness and defect-tolerance despite simple and mechanically inferior brittle building blocks. *Scientific reports*, 1:35.
- Simmons Jr, E. D., Pritzker, K., and Grynblas, M. D. (1991). Age-related changes in the human femoral cortex. *Journal of Orthopaedic Research*, 9(2):155–167.
- Simo, J. and Ju, J. (1987). Strain-and stress-based continuum damage models-I. formulation. *International journal of solids and structures*, 23(7):821–840.
- Simo, J. C., Oliver, J., and Armero, F. (1993). An analysis of strong discontinuities induced by strain-softening in rate-independent inelastic solids. *Computational mechanics*, 12(5):277–296.
- Simo, J. C. and Rifai, M. (1990). A class of mixed assumed strain methods and the method of incompatible modes. *International journal for numerical methods in engineering*, 29(8):1595–1638.
- Simone, A. (2004). Partition of unity-based discontinuous elements for interface phenomena: computational issues. *Communications in Numerical Methods in Engineering*, 20(6):465–478.
- Simone, A., Wells, G. N., and Sluys, L. J. (2003). From continuous to discontinuous failure in a gradient-enhanced continuum damage model. *Computer Methods in Applied Mechanics and Engineering*, 192(41-42):4581–4607.
- Smit, R., Brekelmans, W., and Meijer, H. (1999). Prediction of the large-strain mechanical response of heterogeneous polymer systems: local and global deformation behaviour of a representative volume element of voided polycarbonate. *Journal of the Mechanics and Physics of Solids*, 47(2):201–221.

- Somer, D. D., de Souza Neto, E., Dettmer, W., and Perić, D. (2009). A sub-stepping scheme for multi-scale analysis of solids. *Computer Methods in Applied Mechanics and Engineering*, 198(9-12):1006–1016.
- Song, S. and Waas, A. M. (1993). A nonlinear elastic foundation model for interlaminar fracture of laminated composites. *Composites Engineering*, 3(10):945–959.
- Song, S. H., Paulino, G. H., and Buttlar, W. G. (2006). A bilinear cohesive zone model tailored for fracture of asphalt concrete considering viscoelastic bulk material. *Engineering Fracture Mechanics*, 73(18):2829–2848.
- Song, S. J. and Waas, A. M. (1995). Energy-based mechanical model for mixed mode failure of laminated composites. *AIAA journal*, 33(4):739–745.
- Souza, F. V. and Allen, D. H. (2011). Modeling the transition of microcracks into macrocracks in heterogeneous viscoelastic media using a two-way coupled multiscale model. *International Journal of Solids and Structures*, 48(22-23):3160–3175.
- Stazi, F., Budyn, E., Chessa, J., and Belytschko, T. (2003). An extended finite element method with higher-order elements for curved cracks. *Computational Mechanics*, 31(1-2):38–48.
- Steinmann, P. and Willam, K. (1991). Localization within the framework of micropolar elasto-plasticity. In *Advances in continuum mechanics*, pages 296–313. Springer.
- Stolarska, M., Chopp, D. L., Moës, N., and Belytschko, T. (2001). Modelling crack growth by level sets in the extended finite element method. *International journal for numerical methods in Engineering*, 51(8):943–960.
- Strouboulis, T., Copps, K., and Babuška, I. (2001). The generalized finite element method. *Computer methods in applied mechanics and engineering*, 190(32-33):4081–4193.
- Sukumar, N., Chopp, D. L., and Moran, B. (2003). Extended finite element method and fast marching method for three-dimensional fatigue crack propagation. *Engineering Fracture Mechanics*, 70(1):29–48.
- Sukumar, N., Moës, N., Moran, B., and Belytschko, T. (2000). Extended finite element method for three-dimensional crack modelling. *International journal for numerical methods in engineering*, 48(11):1549–1570.
- Sukumar, N. and Prévost, J.-H. (2003). Modeling quasi-static crack growth with the extended finite element method part i: Computer implementation. *International journal of solids and structures*, 40(26):7513–7537.
- Svenning, E. (2016). A weak penalty formulation remedying traction oscillations in interface elements. *Computer Methods in Applied Mechanics and Engineering*, 310:460–474.

- Svenning, E., Fagerström, M., and Larsson, F. (2016). On computational homogenization of microscale crack propagation. *International Journal for Numerical Methods in Engineering*, 108(1):76–90.
- Svenning, E., Fagerström, M., and Larsson, F. (2017a). Localization aligned weakly periodic boundary conditions. *International Journal for Numerical Methods in Engineering*, 111(5):493–500.
- Svenning, E., Larsson, F., and Fagerström, M. (2017b). Two-scale modeling of fracturing solids using a smeared macro-to-micro discontinuity transition. *Computational Mechanics*, 60(4):627–641.
- Svenning, E., Larsson, F., and Fagerström, M. (2019). A two-scale modeling framework for strain localization in solids: Xfem procedures and computational aspects. *Computers & Structures*, 211:43–54.
- Terada, K., Hori, M., Kyoya, T., and Kikuchi, N. (2000). Simulation of the multi-scale convergence in computational homogenization approaches. *International Journal of Solids and Structures*, 37(16):2285–2311.
- Toro, S., Sánchez, P. J., Blanco, P. J., de Souza Neto, E., Huespe, A. E., and Feijóo, R. (2016a). Multiscale formulation for material failure accounting for cohesive cracks at the macro and micro scales. *International Journal of Plasticity*, 76:75–110.
- Toro, S., Sánchez, P. J., Huespe, A. E., Giusti, S. M., Blanco, P. J., and Feijóo, R. (2014). A two-scale failure model for heterogeneous materials: numerical implementation based on the finite element method. *International Journal for Numerical Methods in Engineering*, 97(5):313–351.
- Toro, S., Sánchez, P. J., Podestá, J. M., Blanco, P. J., Huespe, A. E., and Feijóo, R. A. (2016b). Cohesive surface model for fracture based on a two-scale formulation: computational implementation aspects. *Computational mechanics*, 58(4):549–585.
- Turon, A., Camanho, P. P., Costa, J., and Dávila, C. (2006). A damage model for the simulation of delamination in advanced composites under variable-mode loading. *Mechanics of Materials*, 38(11):1072–1089.
- Turon, A., Davila, C. G., Camanho, P. P., and Costa, J. (2007). An engineering solution for mesh size effects in the simulation of delamination using cohesive zone models. *Engineering fracture mechanics*, 74(10):1665–1682.
- Turteltaub, S., van Hoorn, N., Westbroek, W., and Hirsch, C. (2018). Multiscale analysis of mixed-mode fracture and effective traction-separation relations for composite materials. *Journal of the Mechanics and Physics of Solids*, 117:88–109.
- Tvergaard, V. and Hutchinson, J. W. (1993). The influence of plasticity on mixed mode interface toughness. *Journal of the Mechanics and Physics of Solids*, 41(6):1119–1135.

- Tvergaard, V. and Hutchinson, J. W. (1996). On the toughness of ductile adhesive joints. *Journal of the Mechanics and Physics of Solids*, 44(5):789–800.
- Unger, J. F. (2013). An fe2-x1 approach for multiscale localization phenomena. *Journal of the Mechanics and Physics of Solids*, 61(4):928–948.
- Unger, J. F., Eckardt, S., and Könke, C. (2007). Modelling of cohesive crack growth in concrete structures with the extended finite element method. *Computer methods in applied mechanics and engineering*, 196(41-44):4087–4100.
- Ungsuwarungsri, T. and Knauss, W. G. (1987). The role of damage-softened material behavior in the fracture of composites and adhesives. *International Journal of Fracture*, 35(3):221–241.
- Ural, A. (2011). Cohesive modeling of bone fracture at multiple scales. *Procedia Engineering*, 10:2827–2832.
- Ural, A. and Mischinski, S. (2013). Multiscale modeling of bone fracture using cohesive finite elements. *Engineering Fracture Mechanics*, 103:141–152.
- Ural, A. and Vashishth, D. (2006). Cohesive finite element modeling of age-related toughness loss in human cortical bone. *Journal of biomechanics*, 39(16):2974–2982.
- US Department of Health and Human Services (2004). Bone health and osteoporosis: a report of the surgeon general. *Rockville, MD: US Department of Health and Human Services, Office of the Surgeon General*, 87.
- Van der Meer, F. and Sluys, L. (2009). A phantom node formulation with mixed mode cohesive law for splitting in laminates. *International Journal of Fracture*, 158(2):107.
- Van der Meer, F. P. (2012). Mesolevel modeling of failure in composite laminates: constitutive, kinematic and algorithmic aspects. *Archives of Computational Methods in Engineering*, 19(3):381–425.
- Van Mier, J. G. (2012). *Concrete fracture: a multiscale approach*. CRC press.
- Van Mier, J. G. (2017). *Fracture processes of concrete*. CRC press.
- Vashishth, D. (2004). Rising crack-growth-resistance behavior in cortical bone:: implications for toughness measurements. *Journal of biomechanics*, 37(6):943–946.
- Vashishth, D., Tanner, K., and Bonfield, W. (2000). Contribution, development and morphology of microcracking in cortical bone during crack propagation. *Journal of biomechanics*, 33(9):1169–1174.
- Verhoosel, C. V. and de Borst, R. (2013). A phase-field model for cohesive fracture. *International Journal for numerical methods in Engineering*, 96(1):43–62.

- Verhoosel, C. V., Remmers, J. J., and Gutiérrez, M. A. (2009). A dissipation-based arc-length method for robust simulation of brittle and ductile failure. *International Journal for Numerical Methods in Engineering*, 77(9):1290–1321.
- Verhoosel, C. V., Remmers, J. J., Gutiérrez, M. A., and De Borst, R. (2010). Computational homogenization for adhesive and cohesive failure in quasi-brittle solids. *International Journal for Numerical Methods in Engineering*, 83(8-9):1155–1179.
- Wang, X., Bank, R. A., TeKoppele, J. M., and Agrawal, C. M. (2001). The role of collagen in determining bone mechanical properties. *Journal of orthopaedic research*, 19(6):1021–1026.
- Wang, Y. and Waisman, H. (2016). From diffuse damage to sharp cohesive cracks: A coupled xfm framework for failure analysis of quasi-brittle materials. *Computer Methods in Applied Mechanics and Engineering*, 299:57–89.
- Wells, G. and Sluys, L. (2001a). Three-dimensional embedded discontinuity model for brittle fracture. *International Journal of Solids and Structures*, 38(5):897–913.
- Wells, G. N. and Sluys, L. (2001b). A new method for modelling cohesive cracks using finite elements. *International Journal for Numerical Methods in Engineering*, 50(12):2667–2682.
- Willett, T., Josey, D., Lu, R. X. Z., Minhas, G., and Montesano, J. (2017). The micro-damage process zone during transverse cortical bone fracture: No ears at crack growth initiation. *Journal of the mechanical behavior of biomedical materials*, 74:371–382.
- Wright, T. and Hayes, W. (1977). Fracture mechanics parameters for compact bone-effects of density and specimen thickness. *Journal of Biomechanics*, 10(7):419–425.
- Wu, J.-Y., Li, F.-B., and Xu, S.-L. (2015). Extended embedded finite elements with continuous displacement jumps for the modeling of localized failure in solids. *Computer Methods in Applied Mechanics and Engineering*, 285:346–378.
- Wu, J. Y., Li, J., and Faria, R. (2006). An energy release rate-based plastic-damage model for concrete. *International Journal of Solids and Structures*, 43(3-4):583–612.
- Wu, L., Becker, G., and Noels, L. (2014). Elastic damage to crack transition in a coupled non-local implicit discontinuous galerkin/extrinsic cohesive law framework. *Computer Methods in Applied Mechanics and Engineering*, 279:379–409.
- Xie, D., Salvi, A. G., Sun, C., Waas, A. M., and Caliskan, A. (2006). Discrete cohesive zone model to simulate static fracture in 2d triaxially braided carbon fiber composites. *Journal of Composite Materials*, 40(22):2025–2046.
- Xie, D. and Waas, A. M. (2006). Discrete cohesive zone model for mixed-mode fracture using finite element analysis. *Engineering fracture mechanics*, 73(13):1783–1796.

- Xu, X.-P. and Needleman, A. (1993). Void nucleation by inclusion debonding in a crystal matrix. *Modelling and Simulation in Materials Science and Engineering*, 1(2):111.
- Xu, X.-P. and Needleman, A. (1994). Numerical simulations of fast crack growth in brittle solids. *Journal of the Mechanics and Physics of Solids*, 42(9):1397–1434.
- Yan, J., Mecholsky Jr, J. J., and Clifton, K. B. (2007). How tough is bone? application of elastic–plastic fracture mechanics to bone. *Bone*, 40(2):479–484.
- Yang, Q. and Cox, B. (2005). Cohesive models for damage evolution in laminated composites. *International Journal of Fracture*, 133(2):107–137.
- Yang, Q., Cox, B., Nalla, R., and Ritchie, R. (2006a). Re-evaluating the toughness of human cortical bone. *Bone*, 38(6):878–887.
- Yang, Q., Cox, B. N., Nalla, R. K., and Ritchie, R. (2006b). Fracture length scales in human cortical bone: the necessity of nonlinear fracture models. *Biomaterials*, 27(9):2095–2113.
- Yu, H., Olsen, J. S., Olden, V., Alvaro, A., He, J., and Zhang, Z. (2016). Viscous regularization for cohesive zone modeling under constant displacement: An application to hydrogen embrittlement simulation. *Engineering Fracture Mechanics*, 166:23–42.
- Yvonnet, J., Gonzalez, D., and He, Q.-C. (2009). Numerically explicit potentials for the homogenization of nonlinear elastic heterogeneous materials. *Computer Methods in Applied Mechanics and Engineering*, 198(33-36):2723–2737.
- Zander, N., Ruess, M., Bog, T., Kollmannsberger, S., and Rank, E. (2017). Multi-level hp-adaptivity for cohesive fracture modeling. *International Journal for Numerical Methods in Engineering*, 109(13):1723–1755.
- Zhang, S. and Oskay, C. (2017). Reduced order variational multiscale enrichment method for thermo-mechanical problems. *Computational Mechanics*, 59(6):887–907.
- Zi, G. and Belytschko, T. (2003). New crack-tip elements for xfem and applications to cohesive cracks. *International Journal for Numerical Methods in Engineering*, 57(15):2221–2240.
- Zienkiewicz, O. C. and Zhu, J. Z. (1987). A simple error estimator and adaptive procedure for practical engineering analysis. *International journal for numerical methods in engineering*, 24(2):337–357.
- Zimmermann, E. A., Schaible, E., Bale, H., Barth, H. D., Tang, S. Y., Reichert, P., Busse, B., Alliston, T., Ager, J. W., and Ritchie, R. O. (2011). Age-related changes in the plasticity and toughness of human cortical bone at multiple length scales. *Proceedings of the National Academy of Sciences*, 108(35):14416–14421.

- Ziopoulos, P. (1998). Recent developments in the study of failure of solid biomaterials and bone: 'fracture' and 'pre-fracture' toughness. *Materials Science and Engineering: C*, 6(1):33–40.
- Ziopoulos, P. and Currey, J. (1998). Changes in the stiffness, strength, and toughness of human cortical bone with age. *Bone*, 22(1):57–66.